

# UC Berkeley

## UC Berkeley Electronic Theses and Dissertations

### Title

Molecular Precursors to Actinide Oxide and Nitride Nanomaterials

### Permalink

<https://escholarship.org/uc/item/698120j5>

### Author

Straub, Mark Daniel

### Publication Date

2021

Peer reviewed|Thesis/dissertation

Molecular Precursors to Actinide Oxide and Nitride Nanomaterials

By

Mark D. Straub

A dissertation submitted in partial satisfaction of the

requirements for the degree of

Doctor of Philosophy

in

Chemistry

in the

Graduate Division

of the

University of California, Berkeley

Committee in charge:

Professor John Arnold, Chair

Professor Kenneth Raymond

Professor Karl van Bibber

Spring 2021

## Molecular Precursors to Actinide Oxide and Nitride Nanomaterials

All rights reserved.

Copyright of this Dissertation is held by Mark D. Straub.

This work is protected against unauthorized copying under Title 17, United States Code.

Chapter 2 was adapted with permission from Mark D. Straub, John Arnold, Julianna Fessenden, and Jaqueline Kiplinger. “Recent Advances in Nuclear Forensic Chemistry.” *Anal. Chem.*, 2021, **93**, 3-22. Copyright 2021 American Chemical Society.

Chapter 3 was adapted with permission from Mark D. Straub, Jennifer Leduc, Michael Frank, Aida Raauf, Trevor D. Lohrey, Stefan G. Minasian, Sanjay Mathur, and John Arnold. “Chemical Vapor Deposition of Phase-Pure Uranium Dioxide Thin Films from Uranium(IV) Amidate Precursors.” *Angew. Chem.*, 2019, **58**, 5749-5753. Copyright 2019 Wiley-VCH.

Chapter 4 was adapted with permission from Mark D. Straub, Erik T. Ouellette, Michael A. Boreen, Jacob A. Branson, Alex Ditter, A. L. David Kilcoyne, Trevor D. Lohrey, Matthew A. Marcus, Maria Paley, José Ramirez, David K. Shuh, Stefan G. Minasian, and John Arnold. “Thorium Amidates Function as Single-Source Molecular Precursors for Thorium Dioxide.” *Chem. Commun.*, 2021, in press, with permission from the Royal Society of Chemistry.

Chapter 5 was adapted with permission from Mark D. Straub, Stephan Hohloch, Stefan G. Minasian, and John Arnold. “Homoleptic U(III) and U(IV) Amidate Complexes.” *Dalton Trans.*, 2018, **47**, 1772-1776, with permission from the Royal Society of Chemistry.

Chapter 6 was adapted with permission from Mark D. Straub, Liane M. Moreau, Yusen Qiao, Erik T. Ouellette, Michael A. Boreen, Trevor D. Lohrey, Nicholas S. Settineri, Stephan Hohloch, Corwin H. Booth, Stefan G. Minasian, and John Arnold. “Amidinate Supporting Ligands Influence Molecularity in Formation of Uranium Nitrides.” *Inorg. Chem.*, 2021, in press. Copyright 2021 American Chemical Society.

Abstract

**Molecular Precursors to Actinide Oxide and Nitride Nanomaterials**

By

Mark D. Straub

Doctor of Philosophy in Chemistry

University of California, Berkeley

Professor John Arnold, Chair

**Chapter 1.** The overarching hypothesis and goals of this work are stated. Actinide molecules and nanomaterials are introduced as model systems for nuclear fuels and nuclear forensics. Routes to develop new actinide molecules and materials from bespoke molecular precursors are described.

**Chapter 2.** The current state of nuclear forensic chemistry is reviewed, with discussion of pre- and post-detonation scenarios. Advances in synthetic chemistry and actinide nanomaterials are emphasized, and their relevance to modern nuclear forensic capabilities is highlighted. Numerous real-world case studies from nuclear smuggling and weapons fallout are analyzed and discussed.

**Chapter 3.** Volatile uranium(IV) amidate complexes are synthesized as single-source molecular precursors to uranium oxide films. These complexes are found to decompose to  $\text{UO}_2$  through an alkene elimination mechanism, enabling epitaxial stabilization of stoichiometric  $\text{UO}_2$  on {111} silicon substrates. Chemical vapor deposition (CVD) of these single-source precursors yields crystalline, phase-pure  $\text{UO}_2$  films with a fir tree-like microstructure and a high surface area.

**Chapter 4.** Thorium(IV) amidate complexes are synthesized as volatile single-source molecular precursors for thorium dioxide. The effects of different ligand substituents towards the thermal properties and decomposition mechanism of the precursors are explored. Using X-ray diffraction and spectroscopy to characterize the decomposition products, the purity and crystallinity of  $\text{ThO}_2$  samples formed from these precursors are compared.

**Chapter 5.** The syntheses of the first homoleptic uranium(III) and uranium(IV) amidate complexes are described. These can be interconverted by chemical reduction/oxidation, showing an unusual change in coordination number from four in the uranium(III) complex to eight in the uranium(IV) complex in the solid state structures.

**Chapter 6.** Three new bridging uranium nitride complexes are synthesized from amidinate-supported precursors and their structural and magnetic properties are explored. The amidinate

ligand substituents are seen to affect the composition and nuclearity of the nitride products. Using  $^{15}\text{N}$  labeling and acid hydrolysis, the nitrido ligands in all three complexes are proven to form via two-electron reduction of azide. Uranium complexes in the +3, +4, and +5 oxidation states are synthesized and magnetically characterized to provide a reference for the magnetic behavior of the nitrides, all three of which are found to contain uranium(IV) at each metal center.

**Appendix.** Various projects that have not yet been published are discussed. These include uranium(IV) and uranium(VI) amidate precursors, uranium(IV) heterometallic complexes, actinide triazenide complexes, and precursors for thorium nitride materials.

# Molecular Precursors to Actinide Oxide and Nitride Nanomaterials

## Table of Contents

<b>Acknowledgements</b> .....	iv
<b>Chapter 1. Motivations for the Study of Actinide Molecules and Materials</b> .....	1
Actinide Nanomaterials as Model Systems for Nuclear Fuels .....	2
Selection of Precursors for Actinide Oxide and Nitride Nanomaterials .....	4
Linking the Molecular and Materials Chemistry of the Actinides .....	6
References .....	7
<b>Chapter 2. Recent Advances in Nuclear Forensic Chemistry</b> .....	10
Introduction.....	11
Nuclear Forensics: Objectives and Scope.....	11
Overview of Analytical Methods.....	12
Electromagnetic Spectroscopy and Diffraction .....	15
Radiochemical Techniques .....	20
Mass Spectrometry.....	22
Microanalytical Techniques.....	24
Interface with Synthetic Chemistry .....	30
Post-detonation Analysis .....	34
Conclusions.....	39
References.....	40
<b>Chapter 3. Chemical Vapor Deposition of Phase-Pure Uranium Dioxide Thin Films from Uranium(IV) Amidate Precursors</b> .....	49
Introduction.....	50
Results and Discussion .....	51
Summary and Conclusions .....	58
Experimental.....	58

References.....	66
<b>Chapter 4. Thorium Amidates Function as Single-Source Molecular Precursors for Thorium Dioxide</b> .....	68
Introduction.....	69
Results and Discussion .....	69
Summary and Conclusions .....	73
Experimental.....	74
References.....	85
<b>Chapter 5. Synthesis of Homoleptic Uranium(III) and Uranium(IV) Amidate Complexes</b> .....	88
Introduction.....	89
Results and Discussion .....	89
Summary and Conclusions .....	93
Experimental.....	93
References.....	97
<b>Chapter 6. Amidinate Supporting Ligands Influence Molecularity in Formation of Uranium Nitrides</b> .....	100
Introduction.....	101
Results and Discussion .....	101
Summary and Conclusions .....	110
Experimental.....	110
References.....	123
<b>Appendix</b> .....	126
Uranium Amidates as Precursors for UO <sub>2</sub> Materials .....	127
Uranyl Amidates as Precursors for UO <sub>3</sub> Materials .....	128
Heterometallic Precursors for Uranium-Group 11 Materials .....	130

Actinide Triazenide Complexes.....	131
Precursor for Thorium Nitride Materials .....	135
Experimental .....	135
References.....	146



## Acknowledgements

The Ph.D. process has been a long journey for me, and I am immensely grateful to the people around me who have supported and encouraged me as I figured out how to navigate the challenging landscape of academic research. To my friends, family, advisors, and colleagues who have been there for me, I thank you from the bottom of my heart. Most of all, I am thankful for my girlfriend, Bridget, and for my parents, who have stood by me every step of the way.

When I came to UC Berkeley, I had never performed inorganic synthesis and everything in my research project was new to me. Learning how to use a Schlenk line and work inside a glovebox was challenging, especially when paired with the simultaneous requirements of teaching, applying for fellowships, taking classes, and trying to understand the literature behind a research project that was entirely different from any chemistry I had ever seen. Looking back on these experiences, my time here at UC Berkeley has enabled me to learn so much about how to solve hard problems and become comfortable with the unknown.

Graduate school has been one of the most challenging parts of my life, partly due to the rigorous nature of scientific research and partly due to the difficulties I have faced outside the lab. Before starting my Ph.D., I had spent the previous five months traveling through America, living in a tent and rock climbing nearly every day. Within a week, I jumped into the most difficult academic setting of my life. Instead of spending my time with a crowd of smiling goofball climbers, I was suddenly embroiled in a serious and intense program surrounded by somber faces and high stress. I found myself near the bottom of the intellectual pecking order, and I was disheartened to hear comments from my cohort about how I was “too dumb” to work with on problem sets or that I would almost certainly fail my qualifying exam. We like to brush these things under the rug in academia, but we can only heal the longstanding culture of academic bullying by acknowledging the underbelly of the high-pressure academic environment and address this form of thinking at its root. Neurodiversity has a valuable place in the realm of science, and we do not grow taller by cutting others down. Towards this end, I would like to thank the people who have taken the time to see me as a whole person, especially when I was struggling with my self-image as a scientist. To the people who feel lost, discouraged, and alone, know this: you are seen. Your value does not lie in your ability to grind yourself down to fit into someone else’s mold. Rather, your value comes from seeing the world through a different lens, and from staying true to your own self-identity under immense pressure to conform.

Throughout the academic rigor of graduate school, I have encountered rejected papers, failed projects, bizarre and painful health issues, a global pandemic, and the death of many loved ones. By passing through these trials and coming out on the other end, I feel like I have come to know an inner resilience that will stay with me for the rest of my life. I entered into the tunnel of the Ph.D. scared and naïve, and I leave with confidence, for I now know in my heart that I can weather any storm. Much more than the deep knowledge of a given field, I think that tenacity amid hardship is the true value of gaining a Ph.D., for anyone who walks this path must eventually face a series of obstacles that appear insurmountable and surmount them anyway. In this way, I am incredibly grateful for the knowledge I have gained and for those who have helped to guide me along the path, especially when the sky grew dark and the waters turned murky.

So many of the positive lessons I have learned, and the growth I have experienced as a scientist and as a person, have been a result of the excellent mentorship I have received from my two Ph.D. advisors, John Arnold and Stefan Minasian. The atmosphere of flexibility and independence I have experienced in both labs has contributed immensely to my success as a scientist. Because of John's earnest advice and boundless passion for chemistry, I have been able to explore a tremendous amount of synthetic space and to succeed or fail in my own endeavors, while always knowing that I could ask for guidance at any time and receive it with open arms. Because of Stefan's talent in coordinating and networking, I was able to access many resources that were crucial to the success and to the future of my research projects. Both of you have taught me so much, and I will always be grateful for the knowledge you have given me and for the proficiency you have helped me to develop.

To Jackie Kiplinger and Julianna Fessenden, thank you for taking me under your wing at LANL and for believing in me. That summer internship was huge in helping me find my confidence, and I think our review on nuclear forensics turned out to be exactly what I hoped it would. Los Alamos is a beautiful place, and I really enjoyed my time there, both inside and outside the gates of the national lab.

To Liane Moreau, you taught me everything I know about nanoparticle chemistry, and you were a fantastic mentor to me. I always enjoyed your company and your insights, and I know without a shadow of a doubt that you are a brilliant scientist with a bright future as a new professor. You have an inner light that I have always admired.

To Jade Fostvedt, you brought a culture of positivity and kindness to the Arnold Group that has rippled out in amazing ways. Thank you for showing me that we can succeed in difficult environments by lifting each other up, and that we don't have to sacrifice our individuality to succeed in academia.

To Erik Ouellette and Michael Boreen, you have been a major help on so many of my projects that I don't know where I would be without your assistance. Thank you for your years of assistance with crystallography and for all the papers you have helped edit. I always know that I can count on you to provide feedback and advice.

To Dominic Russo, I've spent so many late nights bantering about science with you. Your ideas come way out of left field to solve the tricky problems we often face in nanoparticle chemistry, and you've moved the project forward in ways that I don't think anyone else could ever have thought up.

To Chris Ye and Joe Brackbill, thanks for listening to my bad jokes, senior grad student grumbling, and screwball ideas. I enjoyed the time spent goofing around in 508 and really appreciate your constant feedback on my projects as I continually distracted you.

To Sheridan Kelly, it is a breath of fresh air to talk with you about books, science, and life. I'm so glad that you decided to join the Arnold and Minasian groups and it makes me happy to pass the torch of my main project to you, as I think you have a sharp mind and a bright future.

To everyone else who has passed through the Arnold and Minasian groups during my time here, thank you for teaching me so much about chemistry and for all the conversations that we have had together. It would not have been the same without all of you.

To the myriad collaborators, researchers, instrument specialists, and support staff who have helped enable my research, thank you for all of your assistance and expertise. There are truly too many people to name, and that shows how invaluable the support of each and every one of you has been throughout this entire process.

To my parents, Dan and Jan, you have always been there for me, especially in my darkest days. I will always love you from the bottom of my heart, and I truly could not have made it through without your unending support and love. I have seen the hardships you have both faced throughout your lives, and knowing that you could find the strength to overcome has been the guiding light that I needed to help me do the same. To my brother, Sam, I am so proud of your path and your strength. You are incredibly talented at so many things, and I can't wait to see you again.

To my girlfriend, Bridget, I owe so much to you. You have been there with me through so many hard nights and helped me to find strength no matter what. You have done so much to support me that I can only barely begin to express it here, but I'll try in a few words. Bridget, I love you so much and I am so glad to be with you.

To my friends in Cal Climbing, I've had so much fun climbing with you all over the years and spinning tales by the campfire. You are some of my favorite people in Berkeley. To my friends scattered across the country, I am so glad to have you in my life. Chris, Josh, Holden, Andrew, Megan, Saumitra, Hannah, Jesse, and many others, thank you for always seeing me for who I truly am and staying by my side.

To my friends and family who passed on before I could graduate, I will never forget you. Marc-Andre Leclerc, you taught me so much about climbing and about life. You were like the big brother I never had. I am eternally grateful for all the lessons you taught me and all the joy you showed me in the mountains. Bud Davis, you always believed in me, and you introduced me to the joy of chemistry. Thank you for always making time and space for me, no matter what. Mike Metrocavich, you were always funny and spontaneous and I will miss your energy. Grandbob, your calm confidence and dry humor always brightened up my day and put a smile on my face. Mom-mom, you were the kindest, sweetest little old lady who still remained tough as nails. Pop-pop, I liked your unique perspectives on things and I will miss you. Grammy, you were always welcoming and warm and you loved to put a smile on my face. All of you meant so much to me and I am eternally grateful for your support and your love throughout my life.

Finally, I owe a debt of gratitude to the natural places that have been my heart and my home throughout my Ph.D. It is easy to spend our time rushing through our checklists and errands in civilization, but to take a step outside into the vastness of the American wilderness is a truly eye-opening experience. It is humbling and inspiring to step back from our hectic routines; to listen to the quiet peace of the wind blowing through the grass, feel the chilly wind of an oncoming storm, bask in the strong confidence of the mountains, and sense the vibrancy of the plants, fungi, and animals that inhabit these places. To be able to climb, hike, and ski in these beautiful places is a privilege that we should never take for granted, for public lands are truly priceless until they are sold forever. Climbing in Yosemite, Lover's Leap, Calaveras Dome, and so many other beautiful places in California has been a real treat; these places have helped me time and time again to find my center and return to my research feeling confident and grounded. I would like to thank the Access Fund for helping to keep these wild places accessible to all. Rock climbing is the fire in my belly, the wind in my hair, the oneness in my soul. By teaching me to channel my drive, face my fears, and push forward into the unknown, climbing has been an invaluable guide to me throughout my Ph.D.

As I move forward into the next stage of my life, I will remain forever grateful for the knowledge I have gained, the mentorship I have received, and the camaraderie I have experienced along the way. In some ways, I have learned more than I ever could have imagined, and I cannot wait to step into the broader world.

# Chapter 1

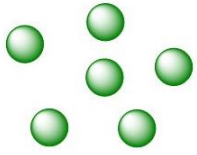
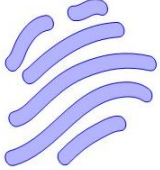

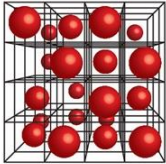
## Motivations for the Study of Actinide Molecules and Materials

## Actinide Nanomaterials as Model Systems for Nuclear Fuels

As we move into a future of steadily increasing power consumption and rising emissions, the need for clean and efficient power production becomes ever more important. In 2019, nuclear power plants were responsible for generating 19.7% of the total energy consumed in the United States, serving as the largest source of clean energy in the nation.<sup>1</sup> Throughout the course of the nuclear program, significant improvements in plant design have led to nuclear reactors that are vastly safer and more efficient than previous iterations.<sup>2</sup> However, even in modern commercial reactors, under 7% of the uranium in nuclear fuel undergoes fission to produce energy; the remainder is relegated to the radioactive waste stream in the form of spent fuel.<sup>3,4</sup> Looking to the future, new nuclear fuel designs have been proposed that could dramatically enhance the efficiency and lifetime of the fuel, resulting in greater power yield and lower waste production.<sup>2,5</sup> Uranium dioxide (UO<sub>2</sub>) fuel is currently used in all nuclear power plants within the United States, but alternative fuel compositions may confer significant benefit.<sup>6</sup> Uranium mononitride (UN) is a prominent example; this material possesses higher thermal conductivity and greater energy density than conventional UO<sub>2</sub> fuel, conferring higher power output and enhanced safety margins against thermal meltdown.<sup>7</sup> Thorium-based fuels have also been proposed to have several advantages over uranium dioxide, including greater resistance to nuclear proliferation and lower quantities of highly radiotoxic transuranic elements in the waste stream.<sup>8,9</sup>

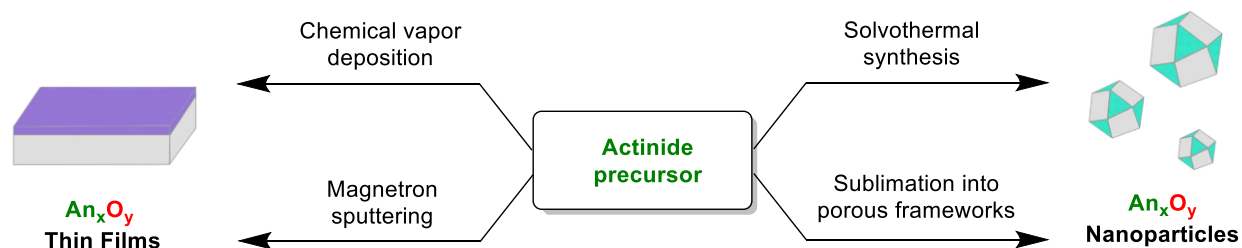
In addition to these alternative fuel compositions, modifications to the structure of conventional actinide oxide fuels have also been proposed to improve efficiency.<sup>10</sup> Upon irradiation with a high neutron flux, porous channels can form in UO<sub>2</sub> fuel pellets at the edges of the material, giving rise to a nanocrystalline morphology called the high burnup structure (HBS).<sup>11</sup> This structural change can enhance plasticity and decrease thermal gradients in UO<sub>2</sub> fuel pellets,<sup>12</sup> but the pores in HBS UO<sub>2</sub> can also trap fission gases and build up high internal pressures, leading to radial pellet cracking and reducing the lifespan of the fuel.<sup>13,14</sup> UO<sub>2</sub> fuel materials with ordered mesoporous channels have been proposed to offer the advantages of HBS fuel while also allowing fission gases to propagate more freely, thus decreasing pressure inside the fuel pellet and enhancing the lifespan of the material.<sup>4,15</sup>

Despite the numerous advantages of these fuels with novel compositions and morphologies, their implementation has been hindered by the economic cost of building reactors compatible with alternative fuel compositions and the difficulty of fabricating nanostructured actinide materials.<sup>4,16</sup> Fortunately, many chemical and physical properties of fuel materials, such as corrosion, reactivity, and thermal decomposition, can be tested in a laboratory setting using model systems.<sup>17,18</sup> Using these model systems, the pros and cons of potential fuel materials can be screened in a rapid and cost-effective manner, informing future reactor design and facilitating the faster and safer development of next-generation commercial nuclear plants. As chemical reactions such as corrosion and oxidation primarily take place at the surface of a material, model systems to study these processes should be designed to have high surface areas.<sup>19</sup> This can be achieved by synthesizing actinide materials with reduced dimensionality, such as nanoparticles (0-D), nanowires (1-D), thin films (2-D), and porous frameworks (3-D).<sup>20</sup>

			
<b>0-D</b>	<b>1-D</b>	<b>2-D</b>	<b>3-D</b>
<b>Nanoparticles</b>	<b>Nanowires</b>	<b>Thin films</b>	<b>Frameworks</b>

**Figure 1.1:** Dimensionality of nanomaterials.

However, there are relatively few known methods to reliably control the morphology of actinide nanomaterials while maintaining the purity of a desired composition and phase.<sup>4,21</sup> This is especially challenging in the case of uranium due to the accessibility of multiple stable oxidation states for uranium materials. At least 10 different stoichiometric compositions of uranium oxide are known, some with multiple phases, in addition to a plethora of ill-defined amorphous and/or nonstoichiometric forms.<sup>22</sup> To further complicate the problem, even compounds that are often considered relatively stable, such as  $\text{UO}_2$ , can oxidize in the presence of air and water to form higher oxides such as  $\text{U}_3\text{O}_7$  and  $\text{U}_4\text{O}_9$ . Formation of these higher oxides can lead to grain boundaries and other defects that can complicate the study of pure materials on the nanoscale as a result of differences in their lattice parameters.<sup>17,23</sup> Some innovative solutions have been proposed to overcome this challenge, including the use of polymer-assisted deposition to epitaxially stabilize  $\text{UO}_2$  and  $\text{UN}_2$  thin films<sup>24</sup> and compositional control of hydrothermally synthesized uranium oxide nanoparticles by varying the solution pH.<sup>25</sup> However, although these techniques can be used to access various phase-pure materials, they are limited to aqueous systems, precluding access to more reactive fuel materials such as UN. Physical deposition methods such as sputtering have been used to generate crystalline thin films of air-sensitive uranium and thorium nitrides,<sup>26,27</sup> but these approaches are limited to the production of 2-D materials. Despite the substantial capabilities of these varied processes, no single method has yet been reported that can produce air-sensitive actinide nanomaterials across multiple dimensionalities. This challenge motivates a bottom-up chemical approach to overcome the aforementioned limitations and create a tunable system for actinide materials synthesis.



**Scheme 1.1:** Techniques used to synthesize actinide oxide nanomaterials.

## Selection of Precursors for Actinide Oxide and Nitride Nanomaterials

Compositional and morphological control of nanomaterials can be achieved through the controlled decomposition of a coordination complex containing the desired elements. In this bottom-up approach, the coordination complex behaves as a “molecular precursor” to the desired material. Molecular precursors can be used to produce nanomaterials with a wide array of compositions and morphologies; this strategy has been applied with great success in transition metal nanoparticle<sup>28–31</sup> and thin film syntheses<sup>32–36</sup>. In addition, the molecular precursor approach provides dimensional flexibility: nanostructured materials from 0-D to 3-D have been synthesized by thermal decomposition of molecular precursors.<sup>37,38</sup> Considering these significant advantages, the development of new molecular precursors for actinide materials could facilitate access to previously-inaccessible actinide nanostructures.<sup>21</sup> Extending this approach to the actinides has proven challenging, however, because of the difficulty in controlling the nanostructure of actinide materials.<sup>4,39</sup>

In order to overcome this challenge, we must be able to synthesize molecular precursors that can undergo clean conversion to form the desired actinide materials. Moreover, we need to understand and control the formation mechanisms of these materials from the precursors, i.e. they cannot be treated as emerging from a black box. This is a critically important consideration in developing bottom-up syntheses for phase-pure actinide oxide ( $An_xO_y$ ) and nitride ( $An_xN_y$ ) nanomaterials across multiple dimensionalities; in order to build these structures, we must first understand how to construct the building blocks and then we must be able to control how they assemble into ordered materials. This can be accomplished by synthesizing molecular precursors with the right elemental composition and thermal properties, then identifying the decomposition mechanisms of these precursors and the materials they form via decomposition, then finally developing a process that can stabilize a specific phase of the desired material.<sup>40</sup>

In this bottom-up synthetic approach, the choice of molecular precursor plays a key role in the formation of the desired nanomaterial. Small changes to precursor ligands can affect the thermal properties, decomposition mechanism, shape, homogeneity, and purity of the final product.<sup>28,40,41</sup> This is readily apparent in chemical vapor deposition (CVD) processes, where alteration of the ligand by as little as one methyl group can mean the difference between high-purity thin films and no deposition at all.<sup>36</sup> Variables that should be considered when selecting a precursor include decomposition temperature, volatility (for vapor phase methods), solubility (for solution methods), redox behavior, compatibility with other reagents, and decomposition mechanism. It is also important to note that an ideal precursor for one type of nanomaterial, e.g. thin films, is not always a good precursor for another nanomaterial, e.g. nanoparticles. For instance, a precursor with sufficient volatility is required for most forms of CVD, yet this requirement is completely null when synthesizing nanoparticles from solution. Similarly, a precursor for a dual-source thin film growth process, such as atomic layer deposition (ALD), may require a different reactivity profile than a precursor for a single-source process.<sup>40</sup> Consequently, it can be useful to develop a small library of precursors and choose the most favorable precursor for each specific application.<sup>42,43</sup> Regardless of the process used, however, understanding the chemical stability and reactivity of the precursor is often paramount to a successful nanomaterials synthesis.

The properties of molecular precursors can be controlled by first choosing an appropriate ligand scaffold, then functionalizing the ligand to optimize the desired properties. The effect of different substituents on physical and chemical properties can thus be used to guide the design of

bespoke precursors for a specific application. For example, high volatility is often found in molecules with weak intermolecular interaction forces. Therefore, choosing a precursor with a small dipole moment can be useful if volatility is a consideration; one way to accomplish this is to use a ligand with branched alkyl substituents, for example.<sup>44</sup> Reactivity can be mediated by changing the degree of steric protection around the metal center, or by varying the electron donating ability of the ligand.<sup>45</sup> Thermal stability is related to the kinetic accessibility of thermodynamically favorable decomposition pathways, and it can be controlled by using substituents that either facilitate or prevent a given decomposition mechanism.<sup>46</sup> In general, precursors that thermolyze via a single mechanism tend to form cleaner, more crystalline products than precursors with multiple accessible decomposition pathways.<sup>40</sup> Using this approach, there is a clear benefit to ligands that can be synthesized in a straightforward and modular fashion, enabling multiple variants to be screened with relative ease.

Upon consideration of these myriad variables, we have selectively designed new uranium and thorium coordination complexes as molecular precursors for actinide oxide and nitride nanomaterials. Uranium and thorium amidate complexes were synthesized here as precursors to UO<sub>2</sub> and ThO<sub>2</sub> materials, and uranium amidinate complexes were synthesized as precursors to U<sub>x</sub>N<sub>y</sub> materials. These precursors were evaluated by thermal stability, decomposition mechanism, reactivity, volatility, solubility, and relative ease of synthesis.



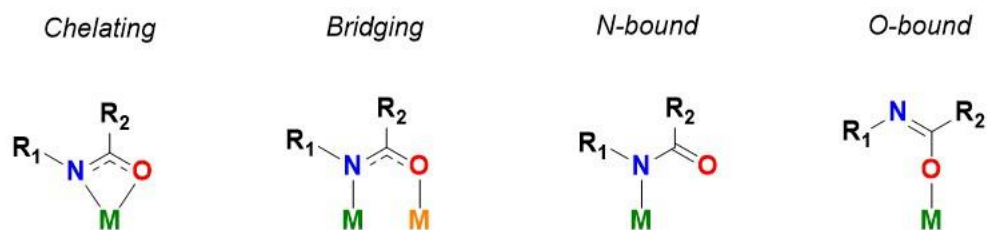
**Figure 1.2:** Ligand systems used in this work.

Metal amidinate complexes have been broadly applied as precursors for chemical vapor deposition of thin films, including metal nitrides.<sup>32,43,46-49</sup> These complexes are often relatively volatile and possess substantial thermal stability. Amidinate ligands can be synthesized in a single step through reaction of an alkyllithium reagent with a carbodiimide, enabling the steric and electronic properties of the ligand to be easily tuned. Additionally, the amidinate ligand framework contains no oxygen or halogen atoms, which could potentially lead to contamination of uranium nitride materials due to the high oxo- and halophilicity of uranium.<sup>22</sup>

Although metal amidate complexes are comparatively less well-studied, they have been used as effective precursors for early transition metal oxide thin films.<sup>36,50</sup> The presence of both oxygen and nitrogen donor atoms allows for a variety of binding modes in metal amidate complexes, with the geometry of binding affected by steric as well as electronic factors.<sup>51</sup> Hard Lewis acids, such as the actinides, are likely to bind amidates more strongly through the oxygen atom, while soft Lewis acids, like the late transition metals, tend to bind more strongly through the nitrogen atom.<sup>52,53</sup> Amidate ligands can be readily synthesized by deprotonation of amides<sup>21</sup> or by insertion of isocyanate into a metal-carbon bond.<sup>54</sup> Both amidinate and amidate complexes were chosen here for use as molecular precursors because of their relatively high volatility, thermal stability, and solubility in nonpolar solvents, in addition to the high degree of steric and electronic tunability of the ligand substituents. Taken together, these variables suggested highly favorable



performance of actinide amidate and amidinate complexes as molecular precursors for the bottom-up synthesis of actinide oxide and nitride nanomaterials.



**Figure 1.3:** Binding modes of amidates to metal centers.<sup>55</sup>

## Linking the Molecular and Materials Chemistry of the Actinides

When designing molecular precursors for actinide nanomaterials, it is important to consider not only the reactivity of the precursor itself, but also the reactive intermediates at all stages of the decomposition process. The composition and morphology of nanomaterials synthesized from molecular precursors are affected heavily by the chemical reactivity of the precursor throughout the entire synthetic process.<sup>28,56</sup> There are numerous ways in which this can occur, and understanding the reactivity of the precursor is often key to controlling formation of the desired product. For example, precursor thermolysis can lead to the formation of clusters, which can further react to form incipient nanoparticles.<sup>57</sup> Decomposition products of the original precursor can undergo unwanted side reactions with nanoparticles formed in solution.<sup>56</sup> Reducing or oxidizing conditions in materials synthesis can greatly impact the composition and phase of the product, especially for materials in which the metal can exist simultaneously in multiple oxidation states, e.g. uranium oxides.<sup>17,25,58</sup> By studying the reactivity of molecular precursors towards small molecules and redox agents, a more complete picture of the decomposition process can be achieved. In this way, fundamental studies into the chemical bonding and reactivity of actinide coordination complexes are tremendously important to inform the rational design of actinide oxide and nitride precursors.

The bonding and reactivity of the actinide elements bears some similarity to both lanthanides and transition metals, with a few key differences. The actinides, like the lanthanides, are large, electrophilic metals that react as hard Lewis acids, forming strong bonds with halides and chalcogenides.<sup>45</sup> Because electrons can be localized in s, p, d, and f orbitals of these elements, there is a formal “32-electron rule” that applies to f-block complexes; however, this theoretical limit is almost never reached. Consequently, steric factors play a major role in the geometry of the f-block elements.<sup>45</sup> Redox reactions in most lanthanides are limited, however, and all lanthanides (with the possible exception of Ce) mainly exist in the +3 oxidation state.<sup>45</sup> In contrast, the actinide elements U, Np, and Pu are stable across a wide range of oxidation states.<sup>59</sup> The redox behavior of these elements bears more similarity to the transition metals, among which reduction and oxidation reactions are well-known and common.<sup>59,60</sup>

Due to the relativistic expansion of the 5f and 6d orbitals in the actinide elements, orbital mixing and bond covalency are substantially more prominent in the actinides than the lanthanides.<sup>61,62</sup> The involvement of the 5f orbitals in bonding significantly affects the behavior of actinide complexes, contributing to the stability of species such as actinyl ions ( $AnO_2^{n+}$ ) and actinocenes, e.g.  $U(COT)_2$ .<sup>63</sup> Uranium has been reported in all oxidation states between U(II) and U(VI), although U(II) and U(III) are not stable in ambient conditions; air-free techniques are required to isolate these reduced species.<sup>22,45</sup> Thorium, by comparison, is only stable as Th(IV) under ambient conditions, although rare examples of Th(II) and Th(III) have been reported.<sup>64,65</sup> Due to their highly reducing behavior, actinides in low oxidation states such as U(III) and Th(III) can promote small molecule activation with a wide variety of substrates such as  $CO_2$ , 2,2'-bipyridine,  $N_2O$ , and organic azides.<sup>66</sup> Through these chemical transformations, molecular analogs to active surfaces in nuclear fuels can be isolated, enabling detailed mechanistic studies to be performed on reactive moieties such as actinide nitride and terminal oxide ligands.<sup>63,67</sup> Using a bottom-up approach, actinide coordination complexes can thus be developed as precursors to molecular and nanostructured systems, both of which can be independently used to model the surface reactivity of nuclear fuel materials.

In summary, the molecular precursor-based approach provides us with a versatile platform that can be used to synthesize actinide oxide and nitride nanomaterials with a range of reduced dimensionalities, from 0-D nanoparticles to 2-D thin films. Superior control of product composition and morphology can be accomplished through a detailed study of the entire synthetic process, from precursor reactivity to growth of the final materials. Using a combination of techniques drawn from organometallic chemistry and materials synthesis, precursors can be rationally designed and optimized for a given application by performing thermolysis and reactivity studies on a group of related coordination complexes. The most viable precursor for any bottom-up synthetic approach can then be chosen based on its decomposition mechanism, thermal properties, and chemical reactivity. By applying this design method to develop new actinide precursors, we have synthesized a variety of uranium and thorium nanomaterials and coordination complexes that can be used as model systems for next-generation nuclear fuels.

## References

- 1 U.S. Energy Information Administration, *Consumption and Efficiency*, 2019.
- 2 M. M. Abu-Khader, *Prog. Nucl. Energy*, 2009, **51**, 225–235.
- 3 Y. Oka, *Nuclear Reactor Design*, Springer, 2014.
- 4 S. J. Zinkle and G. S. Was, *Acta Mater.*, 2013, **61**, 735–758.
- 5 M. Jolkkonen, *GENIUS: Fabrication of Gen-IV nitride fuels*.
- 6 S. J. Zinkle, K. A. Terrani, J. C. Gehin, L. J. Ott and L. L. Snead, *J. Nucl. Mater.*, 2014, **448**, 374–379.
- 7 B. Ebbinghaus, J.-S. Choi, T. Meier, B. Ebbinghaus, J.-S. Choi and T. Meier, in *ANS International 2003 Winter Meeting*, 2003.
- 8 IAEA, *The Use of Thorium in Nuclear Power Reactors*, 1969.
- 9 A. J. Juhasz, R. A. Rarick and R. Rangarajan, *High Efficiency Nuclear Power Plants Using Liquid Fluoride Thorium Reactor Technology October 2009*, 2009.
- 10 P. Makowski, X. Deschanel, A. Grandjean, D. Meyer, G. Toquer and F. Goettmann, *New J. Chem.*, 2012, **36**, 531–541.
- 11 V. V Rondinella and T. Wiss, *Mater. Today*, 2010, **13**, 24–32.

- 12 J. Noirot, L. Desgranges and J. Lamontagne, *J. Nucl. Mater.*, 2008, **372**, 318-339.
- 13 K. Nogita and K. Une, *J. Nucl. Mater.*, 1997, **250**, 244-249.
- 14 W. J. Weber, R. C. Ewing, C. R. A. Catlow, T. Diaz De La Rubia, L. W. Hobbs, C. Kinoshita, H. Matzke, A. T. Motta, M. Nastasi, E. K. H. Salje, E. R. Vance and S. J. Zinkle, *J. Mater. Res.*, 1998, **13**, 1434-1484.
- 15 J. Spino, H. Santa Cruz, R. Jovani-Abril, R. Birtcher and C. Ferrero, *J. Nucl. Mater.*, 2012, **422**, 27-44.
- 16 N. Bauer, R. J. Brecha and G. Luderer, *Proc. Natl. Acad. Sci. U. S. A.*, 2012, **109**, 16805-16810.
- 17 H. Idriss, *Surf. Sci. Rep.*, 2010, **65**, 67-109.
- 18 J. Leduc, M. Frank, L. Jürgensen, D. Graf, A. Raauf and S. Mathur, *ACS Catal.*, 2019.
- 19 U. Diebold, S.-C. Li and M. Schmid, *Annu. Rev. Phys. Chem.*, 2010, **61**, 129-148.
- 20 P. R. Sajanalal, T. S. Sreepasad, A. K. Samal and T. Pradeep, *Nano Rev.*, 2011, **2**, 5883.
- 21 M. D. Straub, J. Leduc, M. Frank, A. Raauf, T. D. Lohrey, S. G. Minasian, S. Mathur and J. Arnold, *Angew. Chem. Int. Ed.*, 2019, **58**, 5749-5753.
- 22 I. Grenthe, J. Drożdżynński, T. Fujino, E. C. Buck, T. E. Albrecht-Schmitt and S. F. Wolf, in *The Chemistry of the Actinide and Transactinide Elements*, Springer Netherlands, Dordrecht, pp. 253-698.
- 23 L. Appel, J. Leduc, C. L. Webster, J. W. Ziller, W. J. Evans and S. Mathur, *Angew. Chem. Int. Ed.*, 2015, **54**, 2209-2213.
- 24 B. L. Scott, J. J. Joyce, T. D. Durakiewicz, R. L. Martin, T. M. McCleskey, E. Bauer, H. Luo and Q. Jia, *Coord. Chem. Rev.*, 2014, **266-267**, 137-154.
- 25 R. Zhao, L. Wang, Z.-J. Gu, L.-Y. Yuan, C.-L. Xiao, Y.-L. Zhao, Z.-F. Chai and W.-Q. Shi, *CrystEngComm*, 2014, **16**, 2645.
- 26 E. L. Bright, S. Rennie, M. Cattelan, N. A. Fox, D. T. Goddard and R. Springell, *Thin Solid Films*, 2018, **661**, 71-77.
- 27 T. Gouder, L. Havela, L. Black, F. Wastin, J. Rebizant, P. Boulet, D. Bouexière, S. Heathman and M. Idiri, *J. Alloys Compd.*, 2002, **336**, 73-76.
- 28 J. Park, J. Joo, G. K. Soon, Y. Jang and T. Hyeon, *Angew. Chem. Int. Ed.*, 2007, **46**, 4630-4660.
- 29 D. D. Vaughn Ii, J. Araujo, P. Meduri, J. F. Callejas, M. A. Hickner and R. E. Schaak, *Chem. Mater.*, 2014, **26**, 6226-6232.
- 30 L. Hu, C. Wang, R. M. Kennedy, L. D. Marks and K. R. Poeppelmeier, *Inorg. Chem.*, 2015, **54**, 740-745.
- 31 N. S. Karan, Y. Chen, Z. Liu and R. Beaulac, *Chem. Mater.*, 2016, **28**, 5601-5605.
- 32 S. B. Kim, C. Yang, T. Powers, L. M. Davis, X. Lou and R. G. Gordon, *Angew. Chem. Int. Ed.*, 2016, **55**, 10228-10233.
- 33 J. E. Bleau, C. J. Carmalt, S. A. O'Neill, I. P. Parkin, A. J. P. White and D. J. Williams, *Polyhedron*, 2005, **24**, 463-468.
- 34 E. Erdem and P. Jakes, *J. Mater. Chem.*, 2009, **19**, 1449-1457.
- 35 C. H. Winter, P. H. Sheridan, T. S. Lewkebandara, M. J. Heeg and J. W. Proscialc, *J. Am. Chem. Soc.*, 1992, **114**, 1095-1097.
- 36 A. L. Catherall, M. S. Hill, A. L. Johnson, G. Kociok-Köhn and M. F. Mahon, *J. Mater. Chem. C*, 2016, **4**, 10731-10739.
- 37 P. Pachfule, M. K. Panda, S. Kandambeth, S. M. Shivaprasad, D. D. Díaz and R. Banerjee, *J. Mater. Chem. A*, 2014, **2**, 7944-7952.

- 38 J. Leduc, J. I. Pacold, D. K. Shuh, C. L. Dong and S. Mathur, *Zeitschrift für Anorg. und Allg. Chemie*, 2017, 12–18.
- 39 Y. Shiokawa, R. Amano, A. Nomura and M. Yagi, *J. Radioanal. Nucl. Chem.*, 1991, **152**, 373–380.
- 40 S. E. Koponen, P. G. Gordon and S. T. Barry, *Polyhedron*, 2016, **108**, 59–66.
- 41 H. Pierson, *Handbook of Chemical Vapor Deposition (CVD)*, 1999.
- 42 L. G. Bloor, C. J. Carmalt and D. Pugh, *Coord. Chem. Rev.*, 2011, **255**, 1293–1318.
- 43 B. S. Lim, A. Rahtu, J.-S. Park and R. G. Gordon, *Inorg. Chem.*, 2003, **42**, 7951–7958.
- 44 D. Dobkin and M. Zuraw, in *Principles of Chemical Vapor Deposition*, 2003, pp. 95–148.
- 45 S. Cotton, *Lanthanide and Actinide Chemistry*, John Wiley & Sons, 2006.
- 46 S. T. Barry, *Coord. Chem. Rev.*, 2013, **257**, 3192–3201.
- 47 M. Gebhard, M. Hellwig, A. Kroll, D. Rogalla, M. Winter, B. Mallick, A. Ludwig, M. Wiesing, A. D. Wieck, G. Grundmeier, A. Devi, D. Schmeißer, J. R. Weber, J. B. Varley and C. Van de Walle, *Dalton Trans.*, 2017, **38**, 819.
- 48 T. B. Thiede, M. Krasnopolski, A. P. Milanov, T. De Los Arcos, A. Ney, H.-W. Becker, D. Rogalla, J. Winter, A. Devi and R. A. Fischer, *J. Chem. Mater.*, 2011, **23**, 1430–1440.
- 49 C. Camp, N. Settineri, J. Lefevre, A. R. Jupp, J. M. Goicoechea, L. Maron and J. Arnold, *Chem. Sci.*, 2015, **6**, 6379–6379.
- 50 T. Perera, *Wayne State University Dissertation*, 2012.
- 51 R. K. Thomson, *University of British Columbia Dissertation*, 2008.
- 52 W. Henderson, A. G. Oliver and C. E. F. Rickard, *Inorg. Chim. Acta*, 2000, **307**, 144–148.
- 53 M. W. Drover, J. A. Love and L. L. Schafer, *Chem. Soc. Rev.*, 2017, **46**, 2913–2940.
- 54 W. J. Evans, J. R. Walensky and J. W. Ziller, *Organometallics*, 2010, **29**, 945–950.
- 55 M. D. Straub, S. Hohloch, S. G. Minasian and J. Arnold, *Dalton Trans.*, 2018, **47**, 1772–1776.
- 56 Y. Xia, Y. Xiong, B. Lim and S. E. Skrabalak, *Angew. Chem. Int. Ed.*, 2009, **48**, 60–103.
- 57 C. Falaise, H. A. Neal and M. Nyman, *Inorg. Chem.*, 2017, **56**, 6591–6598.
- 58 H. He, P. Wang, D. D. Allred, J. Majewski, M. P. Wilkerson and K. D. Rector, *Anal. Chem.*, 2012, **84**, 10380–10387.
- 59 C. J. Burns and M. S. Eisen, in *The Chemistry of the Actinide and Transactinide Elements*, Springer Netherlands, Dordrecht, pp. 2799–2910.
- 60 J. Hartwig, *Organotransition Metal Chemistry: From Bonding to Catalysis*, University Science Books, 2010.
- 61 S. G. Minasian, J. L. Krinsky and J. Arnold, *Chem. Eur. J.*, 2011, **17**, 12234–12245.
- 62 A. Formanuk, A.-M. Ariciu, F. Ortu, R. Beekmeyer, A. Kerridge, F. Tuna, E. J. L. McInnes and D. P. Mills, *Nat. Chem.*, 2017, **9**, 578–583.
- 63 M. A. Boreen and J. Arnold, in *Encyclopedia of Inorganic and Bioinorganic Chemistry*, John Wiley & Sons, Ltd, 2018, pp. 1–15.
- 64 M. S. Wickleder, B. Fourest and P. K. Dorhout, in *The Chemistry of the Actinide and Transactinide Elements*, Springer Netherlands, Dordrecht, pp. 52–160.
- 65 R. R. Langeslay, M. E. Fieser, J. W. Ziller, F. Furche and W. J. Evans, *Chem. Sci.*, 2015, **6**, 517–521.
- 66 S. T. Liddle, *Angew. Chem. Int. Ed.*, 2015, **54**, 8604–8641.
- 67 D. M. King, F. Tuna, E. J. L. McInnes, S. T. Liddle, M. Ephritikhine et al., *Science*, 2012, **337**, 717–20.

## Chapter 2

# Recent Advances in Nuclear Forensic Chemistry

## Introduction

Nuclear forensics is a rapidly growing field with a widespread impact on global nonproliferation. From the beginning, nuclear forensic capabilities have been inextricably bound to existing limitations within chemistry and materials science. As nuclear forensics has continued to develop as a unique field of research, new advances in chemistry have revolutionized our ability to rapidly and quantitatively analyze radioactive materials for attribution. In particular, microanalytical techniques originally developed for nanoscience, such as micro-XRF, SIMS, and SEM-EDX, have enabled spatially-resolved chemical analyses to be performed with only nanograms of material. Such techniques have redefined the paradigm for pre- and post-detonation nuclear forensics, as large quantities of material are no longer necessary for full characterization and attribution. This Review details how modern nuclear forensic techniques have developed from their origins in chemistry, and provides real-world examples of how these techniques have been used to characterize radioactive materials, including fallout from nuclear detonations such as the 1945 Trinity test.

Following the collapse of the Soviet Union in the early 1990s, a variety of nuclear materials were lost, misplaced, or stolen in the resultant political turmoil.<sup>1</sup> These events created a new challenge within international security- the risk of nuclear proliferation by clandestine smuggling of radioactive materials. Illicit nuclear materials were first interdicted in Italy and Switzerland in 1991, and hundreds of cases of nuclear smuggling have since been reported.<sup>1,2</sup> To provide answers regarding the origin and intended use of these intercepted materials, the field of nuclear forensics was created. Nuclear forensics is highly interdisciplinary by nature, involving key contributions from chemistry, materials science, geology, political science, and international law.

Although nuclear forensics is a highly applied field, it is built firmly upon a foundation of fundamental science. Inorganic, analytical, and nuclear chemistry, as well as physics and engineering, have all contributed substantially to the formation of the field, and the improvement of nuclear forensic analysis is inextricably tied to the development of new chemical processes and technologies.<sup>1-10</sup> Most of the techniques used for sample analysis were adapted from pre-existing fields, and new developments in the chemical sciences have contributed heavily to the expansion of nuclear forensic capabilities.<sup>1,2,5,11,12</sup> This Review focuses on the central role of chemistry in the development of modern nuclear forensic science, and also seeks to predict future capabilities based on recent advances published in the chemical literature. Particular emphasis is placed on the burgeoning developments within actinide nanoscience and microanalytical techniques.

## Nuclear Forensics: Objectives and Scope

The principal function of nuclear forensics is to produce sufficient evidence for attribution of seized nuclear materials using analytical methods.<sup>1</sup> Most unclassified publications on this topic focus on pre-detonation nuclear forensics, in which the primary goal is to prevent the assembly and detonation of a nuclear bomb by non-nuclear states or terrorist groups. Consequently, special nuclear materials (SNM, i.e. fissile  $^{233}\text{U}$ ,  $^{235}\text{U}$ , and Pu) used to manufacture nuclear weapons must be carefully monitored, and the interception, detection, and identification of lost or stolen SNM are fundamental to this mission. Prior to the dissolution of the Soviet Union, there were no known cases involving the sale of legitimate SNM on the black market. However, multiple cases of SNM smuggling on a kilogram scale have been intercepted in the following years and subjected to nuclear forensic analysis for source attribution.<sup>1,4,13</sup> In addition to the actinide materials required

to manufacture the core of a fission bomb, uncommon mechanical parts and unusual compounds or alloys may also point towards clandestine nuclear programs.<sup>1,4</sup> Notable examples include spherical beryllium neutron reflectors, components for neutron release such as <sup>210</sup>Po/Be mixed sources, and other chemicals used for nuclear weapons.<sup>1</sup> The possession of these materials does not necessarily indicate the presence of a clandestine nuclear weapons program, but it can be an indicator that further monitoring of the responsible parties may be prudent.<sup>1</sup>

At the time of this publication, the only wartime detonations of nuclear weapons were the 1945 bombings of Hiroshima and Nagasaki by the United States, and pre-detonation nuclear forensics strives to prevent additional nuclear events by intercepting stolen or mismanaged nuclear materials prior to their use in weapons. However, in the event of an unplanned nuclear detonation, capabilities are being developed to enable scientists to work backwards and assign the type and origin of the original bomb. This “blast-to-bomb” analysis is known as post-detonation nuclear forensics, and advances in analytical precision have greatly expanded this sub-field in the last decade.<sup>14–16</sup> Post-detonation forensics is an ongoing subject of intense research at a number of national and international facilities.<sup>4,14,17</sup> Although much of this research is classified, a number of representative post-detonation case studies have been published using declassified data, most notably analyses of the Trinity test site.<sup>12,15,16,18–21</sup> These cases will be discussed at the end of the Review.

Another serious but less catastrophic concern related to nuclear terrorism is the detonation of a radiological dispersal device (RDD), commonly known as a “dirty bomb”. This is a device that uses conventional explosives to disperse a highly radioactive but non-fissile source, such as <sup>60</sup>Co, <sup>137</sup>Cs, <sup>90</sup>Sr, <sup>99</sup>Mo, <sup>241</sup>Am, etc., with the goal of spreading radioactive contamination in a populated area. The detonation of an RDD in an urban area could lead to mass panic and a high economic cost of cleanup and evacuation, causing these devices to be termed “weapons of mass disruption”.<sup>1</sup> While SNMs are highly regulated on an international scope to minimize proliferation, highly radioactive sources that could be used to make an RDD are commonly found in the medical, agricultural, and mining sectors of many countries.<sup>1,4,22</sup> Consequently, detection of these non-nuclear radioisotopes is also of significant importance for international security.<sup>4,13,22</sup>

## Overview of Analytical Methods

Many of the instruments employed for analysis of nuclear materials were initially developed for conventional chemical samples, leading to parallel development of these technologies for academic, industrial, and security applications.<sup>2,3,6,23–25</sup> A handful of previous publications have summarized important analytical methods in nuclear forensics;<sup>1,5,6,26–28</sup> this review will instead focus primarily on detailing the impacts of fundamental and applied chemistry, especially inorganic and materials chemistry, in the development of nuclear forensics. Future capabilities for nuclear forensic science will also be discussed, with an emphasis on recent developments in chemical microanalysis.

Analysis of seized nuclear materials is conventionally divided into two main types: destructive analysis (DA) and nondestructive analysis (NDA) (Table 2.1). Stated simply, DA techniques require destructive sampling or alteration of the material, while NDA techniques leave the physical and chemical form of the material unchanged. Analytical methods within each of these categories provide key pieces to the puzzle, with significant advantages and disadvantages present for each technique.<sup>5,29</sup> In a real-world scenario, an array of tests is generally performed on

a seized material to determine the chemical composition, physical structure, and isotopic ratios present. This multi-pronged approach enables the strengths of numerous forms of analysis to complement one another while overcoming the weaknesses of any given method.<sup>2,4,26,30</sup>

<b>Nondestructive methods</b>	<b>Destructive methods</b>
<b>Gamma spectroscopy</b>	Alpha spectrometry
<b>Neutron detection</b>	Electron microscopy
<b>Optical microscopy</b>	Thermal ionization mass spectrometry
<b>IR and Raman spectroscopy</b>	Inductively-coupled plasma mass spectrometry
<b>X-ray fluorescence</b>	Secondary ion mass spectrometry

**Table 2.1:** *Examples of nondestructive and destructive techniques commonly used in nuclear forensics. Although electron microscopy is sometimes considered nondestructive, beam damage to the sample is often significant.*

To preserve the integrity of the sample and maximize detectable signatures, a seized material is always subject to a battery of NDA tests before it is studied by destructive analysis. For the sake of clarity, a further distinction between “passive” and “active” analysis will also be made here. In a passive analysis procedure, no energy is added into the system preceding detection; examples include detection of radiation that is emitted from the sample in the absence of an added stimulus. This is in comparison with “active” analysis, in which a sample is probed (e.g. by a beam of photons or electrons) and the resulting interactions are measured. Passive analysis generally comprises the first series of tests after a material is interdicted, and will correspondingly be discussed first in this Review.

### **Gamma and Neutron Detection**

Initial NDA methods often allow for relatively rapid identification of the macroscopic form and primary radioactive components of a sample, thereby informing the next steps of analysis. Classification of radioactive material is typically performed first using passive detection methods, such as gamma spectroscopy and neutron counting, to determine the radioisotopes present in the sample without damage or alteration.<sup>31,32</sup> Specific peak energies and ratios are easily resolved using modern high-purity germanium detectors, providing an isotopic fingerprint of the material without causing any physical or chemical changes to the sample.<sup>1,33</sup> The neutron flux emitted by a sample can also be a useful signature, since the rate of neutron emission varies significantly among different nuclear materials.<sup>31,33</sup>

Stationary gamma and neutron detectors are commonly placed at borders and ports to prevent smuggling of radioactive materials.<sup>28,31,34,35</sup> These field detectors are generally designed for rapid response rather than precise measurement, due to the large flux of personnel and freight



through transit boundaries. Recent improvements in detector design have also led to the production of handheld gamma spectrometers with moderate resolution, enabling the determination of common radioisotopes, such as  $^{235}\text{U}$  and  $^{239}\text{Pu}$ , within minutes. Distribution of this technology to inspectors and regulatory bodies has greatly improved the monitoring capability of these agencies, both on-site and apart from nuclear facilities.<sup>34</sup> Suspicious items are flagged for detailed on-site analysis, and seized nuclear materials can then be transported to a lab following interdiction. By using high-resolution instruments and long counting times, gamma spectroscopy and neutron counting can produce diagnostic information about the radioactive isotopes present in the sample, providing valuable clues about how the material was produced and informing the next steps in analysis.

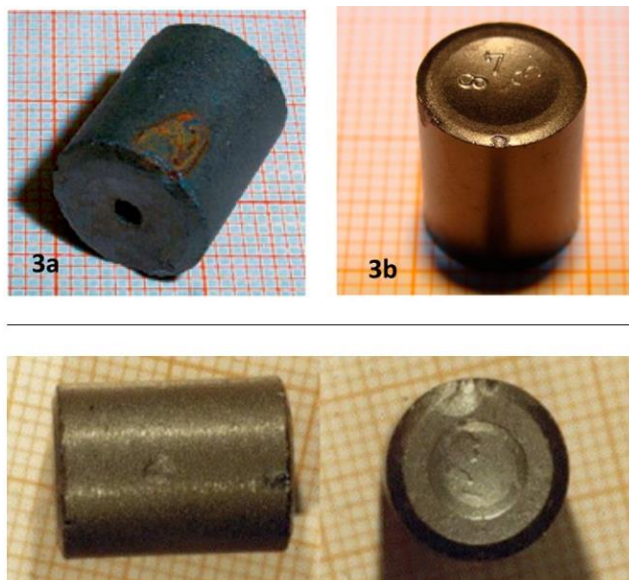
### **Alpha Spectrometry**

For actinide-containing samples, alpha spectrometry is another tool that can be useful for isotopic fingerprinting, as many actinide isotopes decay by alpha particle emission. The characteristic energies of alpha particles provide isotopic fingerprints, enabling quantification of the enrichment and age of actinide-containing samples, as described by Morgenstern and coworkers<sup>36</sup> The high interaction probability of alpha particles with matter requires alpha spectrometry to be performed using thin samples in a vacuum.<sup>31</sup> Although this is still a form of passive detection, destructive sample preparation is required, generally by chemical dissolution of the sample followed by vapor- or electrodeposition of the analyte onto a thin platinum plate for counting.<sup>1</sup> For actinide-containing samples, electrodeposition is generally performed by dissolving the sample in an acidic buffer solution (e.g.  $\text{Na}_2\text{SO}_4/\text{NaHSO}_4$ ), then applying a current and increasing the pH to deposit a thin, uniform layer of the analytes onto a platinum plate. Since minimum thickness and high uniformity are required to minimize self-absorption and backscattering of alpha particles, electrodeposition is preferred over other chemical or physical deposition methods for sample preparation.

While alpha spectrometry is a reasonably effective method to quantify the different actinide isotopes present in a mixed sample, its applications are often more limited than other forms of passive radiation detection, since accurate spectra can only be collected in a vacuum following chemical manipulation. However, alpha spectrometry is a valuable tool in cases when time-sensitive identification of actinide content is required, as sample preparation can be performed more rapidly than most forms of destructive analysis.<sup>37</sup>

### **Optical Characterization**

Certainly worth mentioning, and sometimes overlooked, is the simplest passive fingerprint available: the optical appearance of a sample. Macroscopic features can provide clues to the sample's function- for example, the size and shape of a seized fuel pellet can be compared with documented parameters for different reactor types, narrowing down the possible locations for the initial diversion of nuclear material.<sup>1,2</sup> In most nuclear forensic investigations, optical microscopy is the first method employed to study the appearance and homogeneity of interdicted items.<sup>1</sup> Visual inspection under a microscope can sometimes reveal collateral evidence that can be analyzed in conventional forensic laboratories, and much can be gleaned from the non-radioactive components of a seized material. Fingerprints, hair, fibers, packaging, and other associated pieces of collateral evidence often hold valuable information about a sample's age and origin, and this information can be compared with the results found using nuclear forensic techniques such as chronometry.<sup>38,39</sup>



**Figure 2.1:** (Top) Intercepted fuel pellets with characteristic markings. (a) Uranium fuel pellet with a central hole, usually used in Russian-designed reactors. (b) Uranium fuel pellet with embossed numbers inside a dished end, designed for western light water reactors. Reproduced from Mayer, K.; Wallenius, M.; Varga, Z. *Anal. Chem.* 2015, 87, 11605-11610 (ref 30). Copyright 2015 American Chemical Society.

(Bottom) A uranium pellet from the “Find-1” sample. Reprinted from *J. Alloys Compd.*, Vol. 444-445, Mayer, K.; Wallenius, M.; Fanghänel, T. *Nuclear Forensic Science—From Cradle to Maturity*, pp. 50-56 (ref 2). Copyright 2012, with permission from Elsevier.

Although gamma spectroscopy, neutron counting, and optical characterization are rapid, nondestructive, and vital for classification of a material, these passive methods can rarely provide enough data alone to assign provenance.<sup>1,30</sup> For full and detailed characterization of seized materials, analyses must also be performed in a laboratory setting using active methods.

## Electromagnetic Spectroscopy and Diffraction

The chemical form of a sample, the isotopic ratios of radionuclides, and the impurities present from mining, milling, and reprocessing of nuclear materials are useful signatures for the provenance of a sample and the manufacturing processes used to create it.<sup>7,40-44</sup> Following the initial regimen of gamma spectroscopy and neutron counting, radioactive samples are subjected to a variety of active analyses that provide detailed information about elemental composition and morphology.

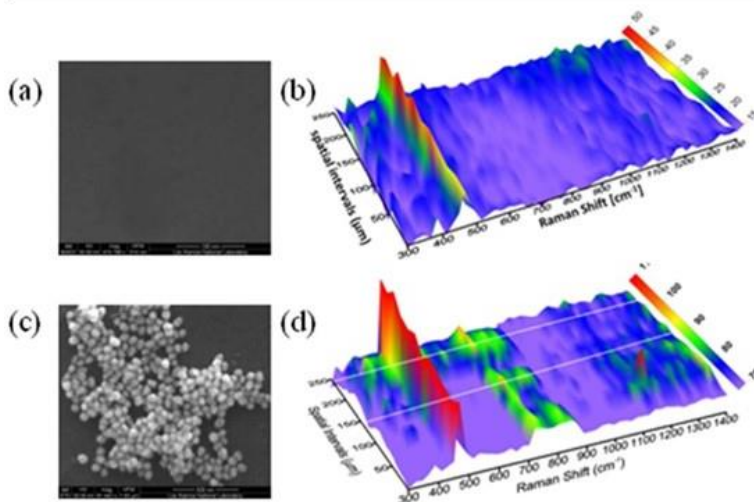
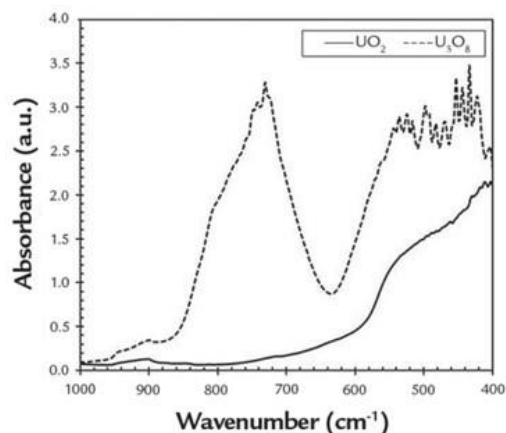
In nearly all situations that require chemical identification of an unknown substance, a wealth of information can be obtained through spectroscopic and diffractive methods. The interactions of electromagnetic radiation with matter have been used to study chemical systems since at least the 19<sup>th</sup> century,<sup>45</sup> and numerous forms of spectroscopy and diffraction have since been applied to nuclear forensic challenges. This section of the Review will discuss a number of nondestructive techniques and briefly introduce the chemical principles involved.

## Vibrational Spectroscopy

Raman and infrared (IR) spectroscopy are both widely used for chemical identification of a wide range of organic and inorganic compounds.<sup>46</sup> These techniques work by probing vibrational transitions of the target molecules, generating a spectroscopic signature of the chemical bonds present in the sample. IR spectroscopy has been in use for well over a century,<sup>47</sup> and its utility for characterization of new molecules cannot be overstated. Many chemistry journals require an IR spectrum to be submitted for every new compound that is published, and a tremendous number of IR spectra are available as a result. Due to the value of IR spectroscopy for chemical fingerprinting of samples, this technique is frequently employed in traditional forensic laboratories.<sup>48</sup> Advantages of conventional IR spectroscopy include facile sample preparation, rapid data acquisition, and relatively low instrument cost.

Within nuclear forensics, IR spectroscopy has been used to characterize the origin of uranium ore concentrates (UOC's or yellow cakes), with the chemical composition of the UOC's providing important clues to where the material was mined and how it was processed.<sup>41</sup> This method is well-described for IR spectroscopy by Varga and coworkers<sup>49</sup> and for Raman spectroscopy by Lin and coworkers.<sup>50</sup> Different compositions of uranium oxide, such as  $\text{UO}_2$  and  $\text{U}_3\text{O}_8$ , can be readily distinguished by IR spectroscopy, providing information about the processing history of the material.<sup>51</sup> IR spectroscopy is also used within nuclear forensics to characterize collateral evidence accompanying seized nuclear materials. In a well-known example, a vial of highly-enriched uranium (HEU) contained in a wax-filled lead pig was seized in Bulgaria, and the wax was subjected to IR spectroscopy, in conjunction with other methods, to determine where the sample had originated. A detailed summary of the Bulgaria case has been written by Moody and coworkers.<sup>1</sup> Handheld Raman spectrometers have also become readily available, allowing inspectors from the International Atomic Energy Agency (IAEA) or law enforcement personnel to rapidly and nondestructively acquire chemical data from their surroundings.<sup>50</sup>

Prominent advances in Raman and IR microanalyses have enabled detailed chemical fingerprinting of nanometer-sized samples, greatly expanding the microanalytical toolkit available to nuclear forensics scientists.<sup>52-56</sup> Atomic force microscopy coupled to IR spectroscopy (AFM-IR) is a recent technique that uses a cantilever tip to record laser-excited vibrations in molecules, bypassing the diffraction limit of infrared light.<sup>55</sup> However, AFM-IR has yet to see widespread adoption due to its recent development. Based on initial promising results spread across a range of materials,<sup>56</sup> this technique may prove valuable for nuclear forensic analysis in future scenarios, especially in cases where sub-micrometer samples are the only material available for chemical fingerprinting. By comparison to the recent introduction of AFM-IR, surface-enhanced Raman spectroscopy (SERS) was developed over forty years ago for analysis of ligands bound to electrode surfaces,<sup>57</sup> but has only recently begun to gain traction for nuclear forensic applications.<sup>52,53</sup> Specific applications of micro-Raman spectroscopy will be discussed in more detail later in the Review.



**Figure 2.2:** (Top) IR spectra of  $\text{UO}_2$  (solid line) and  $\text{U}_3\text{O}_8$  (dashed line). Reproduced from Silva, L. A.; Lameiras, F. S.; Matildes dos Santos, A. M.; Ferraz, W. B.; Barbosa, J. B. S., *Int. Eng. J.*, 2017, 70, 59–62 (ref 51) under a Creative Commons Attribution 4.0 International License (<https://creativecommons.org/licenses/by/4.0/>).

(Bottom) SEM image and (b) space-wavelength Raman spectrum of a uranium oxide thin film. (c) SEM image and (d) space-wavelength Raman spectrum after deposition of  $\text{Au@SiO}_2$  nanoparticles onto the film. Reproduced from He, H.; Wang, P.; Allred, D. D.; Majewski, J.; Wilkerson, M. P.; Rector, K. D. *Anal. Chem.* 2012, 84, 10380–10387 (ref 53). Copyright 2012 American Chemical Society.

## X-Ray Fluorescence

Many of the methods used for NDA of nuclear samples are based on the interactions of X-rays with matter. X-rays interact strongly with the dense electron clouds of the actinide and lanthanide elements, resulting in high-sensitivity techniques for the characterization of nuclear materials and their fission products.

Irradiation of a sample with a collimated X-ray beam can promote electrons in the sample from core orbitals to valence orbitals, causing the prompt emission of fluorescence X-rays as the

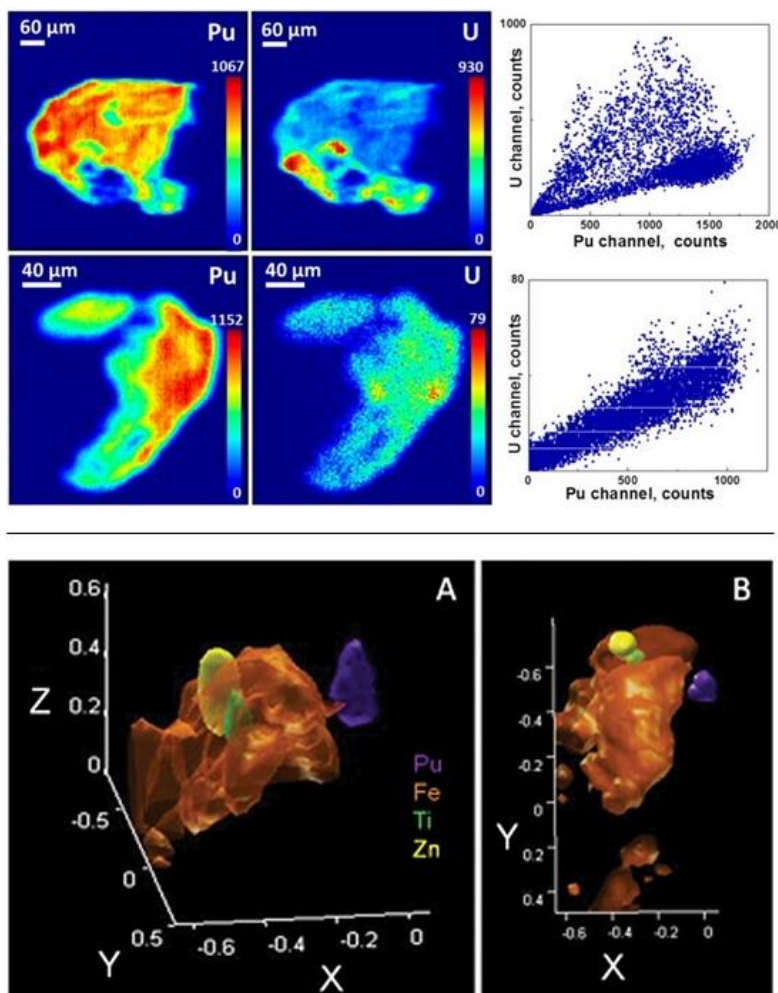
empty core orbitals are filled by other electrons. The characteristic energies of these fluorescence X-rays are element-specific, and the resulting spectrum can be interpreted to quantify multiple elements in a matrix. This technique, known as X-ray fluorescence (XRF), was first conceptualized in 1913 when Henry Moseley correlated individual elements to their characteristic X-ray energies; however, XRF did not see much application until the 1950s, when the first commercial XRF instruments arrived on the market.<sup>58</sup> XRF has long been used in the chemical sciences for elemental analysis due to its high sensitivity, rapid data acquisition, and minimal sample preparation.<sup>23</sup> The main disadvantage of XRF is low sensitivity for light elements ( $Z < 14$ ). XRF is widely applied in nuclear forensics for nondestructive elemental analysis, providing quantification of major constituents and impurities in a sample with only micrograms of material required.<sup>59</sup>

Charlton and coworkers have shown that XRF can be used to quantify the U/Pu ratio in spent nuclear fuel, but information about the fuel pin configuration was necessary for this process.<sup>60</sup> More accurate results for elemental analysis can be obtained using mass spectrometry, but this requires destructive sample preparation and a longer timeframe.

Modern technological developments have enhanced the capabilities of XRF for nuclear forensic analysis; these include portable XRF instruments<sup>24</sup> and also micro-XRF, which will be expanded upon later in the Review. Steeb and coworkers described the use of a handheld XRF spectrometer for on-site detection of RDD components.<sup>62</sup> The isotope  $^{60}\text{Co}$  was used in this study, although most commonly-found radionuclides could presumably be detected in this manner. Portable XRF technology could prove useful by enabling law enforcement and monitoring agencies to rapidly analyze unidentified radioactive sources in nuclear smuggling or domestic terrorism scenarios.

### **X-ray Absorption Spectroscopy**

Core-to-valence electronic transitions in nuclear materials can also be probed using X-ray absorption spectroscopy (XAS), which can be used to quantify the distribution of oxidation states for certain elements in a sample, such as U and Pu. XAS is applied in this manner to measure the chemical speciation of a sample, and is often used in conjunction with another method of elemental analysis such as XRF.<sup>61,63</sup> XAS is also used to measure covalency in actinide bonding, which is still poorly understood in comparison to most other elements of the periodic table.<sup>64</sup> The electronic structure of  $\text{U}_3\text{O}_8$  was studied by Wen and coworkers using XAS and computational methods, and it was seen that mixing of O 2p orbitals with both U 5f and 6d orbitals contributed to bonding in this compound.<sup>65</sup> Bond covalency has a substantial impact on ligand complexation in synthetic chemistry and separation processes, making this an attractive area of research for many radiochemists.<sup>66-68</sup> Access to a synchrotron source for XAS can be a limiting factor for direct analysis of interdicted nuclear materials, but this method can nonetheless provide valuable information when such facilities are available.



**Figure 2.3:** (Top) XRF micrographs of plutonium in Hanford soil particles. Reproduced from Batuk, O. N.; Conradson, S. D.; Aleksandrova, O. N.; Boukhalfa, H.; Burakov, B. E.; Clark, D. L.; Czerwinski, K. R.; Felmy, A. R.; Lezama-Pacheco, J. S.; Kalmykov, S. N. *et al. Environ. Sci. Technol.* 2015, 49, 6474–6484 (ref 61). Copyright 2015 American Chemical Society.

(Bottom) (A) Side-view and (B) top-view confocal XRF 3D mapping of elemental composition in a Pu-contaminated soil sample. Axis labels are in mm. Reproduced from McIntosh, K. G.; Cordes, N. L.; Patterson, B. M.; Havrilla, G. J. *J. Anal. At. Spectrom.*, 2015, 30, 1511–1517 (ref 144), with permission of The Royal Society of Chemistry.

## X-ray Diffraction

In addition to elemental and oxidation state analysis, X-rays are also used to study the phase and chemical structure of materials by X-ray diffraction (XRD).<sup>69</sup> When X-rays pass through a crystalline or microcrystalline sample, they are scattered at angles dictated by the atomic spacing of the crystal lattice. Single-crystal and powder XRD have been used by chemists for molecular structure determination since 1912, when Max von Laue first applied this technique to investigate the wave behavior of X-rays in crystalline materials.<sup>70</sup> XRD is common in nuclear material characterization, as data can be acquired quickly and nondestructively.<sup>71</sup> Typically, XRD is used

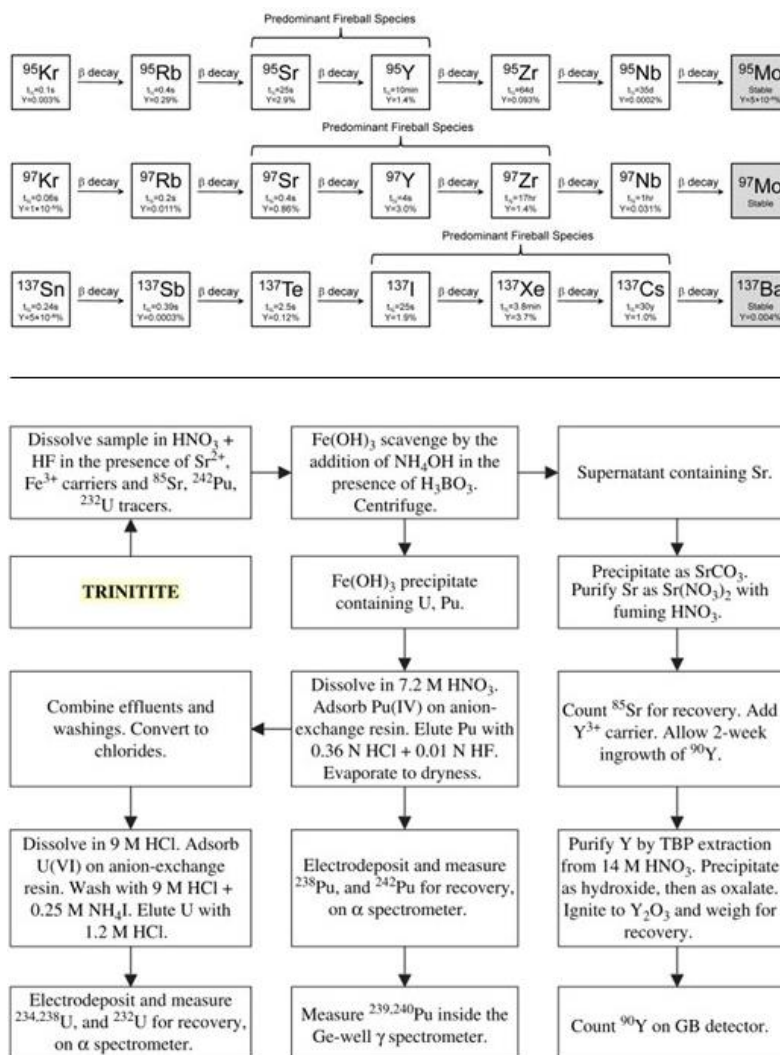
as a supplemental technique in nuclear forensics rather than a standalone form of analysis, since crystallographic data cannot be meaningfully interpreted without some knowledge of elemental composition.<sup>72</sup>

In a study investigating the chemical speciation of soils near the Chernobyl reactor, Wilkerson and coworkers used a combination of XRD and XAS to distinguish between different uranium and plutonium oxides,<sup>73</sup> which can be a challenging problem due to complicated environmental speciation of the actinides.<sup>74</sup> These results showcased the chemical sensitivity of XRD/XAS for environmental samples, and the methods used could be readily applied to samples collected during monitoring operations. Soil sampling near a nuclear site, followed by analysis by XRD/XAS, could be used to detect clandestine activity, such as uranium enrichment or plutonium extraction, by measuring the concentration and chemical form of trace actinides in the areas surrounding the facility.

## **Radiochemical Techniques**

### **Actinide Separations**

Throughout the duration of the Manhattan project, special attention was paid to the chemistry of the actinide elements, enabling the purification and isotopic enrichment of SNMs for use in nuclear weapons.<sup>75</sup> These detailed forays into radiochemistry have yielded a number of effective procedures for separating radioactive mixtures of inorganic compounds; the plutonium-uranium redox extraction (PUREX) process, which is still used to extract plutonium from spent nuclear fuel, is a notable example.<sup>33,76</sup> In the PUREX process, spent fuel is first dissolved in nitric acid, then a solution of tributyl phosphate in kerosene is added to form complexes with Pu and U that are soluble in the organic layer. The fission products are removed in the aqueous layer for disposal, and Pu is chemically reduced to allow separation from U. Chemical reprocessing of spent nuclear fuel is capable of 99.9% recovery of Pu, with separation factors approaching  $10^8$  from fission products.<sup>1</sup> However, the development of improved methods for separating lanthanides from minor actinides, such as Am and Cm, is still a significant challenge within inorganic chemistry, and recent progress has been made in this area using molecular and supramolecular methods.<sup>77</sup> Sample preparation for mass spectrometry often requires extremely precise separation of analytes, and modern separation processes for nuclear forensic analysis are based heavily on radiochemical processes developed during the Manhattan Project.<sup>75</sup>



**Figure 2.4:** (Top) Separation flowchart for analysis of a trinitite sample. Reprinted from *J. Environ. Radioact.*, Vol. 85, Parekh, P. P.; Semkow, T. M.; Torres, M. A.; Haines, D. K.; Cooper, J. M.; Rosenberg, P. M.; Kitto, M. E. *Radioactivity in Trinitite Six Decades Later*, pp. 103-120 (ref 78). Copyright 2006, with permission from Elsevier.

(Bottom) Decay schemes for mass 95, 97, and 137 chains following Pu fission in the Gadget. Reproduced with permission from *Proceedings of the National Academy of Sciences USA*, Hanson, S. K.; Pollington, A. D.; Waidmann, C. R.; Kinman, W. S.; Wende, A. M.; Miller, J. L.; Berger, J. A.; Oldham, W. J.; Selby, H. D. *Proc. Natl. Acad. Sci. U. S. A.* 2016, 113, 8104–8108 (ref 178).

The theory underlying these separations is based heavily in fundamental properties of chemical bonding across the periodic table, including redox-dependent differences in complexation behavior and hard-soft acid base theory.<sup>75,76,79,80</sup> Many of the radiochemical procedures used for sample preparation in nuclear forensics are described by Moody and coworkers.<sup>1</sup> For a more comprehensive discussion of the underlying chemical processes in actinide chemistry, the reader is directed to the compendium assembled by Morss and coworkers, *The Chemistry of the Actinide and Transactinide Elements*, which deals with these topics in substantial



detail.<sup>8</sup> Despite the lengthy history of radiochemical separations that took place throughout the American nuclear program, advancements in actinide separation chemistry are still being made more than 70 years after the Manhattan Project, showcasing the chemical complexity required for these processes.<sup>81–85</sup>

### **Sample Preparation for DA**

Most processes used for DA involve chemistry as a key component, with sample preparation often requiring advanced knowledge of actinide and trace metal speciation and redox behavior.<sup>1,13,80,86</sup> Separations of nuclear samples are particularly challenging due to the complicated mixture of elements that coexist within the material; these are typically a mixture of actinides, decay and fission products, and impurities from mining or milling, and multi-step chromatographic separations are often required for quantitative analysis.<sup>1,75</sup> Consequently, analyte purification can be a lengthy process of manipulations that exploit differences in solubility, oxidation state, and ligand binding profiles of the many elements present in the sample. When working with small quantities of analyte, isotopic carriers are often used to minimize loss of material, but these carriers can render mass spectrometry measurements more difficult to analyze.<sup>87</sup> Prior to analysis, solutions are often standardized using titrimetry or coulometry.

### **Mass Spectrometry**

Mass spectrometry (MS) is one of the most widespread techniques used for DA, due in large part to the extremely high sensitivity for trace isotope detection that is achievable with modern mass spectrometers.<sup>1,2,6,86</sup> Many forms of MS are used widely for industrial, academic, and pharmaceutical applications, and chemists experienced in these techniques are in high demand within the nuclear forensics community.<sup>4,5</sup> The use of MS for analysis of seized nuclear materials is well-documented,<sup>1,2,6,30,86,88</sup> and a comprehensive summary of these methods lies outside the scope of this Review. Instead, an overview of selected MS techniques used for nuclear forensics applications is provided here, and a few common procedures for sample preparation are briefly described.

One of the major nuclear forensic applications for MS is the determination of isotopic ratios within a sample, which provide clues about its provenance, age, and processing history. The isotopic composition of spent nuclear fuel can often provide information about the type of reactor from which it originated. An excellent example, described by Mayer and coworkers in a 2007 review of nuclear forensics,<sup>2</sup> is the first analysis of a seized nuclear material in 1992, performed by the German-based Institute for Transuranic Elements (ITU). The sample, termed “Find-1”, consisted of 72 uranium pellets from a nuclear reactor (*Figure 2.1*). The uranium isotopic composition was analyzed by thermal ionization mass spectrometry (TIMS), and the combination of these results with bulk chemical and physical analysis were sufficient to trace the pellets back to a Russian graphite-moderated reactor. This is an important case study because it represents the first time that a seized nuclear material was analyzed for source attribution. Although the methods used to characterize Find-1 were relatively crude in comparison with modern nuclear forensic capabilities, this case study demonstrates the crucial role of MS in nuclear forensic analysis from the field’s inception.

## Chronometry

The production date of a seized nuclear material is a critical piece of information about its origin, and this information can be extracted from the presence of trace decay products in the sample.<sup>1,33</sup> Following the radiochemical separation of decay products from the parent nuclide, precise isotopic ratios can be measured using mass spectrometry and correlated to a date of processing; this age determination using mother-daughter isotopic ratios is known as chronometry. The buildup of decay products in a sample are governed by the principles of radioactive equilibrium, which are well-described in most radiochemistry textbooks.<sup>33,89</sup> Important chronometers for nuclear materials include the  $^{238}\text{U}/^{234}\text{Th}$  ratio and the  $^{241}\text{Pu}/^{241}\text{Am}$  ratio; a more complete list has been provided by Moody and coworkers.<sup>1</sup>

Accurate chronometry requires effective chemical separations and highly-sensitive detection techniques, with the former achieved using inorganic chemistry and the latter typically accomplished using MS.<sup>5,39</sup> Since multiple chronometers are generally measured for a given sample, intentional age spoofing by isotopic dilution would be extremely difficult and even counterproductive, as mismatched chronometers can provide a fingerprint for intentional obfuscation of data.<sup>1</sup> The applications of chronometry in nuclear forensic analysis have been covered in significant detail elsewhere,<sup>1,39,88,90,91</sup> and an in-depth review of these processes would be redundant in light of these previous articles. However, chronometric studies using data obtained from MS are a critical part of the source attribution process in nuclear forensics,<sup>2,39</sup> comprising one of the primary applications for isotopic data.

## Thermal Ionization Mass Spectrometry

Thermal ionization mass spectrometry (TIMS) is one of the most sensitive and well-studied techniques for nuclear forensic analysis. TIMS can provide highly precise isotopic fingerprinting of elements with low ionization potentials, such as uranium and plutonium.<sup>92</sup> Analysis of a sample using TIMS can be performed using extremely small amounts of sample, with detection limits generally on the order of femtograms to nanograms.<sup>6</sup> Ionization of the analyte is achieved by depositing a chemically-purified sample onto a wire and heating the wire to high temperatures. Isotopic enrichment or burnup of a nuclear material can be readily determined using TIMS; this and other nuclear forensic applications of TIMS have been covered in detail by Aggarwal.<sup>86</sup> Sample preparation for TIMS analysis is generally a complex procedure, involving a series of chemical separation and purification steps.<sup>6,80,86</sup> Due to the sensitivity of TIMS for trace elements, extremely high separation factors must be achieved to collect accurate data from an analyte.

## Inductively-Coupled Plasma Mass Spectrometry

Some of the problems faced by TIMS, such as lengthy sample preparation and low sensitivity for elements with a high ionization potential, can be overcome by using a type of MS with a different ionization mechanism. Inductively-coupled plasma mass spectrometry (ICP-MS) is particularly notable for this purpose due to a number of key advantages over TIMS, and quantification of radioactive materials using ICP-MS has been thoroughly reviewed by Croudace and coworkers.<sup>87</sup> Ionization of samples in ICP-MS is achieved in a localized region of plasma, which is usually generated by laser-induced ionization of argon gas. ICP-MS can be used to detect the majority of elements on the periodic table, and this technique excels at detecting trace elements that can serve as signatures for where a material was processed.<sup>1</sup> ICP-MS is also highly effective for isotopic fingerprinting and chronometry of nuclear materials.<sup>6,87,88</sup>

ICP-MS offers numerous advantages over many other types of MS. In contrast to the lengthy sample preparation required for TIMS, samples analyzed by ICP-MS are comparatively simple to prepare. Examples of sample preparation from various matrices have been presented by Croudace and coworkers.<sup>87</sup> Additionally, elements with high ionization potentials can be detected with extremely high precision using ICP-MS, with current instruments capable of femtogram/gram sensitivity for trace element quantification.<sup>6</sup> Consequently, the popularity of ICP-MS for nuclear forensic analysis has been steadily increasing, and this is a trend that is expected to continue in the coming years.<sup>1</sup>

Solution methods are commonly used when preparing samples for ICP-MS analysis, but quasi-nondestructive measurements can also be performed using laser ablation (LA) ICP-MS. Samples analyzed by LA-ICP-MS require minimal to no chemical pretreatment, and can be ionized directly in the solid state.<sup>93</sup> Marin and coworkers have shown that LA-ICP-MS can determine the enrichment level of HEU with high precision.<sup>94</sup> LA-ICP-MS also enables isotopic measurement on very small areas of a sample, providing additional information about sample homogeneity. This is demonstrated by Reading and coworkers for custom-made, UOC-containing glassy beads, which are designed to model glassy fallout in a post-detonation scenario.<sup>95</sup> This study is noteworthy not only because it showcases the microanalytical capabilities of LA-ICP-MS for nuclear materials, but also because it introduces a new synthetic process that can be used to model nuclear weapon debris in a controlled laboratory setting.

## **Microanalytical Techniques**

Within the last decade, some of the most prominent developments in nuclear forensic analysis have been accomplished using small-scale characterization of samples. In many cases, these microanalytical techniques enable precise chemical and physical information to be acquired from samples too small to be seen by the human eye. The capabilities offered by modern microanalysis have largely arisen from the world of nanoscience; advances in materials chemistry have rapidly introduced a slew of nanomaterials with unique architectures and properties, often in conjunction with improved methods to characterize these structures.<sup>96</sup>

While most of the microanalytical techniques described are already well-established in the chemical sciences, the substantial improvements in resolution, sensitivity, and versatility developed for these methods within the last ten years may dramatically impact the future capabilities accessible to nuclear forensic scientists. One must always consider, however, the limitations of small-scale measurements, especially the possibility of non-representative sampling. Therefore, microanalysis can never wholly supplant measurements performed on bulk material, but is instead most beneficial when used in conjunction with other techniques. With this important caveat in mind, macroscopic samples are not always obtainable, and advanced forms of microanalysis can serve as formidable tools in these situations. Notable examples include on-site monitoring operations for treaty verification and atmospheric particle detection following the hypothetical detonation of a nuclear weapon on foreign soil. The impact of microanalytical techniques such as SIMS, electron and x-ray microscopy, and small-area spectroscopy on nuclear forensic capabilities will be discussed here.

## Secondary Ion Mass Spectrometry

In addition to determining isotopic ratios and trace element composition in a sample, certain forms of MS can be coupled with surface imaging of a material. The use of LA-ICP-MS for this purpose has been discussed briefly, but secondary ion mass spectrometry (SIMS) is currently the most common technique for spatially-resolved MS.<sup>1</sup> SIMS enables concurrent determination of the shape, composition, and isotopic ratios present in a sample, indicating the homogeneity of a sample at relatively small scales (generally on the order of micrometers).<sup>6,97-99</sup> Ionization is achieved by focusing an ion beam onto the sample, causing secondary ions to be ejected. Since the sample is only ionized at its surface, minimal sample preparation is required for SIMS, and imaging is also possible. The use of SIMS for uranium particles has been described in detail by Tamborini and coworkers, who used SIMS to characterize the isotopic ratios in a variety of uranium certified reference materials (CRMs)<sup>100</sup> (Figure 2.5).

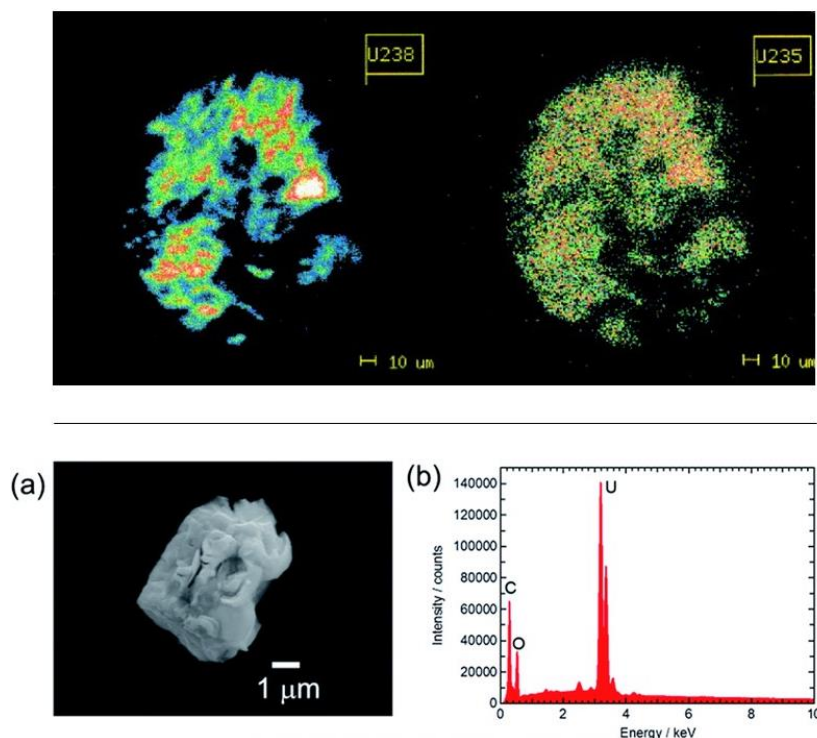
A prominent example of how SIMS can be applied for nuclear forensic purposes is described by Pöllänen and coworkers.<sup>101</sup> In 1966, an accident involving an American B-52 bomber containing four thermonuclear weapons led to the release of these weapons over Palomares, Spain. Fortunately, detonation of these weapons did not occur, but two of the bombs were mechanically destroyed, causing the release of nuclear material into the surrounding areas. Since bulk analysis of contaminated soils can be confounded by the presence of global fallout from past nuclear tests,<sup>102</sup> this study focused on the characterization of individual particles in the soil matrix. Determination of U and Pu isotopic composition was performed using SIMS, and the results were compared with ICP-MS isotopic data and with prior bulk analyses of the soil.<sup>102,103</sup> SIMS data provided accurate quantification of Pu, but the  $^{235}\text{U}/^{238}\text{U}$  isotopic ratio found by SIMS differed from the isotopic ratio found by ICP-MS. The authors of this paper concluded that inhomogeneity of particles may be a contributing factor, but also emphasized the need for more than one form of microanalysis in nuclear particle characterization.

Although SIMS is useful for spatially-resolved isotopic analysis, various other microanalytical techniques are capable of probing finer structural detail within a sample. Perhaps conventional-resolution SIMS is best viewed as a “jack of all trades” within nuclear forensics. Few other methods can provide concurrent elemental analysis, isotopic distribution, and imaging of a sample without requiring lengthy sample preparation, but higher independent sensitivity and precision for each of these characteristics can be separately obtained using other techniques described in this Review. Nevertheless, the versatility of SIMS has carved out a valuable role for this technique within nuclear forensic microanalysis, and the precision of measurements accessible using SIMS continues to improve. NanoSIMS has enabled spatial resolution of approximately 50 nm for isotopic measurements, and this technology has been applied largely to biochemistry and cosmochemistry.<sup>104,105</sup> Recent applications of nanoSIMS for nuclear materials have been described by Wang and coworkers<sup>106</sup> and by Lozano-Perez and coworkers,<sup>107</sup> with the ability to accurately measure light elements such as Li and B cited as a major advantage over other forms of microanalysis.

## Scanning Electron Microscopy

For surface imaging of small samples, scanning electron microscopy (SEM) is one of the most powerful techniques available. This is largely due to the excellent spatial resolution attainable using SEM, which can be on the order of one nanometer.<sup>108,109</sup> Additionally, electron microscopy has been continuously developed as a seminal technique for nanomaterials research throughout the last 80 years,<sup>108,110,111</sup> leading to an extraordinary diversity of applications for this

technique. In addition to conventional imaging of inorganic samples, SEM has been used by chemists for in-situ reaction studies,<sup>25</sup> environmental monitoring,<sup>109</sup> and behavior of materials in cryogenic environments,<sup>112</sup> highlighting the versatility of SEM across a wide range of conditions and samples. Faced by the diffraction limit of visible light, which has only been conditionally overcome by groundbreaking chemistry within the last 25 years,<sup>113,114</sup> it is doubtful that materials chemistry could have advanced to its current state without the imaging capabilities afforded by electron microscopy.<sup>108,111</sup>



**Figure 2.5:** (Top) SIMS isotopic mapping of  $^{238}\text{U}$  (left) and  $^{235}\text{U}$  (right) in a uranium CRM particle. Reprinted from *Spectrochim. Acta B*, Vol. 53, Tamborini, G.; Betti, M.; Forcina, V.; Hiernaut, T.; Giovannone, B.; Koch, L. *Application of Secondary Ion Mass Spectrometry to the Identification of Single Particles of Uranium and Their Isotopic Measurement.*, pp. 1289-1302 (ref 100). Copyright 1998, with permission from Elsevier.

(Bottom) (a) SEM image and (b) EDX spectrum of a uranium oxide particle collected on a cotton swab at a nuclear facility. Reproduced from Yomogida, T.; Esaka, F.; Magara, M. *Anal. Methods*, 2017, 9, 6261–6266 (ref 120), with permission of The Royal Society of Chemistry.

SEM is frequently used for sample imaging and morphological analysis of nuclear materials,<sup>2,5,44,115–118</sup> and does not usually require destructive sample preparation. In many cases, imaging and elemental analysis can also be combined for a given instrument, enabling detailed analysis of the sample on scales of nanometers to micrometers; this is generally achieved using electron-dispersive X-ray spectroscopy (EDX) coupled to SEM (SEM-EDX).<sup>6,116,119</sup> In a study by Yomogida and coworkers, particulate samples collected in a nuclear facility were analyzed by SEM-EDX and compared to a  $\text{U}_3\text{O}_8$  CRM.<sup>120</sup> By combining the imaging and elemental analysis capabilities of SEM-EDX with chemical and isotopic data obtained from Raman spectroscopy and

SIMS, the authors were able to identify the size, morphology, chemical composition, and enrichment of these particles (*Figure 2.5*).

In a related study using SEM-EDX for particle analysis, Olsen and coworkers established a link between the size of  $U_3O_8$  nanoparticles and their calcination temperature, which can be interpreted as a fingerprint to how the material was processed.<sup>44</sup> Software analysis was used to quantitatively characterize the shape and size of particles, highlighting a trend in computer-assisted data processing that will certainly continue to develop in the coming years.

### **Transmission Electron Microscopy**

Transmission electron microscopy (TEM) is closely related to SEM, but substantially different information can be garnered through these complementary forms of electron microscopy. While SEM provides information about the surface of a sample, TEM is used to investigate the internal structure of a material with sub-nanometer resolution.<sup>121</sup> In addition to its imaging capability, TEM also outputs diffraction information, which can be used to determine crystallinity, phase, and grain size in a small sample.<sup>122,123</sup> Excellent Z-contrast is generally observed for actinide- and lanthanide-containing samples due to the large electron clouds and highly-charged nuclei of these elements,<sup>124,125</sup> making TEM a powerful form of characterization for nuclear materials. Disadvantages of TEM include time-consuming and destructive sample preparation and significant beam damage. However, the advantages of TEM are dramatic; no other technique can yield atomic-resolution imaging, diffraction across multiple planes, and elemental analysis all within the same instrument; it is this combination that has long established TEM as the gold standard for advanced characterization of materials at the nanoscale.

In a recent publication by Buck and coworkers,<sup>123</sup> nanoparticles of uranium fission products were found in spent fuel pellets from a light water reactor (LWR), and characterized using SEM and TEM coupled to EDX. Selected-area electron diffraction indicated the presence of numerous crystallites inside the individual particles, with radiation damage proposed as a likely origin for the observed fracturing pattern (*Figure 2.7*). The nanoparticles were composed primarily of a mixture of Mo, Tc, Ru, Rh, and Pd, which crystallized together in the  $\epsilon$ -Ru phase to form particles with diameters from 10-300 nm. Particles of this composition were first described by Bramman and coworkers in 1968, but detailed structural characterization could not be obtained in this earlier publication.<sup>126</sup>

These results provide a useful benchmark for the nanostructure of spent fuel pellets from LWRs. Further investigation of fission product nanoparticles formed under different conditions, such as other reactor fuel designs or weapons-grade materials, may enable more detailed fingerprinting of interdicted nuclear materials based on nanostructural detail.

TEM has also been used to detect microscopic quantities of actinides in environmental samples. Utsunomiya and coworkers have described the imaging, quantification, and elemental analysis of uranium nanocrystals present in colloidal aerosols released from coal plants.<sup>127</sup> Although these colloids had a uranium concentration below 10 ppm, the size, morphology and chemical composition of uranium nanocrystals could still be identified using high-angle annular dark field (HAADF) imaging and electron energy loss spectroscopy (EELS).

Demand for high-resolution TEM (HRTEM) has increased tremendously with the growth of materials chemistry, and significant advances have been made in resolution over the last few decades. The dramatic impact of HRTEM for solid-state chemistry was reviewed by Eyring in 1982,<sup>128</sup> and substantial improvements have been since realized. These advances include

enhancements to resolution and contrast of imaging,<sup>129</sup> the advent of nanoscale scanning TEM (STEM) tomography,<sup>124</sup> and in-situ reaction monitoring by TEM.<sup>25</sup>

Incorporation of these advanced forms of TEM into nuclear forensics laboratories could enable three-dimensional imaging of material defects and in-situ reactivity assays for nanoparticulate samples. These techniques could prove especially useful for environmental monitoring of nuclear activities or chemical studies of post-detonation samples, where sub-micron sized particles may be the only form of material obtainable in certain settings.<sup>130,131</sup>

### **Scanning Transmission X-Ray Microscopy**

In addition to the relatively well-documented methods of SIMS and electron microscopy, other microanalytical techniques also show promise for nuclear materials. Scanning transmission X-ray microscopy (STXM) is a notable example, and the applications of STXM for nuclear forensics have recently been reviewed by Pacold and coworkers.<sup>132</sup> STXM can provide imaging in conjunction with elemental mapping, and absorption of X-rays by the sample can be used to determine the spatial distribution of oxidation states for redox-active metals.<sup>133</sup> Unlike TEM, samples for STXM do not require a vacuum, and beam damage is also significantly lower than for electron beams.<sup>134</sup> STXM is particularly useful for speciation studies of heterogeneous nanoscale samples, especially when detailed information about chemical bonding is desired. Actinide microanalysis using STXM was first described in 2005 by Nilsson and coworkers,<sup>135</sup> where STXM was used to characterize the oxidation state distribution in NpO<sub>2</sub> and PuO<sub>2</sub> nanoparticles. Within five years of this publication, STXM was applied to determine uranium concentration and oxidation state in soils by Michel and coworkers<sup>133</sup> and Denecke and coworkers.<sup>63</sup> The oxidation state of actinides largely affects the migration behavior of these species in the environment,<sup>40,74,136</sup> and the use of STXM to determine actinide speciation at the nanoscale may be useful for environmental monitoring of clandestine nuclear activities by soil sampling.

### **Micro-Raman Spectroscopy**

As materials chemistry has grown rapidly throughout the last half a century, the miniaturization of spectroscopic techniques has been a subject of intense interest in the chemistry community.<sup>137</sup> Faced by the diffraction limit of light, vibrational spectroscopy of sub-micrometer samples was effectively unobtainable. However, a breakthrough occurred in 1974 with the advent of surface-enhanced Raman spectroscopy (SERS),<sup>57</sup> and this technique was continually refined in the next two decades. Single-molecule resolution using SERS was achieved in 1996 by Nie and coworkers,<sup>138</sup> with reported signal enhancement factors approaching 10<sup>15</sup>. By selective adsorption of molecules to a nanostructured surface, tremendous enhancement of Raman signals can be obtained, allowing for spectroscopic measurements to be performed on nanometer-sized samples. Despite the long history of micro-Raman spectroscopy in the chemical sciences, applications of this technique to nuclear forensic challenges have been only sparsely reported. Chemical speciation in uranium oxide thin films was studied by He and coworkers in 2012 using SERS.<sup>53</sup> A monolayer of Au@SiO<sub>2</sub> core-shell nanoparticles was used as the surface enhancement agent, with the authors citing increased plasmon generation of core-shell versus single nanoparticles as the motivation for this system. Raman signal enhancement of up to 10<sup>7</sup> was reported, and SERS was able to distinguish  $\gamma$ -UO<sub>3</sub> from  $\alpha$ -U<sub>3</sub>O<sub>8</sub> with nanometer-scale spatial resolution (*Figure 2.2*). This technique is significant as a nondestructive means to determine the chemical speciation of uranium

oxide at the nanoscale, which can be dramatically affected by the environmental conditions a sample has been subjected to; for example, in a nuclear reactor.<sup>73</sup>

Building upon previous systems for detection of aqueous uranium by SERS,<sup>139–141</sup> Trujillo and coworkers recently published a method to detect uranyl ions using glutathione-functionalized silver colloids as the complexation and sensitization agent.<sup>52</sup> The authors report high selectivity of the colloids for uranyl in matrix of other trace metals, and uranyl detection sensitivity at parts per billion concentration. Moreover, the functionalized colloids are readily used in a handheld Raman spectrometer. This study represents what may be, to date, the most sensitive portable method for uranium detection in a field setting. Potential uses of this technology include groundwater surveys for monitoring applications, and also quantification of uranium migration in a post-detonation event.

### **Micro-XRF**

X-ray fluorescence is another form of spectroscopy that has been adapted relatively recently for small samples. Micro-XRF operates by scanning a small X-ray beam across a surface, providing spatially-resolved elemental analysis of a sample with a resolution of a few tens of microns. Micro-XRF was first applied towards forensics in 2006 by Worley and coworkers as a sensitive and nondestructive means of characterizing the elemental constituents of human fingerprints.<sup>142</sup> Shortly following the adoption of micro-XRF in conventional forensics, nuclear forensic applications of this technology began to develop. Micro-XRF was used by Batuk and coworkers to characterize actinide speciation at a number of contaminated sites, comprising samples from reactor meltdown, fuel reprocessing, weapons development, and disposal operations.<sup>61</sup> Spatial elemental analysis by micro-XRF showed significant variation in the Pu, U, Zr, and O composition of particles based on the location of the soil and the processes by which contaminants were introduced to the site. Chemical species not commonly found under environmental conditions, including mononuclear, non-oxide Pu(IV) compounds, were also detected by micro-XRF; the authors postulate that poorly-understood surface chemistry may play a substantial role in the persistence of these species. Perhaps most notably, non-naturally-occurring U and Pu particles were identified using micro-XRF in samples where bulk analysis did not show these elements to be present above background levels, clearly demonstrating the value of microanalysis as a complementary technique to conventional bulk analysis.

The usefulness of micro-XRF for nuclear forensics was also described in a recent paper by Rim and coworkers, in which two plutonium foils of unknown provenance were analyzed using micro-XRF, gamma spectroscopy, and MS.<sup>143</sup> Major isotopes present in the sample were first determined using gamma spectroscopy, and the elemental homogeneity of the sample was then mapped using micro-XRF. Plutonium was not detected in the sample cladding, suggesting manufacturing conditions conducive to experimental applications. Detection of gallium in the XRF spectra of the foils indicated that alloying had been performed to stabilize the  $\delta$ -phase of Pu, and this conclusion was used to refine the chemical separation procedures used for destructive analysis. Based on combined isotopic, elemental, and morphological data, the foils were identified as super-grade Pu targets for physics experiments at Hanford. This paper highlights the value of using complementary forms of characterization for nuclear forensic analysis, and it also demonstrates the utility of micro-XRF for rapid and nondestructive elemental analysis at the mesoscale.

In another noteworthy example, McIntosh and coworkers employed micro-XRF and 3D confocal XRF to identify individual particles of Pu in soil samples from contaminated areas,



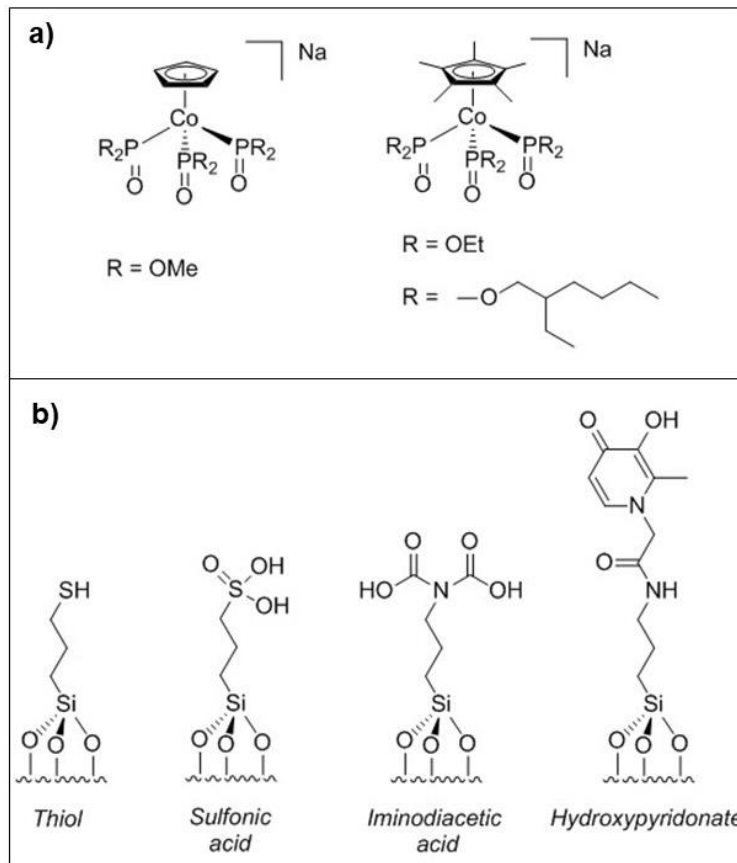
including Palomares, Spain and the Marshall Islands<sup>144</sup> (*Figure 2.3*). Multi-element characterization was performed nondestructively, with a calculated detection limit of <15 ng for Pu. In addition to performing conventional 2D micro-XRF measurements, the authors also introduce 3D confocal XRF to the nuclear forensic sphere. The resulting three-dimensional elemental maps are in good agreement with the 2D micro-XRF images, but the 3D tomographic images deliver a significant improvement in resolution. These measurements carry significance for measuring the environmental migration of Pu in various geological sites, which is vital to sample collection in a post-detonation scenario.<sup>145</sup>

## **Interface with Synthetic Chemistry**

Although nuclear forensics is primarily an analytical field, there are numerous ways that synthetic chemistry has delivered significant improvements to existing nuclear forensic capabilities. Examples of synthetic pursuits relevant to nuclear forensics include the synthesis of thin films for high-speed alpha spectrometry, the design of highly selective materials for analyte sequestration, and the rapid development of actinide nanoscience.

### **Functionalized Polymer Films for Alpha Spectrometry**

Although electrodeposition of thin films for alpha spectrometry can be performed more rapidly than sample preparation for most forms of MS, multiple hours are still required to obtain an electrodeposited sample for analysis. In cases where quantification of alpha emitters is urgently required, rapid sample preparation techniques have been developed using adsorbent polymers that selectively bind actinides. The first application of modified polymer films for alpha spectrometry analysis was described by Gonzales and coworkers in 2009.<sup>146</sup> Using a polymer film functionalized with the actinide-selective ligand DIPEX (= bis(2-ethylhexyl)methanediphosphonic acid), Pu and Am were harvested from solution and the resulting films were counted using alpha spectrometry. Although spectral resolution was good (fwhm ~60 keV), the total yield of actinides adsorbed to the films was low (2-46%). Using a similar methodology, Oldham and coworkers developed films functionalized with carbamoylmethylphosphate ligands, which showed superior resolution (fwhm ~22 keV) but comparable actinide adsorption yields (~30%).<sup>147</sup> Thin films with higher binding efficiency were later reported by Hanson and coworkers using Kläui-type organometallic cobalt complexes spin-coated to a glass substrate<sup>148</sup> (*Figure 2.6*). The Kläui-type ligands, which act as tripodal oxygen donors, were found to bind actinides much more effectively than previous ligands; Np and Pu binding yields for the Kläui-type films were reported to be upwards of 80%.



**Figure 2.6:** a) Klüiver-type ligands used to bind actinides for alpha spectrometry.<sup>148</sup> b) Ligands functionalized onto mesoporous silica surfaces for aqueous actinide sorption.<sup>155</sup>

### Mesoporous Adsorbents for Radionuclides

Mesoporous materials have been widely studied as separation agents,<sup>149</sup> templating agents for nanoparticles,<sup>150</sup> and chemical microreactors.<sup>151</sup> These materials contain pores between 2 and 50 nm in size and can be functionalized for chemical selectivity. Within the nuclear industry, mesoporous materials have been used for wastewater decontamination and for the separation of fission products from complex matrices.<sup>152</sup> The design of mesoporous sorbents for actinide sequestration is an active field of research, and new materials with high selectivities continue to be developed.<sup>153,154</sup>

Mesoporous silica and MnO<sub>2</sub> functionalized with ligands that have a high affinity for actinides, such as hydroxypyridonates, have been shown by Johnson and coworkers to possess notably better actinide sorption ability than conventional actinide sorbents in both ocean and river water<sup>155–157</sup> (Figure 2.6). This metal selectivity could also be controlled by modifying the functionalization of the mesoporous materials: soft Lewis-acidic metals such as Ag were preferred by materials functionalized with thiols, and Cs was preferred by materials functionalized with cyanoferrates. These mesoporous materials were developed to chemically concentrate anthropogenic radionuclides from a matrix containing a large quantity of natural radionuclides such as <sup>40</sup>K, thereby bolstering capabilities for downstream reactor monitoring by gamma spectroscopy.

In addition to selective adsorption of small metal ions, mesoporous materials with a larger pore size can be used to collect large metal clusters. Liu and coworkers reported the reversible sorption of uranyl peroxo cage clusters to the mesoporous silica SBA-15 under neutral and mildly basic conditions.<sup>158</sup> These peroxo clusters are formed in aqueous environments containing a high concentration of uranium and a large radiation flux. Although uranyl peroxo clusters only form in significant concentrations under a very specific set of conditions, they are relatively stable in the environment. Sequestration of these clusters, followed by measurement of their isotopic ratios, could provide a low-profile and cost-effective method for reactor monitoring.

### **Synthesis and Microanalysis of Actinide Oxide Particles**

There is a growing need within the nuclear forensic community for particulate uranium- and plutonium-based CRMs with a known isotopic composition, as most current CRMs for nuclear forensic applications are only available as bulk materials.<sup>130,159–162</sup> Without microanalytical control measurements on independently-verified and standardized particulate materials, forensic analysis of seized nuclear materials could potentially be deemed inadmissible in certain courts.<sup>162,163</sup> Production of these standard materials relies upon the development of controllable synthetic routes, which are in turn dependent upon a mechanistic understanding of the formation processes. Within the last few years, a relatively large amount of progress in this realm has led to the discovery of new or substantially improved processes to synthesize these nanomaterials,<sup>164–170</sup> and has also resulted in significant improvements for their characterization. We predict that a firmer understanding of the chemistry involved in actinide nanomaterials synthesis will result in significant improvements to the quality of reference materials for nuclear forensic analysis, and furthermore, that this research will improve the capability of microanalysis as a tool for nuclear forensic fingerprinting.

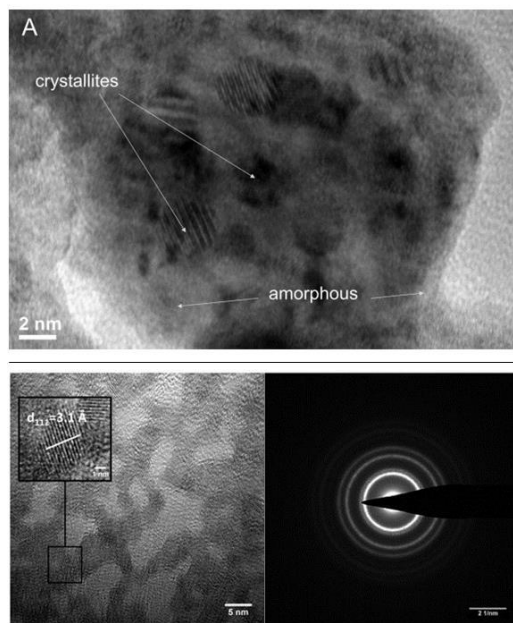
A noteworthy example of controlled nuclear particle synthesis with a known isotopic composition is detailed in a publication by Shinonaga and coworkers, in which spray pyrolysis of a plutonium CRM was employed to form PuO<sub>2</sub> microparticles.<sup>171</sup> SEM-EDX and Raman spectroscopy were used to determine structural information and elemental composition of these microparticles, and detailed isotopic distribution measurements were obtained using MS. This study demonstrates the benefits of microanalysis for small particulate samples of nuclear material, and also provides a benchmark for the physical properties and isotopic distribution observed under controlled conditions.

In a similar, more recent, study by Middendorp and coworkers, the structural properties of uranium oxide microparticles were measured and correlated to their formation conditions in a spray pyrolysis process.<sup>54</sup> One of the main objectives of this research was to establish a direct comparison between the composition and shape of uranium oxide nanoparticles as a result of the conditions of their formation. A combination of SEM-EDX, Raman spectroscopy, and PXRD was used to determine the physical morphology, elemental composition, and crystal orientation of the microparticles. The shape and composition of the resulting oxide particles were significantly affected by the temperature of pyrolysis, as well as the molecular precursor used. These effects are attributed to the differing solubility and decomposition pathways for uranyl chloride, uranyl acetate, and uranyl nitrate. Linking the properties of uranium oxide nanoparticles to their formation conditions may be useful to assign the processing history of particulate uranium oxide samples, which are readily obtained during power plant monitoring operations.<sup>172</sup>

A related publication by Dalodière and coworkers built upon these methods by developing both the synthetic and the analytical capabilities for controlled actinide nanoparticle synthesis.<sup>167</sup>

A combination of STXM, XAS, and TEM were used to study the structure and composition of colloidal  $\text{PuO}_2$  nanoparticles, which are largely responsible for the migration behavior of plutonium within aquatic systems.<sup>136,167,173</sup> Previous studies on  $\text{PuO}_2$  colloids have been limited by poor homogeneity and purity, but these challenges were overcome using a sonochemical synthetic procedure. STXM enabled accurate elemental analysis of the  $\text{PuO}_2$  nanoparticles, and the grain structure of the particles was measured at sub-nanometer resolution using HRTEM (*Figure 2.7*). From these data, a direct comparison was established between the composition and morphology of  $\text{PuO}_2$  nanoparticles synthesized using different routes. Establishing a link between the mechanism of formation and the structural properties of  $\text{PuO}_2$  could have significant impacts for determining the origin of environmental  $\text{PuO}_2$  based on particle morphology, which could in turn be useful for monitoring applications and CRM production.<sup>136,162,173,174</sup>

These three studies represent an important trend in actinide microanalysis. Spanning a period of only five years, substantial advances have been made towards architectural control of actinide particles, and the analytical techniques used to characterize these particles have advanced significantly in this timeframe. As synthetic actinide nanoscience continues to develop throughout the next decade, the resulting chemical and physical information that is gleaned through these studies may greatly enhance the capabilities of nuclear forensic science by significantly decreasing the sample size required to determine a sample's isotopic distribution, chemical form, and origin. Miniaturization of analytical techniques may especially bolster monitoring operations in processing plants and post-detonation scenarios, when large samples cannot be obtained for practical or political reasons.<sup>175</sup>



**Figure 2.7:** (Top) TEM image of fission product crystallites embedded in a 20 nm nanoparticle within a spent fuel pellet. Reprinted from *J. Nucl. Mater.*, Vol. 461, Buck, E. C.; Mausolf, E. J.; McNamara, B. K.; Soderquist, C. Z.; Schwantes, J. M. *Nanostructure of Metallic Particles in Light Water Reactor Used Nuclear Fuel*, pp. 236-243 (ref 123). Copyright 2015, with permission from Elsevier.

*(Bottom) Bright-field TEM image and diffraction pattern of colloiddally-synthesized PuO<sub>2</sub> nanoparticles. Reproduced from Dalodière, E.; Viro, M.; Morosini, V.; Chave, T.; Dumas, T.; Hennig, C.; Wiss, T.; Dieste Blanco, O.; Shuh, D. K.; Tyliszczak, T. et al., Sci. Rep., 2017, 7, 43514 (ref 167) under a Creative Commons Attribution 4.0 International License (<https://creativecommons.org/licenses/by/4.0/>).*

## **Post-Detonation Analysis**

Most nuclear forensic studies published in the open literature focus on pre-detonation scenarios, with the stated goal of preventing nuclear smuggling through source attribution. However, in the event of a nuclear detonation, determining the origin and design of a nuclear weapon is critical to maintain international security.<sup>4</sup> Post-detonation nuclear forensics seeks to address this challenge, with the primary goal of linking isotopic, chemical, and geological signatures produced in a nuclear explosion to the type and origin of the bomb that generated them. Much of the knowledge in this area stems from extensive documentation of the U.S. nuclear weapons testing program.<sup>176</sup> Due to the severe risk of nuclear proliferation from information compiled in nuclear weapons testing documents, the vast majority of post-detonation research remains classified and inaccessible to the general public. This section of the Review seeks to detail the scope of post-detonation nuclear forensics, summarizing relevant studies available in the open literature. Case studies pertaining to the 1945 Trinity Test will be discussed here, and the methodology used in these analyses will be compared with pre-detonation nuclear forensics. Recent developments in synthetic fallout surrogate materials will also be discussed.

### **History and Scope**

On July 16, 1945, the world's first nuclear weapon was detonated at the White Sands Missile Range in New Mexico. This device, known as "The Gadget," marked the beginning of the nuclear era. The Gadget was an implosion-type plutonium bomb with a similar design to the Fat Man bomb dropped over Nagasaki one month later. Most data from the Trinity Test has been declassified, and the site is publicly accessible to scientists and the general public.<sup>20</sup> As a result, the Trinity Site provides a unique opportunity for scientists to conduct unclassified research in a post-detonation scenario.

Characterization of an exploded nuclear device is primarily accomplished through analysis of the radioactive fallout produced by the explosion. This is a challenging problem because significant fractionation of products occurs during and after the blast. Following a nuclear explosion, radioactive particles are distributed both locally and globally, with migration behavior varying largely between different radioisotopes.<sup>176,177</sup> Assigning the yield and design of a nuclear weapon from fallout patterns is often referred to by post-detonation scientists as "unbaking the cake": the fractionation of radionuclides in a nuclear blast introduces a distinct challenge not found in pre-detonation scenarios.<sup>178,179</sup> Consequently, radiological geochemistry is instrumental for predicting, locating, and analyzing elemental dispersion following a nuclear detonation.

The geochemical distribution of products from the Trinity Test was largely affected by the local geology of the test site. Arkosic sand forms a major surface component of the White Sands site, and the heat from the blast famously resulted in the formation of radioactive glass, dubbed Trinitite, from the sand melted in the blast.<sup>19</sup> Initial reports in the 1940s focused almost entirely on the radioactivity of Trinitite, which was mainly treated as a homogeneous radiological material

until evidence was found to the contrary. In 1948, a singular report by Ross described the elemental heterogeneity of Trinitite and proposed formation mechanisms for various components of the glass.<sup>180</sup>

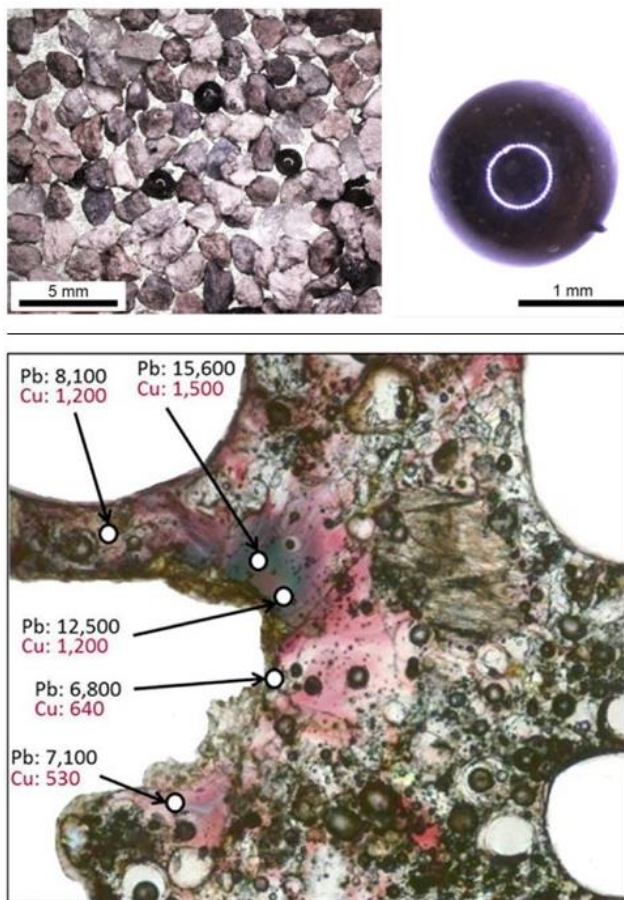
Post-detonation fractionation of radionuclides has been previously discussed in a small handful of articles dating back to the 1960s and 70s,<sup>176,177,181</sup> but the scope of these studies were greatly limited by the absence of accessible microanalytical techniques for the small (often sub-micron) particles generated by nuclear blasts. Detailed chemical and morphological analysis of the debris from the Trinity Test remained mostly unexplored until later decades, and the modern focus on the Trinity Site as a case study for post-detonation forensics has arisen almost entirely within the last ten years.<sup>182</sup>

### **Trinity Fallout Studies**

One of the earliest nuclear forensics-focused studies of Trinitite heterostructure was published by Fahey and coworkers in 2010.<sup>182</sup> Older techniques, such as refractive measurements and autoradiography, were used in conjunction with modern forms of analysis, such as SIMS and spatially-resolved XRF, for elemental mapping of actinides and fission products in the glass. Using the spatial distribution of Pu, U, and Pb isotopes in the samples, the authors were able to determine that a plutonium core with a uranium tamper was used in the device. This landmark publication conclusively demonstrated the potential of fallout debris analysis for post-detonation event attribution, marking the beginning of a surge of research on the formation mechanisms, morphology, and elemental composition of Trinitite.

Radiochemical fractionation of fallout debris is not only a function of the nuclear components of a weapon, but also of the non-nuclear components of the device and the surrounding geological environment. This debris is usually a combination of surface-melted minerals, bomb remnants, and glassy ejection products that coalesce in the atmosphere.<sup>78,183,184</sup> A detailed summary of the formation and morphology of Trinitite was written by Bonamici and coworkers; this paper focused particularly on the bulk components of the glass and their naturally-occurring geological analogues.<sup>145</sup> While most samples of Trinitite are olive-green in appearance, some samples gathered north of the blast possessed a reddish color. Using SEM elemental mapping, Eby and coworkers determined that copper is responsible for this distinctive variation in appearance.<sup>19</sup> The authors concluded that copper and lead globules in red Trinitite specimens were formed from melted pieces of the bomb, indicating that elements present in a bomb's non-nuclear components can be collected and analyzed even after detonation, helping to build a more complete picture of the original makeup of the device.

This concept was also explored by Bellucci and coworkers in a study linking the metals present in Trinitite samples to the specific parts of the device from which these metals originated.<sup>15</sup> Using SEM-EDX for elemental mapping, Fe-Ti inclusions were linked to the explosion tower, Cu grains to the device wiring and core of the device. A follow-up study employed LA-ICP-MS to find the isotopic composition of Pb in Trinitite.<sup>21</sup> The authors were able to correlate the Pb isotopic ratios in Trinitite samples to the Buchans lead mine in Newfoundland, Canada, which was operated by a U.S. mining company during the time of construction of The Gadget. These findings were also corroborated by Koeman and coworkers in a later publication<sup>18</sup> (*Figure 2.8*).



**Figure 2.8:** (Top) (Left) An assortment of Trinitite containing spherical glassy fallout interspersed with coarse soil fragments. (Right) Enlarged image of a glassy fallout particle. The white ring in the center is a reflection of the microscope light. Reprinted from *J. Environ. Radioact.*, Vol. 148, Lewis, L. A.; Knight, K. B.; Matzel, J. E.; Prussin, S. G.; Zimmer, M. M.; Kinman, W. S.; Ryerson, F. J.; Hutcheon, I. D. *Spatially-Resolved Analyses of Aerodynamic Fallout from a Uranium-Fueled Nuclear Test*, pp. 183-195 (ref 185). Copyright 2015, with permission from Elsevier. (Bottom) Optical image of a Trinitite slice analyzed by LA-ICP-MS. Concentrations of Pb and Cu are given in  $\mu\text{g/g}$  at various points of the sample. Reproduced from Koeman, E. C.; Simonetti, A.; Burns, P. C. *Anal. Chem.*, 2015, 87, 5380–5386 (ref 18). Copyright 2015 American Chemical Society.

In addition to providing compositional analysis and reconstruction of The Gadget's components from its fallout, microanalytical techniques such as SIMS and SEM-EDX have also been used to provide a temporal picture of radionuclide fractionation and geochemical mixing in the Trinity detonation. In a recent publication by Lewis and coworkers, the spatially-resolved isotopic heterogeneity of enriched and natural uranium in Trinitite was correlated to the thermal history of the glass.<sup>185</sup> Samples that resided for a longer duration in the fireball were found to have a greater degree of mixing between enriched and natural uranium. These results indicate a means to discriminate between different types of fallout from the same blast, thereby enabling more accurate reconstruction of the parent device (*Figure 2.8*).

The isotopic compositions of fission products in Trinitite have also been correlated with the yield of the device. Using LA-ICP-MS and electron probe microanalysis, Sharp and coworkers detected highly abnormal ratios of lanthanide isotopes in the fallout debris.<sup>16</sup> U and Pu isotopic ratios were also collected, and the combined actinide and lanthanide data were used to calculate the average neutron fluence of the explosion, with contributions from both <sup>239</sup>Pu and <sup>235</sup>U fission. In a related work by Hanson and coworkers,<sup>178</sup> the isotopic ratios of Zr, Mo, and Cs were correlated to device yield. The estimated yield from Zr isotopics was in good agreement with the officially-reported 21 kiloton yield of the device, while Cs isotopics were much less accurate due to heterogeneous fractionation of Cs-containing species.

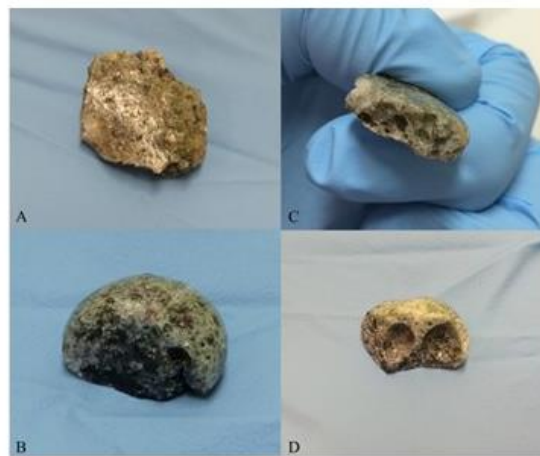
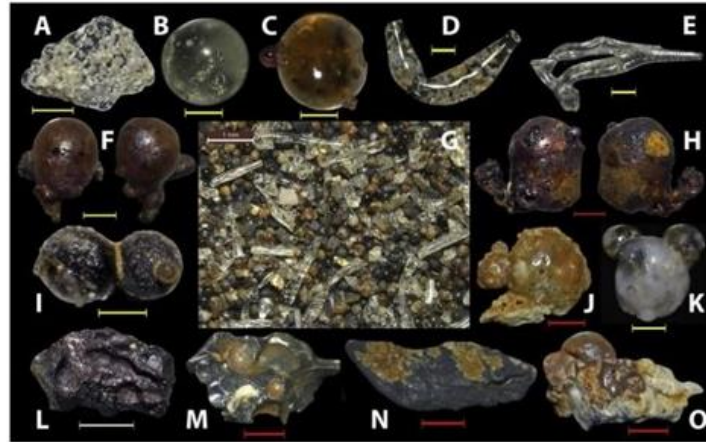
The implications of these Trinity fallout studies are quite significant for post-detonation nuclear forensics. A wealth of information about the composition of the original bomb was garnered from the blast site through nondestructive methods alone, and a detailed reconstruction of the bomb components and yield was accomplished using mass spectrometry. Microanalytical techniques such as SIMS, LA-ICP-MS, and SEM-EDX were a key part of these studies, illustrating the critical role that microanalysis can play in post-detonation scenarios.

### **Hiroshima Fallout Studies**

Due to the stringent classification of information related to nuclear testing, most academic studies involving fallout analysis have been limited to samples of Trinitite. Although these studies are highly valuable for post-detonation nuclear forensics, they represent only one sample type and geological environment. Following the Trinity test in 1945, two other nuclear weapons, Little Boy and Fat Man, were detonated over Japan, prompting the immediate end of World War II. These detonations are the only instances where nuclear weapons were used in real urban areas, and fallout studies in Hiroshima and Nagasaki could produce a wealth of information regarding post-detonation nuclear forensics in non-desert environments.

Historically, all such studies have been classified, but in 2019, the first unclassified study of fallout from the Hiroshima detonation was released by Wannier and coworkers.<sup>186</sup> Fallout samples were collected on beaches located 6 and 12 km from the detonation epicenter, then the samples were sorted by morphological features and analyzed using SEM-EDX and X-ray microdiffraction. These particles were found to be significantly different from known materials produced by meteorites, volcanoes, fireworks, or industrial processes. Although most of the Hiroshima fallout particles were similar in composition to previously-described samples of Trinitite, vesicular and composite glass structures were also present (*Figure 2.9*). Some of these structures have not been previously described in the open literature, and the authors hypothesize their formation may have arisen from vaporized urban building materials. This claim is corroborated by the Si- and Fe-rich composition of the fallout, which aligns with the composition of the concrete and steel used in buildings destroyed by the blast.





**Figure 2.9:** (Top) Different morphologies of fallout particles collected in Hiroshima Bay. Reprinted from *Anthropocene*, Vol. 25, Wannier, M. M. A.; Urreiztieta, M. De; Wenk, H.; Stan, C. V.; Tamura, N.; Yue, B. *Fallout Melt Debris and Aerodynamically-Shaped Glasses in Beach Sands of Hiroshima Bay, Japan, 100196* (ref 186). Copyright 2019, with permission from Elsevier.

(Bottom) Structural comparison of synthetic melt glass (A: surface, D: internal) and trinitite (B: surface, C: internal). This is adapted from Molgaard, J. J., Auxier II, J. D., Giminaro, A. V., Oldham, C. J., Gill, J., Hall, H. L. *Production of Synthetic Nuclear Melt Glass. J. Vis. Exp. (107), e53473, doi:10.3791/53473* (2016) (ref 190).

### Synthetic Fallout Surrogates

In order to further expand the scope of fallout analysis, synthetic reference materials have been developed to mimic real-world and hypothetical fallout samples in numerous environments. Since these surrogate materials are synthesized in a laboratory, they do not contain any information about real-world nuclear tests; as such, surrogate fallout materials serve as valuable tools to strengthen global nuclear forensics capabilities in an open setting.<sup>187</sup>

Synthetic nuclear melt glass is a recent addition to the post-detonation nuclear forensics landscape. One of the earliest surrogate glasses, reported by Carney and coworkers in 2013, was synthesized by incorporating HEU into a silicate polymer, irradiating the composite with a neutron flux to induce fission of  $^{235}\text{U}$ , then annealing the material at 1000 °C.<sup>188</sup> An inhomogeneous

distribution of volatile and refractory fission products was observed, analogous to the fractionation of radionuclides in a nuclear fireball. Following this publication, a more advanced method was designed by Molgaard and coworkers to closely simulate the elemental composition of Trinitite.<sup>189</sup> In this method, a melt of metal oxides and hydroxides was poured into a sand-filled crucible to form a glass, which was then activated by neutron irradiation (*Figure 2.9*). This synthetic melt glass was found to be very similar to Trinitite by XRD and SEM-EDX, and the radionuclide distribution could be modified by alteration of the irradiation time/flux and by the concentration of actinides within the melt. A follow-up publication by the same group delved further into the tunability of these systems, including methods to simulate fallout generated in urban environments.<sup>190</sup>

Perhaps the most valuable application of synthetic fallout surrogates is the ability to predict and model the fallout that could form in real-world locations, both urban and rural, enabling rapid response to a detonation event. Giminaro and coworkers have reported methods to synthesize surrogate post-detonation debris with comparable elemental compositions to the U.S. cities of Houston, TX and New York, NY.<sup>191</sup> In an urban detonation, the fallout matrix would be largely formed from building materials, such as cement, glass, and steel, resulting in complex fallout with a wide range of potential compositions. To tackle this problem, Liezers and coworkers have developed a laser-based method to rapidly synthesize fallout surrogates from nearly any material in a glassy matrix.<sup>192,193</sup> The materials produced displayed a pattern of radionuclide fractionation that was similar to the observed elemental distribution in aerodynamic debris samples from real nuclear tests. Related studies have also used synthetic methods to study the fractionation behavior of aerosols<sup>194</sup> and small particles<sup>195</sup> produced in a detonation event. As this area of research is fairly new, advancements in the production and analysis of simulated post-detonation fallout materials will certainly continue to develop.

## Conclusions

In order to maintain global peace in the nuclear era, the rapid detection and attribution of interdicted nuclear materials is imperative. However, as more countries gain access to nuclear materials for peaceful applications in energy and medicine, the potential for proliferation of nuclear weapons increases. In order to prevent the flow of nuclear weapons into the wrong hands, global nuclear forensics capabilities must continue to evolve. Early reports on nuclear forensics primarily involved well-documented analytical procedures that have been in use for decades,<sup>1,196-198</sup> but recent developments in chemistry and materials science have brought new analytical capabilities to the table. In particular, the development of modern microanalytical techniques has allowed for chemical and physical analyses to be performed on samples of virtually any size and composition. These techniques will serve a prominent role in the future of nuclear forensic science when only ultratrace quantities of material are acquirable, such as environmental monitoring and inspections of nuclear facilities.<sup>130</sup>

In the event of a nuclear detonation, rapid attribution is of paramount importance, and post-detonation nuclear forensics must also continue to grow and develop. Early studies on nuclear fallout were limited by the relatively large quantities of material required for chemical analysis,<sup>176</sup> but microanalytical techniques such as micro-XRF and SEM-EDX have been used to study fallout from the Trinity test in great detail. This area of research has recently expanded into studies of urban fallout from the Hiroshima detonation and the production of synthetic nuclear melt glass to

simulate a large number of geological and urban environments. Future developments in these areas, especially contributions that are accessible within the open literature, will bolster global nonproliferation and attribution capabilities in pre- and post-detonation scenarios.

LA-UR-19-31358

## References

- 1 K. J. Moody, I. D. Hutcheon and P. M. Grant, *Nuclear Forensic Analysis*, CRC Press, Second Ed., 2014.
- 2 K. Mayer, M. Wallenius and T. Fanghänel, *J. Alloys Compd.*, 2007, **444–445**, 50–56.
- 3 K. Mayer, M. Wallenius, Z. Varga, T. Wiss and T. Fanghänel, *Proc. Radiochem. A Suppl. to Radiochim. Acta*, 2011, **1**, 145–149.
- 4 Joint Working Group of the American Physical Society and the American Association for the Advancement of Science, *Nuclear Forensics: Role, State of the Art, and Program Needs*, 2008.
- 5 F. E. Stanley, A. M. Stalcup and H. B. Spitz, *J. Radioanal. Nucl. Chem.*, 2013, **295**, 1385–1393.
- 6 X. Hou, W. Chen, Y. He and B. T. Jones, *Appl. Spectrosc. Rev.*, 2005, **40**, 245–267.
- 7 Z. Varga, J. Krajko, M. Peñkin, M. Novák, Z. Eke, M. Wallenius and K. Mayer, *J. Radioanal. Nucl. Chem.*, 2017, **312**, 639–654.
- 8 L. R. Morss, N. M. Edelstein, J. Fuger and J. J. Katz, *The Chemistry of the Actinide and Transactinide Elements*, Springer, 2006.
- 9 J. M. Haschke and J. L. Stakebake, in *The Chemistry of the Actinide and Transactinide Elements*, Springer, Dordrecht, 2006, pp. 3199–3272.
- 10 V. Fedchenko, *The New Nuclear Forensics*, Oxford University Press, 2015.
- 11 D. E. Crean, C. L. Corkhill, T. Nicholls, R. Tappero, J. M. Collins, N. C. Hyatt, T. Fanghänel, K. Mayer, G. Tamborini, S. Török, G. Falkenberg, A. Alseycz, H. Dahlgaard, P. Wobrauschek, C. Streli, N. Zoeger and M. Betti, *RSC Adv.*, 2015, **5**, 87908–87918.
- 12 J. M. Schwantes, M. Douglas, S. E. Bonde, J. D. Briggs, O. T. Farmer, L. R. Greenwood, E. A. Lepel, C. R. Orton, J. F. Wacker and A. T. Luksic, *Anal. Chem.*, 2009, **81**, 1297–1306.
- 13 I. W. Croudace, P. E. Warwick, D. G. Reading and B. C. Russell, *TrAC Trends Anal. Chem.*, 2016, **85**, 120–129.
- 14 D. W. Podlesak, R. E. Steiner, C. J. Burns, S. P. LaMont and L. Tandon, in *US-Taiwan Nuclear Forensics Meeting*, Taipei, 2012, pp. 1–23.
- 15 J. J. Bellucci and A. Simonetti, *J. Radioanal. Nucl. Chem.*, 2012, **293**, 313–319.
- 16 N. Sharp, W. F. McDonough, B. W. Ticknor, R. D. Ash, P. M. Piccoli and D. T. Borg, *J. Radioanal. Nucl. Chem.*, 2014, **302**, 57–67.
- 17 P. Zhao, R. M. Tinnacher, M. Zavarin and A. B. Kersting, *J. Environ. Radioact.*, 2014, **137**, 163–172.
- 18 E. C. Koeman, A. Simonetti and P. C. Burns, *Anal. Chem.*, 2015, **87**, 5380–5386.

- 19 N. Eby, R. Hermes, N. Charnley and J. A. Smoliga, *Geol. Today*, 2010, **26**, 180–185.
- 20 T. Widner, *Draft Final Report of CDC's LAHDRA Project, Chapter 10*, 2009.
- 21 J. J. Bellucci, A. Simonetti, C. Wallace, E. C. Koeman and P. C. Burns, *Anal. Chem.*, 2013, **85**, 7588–7593.
- 22 S. Manolakos, F. Sinatra, L. Albers, K. Hufford, J. Alberti, E. Nazarov and T. Evans-Nguyen, *Anal. Chem.*, 2016, **88**, 11399–11405.
- 23 M. West, A. T. Ellis, P. J. Potts, C. Strelis, C. Vanhoof, D. Wegrzynek, P. Wobruschek, F. G. Silva, N. Szymanski, A. D. Kroumov, P. Moretto, C. Moulin, L. Valiente, L. A. Konopelko, C. Quétel, P. Vermaercke, J. V. L. Manzano, M. Linsky, E. Cortes, S. Tangpitayakul, L. Plangsangmas, L. Bergamaschi, R. Hearn, A. Simionovici, U. Spillmann, Z. Stachura, T. Stohlker, M. Trassinelli, S. Trotsenko, A. Warczak, O. Wehrhan and E. Ziegler, *J. Anal. At. Spectrom.*, 2010, **25**, 1503.
- 24 K. Tsuji and I. John Wiley & Sons, *X-Ray Spectrometry: Recent Technological Advances*, John Wiley Sons, 2004.
- 25 G. Dehm, J. M. Howe and J. Zweck, *In-situ electron microscopy : applications in physics, chemistry and materials science*, Wiley-VCH, 2012.
- 26 K. Mayer, M. Wallenius and Z. Varga, *Chem. Rev.*, 2013, **113**, 884–900.
- 27 S. A. Stratz, J. A. Gill and H. L. Hall, *Int. J. Nucl. Secur.*, 2016, **2**, 1–15.
- 28 IAEA, *Safeguards Techniques and Equipment*, Vienna, 2003, vol. 1.
- 29 K. Mayer, *Destructive Analytical Measurement Techniques in Nuclear Material Safeguards*, 2015.
- 30 K. Mayer, M. Wallenius and Z. Varga, *Anal. Chem.*, 2015, **87**, 11605–11610.
- 31 G. F. Knoll, *Radiation detection and measurement*, John Wiley, 2010.
- 32 K. J. Hofstetter, D. M. Beals, J. E. Halverson, E. Villa-Aleman and D. W. Hayes, *J. Radioanal. Nucl. Chem.*, 2001, **248**, 683–687.
- 33 G. R. Choppin, G. R. Choppin, J.-O. Liljenzin and J. Rydberg, *Radiochemistry and nuclear chemistry*, Butterworth-Heinemann, 2002.
- 34 U.S. Department of Homeland Security, *Neutron-Detecting Personal Radiation Detectors ( PRDs ) and Spectroscopic PRDs Market Survey Report*, 2015.
- 35 IAEA, *Detection of radioactive materials at borders*, Vienna, 2002.
- 36 A. Morgenstern, C. Apostolidis and K. Mayer, *Anal. Chem.*, 2002, **74**, 5513–5516.
- 37 S. K. Aggarwal, L. W. Leveille, D. Lariviere, B. Busche, T. S. Zemanian, G. J. Fryxell, A. Alonso, X. Mougeot, V. Jobbágy, M. Rodrigues, R. Van Ammel, H. Stroh, A. Luca, E. Coccia, V. Fafone, C. Bucci and A. Rotilio, *Anal. Methods*, 2016, **8**, 5353–5371.
- 38 M. Wallenius, K. Mayer and I. Ray, *Forensic Sci. Int.*, 2006, **156**, 55–62.
- 39 F. E. Stanley, S. E. Glover, A. M. Stalcup, H. B. Spitz, D. M. Beals and J. Rad, *J. Anal. At. Spectrom.*, 2012, **27**, 1821.
- 40 K. Maher, J. R. Bargar and G. E. Brown, *Inorg. Chem.*, 2013, **52**, 3510–3532.
- 41 Z. Varga, M. Wallenius, K. Mayer, E. Keegan and S. Millet, *Anal. Chem.*, 2009, **81**, 8327–8334.
- 42 E. Balboni, N. Jones, T. Spano, A. Simonetti and P. C. Burns, *Appl. Geochemistry*, 2016,

- 74, 24–32.
- 43 D. Mer Lin Ho, D. Manara, Z. Varga, L. Fongaro, A. Nicholl, M. Ernstberger, A. Berlizov, P. Lindqvist-Reis, T. Fanghaenel and K. Mayer, in *IAEA Nuclear Forensics Conference 2014*, 2014.
- 44 A. M. Olsen, B. Richards, I. Schwerdt, S. Heffernan, R. Lusk, B. Smith, E. Jurrus, C. Ruggiero and L. W. McDonald, *Anal. Chem.*, 2017, **89**, 3177–3183.
- 45 N. C. Thomas, *J. Chem. Educ.*, 1991, **68**, 631–634.
- 46 P. Larkin, *Infrared and raman spectroscopy: principles and spectral interpretation*, Elsevier, 2011.
- 47 In *Infrared and Raman Spectroscopy*, Wiley-VCH Verlag GmbH, Weinheim, Germany, pp. 1–5.
- 48 A. V. Ewing and S. G. Kazarian, *Analyst*, 2017, **142**, 257–272.
- 49 Z. Varga, B. Öztürk, M. Meppen, K. Mayer, M. Wallenius and C. Apostolidis, *Radiochim. Acta*, 2011, **99**, 807–813.
- 50 D. H. M. Lin, D. Manara, Z. Varga, A. Berlizov, T. Fanghänel and K. Mayer, *Radiochim. Acta*, 2013, **101**, 779–784.
- 51 L. A. Silva, F. S. Lameiras, A. M. Matildes dos Santos, W. B. Ferraz and J. B. S. Barbosa, *Int. Eng. J.*, 2017, **70**, 59–62.
- 52 M. J. Trujillo, D. M. Jenkins, J. A. Bradshaw, J. P. Camden, M. Senō, T. Itagaki, R. J. Harrison, J. P. Camden and D. M. Jenkins, *Anal. Methods*, 2017, **9**, 1575–1579.
- 53 H. He, P. Wang, D. D. Allred, J. Majewski, M. P. Wilkerson and K. D. Rector, *Anal. Chem.*, 2012, **84**, 10380–10387.
- 54 R. Middendorp, M. Dürr, A. Knott, F. Pointurier, D. Ferreira Sanchez, V. Samson and D. Grolimund, *Anal. Chem.*, 2017, **89**, 4721–4728.
- 55 C. Prater, K. Kjoller and R. Shetty, *Mater. Today*, 2010, **13**, 56–60.
- 56 M. Unger, C. Marcott, M. Unger and C. Marcott, in *Encyclopedia of Analytical Chemistry*, John Wiley & Sons, Ltd, Chichester, UK, 2017, pp. 1–26.
- 57 M. Fleischmann, P. J. Hendra and A. J. McQuillan, *Chem. Phys. Lett.*, 1974, **26**, 163–166.
- 58 R. Jenkins, in *X-Ray Fluorescence Spectrometry, Second Edition*, 2012.
- 59 D. L. Donohue, *Anal. Chem.*, 2002, **74**, 28 A-35 A.
- 60 W. S. Charlton, D. Strohmeyer, A. Stafford, O. Ridge, A. S. Hoover, C. Rudy and L. Alamos, *The use of self-induced XRF to quantify the Pu content in PWR spent nuclear fuel*, 2009.
- 61 J. L. Steeb, C. J. Mertz, M. R. Finck, G. Engelstad, K. P. Carney and D. B. Chamberlain, *J. Radioanal. Nucl. Chem.*, 2016, **307**, 751–760.
- 62 M. A. Denecke, P. Michel, T. Schäfer, F. Huber, K. Rickers, J. Rothe, K. Dardenne, B. Brendebach, T. Vitova and M. Elie, *J. Phys. Conf. Ser.*, 2009, **190**, 012187.
- 63 O. N. Batuk, S. D. Conradson, O. N. Aleksandrova, H. Boukhalfa, B. E. Burakov, D. L. Clark, K. R. Czerwinski, A. R. Felmy, J. S. Lezama-Pacheco, S. N. Kalmykov, D. A. Moore, B. F. Myasoedov, D. T. Reed, D. D. Reilly, R. C. Roback, I. E. Vlasova, S. M. Webb and M. P. Wilkerson, *Environ. Sci. Technol.*, 2015, **49**, 6474–6484.

- 64 S. G. Minasian, J. M. Keith, E. R. Batista, K. S. Boland, D. L. Clark, S. A. Kozimor, R. L. Martin, D. K. Shuh and T. Tylliszczak, *Chem. Sci.*, 2014, **5**, 351–359.
- 65 X.-D. Wen, M. W. Löble, E. R. Batista, E. Bauer, K. S. Boland, A. K. Burrell, S. D. Conradson, S. R. Daly, S. A. Kozimor, S. G. Minasian, R. L. Martin, T. M. McCleskey, B. L. Scott, D. K. Shuh and T. Tylliszczak, *J. Electron Spectros. Relat. Phenomena*, 2014, **194**, 81–87.
- 66 N. Kaltsoyannis, *Inorg. Chem.*, 2013, **52**, 3407–3413.
- 67 S. M. Butorin, K. O. Kvashnina, J. R. Vegelius, D. Meyer and D. K. Shuh, *Proc. Natl. Acad. Sci. U. S. A.*, 2016, **113**, 8093–7.
- 68 A. Formanuk, A.-M. Ariciu, F. Ortu, R. Beekmeyer, A. Kerridge, F. Tuna, E. J. L. McInnes and D. P. Mills, *Nat. Chem.*, 2017, **9**, 578–583.
- 69 E. Zolotoyabko, *Basic concepts of X-ray diffraction*, Wiley-VCH, 1st edn., 2014.
- 70 W. Friedrich, P. Knipping and M. Laue, *Ann. Phys.*, 1913, **346**, 971–988.
- 71 Y. A. Teterin, A. J. Popel, K. I. Maslakov, A. Y. Teterin, K. E. Ivanov, S. N. Kalmykov, R. Springell, T. B. Scott and I. Farnan, *Inorg. Chem.*, 2016, **55**, 8059–8070.
- 72 G. S. Girolami, *X-ray crystallography*, University Science Books, 2015.
- 73 M. Wilkerson, *Molecular Forensic Science of Nuclear Materials*, Baltimore, MD, 2010.
- 74 C. Degueldre, in *The Chemistry of the Actinide and Transactinide Elements*, Springer Netherlands, Dordrecht, pp. 3013–3085.
- 75 K. L. Nash, C. Madic, J. N. Mathur and J. Lacquement, in *The Chemistry of the Actinide and Transactinide Elements*, Springer Netherlands, Dordrecht, pp. 2622–2798.
- 76 United States, US2924506, 1947.
- 77 J. Veliscek-Carolan, *J. Hazard. Mater.*, 2016, **318**, 266–281.
- 78 A. Morgenstern, C. Apostolidis, R. Carlos-Marquez, K. Mayer and R. Molinet, *Radiochim. Acta*, 2002, **90**, 81–85.
- 79 J. W. Grate, M. J. O’Hara, A. F. Farawila, M. Douglas, M. M. Haney, S. L. Petersen, T. C. Maiti and C. L. Aardahl, *Anal. Chem.*, 2011, **83**, 9086–9091.
- 80 M. A. Higginson, P. Thompson, O. J. Marsden, F. R. Livens, L. M. Harwood, F. W. Lewis, M. J. Hudson and S. L. Heath, *Radiochim. Acta*, 2015, **103**, 687–694.
- 81 X. Dai and S. Kramer-Tremblay, *Anal. Chem.*, 2014, **86**, 5441–5447.
- 82 J. M. Richards and R. Sudowe, *Anal. Chem.*, 2016, **88**, 4605–4608.
- 83 J. A. Shusterman, H. E. Mason, J. Bowers, A. Bruchet, E. C. Uribe, A. B. Kersting and H. Nitsche, *ACS Appl. Mater. Interfaces*, 2015, **7**, 20591–20599.
- 84 S. Demir, N. K. Brune, J. F. Van Humbeck, J. A. Mason, T. V. Plakhova, S. Wang, G. Tian, S. G. Minasian, T. Tylliszczak, T. Yaita, T. Kobayashi, S. N. Kalmykov, H. Shiwaku, D. K. Shuh and J. R. Long, *ACS Cent. Sci.*, 2016, **2**, 253–265.
- 85 S. K. Aggarwal, M. Sharma, K. Mezger, A. Kaltenbach, O. Rienitz, V. S. Sullivan, K. P. Carney, M. R. Finck, J. J. Giglio, D. B. Chamberlain, H. Ottmar, G. Rasmussen, A. Schubert, G. Tamborini, H. Thiele, W. Wagner, C. Walker and E. Zuleger, *Anal. Methods*, 2016, **8**, 942–957.
- 86 I. W. Croudace, B. C. Russell, P. W. Warwick, M. Aubert, G. Stadelmann, E. Dupont, I.

- AlMahamid, G. Tiang, L. Rao, W. Lukens, P. Cassette, S. Panebianco, A. Letourneau, F. Chartier and W. Zu, *J. Anal. At. Spectrom.*, 2017, **32**, 494–526.
- 87 Z. Varga, A. Nicholl, M. Wallenius and K. Mayer, *J. Radioanal. Nucl. Chem.*, 2016, **307**, 1919–1926.
- 88 W. D. Loveland, D. J. Morrissey and G. T. Seaborg, in *Modern Nuclear Chemistry*, John Wiley & Sons, Inc., Hoboken, NJ, USA, 2005, pp. 57–89.
- 89 R. Fitzgerald, K. G. W. Inn and C. Horgan, *J. Radioanal. Nucl. Chem.*, 2016, **307**, 2521–2528.
- 90 M. J. Kristo, A. M. Gaffney, N. Marks, K. Knight, W. S. Cassata and I. D. Hutcheon, *Annu. Rev. Earth Planet. Sci.*, 2016, **44**, 555–579.
- 91 L. Pajo, G. Tamborini, G. Rasmussen, K. Mayer and L. Koch, *Spectrochim. Acta Part B At. Spectrosc.*, 2001, **56**, 541–549.
- 92 M. K. Dustin, E. C. Koeman, A. Simonetti, Z. Torrano and P. C. Burns, *Appl. Spectrosc.*, 2016, **70**, 1446–1455.
- 93 R. C. Marin, J. E. S. Sarkis and M. R. L. Nascimento, *J. Radioanal. Nucl. Chem.*, 2013, **295**, 99–104.
- 94 D. G. Reading, I. W. Croudace and P. E. Warwick, *Anal. Chem.*, 2017, **89**, 6006–6014.
- 95 M. Husain and Z. H. Khan, *Advances in Nanomaterials*, Springer, 2016.
- 96 P. M. L. Hedberg, P. Peres, F. Fernandes, L. Renaud, C. D. Coath, C. J. Hawkesworth, S. Sakurai, S. Usuda and S. Usuda, *J. Anal. At. Spectrom.*, 2015, **30**, 2516–2524.
- 97 H. E. Hocking, Air Force Institute of Technology, 2011.
- 98 J. Park, T. H. Kim, C.-G. Lee, J. Lee, S. H. Lim, S. H. Han and K. Song, *J. Radioanal. Nucl. Chem.*, 2017, **311**, 1535–1544.
- 99 G. Tamborini, M. Betti, V. Forcina, T. Hiernaut, B. Giovannone and L. Koch, *Spectrochim. Acta Part B At. Spectrosc.*, 1998, **53**, 1289–1302.
- 100 R. Pöllänen, M. E. Ketterer, S. Lehto, M. Hokkanen, T. K. Ikäheimonen, T. Siiskonen, M. Moring, M. P. Rubio Montero and A. Martín Sánchez, *J. Environ. Radioact.*, 2006, **90**, 15–28.
- 101 P. Rubio Montero and A. Martín Sánchez, *J. Environ. Radioact.*, 2001, **55**, 157–165.
- 102 C. Gascó, M. P. Antón, A. Espinosa, A. Aragón, A. Álvarez, N. Navarro and E. García-Torano, *J. Radioanal. Nucl. Chem.*, **222**, 81–86.
- 103 K. L. Moore, E. Lombi, F.-J. Zhao and C. R. M. Grovenor, *Anal. Bioanal. Chem.*, 2012, **402**, 3263–3273.
- 104 P. Hoppe, S. Cohen and A. Meibom, *Geostand. Geoanalytical Res.*, 2013, **37**, 111–154.
- 105 Z. Wang, J. Liu, Y. Zhou, J. J. Neeway, D. K. Schreiber, J. V. Crum, J. V. Ryan, X.-L. Wang, F. Wang and Z. Zhu, *Surf. Interface Anal.*, 2016, **48**, 1392–1401.
- 106 S. Lozano-Perez, M. Schröder, T. Yamada, T. Terachi, C. A. English and C. R. M. Grovenor, *Appl. Surf. Sci.*, 2008, **255**, 1541–1543.
- 107 P. W. Hawkes, *The Beginnings of electron microscopy*, Elsevier Science, 2013.
- 108 J.-M. Volland, *Mar. Ecol.*, 2016, **37**, 235–235.
- 109 A. Bogner, P.-H. Jouneau, G. Thollet, D. Basset and C. Gauthier, *Micron*, 2007, **38**, 390–

- 401.
- 110 E. A. Gulbransen, R. T. Phelps and A. Langer, *Ind. Eng. Chem. Anal. Ed.*, 1945, **17**, 646–652.
- 111 P. Echlin, *J. Microsc.*, 1978, **112**, 47–61.
- 112 T. A. Klar and S. W. Hell, *Opt. Lett.*, 1999, **24**, 954.
- 113 S. W. Hell and J. Wichmann, *Opt. Lett.*, 1994, **19**, 780.
- 114 X. Wang, Z. Long, R. Bin, R. Yang, Q. Pan, F. Li, L. Luo, Y. Hu and K. Liu, *Inorg. Chem.*, 2016, **55**, 10835–10838.
- 115 T. Murakami, T. Sato, T. Ohnuki and H. Isobe, *Chem. Geol.*, 2005, **221**, 117–126.
- 116 M. Lee and M. Yang, *J. Hazard. Mater.*, 2010, **173**, 589–596.
- 117 M. Islam and R. Patel, *J. Hazard. Mater.*, 2008, **156**, 509–520.
- 118 Y. Ranebo, N. Niagolova, N. Erdmann, M. Eriksson, G. Tamborini and M. Betti, *Anal. Chem.*, 2010, **82**, 4055–4062.
- 119 T. Yomogida, F. Esaka and M. Magara, *Anal. Methods*, 2017, **9**, 6261–6266.
- 120 J. S. Anderson, *Proc. Indian Acad. Sci. - Sect. A, Chem. Sci.*, **87**, 295–329.
- 121 K. Nogita and K. Une, *J. Nucl. Mater.*, 1997, **250**, 244–249.
- 122 E. C. Buck, E. J. Mausolf, B. K. McNamara, C. Z. Soderquist and J. M. Schwantes, *J. Nucl. Mater.*, 2015, **461**, 236–243.
- 123 P. A. Midgley and M. Weyland, in *Scanning Transmission Electron Microscopy*, Springer New York, New York, NY, 2011, pp. 353–392.
- 124 D. Hudry, J.-C. Griveau, C. Apostolidis, O. Walter, E. Colineau, G. Rasmussen, D. Wang, V. S. K. Chakravadhala, E. Courtois, C. Kübel and D. Meyer, *Nano Res.*, 2014, **7**, 119–131.
- 125 J. I. Bramman, R. M. Sharpe, D. Thom and G. Yates, *J. Nucl. Mater.*, 1968, **25**, 201–215.
- 126 S. Utsunomiya and R. C. Ewing, *Environ. Sci. Technol.*, 2003, **37**, 786–791.
- 127 L. Eyring, *Ultramicroscopy*, 1982, **8**, 39–58.
- 128 Angus Kirkland and Neil Young, *Microsc. Anal.*, 2012, 19–24.
- 129 K. G. W. Inn, C. M. Johnson, W. Oldham, S. Jerome, L. Tandon, T. Schaaff, R. Jones, D. Mackney, P. MacKill, B. Palmer, D. Smith, S. LaMont and J. Griggs, *J. Radioanal. Nucl. Chem.*, 2013, **296**, 5–22.
- 130 M. Eriksson, J. Osán, J. Jernström, D. Wegrzynek, R. Simon, E. Chinea-Cano, A. Markowicz, S. Bamford, G. Tamborini, S. Török, G. Falkenberg, A. Alsecz, H. Dahlgaard, P. Wobrauschek, C. Streli, N. Zoeger and M. Betti, *Spectrochim. Acta Part B At. Spectrosc.*, 2005, **60**, 455–469.
- 131 J. I. Pacold, A. B. Altman, K. B. Knight and K. S. Holliday, *Analyst*, 2018, **143**, 1349–1357.
- 132 P. Michel, T. Schäfer, M. A. Denecke, B. Brendebach, K. Dardenne, F. Huber and J. Rothe, *J. Phys. Conf. Ser.*, 2009, **186**, 012090.
- 133 R. D. Arrua, A. P. Hitchcock, W. B. Hon, M. West and E. F. Hilder, *Anal. Chem.*, 2014, **86**, 2876–2881.
- 134 H. J. Nilsson, T. Tyliczszak, R. E. Wilson, L. Werme and D. K. Shuh, *Anal. Bioanal. Chem.*,



- 2005, **383**, 41–47.
- 135 C. Walther and M. A. Denecke, *Chem. Rev.*, 2013, **113**, 995–1015.
- 136 J. Uddin, *Macro to nano spectroscopy*, InTech, 2012.
- 137 S. Nie and S. R. Emory, *Science (80-. )*, 1997, **275**, 1102–1106.
- 138 D. Bhandari, S. M. Wells, S. T. Retterer and M. J. Sepaniak, *Anal. Chem.*, 2009, **81**, 8061–8067.
- 139 C. Ruan, W. Luo, W. Wang and B. Gu, *Anal. Chim. Acta*, 2007, **605**, 80–86.
- 140 G. Lu, T. Z. Forbes, A. J. Haes, P. Nordlander, R. Marino, T. Shelly, E. Melaro, A. M. Donohoe, R. L. Jones, J. Plain, P. M. Adam, R. Boukherroub and S. Szunerits, *Analyst*, 2016, **141**, 5137–5143.
- 141 C. G. Worley, S. S. Wiltshire, T. C. Miller, G. J. Havrilla and V. Majidi, *J. Forensic Sci.*, 2006, **51**, 57–63.
- 142 J. H. Rim, K. J. Kuhn, L. Tandon, N. Xu, D. R. Porterfield, C. G. Worley, M. R. Thomas, K. J. Spencer, F. E. Stanley, E. J. Lujan, K. Garduno and H. R. Trellue, *Forensic Sci. Int.*, 2017, **273**, e1–e9.
- 143 K. G. McIntosh, N. L. Cordes, B. M. Patterson and G. J. Havrilla, *J. Anal. At. Spectrom.*, 2015, **30**, 1511–1517.
- 144 C. E. Bonamici, W. S. Kinman, J. H. Fournelle, M. M. Zimmer, A. D. Pollington and K. D. Rector, *Contrib. to Mineral. Petrol.*
- 145 D. S. Peterson and E. R. Gonzales, *J. Radioanal. Nucl. Chem.*, 2009, **282**, 543–547.
- 146 W. J. Oldham, D. E. Dry and A. H. Mueller, *J. Radioanal. Nucl. Chem.*, 2009, **282**, 585–589.
- 147 S. K. Hanson, A. H. Mueller and W. J. Oldham, *Anal. Chem.*, 2014, **86**, 1153–1159.
- 148 B. E. Johnson, P. H. Santschi, R. Shane Addleman, M. Douglas, J. D. Davidson, G. E. Fryxell and J. M. Schwantes, *Appl. Radiat. Isot.*, 2011, **69**, 205–216.
- 149 Z. A. Alothman, *Materials (Basel)*, 2012, **5**, 2874–2902.
- 150 P. Pachfule, M. K. Panda, S. Kandambeth, S. M. Shivaprasad, D. D. Díaz and R. Banerjee, *J. Mater. Chem. A*, 2014, **2**, 7944–7952.
- 151 A. Tanimu, S. Jaenicke and K. Alhooshani, *Chem. Eng. J.*, 2017, **327**, 792–821.
- 152 P. Makowski, X. Deschanel, A. Grandjean, D. Meyer, G. Toquer and F. Goettmann, *New J. Chem.*, 2012, **36**, 531–541.
- 153 J. Shusterman, H. Mason, A. Bruchet, M. Zavarin, A. B. Kersting and H. Nitsche, *Dalt. Trans.*, 2014, **43**, 16649–16658.
- 154 T. Parsons-Moss, J. Wang, S. Jones, E. May, D. Olive, Z. Dai, M. Zavarin, A. B. Kersting, D. Zhao and H. Nitsche, *J. Mater. Chem. A*, 2014, **2**, 11209–11221.
- 155 B. E. Johnson, P. H. Santschi, R. S. Addleman, M. Douglas, J. Davidson, G. E. Fryxell and J. M. Schwantes, *Anal. Chim. Acta*, 2011, **708**, 52–60.
- 156 B. E. Johnson, P. H. Santschi, C.-Y. Chuang, S. Otosaka, R. S. Addleman, M. Douglas, R. D. Rutledge, W. Chouyyok, J. D. Davidson, G. E. Fryxell and J. M. Schwantes, *Environ. Sci. Technol.*, 2012, **46**, 11251–11258.
- 157 Y. Liu, A. Czarnecki, J. E. S. Szymanowski, G. E. Sigmon and P. C. Burns, *J. Radioanal.*

- Nucl. Chem.*, 2016, **310**, 453–462.
- 158 K. G. W. Inn, H. Kurosaki, C. Frechou, C. Gilligan, R. Jones, S. LaMont, J. Leggitt, C. Li, K. McCroan and R. Swatski, *Appl. Radiat. Isot.*, 2008, **66**, 835–840.
- 159 K. J. Mathew, F. E. Stanley, M. R. Thomas, K. J. Spencer, L. P. Colletti, L. Tandon, S. Kappel, A. Koepf, J. Poths, A. Köpf, J. Poths and K. Mathew, *Anal. Methods*, 2016, **8**, 7289–7305.
- 160 K. Essex, Richard; Mann, Jacqueline; Tyra, Mark; Lavelle, *Nuclear Forensics Reference Material (RM) Program*, 2017.
- 161 R. Jakopič, M. Sturm, M. Kraiem, S. Richter and Y. Aregbe, *J. Environ. Radioact.*, 2013, **125**, 17–22.
- 162 D. Roudil, C. Rigaux, C. Rivier, J. C. Hubinois and L. Aufore, *Procedia Chem.*, 2012, **7**, 709–715.
- 163 Q. Wang, G.-D. Li, S. Xu, J.-X. Li and J.-S. Chen, *J. Mater. Chem.*, 2008, **18**, 1146.
- 164 P. Bots, K. Morris, R. Hibberd, G. T. W. Law, J. F. W. Mosselmans, A. P. Brown, J. Douth, A. J. Smith and S. Shaw, *Langmuir*, 2014, **30**, 14396–14405.
- 165 L. Wang, R. Zhao, X. Wang, T. S. Ulmer and E. Al., *CrystEngComm*, 2014, **16**, 10469–10475.
- 166 E. Dalodière, M. Viro, V. Morosini, T. Chave, T. Dumas, C. Hennig, T. Wiss, O. Dieste Blanco, D. K. Shuh, T. Tyliczak, L. Venault, P. Moisy and S. I. Nikitenko, *Sci. Rep.*, 2017, **7**, 43514.
- 167 D. Hudry, C. Apostolidis, O. Walter, T. Gouder, E. Courtois, C. Kübel and D. Meyer, *Chem. - A Eur. J.*, 2012, **18**, 8283–8287.
- 168 H. Wu, Y. Yang and Y. C. Cao, *J. Am. Chem. Soc.*, 2006, **128**, 16522–16523.
- 169 M. D. Straub, J. Leduc, M. Frank, A. Raauf, T. D. Lohrey, S. G. Minasian, S. Mathur and J. Arnold, *Angew. Chemie - Int. Ed.*, 2019, **58**, 5749–5753.
- 170 T. Shinonaga, D. Donohue, H. Aigner, S. Bürger, D. Klose, T. Kärkelä, R. Zilliacus, A. Auvinen, O. Marie and F. Pointurier, *Anal. Chem.*, 2012, **84**, 2638–2646.
- 171 A. D. Pollington, W. S. Kinman, S. K. Hanson and R. E. Steiner, *J. Radioanal. Nucl. Chem.*, 2016, **307**, 2109–2115.
- 172 A. Y. Romanchuk, S. N. Kalmykov, A. B. Kersting and M. Zavarin, *Russ. Chem. Rev.*, 2016, **85**, 995–1010.
- 173 D. L. Clark, S. S. Hecker, G. D. Jarvinen and M. P. Neu, in *The Chemistry of the Actinide and Transactinide Elements*, Springer Netherlands, Dordrecht, pp. 813–1264.
- 174 D. L. Donohue, *Key tools for nuclear inspections*, 2002, vol. 44.
- 175 S. Glasstone and P. J. Dolan, *The Effects of Nuclear Weapons*, Third., 1977.
- 176 E. C. Freiling, *Science*, 1961, **133**, 1991–1998.
- 177 S. K. Hanson, A. D. Pollington, C. R. Waidmann, W. S. Kinman, A. M. Wende, J. L. Miller, J. A. Berger, W. J. Oldham and H. D. Selby, *Proc. Natl. Acad. Sci. U. S. A.*, 2016, **113**, 8104–8.
- 178 Committee on Nuclear Forensics - National Research Council, *Nuclear Forensics: A Capability at Risk (Abbreviated Version)*, 2010.

- 179 C. Ross, *Am. Mineral.*, 1948, **33**, 360–362.
- 180 E. C. Freiling and M. A. Kay, *Nature*, 1966, **209**, 694–696.
- 181 A. J. Fahey, C. J. Zeissler, D. E. Newbury, J. Davis and R. M. Lindstrom, *Proc. Natl. Acad. Sci.*, 2010, **107**, 20207–20212.
- 182 R. E. Hermes and W. B. Strickfaden, *Nucl. Weapons J.*, 2005, **2**, 2–7.
- 183 P. P. Parekh, T. M. Semkow, M. A. Torres, D. K. Haines, J. M. Cooper, P. M. Rosenberg and M. E. Kitto, *J. Environ. Radioact.*, 2006, **85**, 103–120.
- 184 F. Belloni, J. Himbert, O. Marzocchi and V. Romanello, *J. Environ. Radioact.*, 2011, **102**, 852–862.
- 185 L. A. Lewis, K. B. Knight, J. E. Matzel, S. G. Prussin, M. M. Zimmer, W. S. Kinman, F. J. Ryerson and I. D. Hutcheon, *J. Environ. Radioact.*, 2015, **148**, 183–195.
- 186 M. M. A. Wannier, M. De Urreiztieta, H. Wenk, C. V Stan, N. Tamura and B. Yue, *Anthropocene*, 2019, **25**, 100196.
- 187 J. P. Auxier, J. D. Auxier and H. L. Hall, *J. Environ. Radioact.*, 2017, **171**, 246–252.
- 188 K. P. Carney, M. R. Finck, C. A. Mcgrath, L. R. Martin and R. R. Lewis, *J. Radioanal. Nucl. Chem.*, 2014, **299**, 363–372.
- 189 J. J. Molgaard, J. D. Auxier, A. V. Giminaro, C. J. Oldham, M. T. Cook, S. A. Young and H. L. Hall, *J. Radioanal. Nucl. Chem.*, 2015, **304**, 1293–1301.
- 190 J. J. Molgaard, J. D. A. Li, A. V Giminaro, C. J. Oldham, J. Gill and H. L. Hall, *J. Vis. Exp.*, 2016, 1–7.
- 191 A. V. Giminaro, S. A. Stratz, J. A. Gill, J. P. Auxier, C. J. Oldham, M. T. Cook, J. D. Auxier, J. J. Molgaard and H. L. Hall, *J. Radioanal. Nucl. Chem.*, 2015, **306**, 175–181.
- 192 M. Liezers, A. J. Fahey, A. J. Carman and G. C. Eiden, *J. Radioanal. Nucl. Chem.*, 2015, **304**, 705–715.
- 193 M. Liezers, M. C. Endres, A. J. Carman and G. C. Eiden, *J. Radioanal. Nucl. Chem.*, 2018, **318**, 71–77.
- 194 R. J. M. Konings, L. R. Morss and J. Fuger, in *The Chemistry of the Actinide and Transactinide Elements*, Springer Netherlands, Dordrecht, pp. 2113–2224.
- 195 S. D. Harvey, M. Liezers, K. C. Antolick, B. J. Garcia, L. E. Sweet, A. J. Carman and G. C. Eiden, *J. Radioanal. Nucl. Chem.*, 2013, **298**, 1885–1898.
- 196 K. J. Moody and P. M. Grant, *J. Radioanal. Nucl. Chem.*, 1999, **241**, 157–167.
- 197 I. L. F. Ray, T. Wiss and H. Thiele, *Recent developments and case studies in nuclear forensic science*, 2002.
- 198 G. Capannesi, C. Vicini, A. Rosada and P. Avino, *Forensic Sci. Int.*, 2010, **199**, 15–21.

## Chapter 3

# Chemical Vapor Deposition of Phase-Pure Uranium Dioxide Thin Films from Uranium(IV) Amidate Precursors

## Introduction

The efficiency and safety profiles of nuclear reactors are heavily impacted by the surface chemistry of the fuel materials used in the reactor core.<sup>1</sup> Defect formation and void swelling in UO<sub>2</sub> fuel pellets dramatically reduce the lifetime and energy output of these materials, but direct study of the surface oxidation processes that cause these defects can be challenging due to the chemical complexity and extreme radioactivity of spent fuels.<sup>1-3</sup> Due to their large active surface areas, phase-pure UO<sub>2</sub> thin films can serve as excellent model systems for the chemical and physical changes that occur at the grain boundaries of bulk UO<sub>2</sub> fuel pellets.

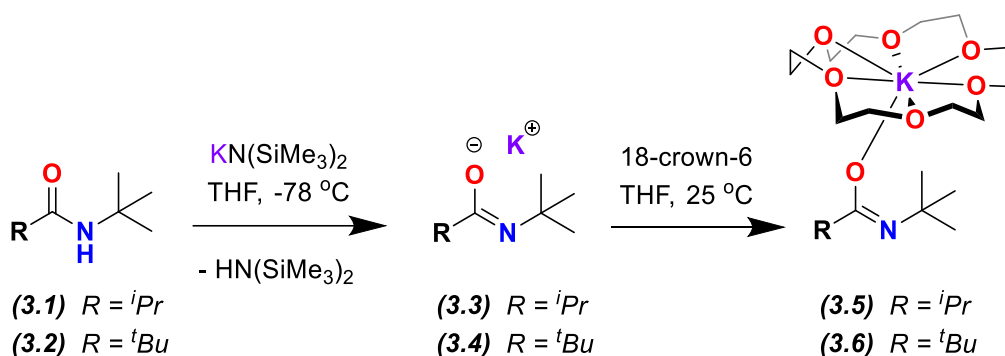
Uranium oxide thin films have been fabricated using both solution<sup>4-6</sup> and sputtering<sup>7-10</sup> methods; however, achieving stoichiometric control in the resulting films has been challenging due to the wide array of accessible uranium oxide phases and the facile interconversion of these phases at grain boundaries.<sup>5,11</sup> Consequently, many published studies on uranium oxide have been performed using materials with a varying degree of amorphous or polycrystalline character.<sup>12</sup> McClesky and coworkers have used an innovative polymer-assisted deposition technique from UO<sub>2</sub>(NO<sub>3</sub>)<sub>2</sub> precursors to produce UO<sub>2</sub> and U<sub>3</sub>O<sub>8</sub> thin films; epitaxial matching of the desired uranium oxide phase to the substrate, followed by annealing at 1000 °C, resulted in phase-pure films.<sup>12,13</sup> Chemical vapor deposition (CVD) is an additional promising route, with the added benefit that direct synthesis of uranium oxide films from a single-source molecular precursor could facilitate enhanced tunability of the growth process through rational control of the decomposition mechanism and rate.<sup>14</sup> However, the preparation of phase-pure thin films in a CVD process can be challenging, as the precursors must be both sufficiently volatile and decompose cleanly by a single mechanism to minimize the formation of side products.<sup>15</sup>

The last few decades have yielded an enormous amount of research into volatile transition metal and lanthanide complexes, which are used as molecular precursors for CVD of metal oxide, nitride, sulfide, and carbide thin films.<sup>14,16-22</sup> In contrast to the myriad quantity of CVD precursors that have been described for these metals, only a small handful of uranium oxide CVD precursors have ever been reported. The first gas-phase synthesis of uranium oxide thin films was accomplished by heating a uranyl  $\beta$ -diketonate precursor above 400 °C in the presence of O<sub>2</sub> or H<sub>2</sub>O; however, the oxidizing environment of these reactive gases prevented the formation of phase-pure UO<sub>2</sub> films.<sup>23</sup> In a more recent single-source process, films containing a mixture of uranium oxides were synthesized via thermal CVD from fluorinated uranium heteroarylalkenolate precursors.<sup>24</sup>

We sought to develop a class of volatile, non-fluorinated precursors with an easily-accessible thermal decomposition pathway to UO<sub>2</sub>, thereby minimizing the heat required to form phase-pure UO<sub>2</sub> films. Based on previous research in our group<sup>25</sup> and promising results from related transition metal systems,<sup>26-28</sup> we turned to uranium amidate complexes to meet these requirements. Amidate ligand substituents can be readily varied to cover a wide range of steric and electronic properties, enabling control over the geometry, thermal stability, volatility, and decomposition mechanisms of the resulting metal complexes. Using new U<sup>IV</sup> amidate precursors with a well-defined decomposition mechanism, we synthesized crystalline, phase-pure UO<sub>2</sub> films via CVD.

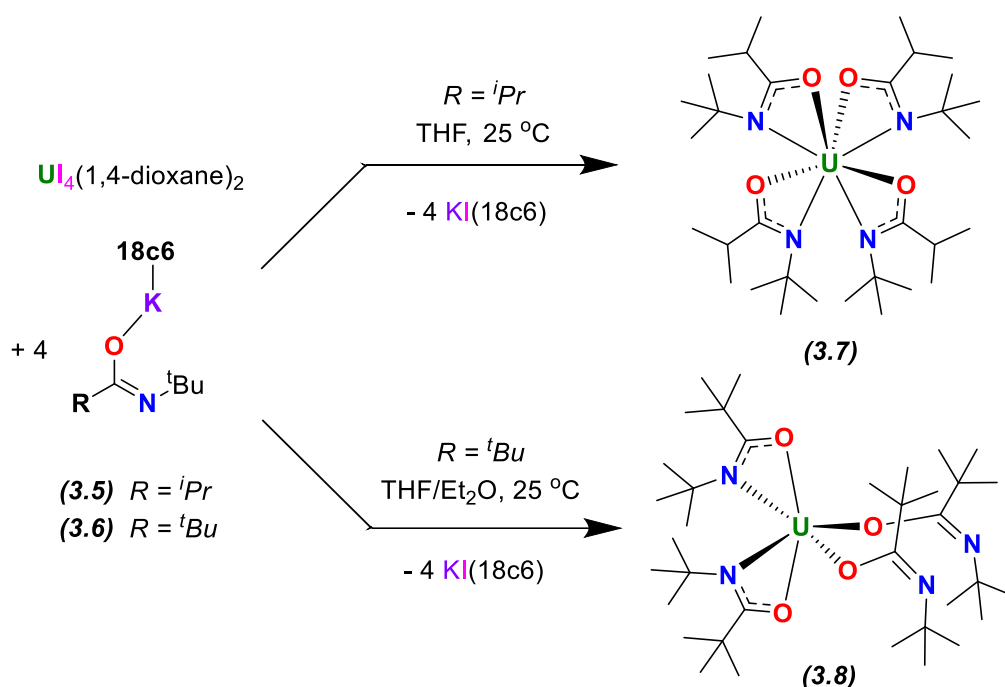
## Results and Discussion

The amide proligands *N-tert*-butylisobutyramide (H(ITA)) (**3.1**) and *N-tert*-butylpivalamide (H(TTA)) (**3.2**) were synthesized according to literature methods<sup>29</sup> and purified by sublimation using a cryogenic sublimator at 10 mTorr. Deprotonation of **3.1** and **3.2** with KN(SiMe<sub>3</sub>)<sub>2</sub> in THF generated the corresponding potassium amidates K(ITA) (**3.3**) and K(TTA) (**3.4**) in high yield. As we have observed previously in related systems,<sup>25</sup> using these potassium amidates directly for the metalation of uranium led to the formation of undesirable –ate complexes, resulting in poor yields of the anticipated products. This was overcome by adding 18-crown-6 to **3.3** and **3.4** to give the crowned potassium amidates K(ITA)(18c6) (**3.5**) and K(ITA)(18c6) (**3.6**) in near-quantitative yield (Scheme 3.1); these ligand salts performed much more favorably for metalation of uranium.



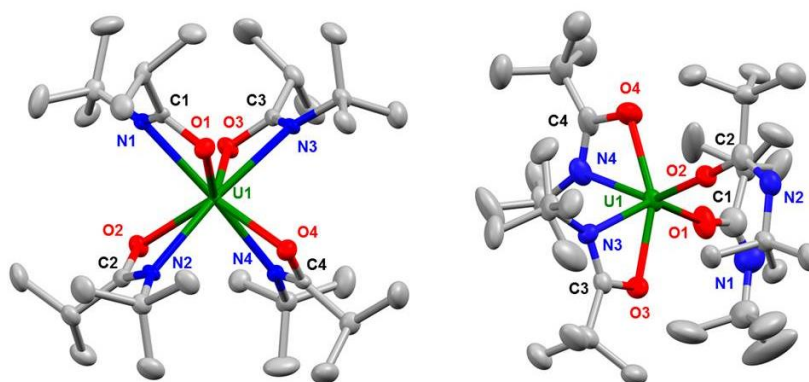
**Scheme 3.1:** Synthesis of the crowned potassium amidates K(ITA)(18c6) (**3.5**) and K(TTA)(18c6) (**3.6**).

The homoleptic amidate complexes U(ITA)<sub>4</sub> (**3.7**) and U(TTA)<sub>4</sub> (**3.8**) were synthesized by treating UI<sub>4</sub>(1,4-dioxane)<sub>2</sub> with four equivalents of **3.5** or **3.6**, respectively (Scheme 3.2). We also synthesized **3.7** and **3.8** via a protonolysis route with [(Me<sub>3</sub>Si)<sub>2</sub>N]<sub>2</sub>U[κ<sup>2</sup>-(*C,N*)-CH<sub>2</sub>Si(Me)<sub>2</sub>N(SiMe<sub>3</sub>)] and **3.1** or **3.2**, but yields were lower using this method. Green crystals of **3.7** and teal crystals of **3.8** suitable for X-ray diffraction were grown from Et<sub>2</sub>O and pentane, respectively.



**Scheme 3.2:** Synthesis of  $\text{U}(\text{ITA})_4$  (**3.7**) and  $\text{U}(\text{TTA})_4$  (**3.8**).

Although the proligands **3.1** and **3.2** are comparable sterically, we observed different molecular geometries for **3.7** and **3.8**. Crystallographic analysis of **3.7** showed this molecule to be eight-coordinate and  $D_{2d}$  symmetric, with all four amidate ligands chelated ( $\kappa_2\text{-N,O}$ ) to the uranium center. By comparison, **3.8** is six-coordinate and  $C_1$  symmetric, with two ( $\kappa_2\text{-N,O}$ ) amidate ligands and two ( $\kappa_1\text{-O}$ ) amidate ligands bound to the uranium center. This difference in geometry can possibly be attributed to the higher electron donating effect of the *tert*-butyl vs. *iso*-propyl substituents on the amidate backbone, disfavoring electron donation from the lone pairs on all four nitrogen atoms to the uranium center in **3.8**; however, it is also possible that the larger steric bulk of the  $\text{C-}^t\text{Bu}$  substituent contributes to the lower coordination number of **3.8**.



**Figure 3.1:** 50% probability thermal ellipsoid view of  $\text{U}(\text{ITA})_4$  (**3.7**) (left) and  $\text{U}(\text{TTA})_4$  (**3.8**) (right). Hydrogen atoms are omitted for clarity.

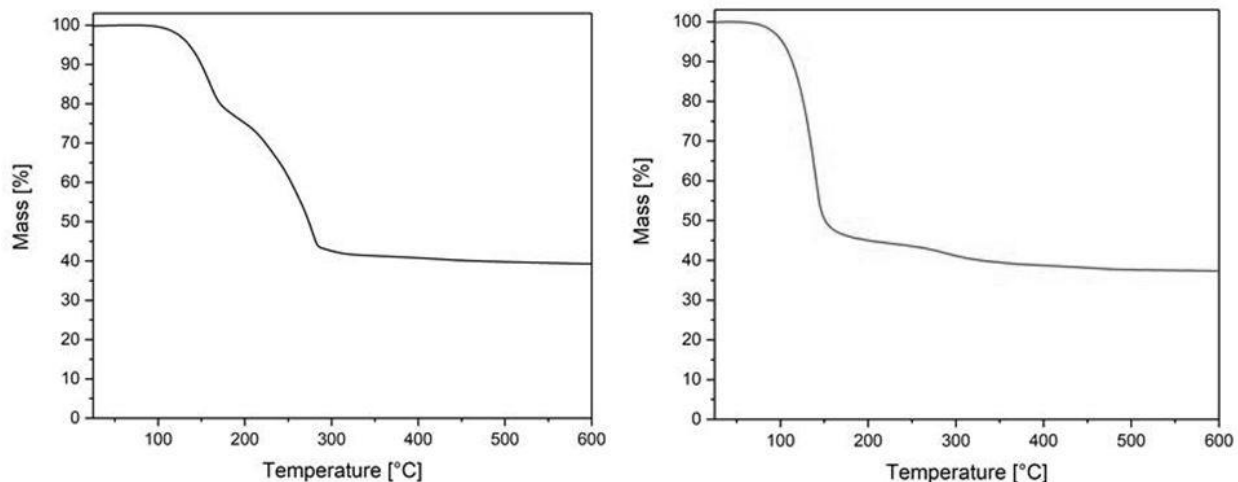
**Table 3.1:** Selected bond lengths in **3.7** and **3.8**.

Atoms	Bond lengths (Å)	
	<b>3.7</b>	<b>3.8</b>
U1 – O1	2.333(2)	2.123(5)
U1 – O2	2.350(2)	2.135(4)
U1 – O3	2.366(2)	2.284(4)
U1 – O4	2.346(2)	2.296(4)
U1 – N1	2.499(3)	-
U1 – N2	2.507(2)	-
U1 – N3	2.502(2)	2.495(5)
U1 – N4	2.493(3)	2.457(5)
C1 – O1	1.307(4)	1.375(9)
C2 – O2	1.311(3)	1.361(7)
C3 – O3	1.296(4)	1.323(7)
C4 – O4	1.303(4)	1.323(7)
C1 – N1	1.305(4)	1.141(11)
C2 – N2	1.292(4)	1.240(9)
C3 – N3	1.296(4)	1.297(8)
C4 – N4	1.310(4)	1.309(9)

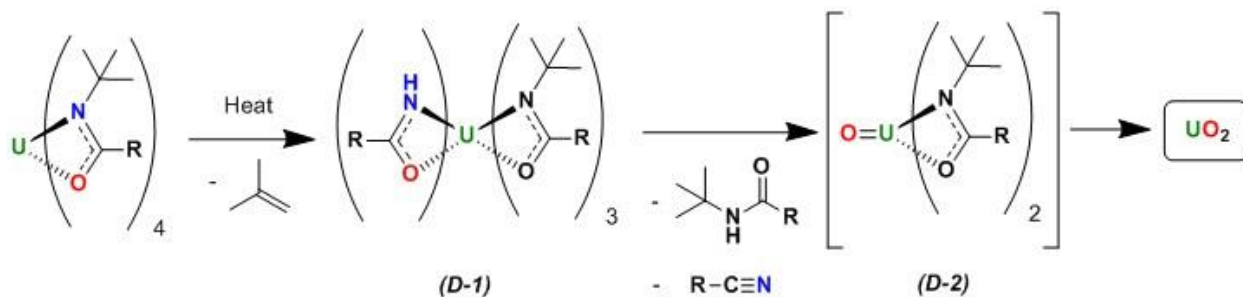
The U-O and U-N bond lengths in **3.7** are comparable to the analogous U-O and U-N bonds of the chelated amidates in **3.8** (2.284(4) and 2.296(4) Å for U-O). However, the U-O bonds of the O-bound amidates in **3.8** are substantially shorter (2.123(5) and 2.135(4) Å), suggesting increased localization of electron density on the oxygen atoms of these ligands when bound  $\kappa_1$ -O. Providing further support for this claim, the O-bound ligands in **3.8** also possess longer C-O bonds (1.375(9) and 1.361(7) Å) and shorter C-N bonds (1.141(11) and 1.240(9) Å for C-N) than their chelated counterparts (1.323(7) and 1.323(7) Å for C-O; 1.297(8) and 1.309(9) Å).

The thermal decomposition of the precursors was further investigated using thermogravimetric (TG) analysis (Figure 3.2). Precursor **3.7** showed an onset of decomposition at 85 °C, while precursor **3.8** showed an onset of decomposition at 70 °C. The experimentally detected overall weight losses of **3.7** (65.0%) and **3.8** (62.7%) are lower than the theoretical values of 66.5% and 68.8% for the formation of UO<sub>2</sub>, suggesting the potential incorporation of carbon impurities; this mass difference is substantially more prominent for precursor **3.7** than for precursor **3.8**.





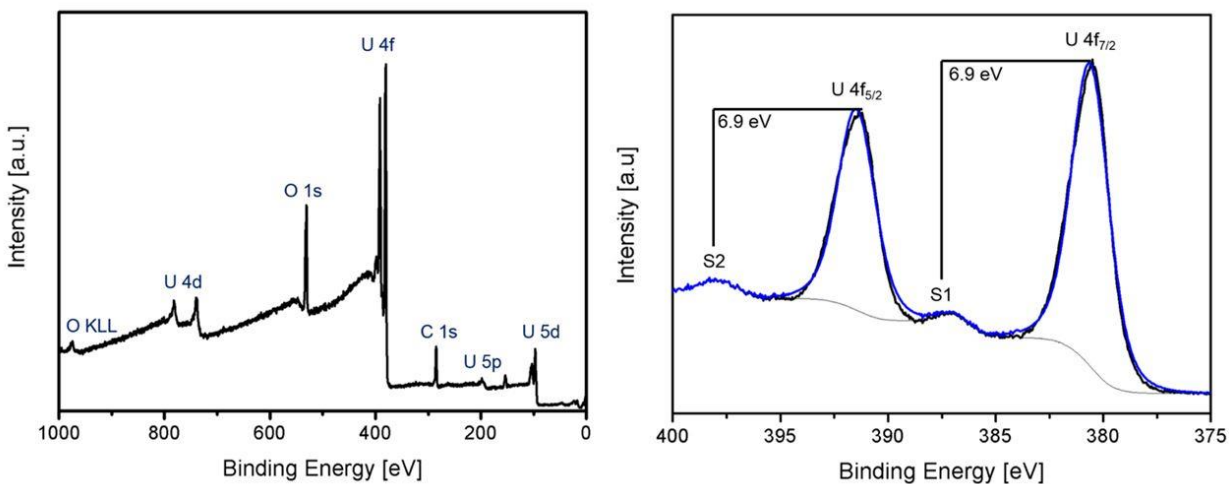
**Figure 3.2:** Thermograms of **3.7** (left) and **3.8** (right) collected under nitrogen at a heating rate of 5 °C/min.



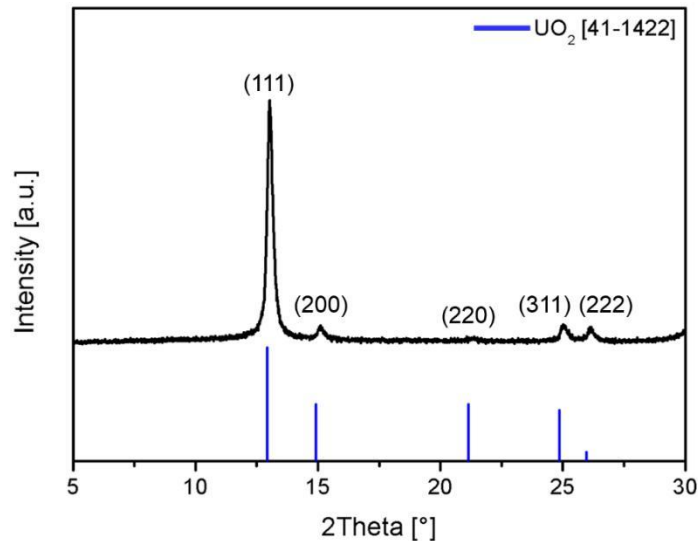
**Scheme 3.3:** Proposed decomposition mechanism of **3.7** and **3.8**. Alkene, amide, and nitrile byproducts were observed by NMR; intermediate decomposition products **D-1** and **D-2** are postulated.

To elucidate the decomposition mechanism of these precursors to uranium oxide, solid samples of **3.7** and **3.8** were heated to 300 °C in sealed J-Young tubes under a nitrogen atmosphere. The tubes were then cooled with liquid nitrogen to condense volatile decomposition products, and C<sub>6</sub>D<sub>6</sub> was added for NMR analysis. Three main products were visible in the resulting <sup>1</sup>H NMR spectra of the decomposed precursors: the amides **3.1** or **3.2**, isobutyronitrile (from **3.7**) or pivalonitrile (from **3.8**), and isobutylene (Figures 3.8 and 3.9). A small amount of insoluble black uranium oxide precipitate was also observed. These products are consistent with an alkene elimination mechanism (Scheme 3.3), as reported previously for related homoleptic Zr(IV) amidates.<sup>26</sup> We also observed slow formation of the same products by heating solutions of **3.7** and **3.8** to 150 °C in d<sub>8</sub>-toluene over the course of multiple days. In the first decomposition step, isobutylene elimination from a nitrogen atom generates a hemiamidate intermediate (**D-1**). This hemiamidate then undergoes protonolysis with another amidate ligand to promote the elimination of one equivalent each of amide and nitrile, leaving an oxygen atom bound to the uranium center (**D-2**). Because this is a low-coordinate system, it is likely that the intermediate **D-2** aggregates prior to elimination of additional ligands. A second iteration of this process yields UO<sub>2</sub> and one more equivalent each of isobutylene, amide, and nitrile.

Complexes **3.7** and **3.8** were both tested as  $\text{UO}_2$  thin film precursors in a cold wall thermal CVD reactor. We were interested to determine if the oxidation state of the precursors would be retained in the CVD-generated materials to form stoichiometric  $\text{UO}_2$  films, as suggested by the thermal decomposition experiments. As the sublimation temperatures and decomposition temperatures at a pressure of  $10^{-3}$  mbar were in very close vicinity ( $\sim 130$  °C for **3.7**,  $\sim 120$  °C for **3.8**), CVD experiments were performed at a pressure of  $10^{-6}$  mbar to favor sublimation of the precursors. In order to ensure a proper precursor flow, the precursor temperatures were set to 160 °C. Since TG analysis displayed a complete decomposition of both precursors at a temperature of 500 °C, substrate temperatures of 500 °C were chosen for both CVD processes. Precursor **3.7** sublimed without prior decomposition in the precursor flask, and black films were generated during the CVD process. In contrast, the deposition process using complex **3.8** was not successful; we postulate this may be due to the weakly bound  $\kappa\text{-I-O}$  coordinated ligands and thus thermal instability of the precursor.

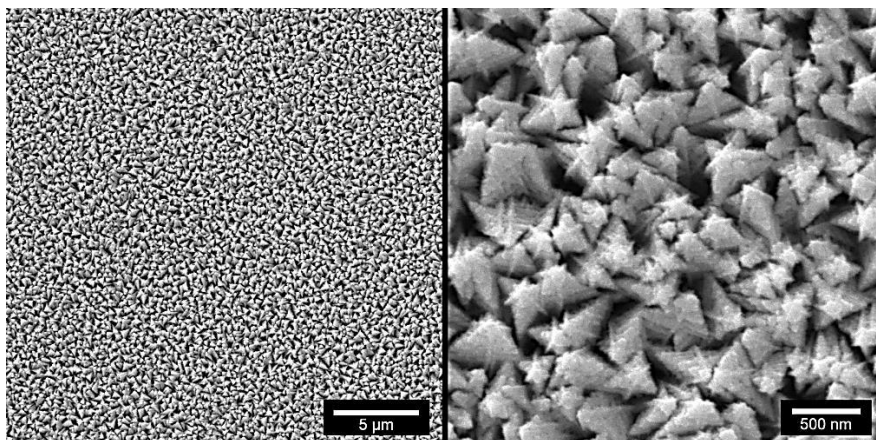


**Figure 3.3:** XPS survey spectrum (left) and high-resolution U 4f XPS spectrum (right) of crystalline  $\text{UO}_2$  films prepared via CVD using **3.7**.

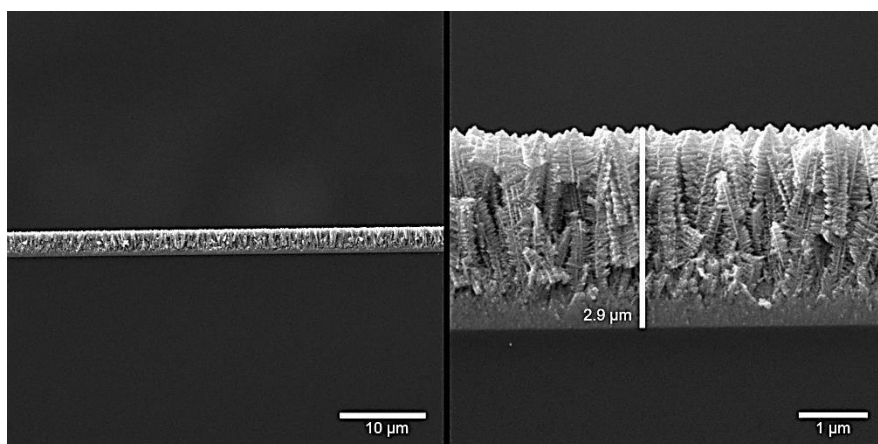


**Figure 3.4:** Powder XRD pattern of the film deposited using 3.7 at a precursor temperature of 160 °C and a substrate temperature of 500 °C.

Following the deposition process, the films were characterized without an additional annealing step to determine if UO<sub>2</sub> was prepared directly. As shown by XPS (Figure 3.3) and XRD (Figure 3.4) analyses, the film surface and the bulk are composed of phase-pure UO<sub>2</sub>. This finding is noteworthy given the pronounced tendency of uranium dioxide to exhibit surface oxidation resulting in hyperstoichiometric compositions (O:U > 2:1). The XPS survey spectrum exhibited signals attributable solely to uranium, oxygen and carbon (Figure 3.3, left). The high-resolution U 4f XPS spectrum showed two main signals at 380.4 eV and 391.4 eV, corresponding to the U 4f<sub>7/2</sub> and U 4f<sub>5/2</sub> orbitals, respectively (Figure 3.3, right). The peak positions of the main signals and the satellites (binding energy distance to the main signals of  $DE_{\text{sat}} = 6.9$  eV) are consistent with the reported data.<sup>[5]</sup> The Bragg reflections in the XRD pattern were assigned to cubic fluorite-type UO<sub>2</sub> (Figure 3.4). The peaks at  $2\theta = 13.0^\circ$ ,  $15.0^\circ$ ,  $21.2^\circ$ ,  $24.9^\circ$  and  $26.0^\circ$  were indexed to the (111), (200), (220), (311) and (222) planes, respectively. As the diffraction peaks are broadened anisotropically, the crystallite sizes were calculated using the Scherrer equation and amounted to 146 nm, 195 nm and 99 nm for the (111)/(222), (200) and (311) planes, respectively. Whereas the anisotropic broadening suggests the formation of anisotropic crystallite shapes, the predominant intensity of the reflection indexed to the (111) plane hints towards a preferred growth direction that was confirmed by the surface topography (Figure 3.5). Taken together, these results strongly suggest that phase-pure UO<sub>2</sub> films were prepared directly via decomposition of the molecular precursor.



**Figure 3.5:** Top-view SEM images with different magnifications of crystalline  $\text{UO}_2$  films, prepared via CVD from precursor 3.7.



**Figure 3.6:** Side-view SEM images with different magnifications of crystalline  $\text{UO}_2$  films, prepared via CVD from precursor 3.7. The thickness of these films is  $2.9 \mu\text{m}$ .

The vapor-deposited  $\text{UO}_2$  films exhibited a homogeneous distribution of fir tree-like structures at the surface and good adhesion to the silicon substrate, as depicted in the top-view (Figure 3.5) and side-view (Figure 3.6) SEM images, respectively. The side-view SEM images additionally revealed the formation of a dense layer with a thickness of  $\sim 400 \text{ nm}$  at the substrate interface, which seamlessly continues into a branch-like structure with a thickness of  $\sim 2.5 \mu\text{m}$ . This change in the microstructure from 2-D to 1-D growth is likely due to the good lattice match between silicon ( $a = 5.431 \text{ \AA}$ ) and  $\text{UO}_2$  ( $a = 5.471 \text{ \AA}$ ), which facilitates epitaxial growth of  $\text{UO}_2$  onto Si up to a thickness of ca.  $400 \text{ nm}$ . Beyond this thickness, the cubic  $\text{UO}_2$  crystals act as seeds for 1-D nanostructures that grow with equal probability in multiple directions, leading to the formation of branch-like structures.

## Summary and Conclusions

In summary, we have developed an effective single-source route to fabricate crystalline, phase-pure UO<sub>2</sub> films through chemical vapor deposition of U<sup>IV</sup> amidate molecular precursors, which decompose cleanly via alkene elimination. Small changes in the ligand substituents were seen to affect both the molecular geometry and the decomposition behavior of the precursors, with the 8-coordinate complex **3.7** performing much more favorably for thin film deposition than the 6-coordinate complex **3.8**. XRD and XPS measurements confirmed the vapor-deposited uranium oxide films to be stoichiometric UO<sub>2</sub>, and SEM images showed good epitaxial growth of the UO<sub>2</sub> layer onto the Si substrate. Above a film thickness of ca. 400 nm, the UO<sub>2</sub> crystals formed fir tree-like structures with isotropic growth of 1-D branches and a large accessible surface area. Given the anisotropic microstructure and high surface area of these films, in conjunction with high charge carrier mobilities in UO<sub>2</sub>, these films may be good candidates as photoanodes in photoelectrochemical water splitting reactions.

## Experimental

### Materials and Methods

Unless otherwise noted, all syntheses were performed using standard Schlenk techniques under an atmosphere of nitrogen or in an MBraun glovebox under an atmosphere of nitrogen. Glassware, cannulae, and Celite were stored in an oven at 160 °C for at least 12 hours prior to use. 3 Å and 4 Å molecular sieves were activated by heating under vacuum at 300 °C for 24 hours. Hexane, pentane, toluene, diethyl ether, tetrahydrofuran, and acetonitrile were purified by passage through a column of activated alumina prior to use. C<sub>6</sub>D<sub>6</sub> and d<sub>8</sub>-toluene were purchased from Cambridge Isotope Labs and stored over 4 Å molecular sieves. C<sub>5</sub>D<sub>5</sub>N was purchased from Cambridge Isotope Labs and stored over 3 Å molecular sieves. CDCl<sub>3</sub> was purchased from Cambridge Isotope Labs and used as received. H(ITA) (**3.1**) and H(TTA) (**3.2**) were prepared according to literature methods<sup>26,29</sup> and purified by sublimation at 60 °C, 10 mTorr. U<sub>4</sub>(1,4-dioxane)<sub>2</sub> and [(Me<sub>3</sub>Si)<sub>2</sub>N]<sub>2</sub>U[κ<sup>2</sup>-(C,N)-CH<sub>2</sub>Si(Me)<sub>2</sub>N(SiMe<sub>3</sub>)] were prepared according to literature methods.<sup>30,31</sup> All other chemicals were purchased from Sigma-Aldrich or Acros Organics and used as received. <sup>1</sup>H and <sup>13</sup>C NMR spectra were recorded at room temperature using Bruker AV-600, AV-500, AVB-400, and AV-300 spectrometers. <sup>1</sup>H chemical shifts were referenced to C<sub>6</sub>D<sub>5</sub>H (δ = 7.16 ppm), C<sub>5</sub>D<sub>4</sub>HN (δ<sub>1</sub> = 8.74 ppm), C<sub>6</sub>D<sub>4</sub>HCD<sub>3</sub> (δ<sub>1</sub> = 7.09 ppm), and CHCl<sub>3</sub> (δ = 7.26 ppm). <sup>13</sup>C chemical shifts were referenced to C<sub>6</sub>D<sub>6</sub> (δ = 128.06 ppm) and C<sub>5</sub>D<sub>5</sub>N (δ<sub>1</sub> = 150.35 ppm). Samples for IR spectroscopy were prepared as Nujol mulls, and spectra were taken in KBr plates using a Nicolet iS10 spectrometer. Melting points were determined in sealed tubes under an atmosphere of nitrogen using a Stanford Research Systems OptiMelt instrument and are reported uncorrected.

### Synthesis of compounds

**K(ITA) (3.3):** A THF solution (20 mL) of KN(SiMe<sub>3</sub>)<sub>2</sub> (2.22 g, 11.1 mmol) was added to a stirred THF solution (40 mL) of **3.1** (1.52 g, 10.6 mmol) maintained at -78 °C via cannula. After stirring at room temperature for 16 h, the solvent was removed *in vacuo* to give an off-white powder. This powder was washed with toluene (15 mL), then hexane (30 mL) to remove impurities, and then

trituated with hexane and dried *in vacuo* to give the product as a colorless powder. (1.66 g, 86% yield)

IR (cm<sup>-1</sup>): 1575 (m), 1557 (m), 1544 (m), 1336 (m), 1306 (w), 1282 (w), 1070 (m), 949 (w), 907 (w), 891 (w), 774 (w), 654 (w), 501 (w). <sup>1</sup>H NMR (C<sub>5</sub>D<sub>5</sub>N, 500 MHz): δ 2.89 (m, 1H, CH(CH<sub>3</sub>)<sub>2</sub>), 1.82 (s, 9H, C(CH<sub>3</sub>)<sub>3</sub>), 1.46 (d, 6H, CH(CH<sub>3</sub>)<sub>2</sub>).

<sup>13</sup>C NMR (C<sub>5</sub>D<sub>5</sub>N, 400 MHz): δ 176.61 (NCO), 51.69 (C(CH<sub>3</sub>)<sub>3</sub>), 39.82 (CH(CH<sub>3</sub>)<sub>2</sub>), 32.39 (C(CH<sub>3</sub>)<sub>3</sub>), 23.10 (CH(CH<sub>3</sub>)<sub>2</sub>).

**K(TTA) (3.4):** A THF solution (50 mL) of KN(SiMe<sub>3</sub>)<sub>2</sub> (10.0 g, 50.1 mmol) was added to a stirred THF solution (70 mL) of **3.2** (7.51 g, 47.7 mmol) maintained at -78 °C via cannula. After stirring at room temperature for 16 h, the solvent was removed *in vacuo* to give an off-white powder. This powder was washed with toluene (20 mL), then hexane (30 mL) to remove impurities, and then trituated with hexane and dried *in vacuo* to give the product as a colorless powder. (8.60 g, 92% yield)

IR (cm<sup>-1</sup>): 1534 (s), 1490 (w), 1147 (m), 1319 (s), 1233 (m), 1193 (w), 1092 (w), 917 (w), 887 (w), 816 (w), 779 (w), 654 (w), 586 (w), 521 (w), 502 (w).

<sup>13</sup>C NMR (C<sub>5</sub>D<sub>5</sub>N, 400 MHz): δ 177.05 (NCO), 51.81 (NC(CH<sub>3</sub>)<sub>3</sub>), 40.31 (CC(CH<sub>3</sub>)<sub>3</sub>), 32.62 (NC(CH<sub>3</sub>)<sub>3</sub>), 31.58 (CC(CH<sub>3</sub>)<sub>3</sub>).

**K(ITA)(18c6) (3.5):** THF (50 mL) was added to a flask containing **3.3** (3.00 g, 16.5 mmol) and 18-crown-6 (4.37 g, 16.5 mmol) at room temperature. The solution was stirred for 1 h, then the solvent was removed *in vacuo* to give the product as a colorless powder. (7.21 g, 98% yield)

IR (cm<sup>-1</sup>): 1558 (s), 1353 (m), 1328 (m), 1306 (w), 1285 (w), 1274 (w), 1252 (w), 1208 (w), 1109 (s), 962 (s), 890 (w), 863 (w), 836 (w).

<sup>1</sup>H NMR (C<sub>6</sub>D<sub>6</sub>, 500 MHz): δ 3.14 (s, 24H, OCH<sub>2</sub>), 3.05 (m, 1H, CH(CH<sub>3</sub>)<sub>2</sub>), 1.99 (s, 9H, C(CH<sub>3</sub>)<sub>3</sub>), 1.60 (d, 6H, CH(CH<sub>3</sub>)<sub>2</sub>).

<sup>13</sup>C NMR (C<sub>6</sub>D<sub>6</sub>, 600 MHz): δ 175.14 (NCO), 70.11 (OCH<sub>2</sub>), 51.31 (C(CH<sub>3</sub>)<sub>3</sub>), 39.57 (CH(CH<sub>3</sub>)<sub>2</sub>), 32.17 (C(CH<sub>3</sub>)<sub>3</sub>), 23.20 (CH(CH<sub>3</sub>)<sub>2</sub>).

**K(TTA)(18c6) (3.6):** THF (50 mL) was added to a flask containing **3.4** (3.40 g, 17.4 mmol) and 18-crown-6 (4.60 g, 17.4 mmol) at room temperature. The solution was stirred for 1 h, then the solvent was removed *in vacuo* to give the product as a colorless powder. (7.89 g, 99% yield)

IR (cm<sup>-1</sup>): 1545 (s), 1353 (m), 1319 (m), 1285 (w), 1249 (w), 1233 (w), 1112 (s), 965 (m), 918 (w), 887 (w), 838 (w).

<sup>1</sup>H NMR (C<sub>6</sub>D<sub>6</sub>, 300 MHz): δ 3.13 (s, 24H, OCH<sub>2</sub>), 1.98 (s, 9H, C(CH<sub>3</sub>)<sub>3</sub>), 1.80 (s, 9H, C(CH<sub>3</sub>)<sub>3</sub>).

<sup>13</sup>C NMR (C<sub>6</sub>D<sub>6</sub>, 600 MHz): δ 176.14 (NCO), 70.08 (OCH<sub>2</sub>), 51.35 (NC(CH<sub>3</sub>)<sub>3</sub>), 39.96 (CC(CH<sub>3</sub>)<sub>3</sub>), 32.17 (NC(CH<sub>3</sub>)<sub>3</sub>), 31.51 (CC(CH<sub>3</sub>)<sub>3</sub>).

**U(ITA)<sub>4</sub> (3.7):** *Method 1-* A THF solution (25 mL) of UI<sub>4</sub>(1,4-dioxane)<sub>2</sub> (3.45 g, 3.74 mmol) was added dropwise to a stirred 1:1 THF:Et<sub>2</sub>O solution (200 mL) of **3.5** (6.65 g, 14.9 mmol) cooled to -78 °C. After the addition of UI<sub>4</sub>(1,4-dioxane)<sub>2</sub> was complete, the cold bath was removed, and the color of the solution changed from deep red to cloudy green. The solution was stirred for 2 d and then the solvent was removed *in vacuo*. The product was extracted with Et<sub>2</sub>O (100 mL) and THF (20 mL), then the solvents were removed *in vacuo* to give a green oil. Hexane (150 mL) was added to give a green solution, which was then filtered and cooled to -40 °C for 24 h, yielding green

crystals. These crystals were washed twice with acetonitrile (10 mL) to give the pure product. (2.11 g, 70% yield)

*Method 2-* A toluene solution (10 mL) of **3.1** (136 mg, 0.585 mmol) was added dropwise to a stirred toluene solution (2 mL) of  $[(\text{Me}_3\text{Si})_2\text{N}]_2\text{U}[\kappa^2\text{-(C,N)-CH}_2\text{Si(Me)}_2\text{N(SiMe}_3)]$  (149 mg, 0.207 mmol) at room temperature. The solution was heated to reflux for 20 h, and then the solvent was removed *in vacuo*. Toluene (3 mL) was added to the resulting brown oil to give a brown solution. This solution was filtered and cooled to  $-40\text{ }^\circ\text{C}$  for 24 h, resulting in a mixture of green and brown crystals. These crystals were washed with acetonitrile, then recrystallized from pentane, yielding the product as green crystals. (45 mg, 27% yield)

*Method 3-* A THF solution (2 mL) of  $\text{UI}_4(1,4\text{-dioxane})_2$  (300 mg, 0.325 mmol) was added dropwise to a stirred THF solution (8 mL) of **3.3** (254 mg, 1.40 mmol) at room temperature. Following the addition of  $\text{UI}_4(1,4\text{-dioxane})_2$ , the color of the solution changed from deep red to cloudy green. The solution was stirred for 2 d and then the solvent was removed *in vacuo*. Pentane (5 mL) was added to the resulting green oil to give a green solution. This solution was filtered to remove insoluble KI, concentrated to a volume of 2 mL, and cooled to  $-40\text{ }^\circ\text{C}$  for 24 h, yielding green crystals. These crystals were washed with acetonitrile, then recrystallized from pentane. (54 mg, 19% yield)

IR ( $\text{cm}^{-1}$ ): 1693 (w), 1541 (m), 1348 (m), 1300 (w), 1210 (w), 1070 (w), 1011 (w), 894 (w), 811 (w), 643 (w), 586 (w).  $^1\text{H NMR}$  ( $\text{C}_6\text{D}_6$ , 400 MHz):  $\delta$  4.36 (s, 4H,  $\text{CH}(\text{CH}_3)_2$ ), 2.66 (s, 24H,  $\text{CH}(\text{CH}_3)_2$ ), -1.24 (s, 36H,  $\text{C}(\text{CH}_3)_3$ ). Melting point: slowly decomposes above  $140\text{ }^\circ\text{C}$ ; sublimation is also observed. EA calcd: C: 47.63%, H: 7.99%, N: 6.94%. Found: C: 47.55%, H: 7.84%, N: 6.97%.

#### **U(TTA)<sub>4</sub> (3.8):**

*Method 1-* A THF solution (25 mL) of  $\text{UI}_4(1,4\text{-dioxane})_2$  (3.10 g, 3.36 mmol) was added dropwise to a stirred 3:2 THF:Et<sub>2</sub>O solution (100 mL) of **3.6** (6.10 g, 13.3 mmol) cooled to  $-78\text{ }^\circ\text{C}$ . After the addition of  $\text{UI}_4(1,4\text{-dioxane})_2$  was complete, the cold bath was removed, and the color of the solution changed from deep red to cloudy green. The solution was stirred for 2 d and then the solvent was removed *in vacuo*. The product was extracted with Et<sub>2</sub>O (60 mL), which was then removed *in vacuo* to give a teal oil. Pentane (20 mL) was added to give a teal solution, which was then filtered, concentrated to a final volume of 10 mL, and cooled to  $-40\text{ }^\circ\text{C}$  for 24 h, yielding teal crystals. These were recrystallized from pentane to give the pure product. (1.58 g, 55% yield)

*Method 2-* A THF solution (2 mL) of  $\text{UI}_4(1,4\text{-dioxane})_2$  (302 mg, 0.325 mmol) was added dropwise to a stirred THF solution (10 mL) of **3.4** (256 mg, 1.31 mmol) at room temperature. Following the addition of  $\text{UI}_4(1,4\text{-dioxane})_2$ , the color of the solution changed from deep red to cloudy green. The solution was stirred for 2 d and then the solvent was removed *in vacuo*. Pentane (5 mL) was added to the resulting greenish-brown solids to give a deep green solution. The solution was filtered to remove insoluble KI, concentrated to a volume of 1 mL, and cooled to  $-40\text{ }^\circ\text{C}$  for 24 h, yielding teal crystals. These crystals were quickly washed with acetonitrile, then recrystallized from pentane. (52 mg, 18% yield)

IR ( $\text{cm}^{-1}$ ): 1645 (m), 1511 (m), 1363 (m), 1295 (w), 1268 (w), 1218 (w), 1183 (w), 1122 (m), 1092 (m), 1027 (w), 990 (w), 934 (w), 879 (w), 813 (w), 801 (w), 738 (w), 659 (w), 609 (w), 577 (w), 546 (w).  $^1\text{H NMR}$  ( $\text{C}_6\text{D}_6$ , 400 MHz):  $\delta$  6.63 (s, 18H,  $\text{C}(\text{CH}_3)_3$ ), 1.27 (s, 18H,  $\text{C}(\text{CH}_3)_3$ ), 0.45 (s, 18H,  $\text{C}(\text{CH}_3)_3$ ), -5.61 (s, 18H,  $\text{C}(\text{CH}_3)_3$ ). Melting point: slowly decomposes above  $120\text{ }^\circ\text{C}$ ; sublimation is also observed. EA calcd: C: 50.06%, H: 8.41%, N: 6.49%. Found: C: 49.99%, H: 8.53%, N: 6.42%.

## Materials Characterization

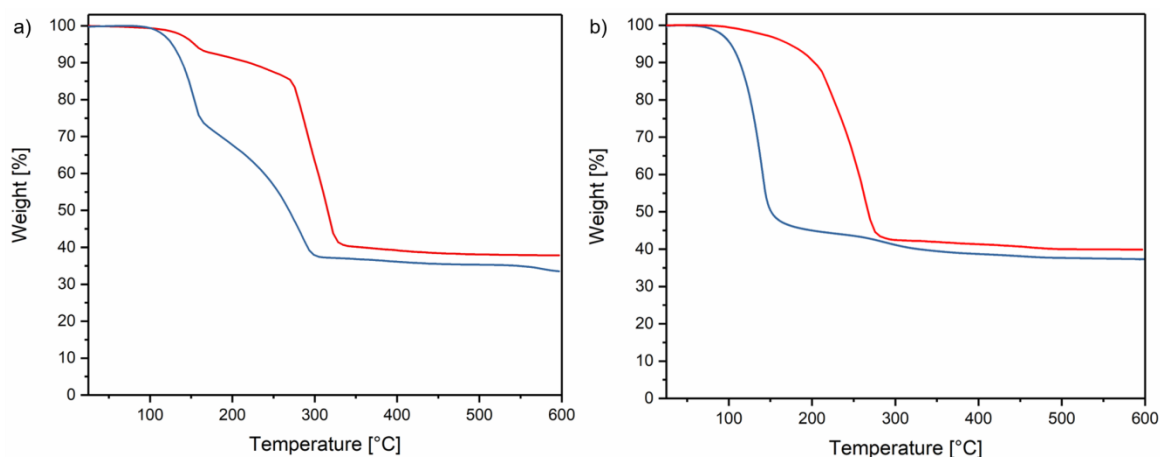
Room-temperature powder X-ray diffraction (XRD) was performed on a STOE-STADI MP diffractometer operating in the reflection mode using Cu K $\alpha$  ( $\lambda = 1.5406 \text{ \AA}$ ) radiation. The microstructures of the samples were examined using field-emission scanning electron microscopy (FE-SEM, FEI Nova NanoSEM 430). X-ray photoelectron spectroscopy (XPS) measurements were carried out using an ESCA M-Probe spectrometer (*Surface Science Instruments SSI*) under Al K $\alpha$  excitation (1486.6 eV) at a pressure of  $10^{-9}$  mbar. Correction to the binding energies was done in reference to the C 1s signal (284.8 eV). Spectral corrections and composition calculations were performed using *CasaXPS*. TG measurements were performed with samples prepared in an argon dry box and filled into Al<sub>2</sub>O<sub>3</sub> pans prior to transfer into the apparatus (Mettler-Toledo GmbH, Germany, TGA 1, Gas-controller GC 200). For the transfer, the pans were sealed into inert vials and put onto the scale using a nitrogen counterflow. Measurements were performed at heating rates of 5 and 10 °C/min under a nitrogen atmosphere.

## TG Analysis of 3.7 and 3.8

The decomposition of **3.7** and **3.8** were investigated using different heating rates to determine if the decomposition mechanism could be monitored by TGA. Using a heating rate of 10 °C/min, precursor **3.7** decomposed in two steps that were resolvable by TG analysis, starting at a decomposition temperature of 105 °C and an initial mass loss of 7%, which may correspond to loss of isobutylene (theoretical mass loss of 5.5%). A second decomposition step was observed at 160 °C with a mass loss of 55.2%. (Figure 3.7, red). By comparison, at a heating rate of 10 °C/min, precursor **3.8** decomposed in a single step resolvable by TG analysis, starting at a decomposition temperature of 100 °C (Figure 3.7, red). The experimentally detected overall weight losses of **3.7** (62.2%) and **3.8** (60.1%) are lower than the theoretical values of 66.5% and 68.8% for the formation of UO<sub>2</sub>, pointing towards the incorporation of carbon impurities.

TG measurements were also performed with a lower heating rate of 5 °C/min (Figure 3.7, blue). At this lower heating rate, the onset of decomposition occurs at 85 °C (for **3.7**) and 70 °C (for **3.8**) compared to 105 °C and 100 °C found for heating rates of 10 °C/min, respectively. Moreover, less impurities were incorporated in the decomposition products of both precursors using a lower heating rate. The measured mass losses amount to 65.0% and 62.7% for **3.7** and **3.8**, respectively, and are closer to the theoretical values for the formation of UO<sub>2</sub>. However, the lower heating rate did not result in the deconvolution of the decomposition steps. Instead, the initial mass loss increased for decomposition of **3.7** (25% vs. 7% at a heating rate of 10 °C/min) hinting towards the simultaneous decomposition of different fragments. Thus, the thermal decomposition of the solid compound is dependent on the heating rate.



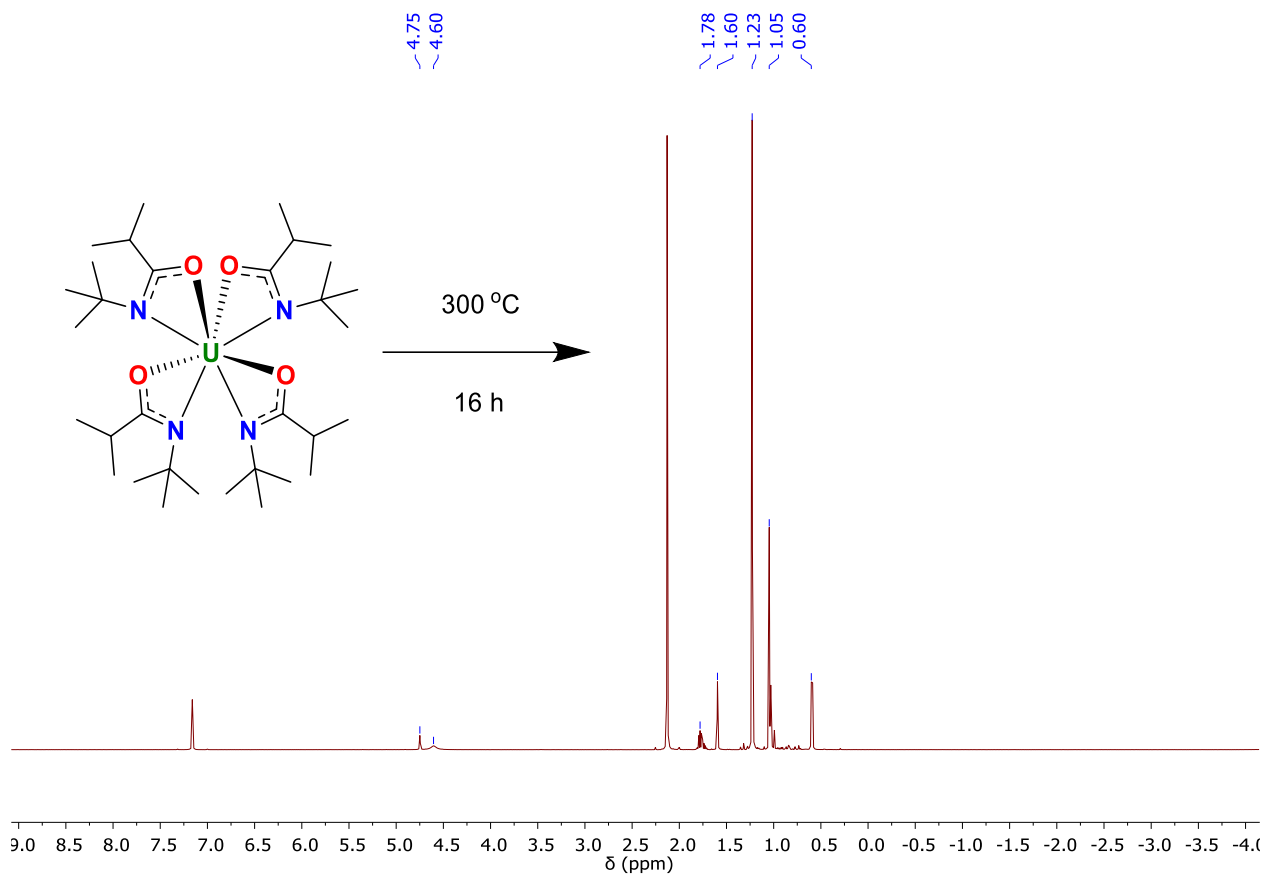


**Figure 3.7:** TG measurements of **3.7** (left) and **3.8** (right) at heating rates of 10 °C/min (red) and 5 °C/min (blue) collected under nitrogen.

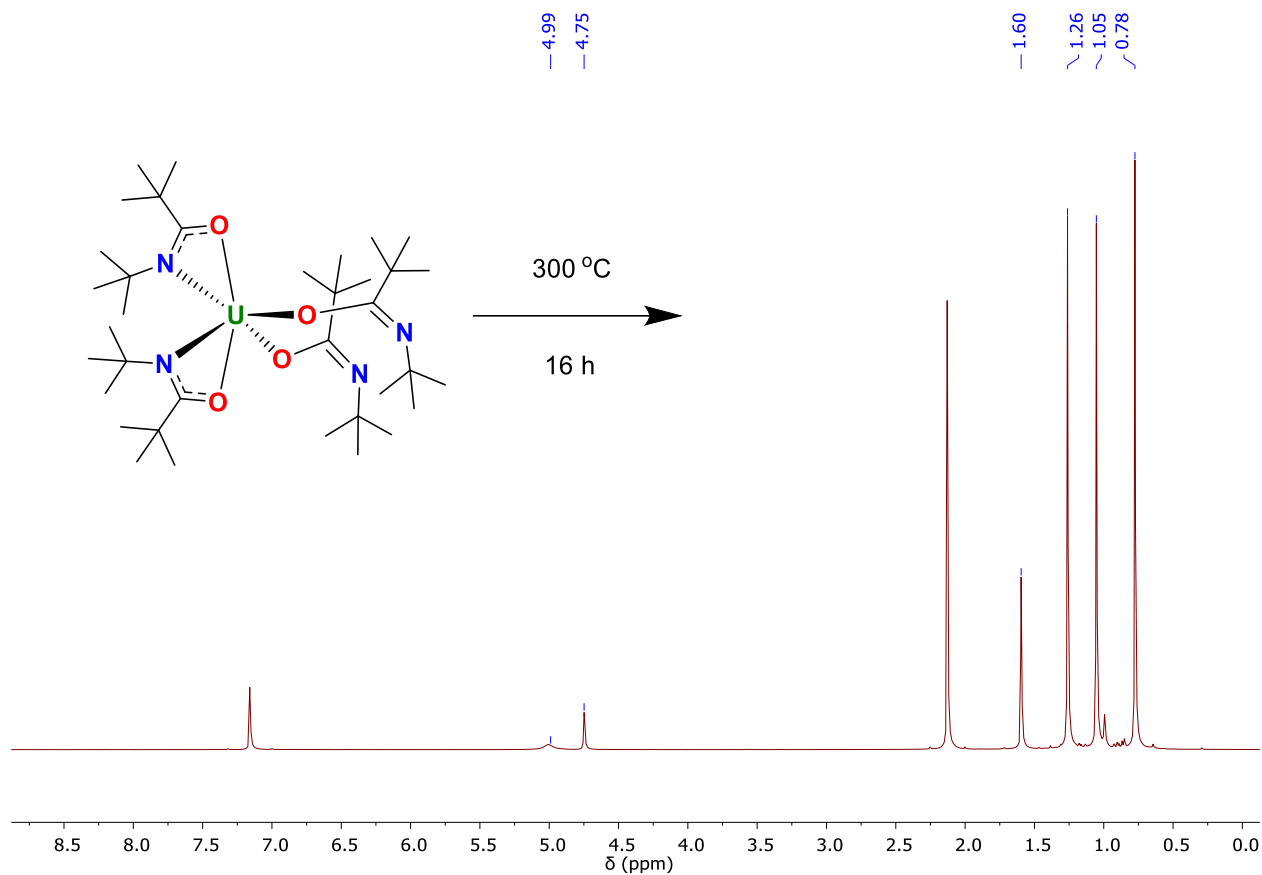
### NMR Decomposition Studies of **3.7** and **3.8**

*Method 1-* **3.7** and **3.8** (10 mg each) were added to separate J-young tubes inside a nitrogen glovebox. The tubes were brought out of the glovebox and heated to 300 °C for 16 h. After cooling down to room temperature, the tubes were brought back into the glovebox and placed into a liquid nitrogen-cooled cold well for 20 minutes to condense volatile decomposition products. A solution of hexamethylbenzene (1.0 mg) in C<sub>6</sub>D<sub>6</sub> (0.50 mL) was quickly added to each tube, then the tubes were capped and allowed to warm to room temperature before collecting NMR spectra.

*Method 2-* **3.7** and **3.8** (10 mg each) were added to separate J-young tubes inside a nitrogen glovebox. A solution of HMDSO (1.0 mg) in d<sub>8</sub>-toluene (0.50 mL) was added to each tube, then the tubes were brought out of the glovebox and heated to 150 °C for 4 d. The tubes were allowed to cool to room temperature before collecting NMR spectra.



**Figure 3.8:**  $^1\text{H}$  NMR spectrum of the products formed by heating a solid sample of **3.7** to  $300\text{ }^\circ\text{C}$  for 16 h. This spectrum was collected at  $21\text{ }^\circ\text{C}$  in  $\text{C}_6\text{D}_6$ . The isobutylene resonances are present at 4.75 and 1.60 ppm, the isobutyronitrile resonances are present at 1.78 and 0.60 ppm, and the resonances from **3.1** are present at 4.60, 1.78, 1.23, and 1.05 ppm. The peak at 2.13 ppm is from  $\text{C}_6\text{Me}_6$  (internal standard).



**Figure 3.9:**  $^1\text{H}$  NMR spectrum of the products formed by heating a solid sample of **3.8** to  $300^\circ\text{C}$  for 16 h. This spectrum was collected at  $21^\circ\text{C}$  in  $\text{C}_6\text{D}_6$ . The isobutylene resonances are present at 4.75 and 1.60 ppm, the pivalonitrile resonance is present at 0.78 ppm, and the resonances from **3.2** are present at 4.99, 1.26, and 1.05 ppm. The peak at 2.13 ppm is from  $\text{C}_6\text{Me}_6$  (internal standard).

### Preparation of $\text{UO}_2$ films via gas phase deposition of **3.7**

The gas phase deposition of  $\text{UO}_2$  layers was performed using 60 mg of **3.7** as precursor in a horizontal cold-wall CVD reactor. The precursor temperature was kept constant at  $160^\circ\text{C}$  to ensure a homogenous gas flow. The precursor flux was guided to an inductively heated substrate with a substrate temperature of  $500^\circ\text{C}$  using low pressure ( $\sim 3 \times 10^{-6}$  mbar). The deposition time was set to 10 minutes. The substrates (silicon wafers, silicon nitride windows) were attached to the substrate holder using silver paste.

### X-Ray Crystallography

X-ray structural determination was performed at CHEXRAY, University of California, Berkeley, on a Bruker APEX II Quazar diffractometer or at the Advanced Light Source (ALS) station 11.3.1 at Lawrence Berkeley National Laboratory. The Bruker Quazar is a Kappa geometry three-circle diffractometer that couples a charge-coupled device (CCD) detector with a sealed-tube source of monochromatized  $\text{Mo K}_\alpha$  radiation. Structural data collected at ALS station 11.3.1 utilized a silicon monochromated beam of 16 keV ( $\lambda = 0.7749 \text{ \AA}$ ) synchrotron radiation. Crystals

of appropriate size and quality were coated in Paratone-N oil and mounted on a Kapton loop. The loop was transferred to the diffractometer, centered in the beam, and cooled by a nitrogen flow low-temperature apparatus that had been previously calibrated by a thermocouple placed at the same position as the crystal. All data collection was carried out at 100 K. The data were corrected for Lorentz and polarization effects; no correction for crystal decay was applied. An empirical absorption correction based on comparison of redundant and equivalent reflections was applied using SADABS. All software used for diffraction data processing and crystal-structure solution and refinement are contained in the APEX3 program suite (Bruker AXS, Madison, WI). Thermal parameters for all non-hydrogen atoms were refined anisotropically.<sup>32-36</sup> CCDC numbers for compounds **3.7** and **3.8** can be found in Table 3.2. The CIF files can be downloaded free of charge from <https://summary.ccdc.cam.ac.uk/structure-summary-form>.

**Table 3.2:** Crystallographic details for **3.7** and **3.8**.

	<b>3.7</b>	<b>3.8</b>
Chemical formula	C <sub>32</sub> H <sub>64</sub> N <sub>4</sub> O <sub>4</sub> U <sub>1</sub>	C <sub>36</sub> H <sub>72</sub> N <sub>4</sub> O <sub>4</sub> U <sub>1</sub>
<i>M<sub>r</sub></i>	806.90	863.00
Crystal system	Monoclinic	Orthorhombic
Space group	P2 <sub>1</sub> /n	P2 <sub>1</sub> 2 <sub>1</sub> 2 <sub>1</sub>
a (Å)	8.8167(4)	11.9593(7)
b (Å)	24.5977(11)	17.2924(10)
c (Å)	17.1899(8)	20.3202(12)
α (°)	90	90
β (°)	95.090(2)	90
γ (°)	90	90
V (Å <sup>3</sup> )	3713.3(3)	4202.3(4)
Z	4	4
Density (g/cm <sup>3</sup> )	1.443	1.364
F(000)	1632	1760
Radiation Type	Mo K <sub>α</sub>	Synchrotron
μ (mm <sup>-1</sup> )	4.408	1.813
Abs. corr. type	Multi-scan	Multi-scan
Abs. corr. T <sub>min</sub>	0.375	0.630
Abs. corr. T <sub>max</sub>	0.491	0.746
Crystal size (mm)	0.27 x 0.25 x 0.20	0.14 x 0.10 x 0.05
Meas. Refl.	83931	55297
Indep. Refl.	7622	7682
Obsvd. [ <i>I</i> > 2σ( <i>I</i> )] refl.	5461	7601
R <sub>int</sub>	0.0315	0.0389
R [ <i>F</i> <sup>2</sup> > 2σ( <i>F</i> <sup>2</sup> )], wR( <i>F</i> <sup>2</sup> )	0.0262, 0.0722	0.0260, 0.0638
S	1.050	1.056
Δρ <sub>max</sub> , Δρ <sub>min</sub> (e Å <sup>-3</sup> )	2.309, -0.735	1.383, -1.345
CCDC	1884806	1884807

## References

- 1 S. J. Zinkle and G. S. Was, *Acta Mater.*, 2013, **61**, 735–758.
- 2 S. J. Zinkle, K. A. Terrani, J. C. Gehin, L. J. Ott and L. L. Snead, *J. Nucl. Mater.*, 2014, **448**, 374–379.
- 3 K. Nogita and K. Une, *J. Nucl. Mater.*, 1997, **250**, 244–249.
- 4 S. R. Qiu, C. Amrhein, M. L. Hunt, R. Pfeffer, B. Yakshinskiy, L. Zhang, T. E. Madey and J. A. Yarmoff, *Appl. Surf. Sci.*, 2001, **181**, 211–224.
- 5 H. Idriss, *Surf. Sci. Rep.*, 2010, **65**, 67–109.
- 6 T. T. Meek, B. Von Roedern, P. G. Clem and R. J. Hanrahan, *Mater. Lett.*, 2005, **59**, 1085–1088.
- 7 T. S. Noggle and J. O. Stiegler, *J. Appl. Phys.*, 1960, **31**, 2199–2208.
- 8 Q. Chen, X. Lai, B. Bai and M. Chu, *Appl. Surf. Sci.*, 2010, **256**, 3047–3050.
- 9 J. Lin, I. Dahan, B. Valderrama and M. V. Manuel, *Appl. Surf. Sci.*, 2014, **301**, 475–480.
- 10 M. M. Strehle, B. J. Heuser, M. S. Elbakhshwan, X. Han, D. J. Gennardo, H. K. Pappas and H. Ju, *Thin Solid Films*, 2012, **520**, 5616–5626.
- 11 R. J. McEachern and P. Taylor, *J. Nucl. Mater.*, 1998, **254**, 87–121.
- 12 A. K. Burrell, T. M. McCleskey, P. Shukla, H. Wang, T. Durakiewicz, D. P. Moore, C. G. Olson, J. J. Joyce and Q. Jia, *Adv. Mater.*, 2007, **19**, 3559–3563.
- 13 B. L. Scott, J. J. Joyce, T. D. Durakiewicz, R. L. Martin, T. M. McCleskey, E. Bauer, H. Luo and Q. Jia, *Coord. Chem. Rev.*, 2014, **266–267**, 137–154.
- 14 H. Pierson, *Handbook of Chemical Vapor Deposition (CVD)*, 1999.
- 15 S. T. Barry, *Coord. Chem. Rev.*, 2013, **257**, 3192–3201.
- 16 F. T. Edelmann, *Chem. Soc. Rev. Chem. Soc. Rev.*, 2012, **41**, 7649–7964.
- 17 B. S. Lim, A. Rahtu, J.-S. Park and R. G. Gordon, *Inorg. Chem.*, 2003, **42**, 7951–7958.
- 18 T. B. Thiede, M. Krasnopolski, A. P. Milanov, T. De Los Arcos, A. Ney, H.-W. Becker, D. Rogalla, J. Winter, A. Devi and R. A. Fischer, *Chem. Mater.*, 2011, **23**, 1430–1440.
- 19 M. Gebhard, M. Hellwig, A. Kroll, D. Rogalla, M. Winter, B. Mallick, A. Ludwig, M. Wiesing, A. D. Wieck, G. Grundmeier, A. Devi, D. Schmeißer, J. R. Weber, J. B. Varley and C. Van de Walle, *Dalton Trans.*, 2017, **38**, 819.
- 20 R. C. Smith, T. Ma, N. Hoilien, L. Y. Tsung, M. J. Bevan, L. Colombo, J. Roberts, S. A. Campbell and W. L. Gladfelter, *Adv. Mater. Opt. Electron.*, 2000, **10**, 105–114.
- 21 Y. Shi and L. Li, *Chem. Soc. Rev.*, 2015, **44**, 2744–2756.
- 22 C. H. Winter, P. H. Sheridan, T. S. Lewkebandara, M. J. Heeg and J. W. Proscialc, *J. Am. Chem. Soc.*, 1992, **114**, 1095–1097.
- 23 Y. Shiokawa, R. Amano, A. Nomura and M. Yagi, *J. Radioanal.*, 1991, **152**, 373–380.
- 24 L. Appel, J. Leduc, C. L. Webster, J. W. Ziller, W. J. Evans and S. Mathur, *Angew. Chem. Int. Ed.*, 2015, **54**, 2209–2213.
- 25 M. D. Straub, S. Hohloch, S. G. Minasian and J. Arnold, *Dalton Trans.*, 2018, **47**, 1772–1776.
- 26 A. L. Catherall, M. S. Hill, A. L. Johnson, G. Kociok-Köhn and M. F. Mahon, *J. Mater. Chem. C*, 2016, **4**, 10731–10739.
- 27 T. Perera, *Wayne State University Dissertation*, 2012.
- 28 M. C. Karunarathne, J. W. Baumann, M. J. Heeg, P. D. Martin and C. H. Winter, *J. Organomet. Chem.*, 2017, **847**, 204–212.

- 29 C. Li, R. K. Thomson, B. Gillon, B. O. Patrick and L. L. Schafer, *Chem. Commun.*, 2003, **98**, 2462.
- 30 M. J. Monreal, R. K. Thomson, T. Cantat, N. E. Travia, B. L. Scott and J. L. Kiplinger, *Organometallics*, 2011, **30**, 2031–2038.
- 31 S. J. Simpson, H. W. Turner and R. A. Andersen, *Inorg. Chem.*, 1981, **20**, 2991–2995.
- 32 SMART: Area Detector Software Package; Bruker Analytical X-ray Systems Inc., Madison, WI, **2003**.
- 33 SADABS: Bruker-Nonius Area Detector Scaling and Absorption, V2.05; Bruker Analytical X-ray Systems Inc., Madison, WI, **2003**.
- 34 G. M. Sheldrick, *Acta Cryst.*, **2007**, *A64*, 112–122.
- 35 C. L. Barnes, *J. Appl. Crystallogr.*, **1997**, *30*, 568–568.
- 36 P. van der Sluis and A. L. Spek, *Acta Cryst.*, **1990**, *A46*, 194–201.

## Chapter 4

# Thorium Amidates Function as Single-Source Molecular Precursors for Thorium Dioxide

## Introduction

The chemistry of the early actinides is currently in a resurgence, with tremendous contributions towards new ligand systems<sup>1-5</sup> and advances in actinide materials.<sup>1,6-13</sup> Research in thorium chemistry is often motivated by the global push for energy production, and thorium-fueled reactors are predicted to offer multiple advantages over conventional uranium dioxide-fueled reactors.<sup>14-17</sup> These include significantly lower production of radiotoxic transuranic elements in the thorium fuel cycle<sup>18</sup> and greater earth-abundance of thorium versus uranium.<sup>19</sup> Despite these advantages, some concerns have been expressed about the possibility of component failure in thorium reactors due to poorly-understood chemical behavior under long-term operating conditions.<sup>14,20</sup> Given that solid-state reactions such as corrosion and deposition typically occur at material interfaces, high surface area actinide nanomaterials, such as thin films and nanoparticles, serve as excellent models for studying these processes in bulk systems such as conventional oxide and mixed oxide (MOX) nuclear fuels.<sup>21-27</sup>

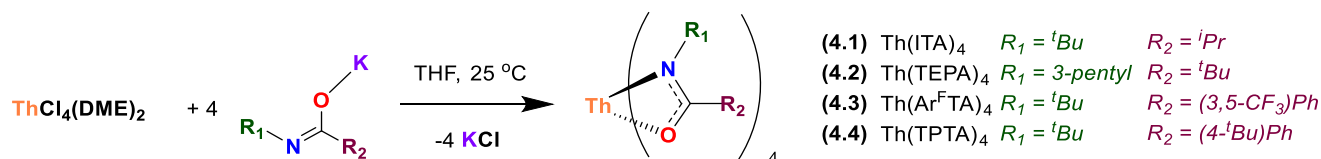
Synthesizing well-defined thorium materials from molecular precursors has proven challenging due to the small pool of known thorium precursors and a limited mechanistic understanding of the conversion processes from actinide molecules to materials.<sup>27-29</sup> To address this gap in knowledge, bespoke precursors can be rationally designed with a readily-accessible decomposition pathway, enabling clean formation of the desired materials through careful control of the chemical behavior of the precursor.<sup>30</sup> In addition to a well-defined decomposition mechanism, ideal precursors for actinide materials should possess adequate thermal stability and volatility, enabling the use of gas-phase methods such as chemical vapor deposition (CVD), atomic layer deposition (ALD), and framework-templated nanoparticle synthesis.<sup>27,30-37</sup> Single-source precursors, which contain all necessary elements for the target material in suitable ratios, are particularly desirable because they avoid the need for reactive secondary gases that can introduce harsh conditions and greater complexity to the decomposition process.<sup>38,39</sup>

As a first step towards satisfying these requirements in thorium precursor design, we turned to amidate ligands, which are formed by deprotonation of organic amides. Due to their significant thermal stability and volatility, metal amidate complexes have been used as molecular precursors for metal oxide film deposition, yielding phase-pure films through a well-defined decomposition pathway.<sup>39-41</sup> While there is some precedent for uranium amidates,<sup>39,42-44</sup> no homoleptic thorium amidates have been reported. Here we describe the synthesis of homoleptic thorium amidate complexes as single-source molecular precursors to ThO<sub>2</sub> and describe the mechanism of their thermal decomposition to ThO<sub>2</sub>.

## Results and Discussion

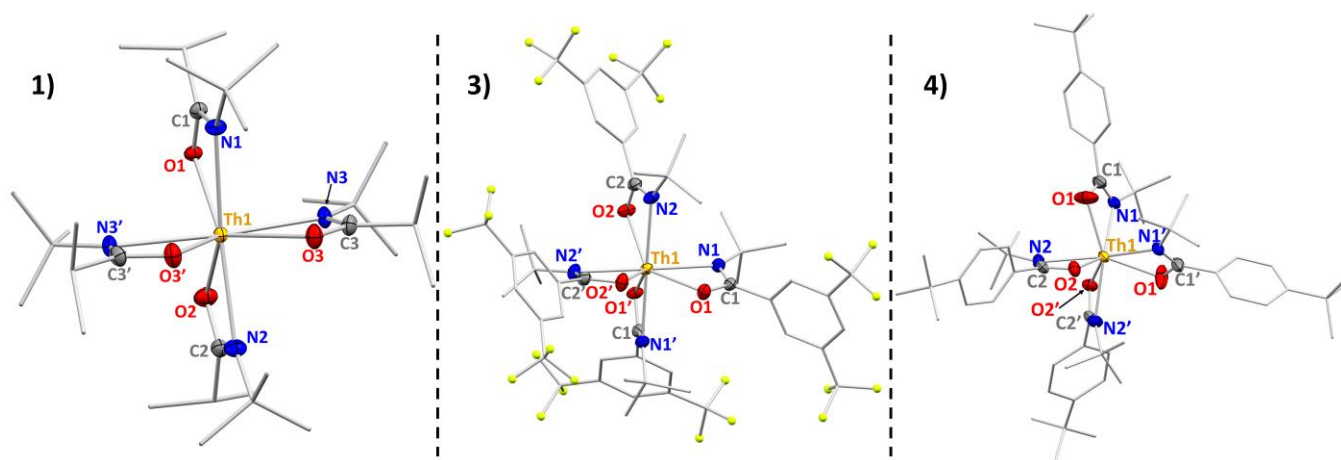
Deprotonation of the amides *N*-*tert*-butylisobutyramide (H(ITA)), *N*-*tert*-butyl-(4-*tert*-butyl)benzamide (H(TPTA)), *N*-(3-pentyl)pivalamide (H(TEPA)), and *N*-*tert*-butyl-(3,5-bis(trifluoromethyl))benzamide (H(Ar<sup>F</sup>TA)) with KN(SiMe<sub>3</sub>)<sub>2</sub> in THF yielded the corresponding potassium amidate salts as colorless powders. The homoleptic thorium amidate complexes Th(ITA)<sub>4</sub> (**4.1**), Th(TEPA)<sub>4</sub> (**4.2**), Th(Ar<sup>F</sup>TA)<sub>4</sub> (**4.3**), and Th(TPTA)<sub>4</sub> (**4.4**) were synthesized via salt metathesis reactions between ThCl<sub>4</sub>(DME)<sub>2</sub> and four equivalents of potassium amidate in THF (Scheme 1) and isolated as colorless, air-sensitive crystals.





**Scheme 4.1:** Synthesis of homoleptic thorium amidate complexes (4.1–4.4).

Single crystal X-ray crystallographic data for **4.1**, **4.3**, and **4.4** revealed these complexes to be 8-coordinate with all four amidate ligands binding in a  $\kappa^2\text{-O,N}$  geometry; this ligand coordination mode has also been observed in transition metal<sup>40,41,45</sup> and uranium<sup>39,42,43</sup> complexes (Figure 4.1). Complexes **4.1** and **4.3** adopt pseudo- $D_{2d}$  structural geometries, with two sets of amidate ligands related by approximate mirror symmetry, whereas **4.4** displays a lower-symmetry pseudo- $S_4$  dodecahedral geometry. The four N atoms in **4.3** lie in a square plane relative to the Th center, while there is a distortion of the N atoms from this plane in **4.1** and **4.4**. Solid-state structures of **4.1**, **4.3**, and **4.4** show Th–O and Th–N bond ranges of 2.331(3)–2.444(2) and 2.522(7)–2.565(2) Å, respectively (Table S2). Within the amidate ligands, the O–C–N angles ranged from 114.9(7)–118.0(9)°, and the C–O and C–N bond lengths ranged from 1.301(3)–1.315(7) and 1.255(9)–1.303(6) Å. These metrical parameters are comparable to reported values for structurally similar uranium amidate complexes.<sup>39,42</sup> Attempts to solve the solid-state structure of **4.2** were unsuccessful due to ligand disorder.

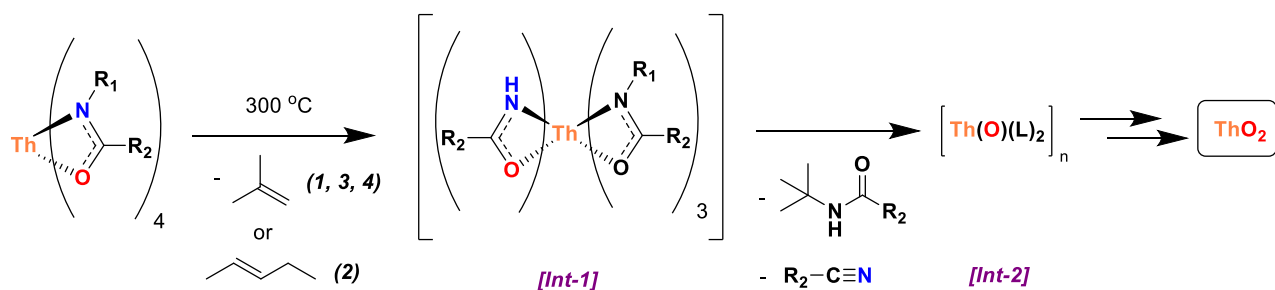


**Figure 4.1:** X-ray crystal structures of **4.1** (left), **4.3** (center), and **4.4** (right) with 50% probability ellipsoids. Hydrogen atoms are omitted, and amidate substituents are represented as capped sticks for clarity.

All four complexes (**4.1–4.4**) could be vaporized by heating under atmospheric pressure. Sublimation of the bis(alkyl) amidates **4.1** and **4.2** was observed at 261 °C and 190 °C, respectively, with no sign of decomposition. Compound **4.4** sublimed at 220 °C, although a small amount of amide was also identified in the sublimate, indicating simultaneous sublimation and gradual decomposition at this temperature. The fluorinated amidate **4.3** melted at 148 °C and vaporized readily at higher temperatures. Compound **4.3** was thus the most volatile, despite having the

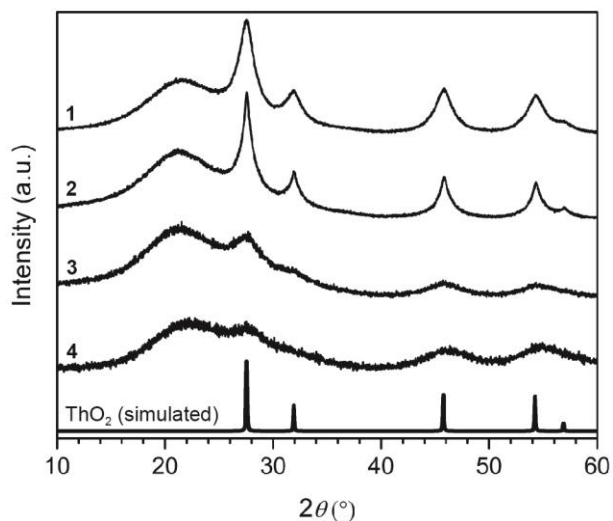
highest molecular weight of the four complexes. This can most likely be attributed to weak intermolecular interactions in **4.3** as a function of low dispersion forces between fluorinated substituents.<sup>31</sup>

To study the mechanism of decomposition of these precursors to ThO<sub>2</sub>, solid samples of **4.1-4.4** were heated to 300 °C in sealed NMR tubes under nitrogen. This procedure was sufficient to decompose **4.1**, **4.3**, and **4.4**; however, **4.2** did not decompose in the solid-state at this temperature even after heating for one week. The higher decomposition temperature of **4.2** is likely due to the increased kinetic barrier of alkene elimination from a secondary alkyl vs. a tertiary alkyl substituent.<sup>46</sup> However, slight decomposition of **4.2** was observed by heating a d<sub>18</sub>-decalin solution of **4.2** to 240 °C for 2 weeks. Based on our previous results with related uranium amidate through an alkene elimination mechanism (Scheme 4.2). Indeed, NMR studies of the decomposition products provided strong evidence for this mechanism: clean formation of the expected alkene, amide, and nitrile products were observed for all four species (Figures 4.5-4.9).



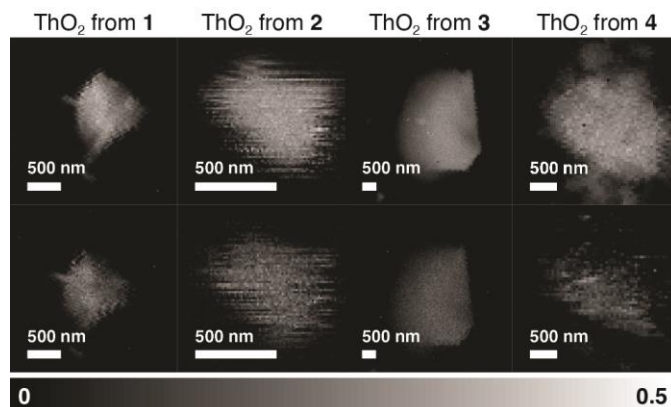
**Scheme 4.2:** Proposed decomposition mechanism for complexes **4.1-4.4**. Alkene, amide, and nitrile byproducts were observed directly by <sup>1</sup>H NMR spectroscopy. Intermediate decomposition products **Int-1** and **Int-2** are postulated.

Preliminary tests of the viability of complexes **4.1-4.4** as single-source precursors to ThO<sub>2</sub> were conducted by pyrolyzing the samples in quartz tubes sealed under a nitrogen atmosphere. Analysis using powder X-ray diffraction (PXRD) confirmed that pyrolysis of all four precursors produced ThO<sub>2</sub> (Figure 4.2). Qualitatively, the presence of sharper diffraction peaks for the ThO<sub>2</sub> products prepared from **4.1** and **4.2** relative to **4.3** and **4.4** suggested greater crystallinity of the ThO<sub>2</sub> prepared from C-alkyl amidates relative to C-aryl amidates.

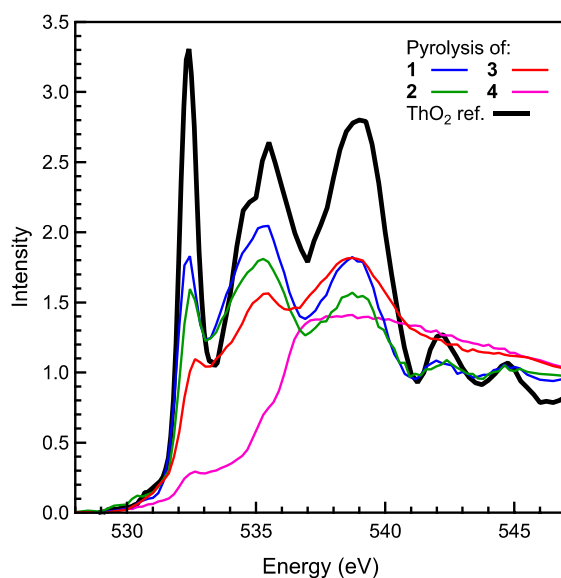


**Figure 4.2:** Powder X-ray diffraction patterns of the products formed by pyrolysis of **4.1-4.4** compared with a  $\text{ThO}_2$  simulation.

To probe chemical purity, oxygen K-edge X-ray absorption spectroscopy was performed with a scanning transmission X-ray microscope (STXM-XAS). Figure 4.3 shows a selection of elemental maps obtained from representative particles, demonstrating homogenous distributions of O and Th on the micron scale. Averaged O K-edge XAS data obtained from multiple micron-scale particles are compared with a reference spectrum of pure  $\text{ThO}_2$  in Figure 4.4.<sup>27,47</sup> The overall spectral profiles for the  $\text{ThO}_2$  prepared from precursors **4.1** and **4.2** agreed well with the  $\text{ThO}_2$  reference data, with similar intense features found in all three spectra at low energies (532.4, 535.5, 539.0 eV) and high energies (542.3, 544.7 eV). The O K-edge spectrum obtained for  $\text{ThO}_2$  prepared from the C-aryl amidate precursor **4.3** also exhibited features that were characteristic of  $\text{ThO}_2$ , however, the weaker relative intensities and disappearance of high-energy features suggested that other oxygen-containing impurities were present in the sample. An even more significant deviation from the  $\text{ThO}_2$  reference was observed in the O K-edge XAS for  $\text{ThO}_2$  from **4.4**, which showed signatures of  $\text{ThO}_2$  that were barely discernable from other absorptions. Taken together with the PXRD results described above, the O K-edge XAS data suggest that  $\text{ThO}_2$  samples prepared from the C-alkyl amidates **4.1** and **4.2** had both higher crystallinity and greater compositional purity than the  $\text{ThO}_2$  samples prepared from the C-aryl amidates **4.3** and **4.4**.



**Figure 4.3:** Representative elemental difference maps of micron-scale  $\text{ThO}_2$  particles formed by pyrolysis of **4.1-4.4** that were used to obtain X-ray absorption spectra. Lighter regions in the elemental maps correspond to greater concentration of the absorbing atom and were obtained by subtraction of two images: one taken at an energy just below the X-ray absorption edge and another taken at the absorption maximum.



**Figure 4.4:** Plot comparing the O K-edge XAS for the  $\text{ThO}_2$  products obtained by pyrolysis of thorium amidates **4.1-4.4** and a  $\text{ThO}_2$  reference.

## Summary and Conclusions

In conclusion, we have synthesized the first homoleptic thorium amidate complexes and demonstrated their viability as single-source molecular precursors to  $\text{ThO}_2$  materials. All complexes displayed sufficient volatility for metal-organic chemical vapor deposition and could be readily sublimed under partial vacuum and atmospheric pressures. Preliminary thermal decomposition studies showed that the complexes can all undergo an alkene elimination

mechanism to yield ThO<sub>2</sub> without the need for an external oxygen source; however, differences in the PXRD and STXM-XAS suggest that ligand substitution can be modified to improve crystallinity and compositional purity. Along these lines, metal-organic chemical vapor decomposition of the most promising C-alkyl amidates **4.1** and **4.2** and in-depth characterization of the as-formed ThO<sub>2</sub> materials is the subject of ongoing work.

## Experimental

### Materials and Methods

Unless otherwise noted, all syntheses were performed using standard Schlenk techniques under an atmosphere of nitrogen or in an MBraun glovebox under an atmosphere of nitrogen. Glassware, cannulae, and Celite were stored in an oven at 160 °C for at least 12 hours prior to use. 3 Å and 4 Å molecular sieves were activated by heating under vacuum at 300 °C for 24 hours. <sup>1</sup>H, <sup>13</sup>C, and <sup>19</sup>F NMR spectra were recorded at room temperature using Bruker AV-600, AV-500, AVB-400, AVQ-400, and AV-300 spectrometers. <sup>1</sup>H chemical shifts were referenced to C<sub>6</sub>D<sub>5</sub>H (δ = 7.16 ppm), C<sub>5</sub>D<sub>4</sub>HN (δ<sub>1</sub> = 8.74 ppm), and CHCl<sub>3</sub> (δ = 7.26 ppm). <sup>13</sup>C chemical shifts were referenced to C<sub>6</sub>D<sub>6</sub> (δ = 128.39 ppm) and C<sub>5</sub>D<sub>5</sub>N (δ<sub>1</sub> = 150.35 ppm). <sup>19</sup>F chemical shifts were referenced to an external standard of C<sub>6</sub>H<sub>5</sub>F (δ = -113.11 ppm). Samples for IR spectroscopy were prepared as Nujol mulls, and spectra were taken in KBr plates using a Nicolet iS10 spectrometer. Melting points were determined in sealed tubes under an atmosphere of nitrogen using a Stanford Research Systems OptiMelt instrument and are reported uncorrected.

Hexane, pentane, toluene, benzene, diethyl ether, and tetrahydrofuran (THF) were purified by passage through a column of activated alumina and degassed by sparging with nitrogen. C<sub>6</sub>D<sub>6</sub> was purchased from Cambridge Isotope Labs, degassed with two freeze-pump-thaw cycles, and stored over 4 Å molecular sieves. C<sub>5</sub>D<sub>5</sub>N was purchased from Cambridge Isotope Labs and stored over 3 Å molecular sieves. d<sub>18</sub>-Decalin was purchased from Sigma-Aldrich and stored over 4 Å molecular sieves. CDCl<sub>3</sub> was purchased from Cambridge Isotope Labs and used as received. The amide proligands *N*-*tert*-butylisobutyramide (H(ITA)), *N*-*tert*-butyl-(4-*tert*-butyl)benzamide (H(TPTA)), *N*-(3-pentyl)pivalamide (H(TEPA)), and *N*-*tert*-butyl-(3,5-bis(trifluoromethyl))benzamide (H(Ar<sup>F</sup>TA)) were synthesized according to literature methods<sup>39,45,48,49</sup> and purified by sublimation. ThCl<sub>4</sub>(DME)<sub>2</sub> was synthesized according to literature procedures.<sup>50</sup> Unless otherwise specified, all other chemicals were purchased from Sigma-Aldrich or Acros Organics and used as received.

### Synthesis of Compounds

**K(ITA):** A THF solution (20 mL) of KN(SiMe<sub>3</sub>)<sub>2</sub> (2.22 g, 11.1 mmol) was added via cannula to a stirred THF solution (40 mL) of H(ITA) (1.52 g, 10.6 mmol) maintained at -78 °C. After stirring at room temperature for 16 h, the solvent was removed *in vacuo* to give an off-white powder. This powder was washed with toluene (15 mL), then hexane (30 mL) to remove impurities, and then triturated with hexane and dried *in vacuo* to give the product as a colorless powder. (1.66 g, 86% yield)

<sup>1</sup>H NMR (C<sub>5</sub>D<sub>5</sub>N, 500 MHz): δ 2.89 (m, 1H, CH(CH<sub>3</sub>)<sub>2</sub>), 1.82 (s, 9H, C(CH<sub>3</sub>)<sub>3</sub>), 1.46 (d, 6H, CH(CH<sub>3</sub>)<sub>2</sub>).

$^{13}\text{C}$  NMR ( $\text{C}_5\text{D}_5\text{N}$ , 101 MHz):  $\delta$  176.61 (NCO), 51.69 ( $\text{C}(\text{CH}_3)_3$ ), 39.82 ( $\text{CH}(\text{CH}_3)_2$ ), 32.39 ( $\text{C}(\text{CH}_3)_3$ ), 23.10 ( $\text{CH}(\text{CH}_3)_2$ ).

IR ( $\text{cm}^{-1}$ ): 1575 (m), 1557 (m), 1544 (m), 1336 (m), 1306 (w), 1282 (w), 1070 (m), 949 (w), 907 (w), 891 (w), 774 (w), 654 (w), 501 (w).

**K(TEPA):** A THF solution (50 mL) of  $\text{KN}(\text{SiMe}_3)_2$  (4.90 g, 24.6 mmol) was added via cannula to a stirred THF solution (60 mL) of H(TEPA) (4.11 g, 23.9 mmol) maintained at  $-78\text{ }^\circ\text{C}$ . The resulting solution was slowly warmed to room temperature and stirred for 16 h, then the solvent was removed *in vacuo* to give an off-white powder. This powder was washed with hexane (30 mL) to remove impurities, then dried *in vacuo* to give the product as a colorless powder. (4.91 g, 98% yield)

$^1\text{H}$  NMR ( $\text{C}_5\text{D}_5\text{N}$ , 400 MHz):  $\delta$  4.15 (m, 1H,  $\text{CH}(\text{CH}_2\text{CH}_3)_2$ ), 1.81 (m, 4H,  $\text{CH}(\text{CH}_2\text{CH}_3)_2$ ), 1.64 (s, 9H,  $\text{C}(\text{CH}_3)_3$ ), 1.18 (t, 6H,  $\text{CH}(\text{CH}_2\text{CH}_3)_2$ ).

$^{13}\text{C}$  NMR ( $\text{C}_5\text{D}_5\text{N}$ , 151 MHz):  $\delta$  177.31 (NCO), 56.88 ( $\text{C}(\text{CH}_3)_3$ ), 39.89 ( $\text{CHCH}_2\text{CH}_3$ ), 31.42 ( $\text{C}(\text{CH}_3)_3$ ), 31.13 ( $\text{CHCH}_2\text{CH}_3$ ), 12.49 ( $\text{CHCH}_2\text{CH}_3$ ).

IR ( $\text{cm}^{-1}$ ): 1534 (s), 1486 (m), 1387 (m), 1341 (m), 1327 (m), 1313 (m), 1213 (m), 1154 (w), 1122 (w), 1029 (w), 910 (w), 860 (w), 776 (w), 577 (w), 554 (w), 529 (w).

**K(TPTA):** A THF solution (100 mL) of  $\text{KN}(\text{SiMe}_3)_2$  (7.52 g, 37.7 mmol) was added via cannula to a stirred THF solution (150 mL) of H(TPTA) (8.00 g, 34.3 mmol) maintained at  $-78\text{ }^\circ\text{C}$ . The resulting solution was slowly warmed to room temperature and stirred for 16 h, then the solvent was removed *in vacuo* to give an off-white powder. This powder was washed twice with  $\text{Et}_2\text{O}$  (30 mL) to remove impurities, then dried *in vacuo* to give the product as a colorless powder. (8.62 g, 93% yield)

$^1\text{H}$  NMR ( $\text{C}_5\text{D}_5\text{N}$ , 400 MHz):  $\delta$  8.66 (d, 2H, Ph-H), 7.36 (d, 2H, Ph-H), 1.88 (s, 9H,  $\text{C}(\text{CH}_3)_3$ ), 1.25 (s, 9H,  $\text{C}(\text{CH}_3)_3$ ).

$^{13}\text{C}$  NMR ( $\text{C}_5\text{D}_5\text{N}$ , 151 MHz):  $\delta$  150.35 (NCO), 129.51 (Ph), 124.44 (Ph), 52.03 ( $\text{NC}(\text{CH}_3)_3$ ), 34.48 ( $\text{PhC}(\text{CH}_3)_3$ ), 32.73 ( $\text{NC}(\text{CH}_3)_3$ ), 29.61 ( $\text{PhC}(\text{CH}_3)_3$ ). Two additional resonances corresponding to the phenyl carbons are obscured by the resonances from residual pyridine.

IR ( $\text{cm}^{-1}$ ): 1577 (m), 1544 (m), 1336 (m), 1267 (w), 1230 (w), 1211 (w), 1139 (w), 1105 (w), 1013 (w), 881 (w), 855 (w), 725 (w), 712 (w).

**K(Ar<sup>F</sup>TA):** A THF solution (30 mL) of  $\text{KN}(\text{SiMe}_3)_2$  (0.86 g, 4.37 mmol) was added via cannula to a stirred THF solution (50 mL) of H(Ar<sup>F</sup>TA) (1.31 g, 4.17 mmol) maintained at  $-78\text{ }^\circ\text{C}$ . The resulting solution was slowly warmed to room temperature and stirred for 16 h, then the solvent was removed *in vacuo* to give an off-white powder. This powder was washed with hexane (50 mL) to remove impurities, then dried *in vacuo* to give the product as a colorless powder. (1.28 g, 87% yield)

$^1\text{H}$  NMR ( $\text{C}_5\text{D}_5\text{N}$ , 600 MHz):  $\delta$  9.33 (s, 2H, Ph-H), 7.85 (s, 1H, Ph-H), 1.88 (s, 9H,  $\text{C}(\text{CH}_3)_3$ ).

$^{13}\text{C}$  NMR ( $\text{C}_5\text{D}_5\text{N}$ , 151 MHz):  $\delta$  162.78 (NCO), 150.84 (Ph), 129.76 (q, Ph-CF<sub>3</sub>), 129.38 (Ph), 126.22 (q, Ph-CF<sub>3</sub>), 120.21 (Ph), 52.52 ( $\text{C}(\text{CH}_3)_3$ ), 32.02 ( $\text{C}(\text{CH}_3)_3$ ).

$^{19}\text{F}$  NMR ( $\text{C}_5\text{D}_5\text{N}$ , 565 MHz):  $\delta$  -63.60 (CF<sub>3</sub>).

IR ( $\text{cm}^{-1}$ ): 1622 (w), 1560 (m), 1353 (w), 1308 (m), 1282 (s), 1247 (w), 1170 (m), 1122 (m), 936 (w), 905 (w), 889 (w), 844 (w), 795 (w), 774 (w), 710 (w), 695 (w), 682 (m).

**Th(ITA)<sub>4</sub> (4.1):** A THF solution (2 mL) of ThCl<sub>4</sub>(DME)<sub>2</sub> (138 mg, 0.250 mmol) was added dropwise to a THF solution (6 mL) of K(ITA) (181 mg, 0.999 mmol). The colorless solution turned cloudy over the course of the reaction. The solution was stirred for 3 d, then the solvent was removed *in vacuo* and the product was extracted into Et<sub>2</sub>O (3 mL). The resulting colorless solution was filtered to remove insoluble KCl, concentrated to 1 mL, and cooled to -40 °C, yielding colorless crystals (113 mg, 57% yield).

<sup>1</sup>H NMR (C<sub>6</sub>D<sub>6</sub>, 600 MHz): δ 2.70 (m, 4H, CH(CH<sub>3</sub>)<sub>2</sub>), 1.35 (s, 36H, C(CH<sub>3</sub>)<sub>3</sub>), 1.21 (d, 24H, CH(CH<sub>3</sub>)<sub>2</sub>).

<sup>13</sup>C NMR (C<sub>6</sub>D<sub>6</sub>, 151 MHz): δ 186.84 (NCO), 51.74 (NC(CH<sub>3</sub>)<sub>3</sub>), 34.39 (CC(CH<sub>3</sub>)<sub>3</sub>), 31.69 (NC(CH<sub>3</sub>)<sub>3</sub>), 19.76 (CC(CH<sub>3</sub>)<sub>3</sub>).

IR (cm<sup>-1</sup>): 1544 (m), 1491 (w), 1389 (m), 1365 (m), 1345 (m), 1301 (m), 1210 (m), 1070 (m), 1036 (w), 1012 (m), 919 (w), 894 (w), 815 (w), 746 (w), 644 (w), 586 (w).

EA calcd for C<sub>32</sub>H<sub>64</sub>N<sub>4</sub>O<sub>4</sub>Th: C: 47.99%, H: 8.05%, N: 7.00%. Found: C: 47.83%, H: 8.06%, N: 6.81%.

Sublimation point: 261 °C.

**Th(TEPA)<sub>4</sub> (4.2):** A THF solution (3 mL) of ThCl<sub>4</sub>(DME)<sub>2</sub> (303 mg, 0.548 mmol) was added dropwise to a THF solution (10 mL) of K(TEPA) (459 mg, 2.19 mmol). The colorless solution turned cloudy over the course of the reaction. The solution was stirred for 3 d, then the solvent was removed *in vacuo* and the resulting solids were triturated with hexane (3 mL). The product was extracted into Et<sub>2</sub>O (10 mL) then the resulting colorless solution was filtered to remove insoluble KCl, concentrated to 5 mL, and cooled to -40 °C, yielding colorless crystals (399 mg, 80% yield).

<sup>1</sup>H NMR (C<sub>6</sub>D<sub>6</sub>, 400 MHz): δ 3.80 (m, 4H, CH(CH<sub>2</sub>CH<sub>3</sub>)<sub>2</sub>), 1.85 and 1.76 (dm, 16H, CH(CH<sub>2</sub>CH<sub>3</sub>)<sub>2</sub>), 1.30 (s, 36H, C(CH<sub>3</sub>)<sub>3</sub>), 1.05 (t, 24H, CH(CH<sub>2</sub>CH<sub>3</sub>)<sub>2</sub>).

<sup>13</sup>C NMR (C<sub>6</sub>D<sub>6</sub>, 151 MHz): δ 185.64 (NCO), 60.21 (C(CH<sub>3</sub>)<sub>3</sub>), 41.27 (CHCH<sub>2</sub>CH<sub>3</sub>), 29.87 (CHCH<sub>2</sub>CH<sub>3</sub>), 29.07 (C(CH<sub>3</sub>)<sub>3</sub>), 12.55 (CHCH<sub>2</sub>CH<sub>3</sub>).

IR (cm<sup>-1</sup>): 1588 (w), 1524 (s), 1491 (w), 1476 (m), 1403 (m), 1363 (m), 1336 (s), 1310 (w), 1208 (m), 1162 (w), 1141 (m), 1051 (m), 1017 (w), 922 (w), 872 (w), 852 (w), 802 (w), 746 (w), 606 (m), 587 (m).

EA calcd for C<sub>40</sub>H<sub>80</sub>N<sub>4</sub>O<sub>4</sub>Th: C: 52.61%, H: 8.83%, N: 6.14%. Found: 52.33%, H: 8.99%, N: 6.05%.

Sublimation point: 190 °C.

**Th(Ar<sup>F</sup>TA)<sub>4</sub> (4.3):** A THF solution (1 mL) of ThCl<sub>4</sub>(DME)<sub>2</sub> (57 mg, 0.103 mmol) was added dropwise to a THF solution (3 mL) of K(Ar<sup>F</sup>TA) (145 mg, 0.413 mmol). The colorless solution turned cloudy over the course of the reaction. The solution was stirred for 3 d, then the solvent was removed *in vacuo* and the product was extracted into hexane (10 mL). The resulting colorless solution was filtered to remove insoluble KCl, concentrated to 5 mL, and cooled to -40 °C, yielding colorless crystals (81 mg, 56% yield).

<sup>1</sup>H NMR (C<sub>6</sub>D<sub>6</sub>, 600 MHz): δ 7.95 (s, 8H, Ph-H), 7.66 (s, 4H, Ph-H), 1.16 (s, 36H, C(CH<sub>3</sub>)<sub>3</sub>).

<sup>13</sup>C NMR (C<sub>6</sub>D<sub>6</sub>, 151 MHz): δ 175.97 (NCO), 142.49 (Ph), 132.50 (q, Ph-CF<sub>3</sub>), 127.13 (Ph), 124.64 (q, Ph-CF<sub>3</sub>), 123.23 (Ph), 54.28 (C(CH<sub>3</sub>)<sub>3</sub>), 32.41 (C(CH<sub>3</sub>)<sub>3</sub>).

<sup>19</sup>F NMR (C<sub>6</sub>D<sub>6</sub>, 565 MHz): δ -63.36 (CF<sub>3</sub>).

IR (cm<sup>-1</sup>): 1621 (w), 1544 (w), 1328 (m), 1279 (m), 1217 (w), 1183 (m), 1146 (m), 903 (w), 845 (w), 794 (w), 682 (w), 599 (w).

EA calcd for C<sub>52</sub>H<sub>48</sub>F<sub>24</sub>N<sub>4</sub>O<sub>4</sub>Th: C: 42.17%, H: 3.27%, N: 3.78%. Found: C: 42.07%, H: 3.04%, N: 3.73%.

Melting point: 148-150 °C; vaporizes slowly above 150 °C.

**Th(TPTA)<sub>4</sub> (4.4):** A THF solution (1 mL) of ThCl<sub>4</sub>(DME)<sub>2</sub> (48 mg, 0.086 mmol) was added dropwise to a THF solution (3 mL) of K(TPTA) (93 mg, 0.344 mmol). The colorless solution turned cloudy over the course of the reaction. The solution was stirred for 3 d, then the solvent was removed *in vacuo* and the product was extracted into hexane (5 mL). The resulting colorless solution was filtered to remove insoluble KCl, concentrated to 1 mL, and cooled to -40 °C, yielding colorless crystals (85 mg, 85% yield).

<sup>1</sup>H NMR (C<sub>6</sub>D<sub>6</sub>, 400 MHz): δ 7.61 (d, 8H, Ph-*H*), 7.27 (d, 8H, Ph-*H*), 1.53 (s, 36H, C(CH<sub>3</sub>)<sub>3</sub>), 1.18 (s, 36H, C(CH<sub>3</sub>)<sub>3</sub>).

<sup>13</sup>C NMR (C<sub>6</sub>D<sub>6</sub>, 151 MHz): δ 179.76 (NCO), 151.36 (*PhCO*), 138.84 (*Ph*), 126.68 (*Ph*), 125.19 (*PhCC*), 53.49 (NC(CH<sub>3</sub>)<sub>3</sub>), 34.67 (PhC(CH<sub>3</sub>)<sub>3</sub>), 32.74 (NC(CH<sub>3</sub>)<sub>3</sub>), 31.36 (PhC(CH<sub>3</sub>)<sub>3</sub>).

IR (cm<sup>-1</sup>): 1682 (w), 1643 (w), 1611 (w), 1548 (m), 1525 (w), 1364 (m), 1269 (w), 1223 (w), 1148 (w), 1117 (w), 1105 (w), 1036 (w), 985 (m), 920 (w), 845 (m), 812 (w), 767 (w), 752 (w), 652 (w), 577 (w), 540 (w).

EA calcd for C<sub>60</sub>H<sub>88</sub>N<sub>4</sub>O<sub>4</sub>Th: C: 62.05%, H: 7.64%, N: 4.82%. Found: C: 61.97%, H: 7.59%, N: 4.78%.

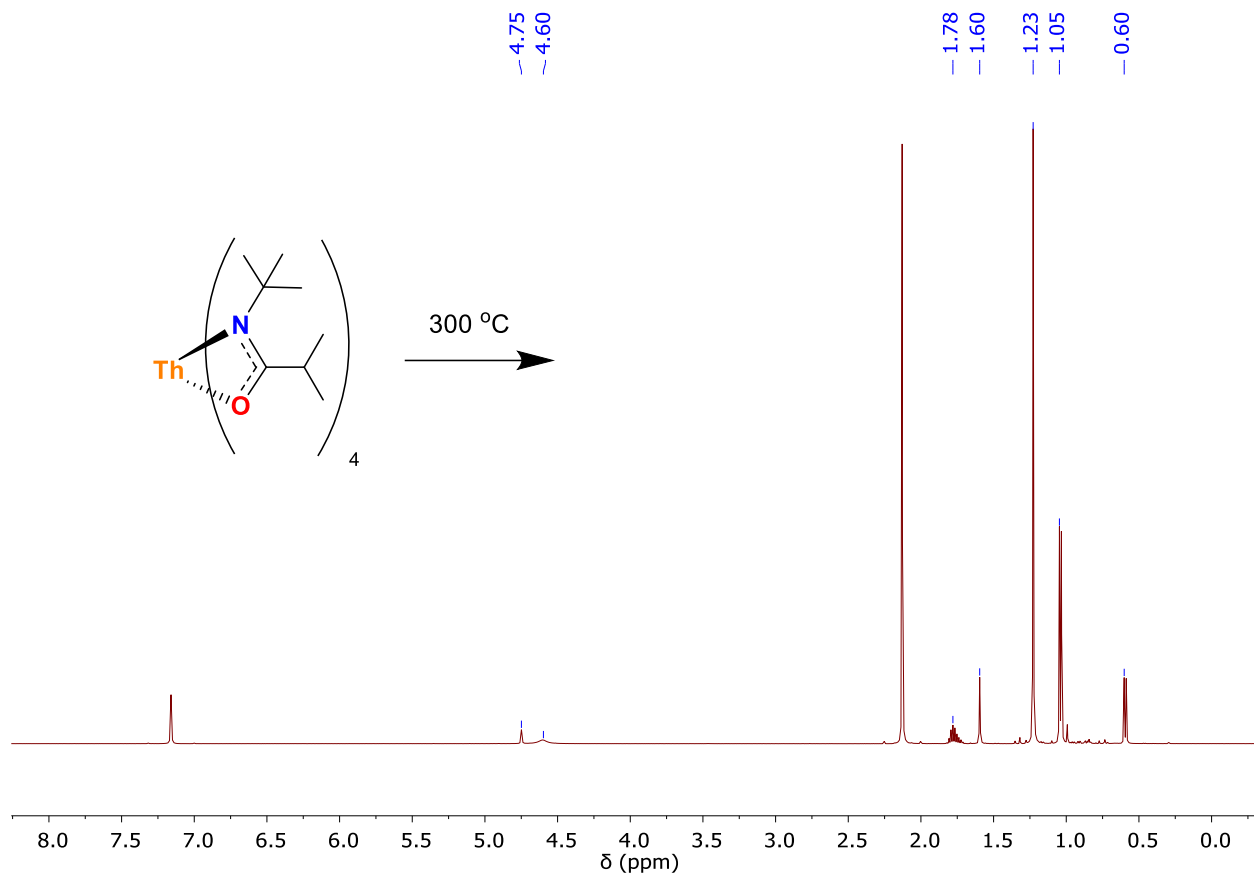
Sublimation point: 220 °C; minor decomposition is also observed.

### NMR Decomposition Studies

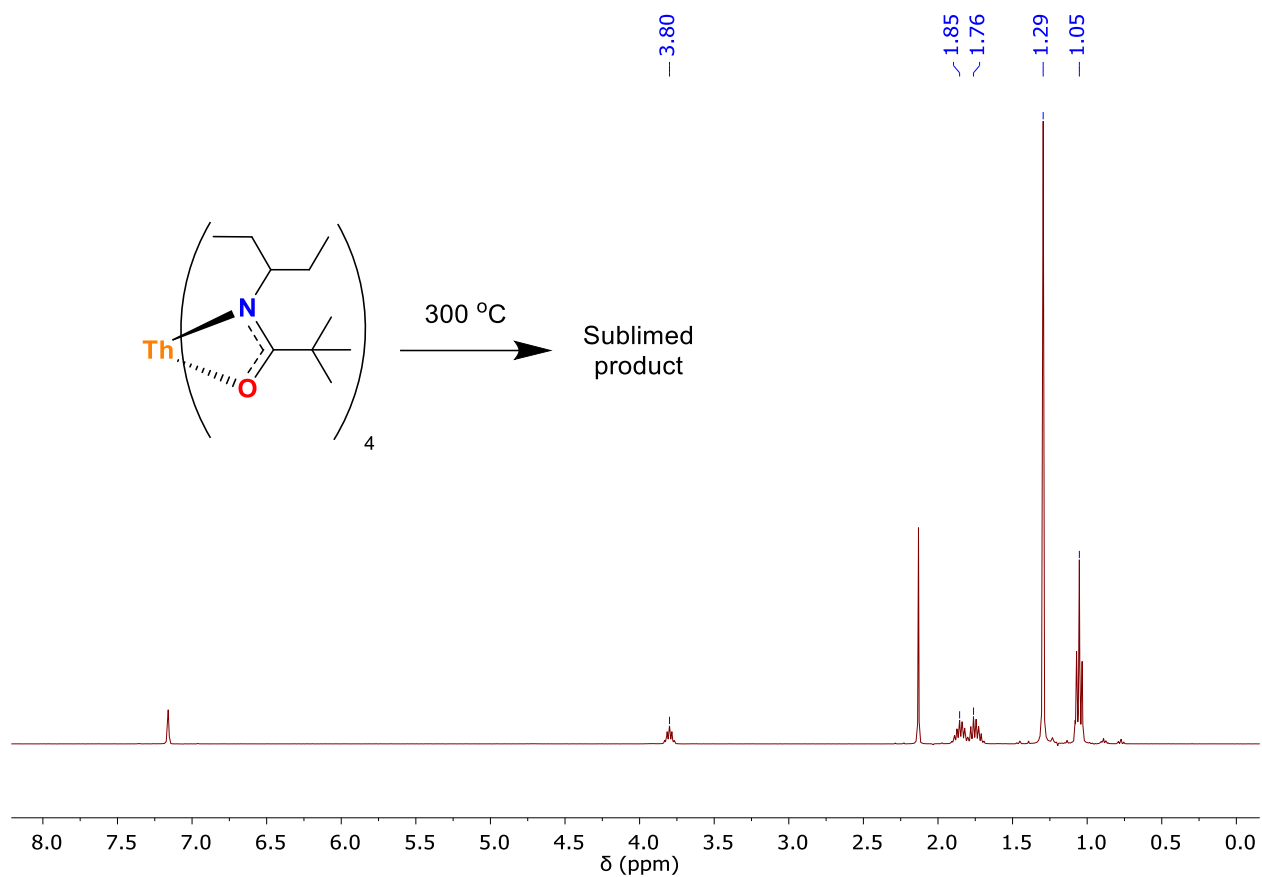
Compounds **4.1-4.4** (10 mg each) were added to separate J. Young NMR tubes inside a nitrogen glovebox. The tubes were sealed and brought out of the glovebox and heated to 300 °C in an aluminum heating block for 16 h. After cooling down to room temperature, the tubes were brought back into the glovebox and placed into a liquid nitrogen-cooled cold well for 15 minutes to condense volatile decomposition products. A solution of hexamethylbenzene (1.0 mg) in C<sub>6</sub>D<sub>6</sub> (0.50 mL) was quickly added to each tube, then the tubes were capped and allowed to warm to room temperature before collecting NMR spectra.

As compound **4.2** was observed to sublime completely when heated as a solid, decomposition was achieved by heating a solution of **4.2** (10 mg) in d<sub>18</sub>-decalin (mixture of *cis* and *trans* isomers) at 240 °C for 2 weeks. Although only partial decomposition was observed over this timeframe, the decomposition products were detectable by <sup>1</sup>H NMR, and their identities were confirmed by spiking the solution with H(TEPA), pivalonitrile, and 2-pentene.

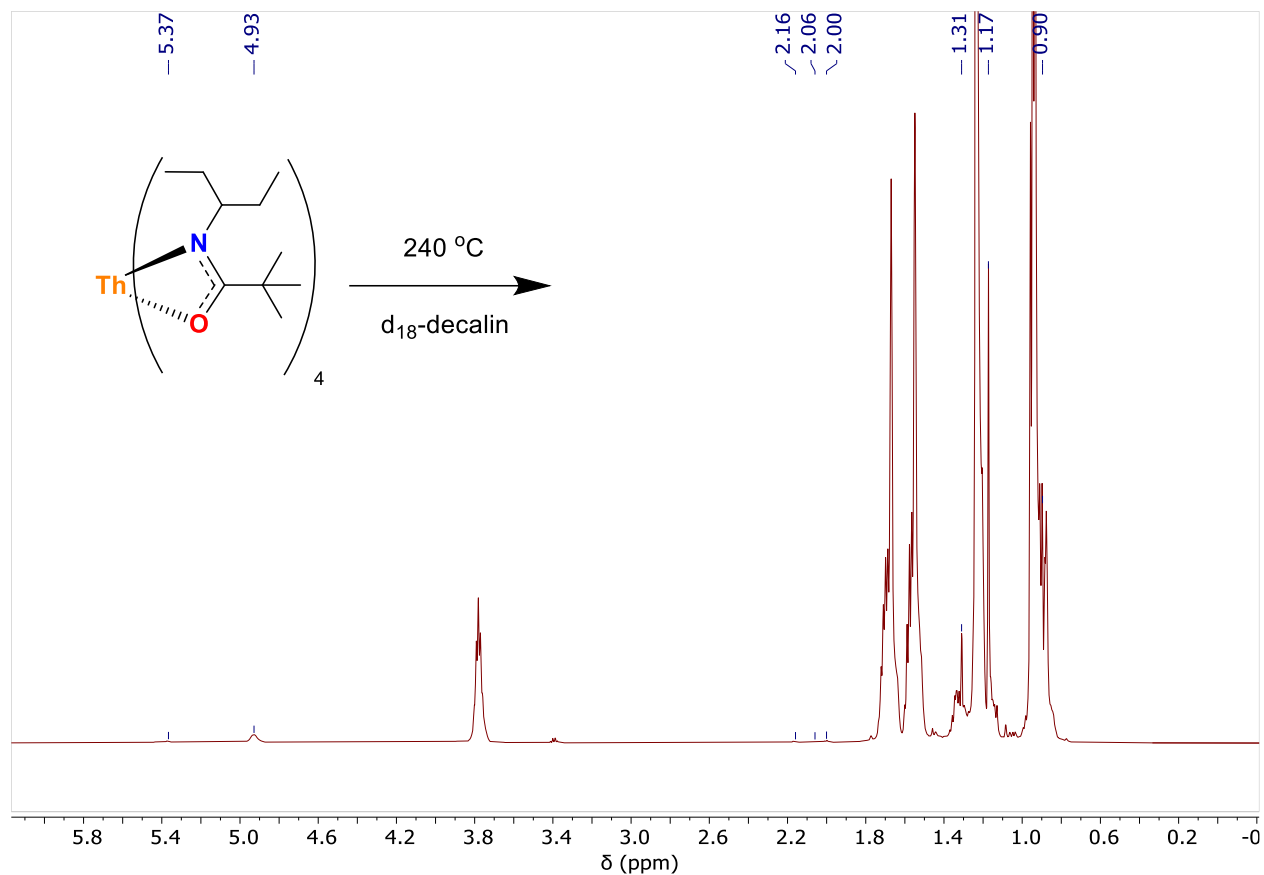




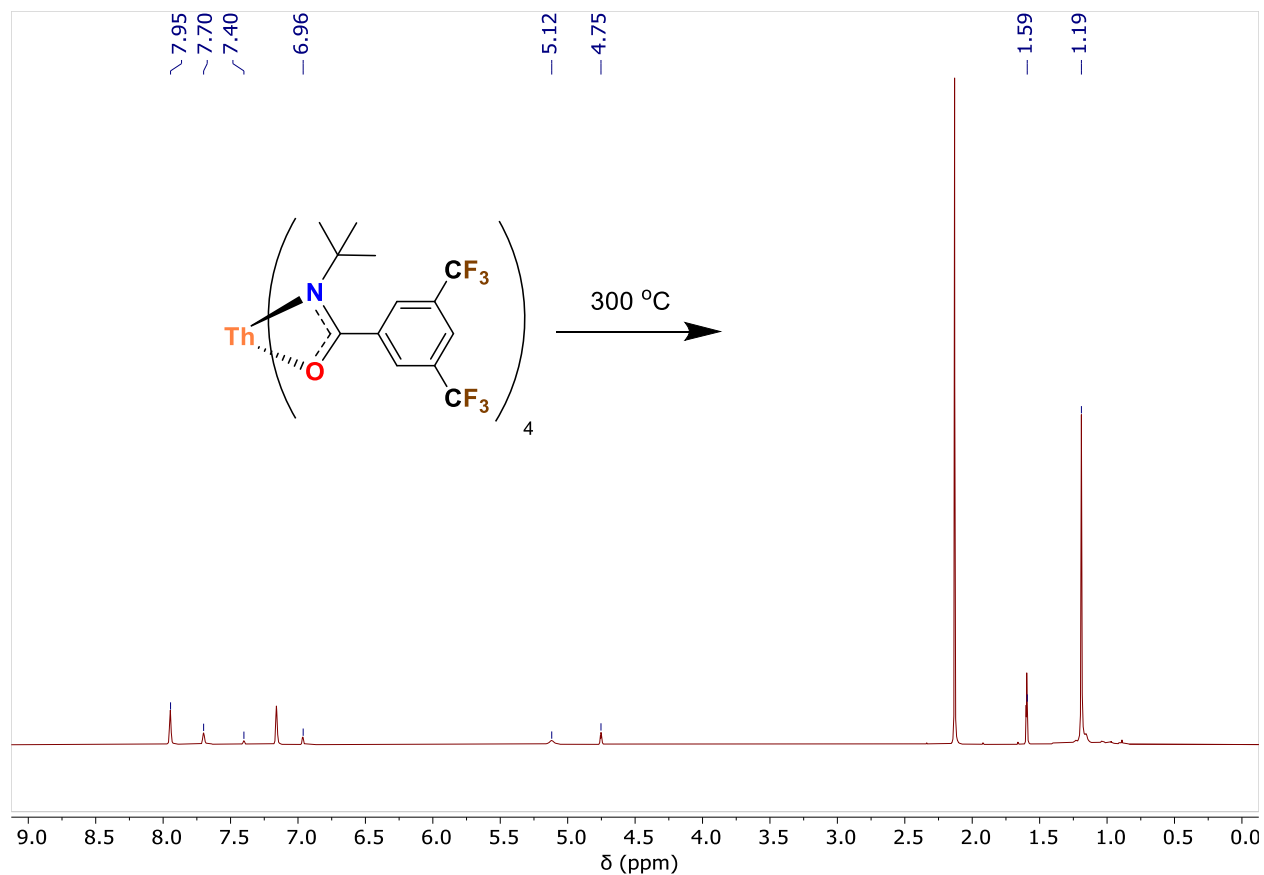
**Figure 4.5:**  $^1\text{H}$  NMR spectrum in  $\text{C}_6\text{D}_6$  of the products formed by heating a solid sample of **4.1** to  $300\text{ }^\circ\text{C}$  for 16 h. The isobutylene resonances are present at 4.75 and 1.60 ppm, the isobutyronitrile resonances are present at 1.78 and 0.60 ppm, and the H(ITA) resonances are present at 4.60, 1.78, 1.23, and 1.05 ppm. The peak at 2.13 ppm is from  $\text{C}_6\text{Me}_6$  (internal standard).



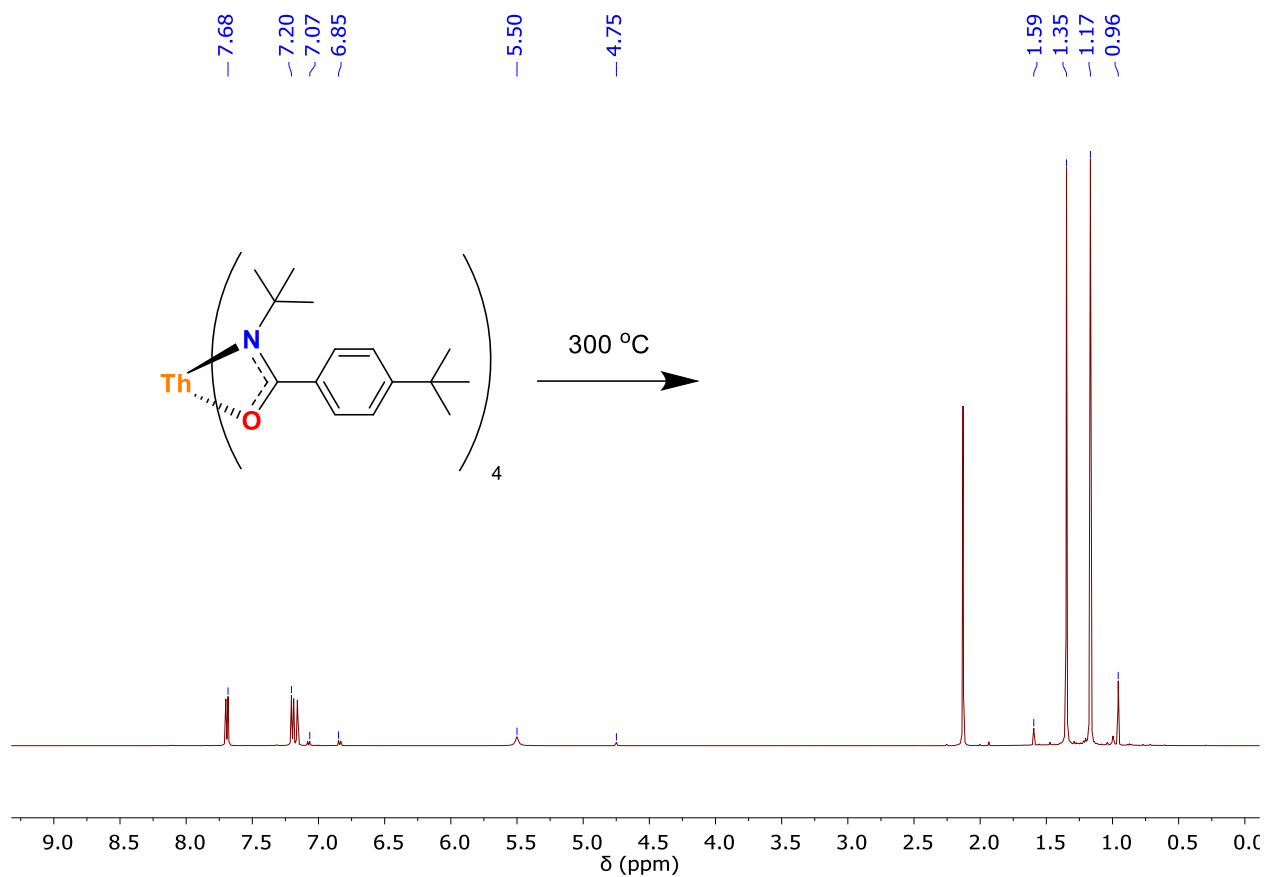
**Figure 4.6:**  $^1\text{H}$  NMR spectrum in  $\text{C}_6\text{D}_6$  of **4.2** after heating a solid sample to  $300\text{ }^\circ\text{C}$  for 16 h. Under these conditions, **4.2** sublimed completely; no decomposition was observed. The peak at 2.13 ppm is from  $\text{C}_6\text{Me}_6$  (internal standard).



**Figure 4.7:**  $^1\text{H}$  NMR spectrum in  $\text{C}_6\text{D}_6$  of the products formed by heating a sample of **4.2** to  $240\text{ }^{\circ}\text{C}$  for 2 weeks in  $d_{18}$ -decalin. Although most of the starting material was still present after this time, decomposition products were present in sufficient quantities to facilitate identification and their presence was confirmed by spiking. The pivalonitrile resonance is present at 1.31 ppm, the  $\text{H}(\text{TEPA})$  resonances are present at 4.93, 1.17, and 0.90 ppm, and the 2-pentene resonances are present at 5.37, 2.16, 2.06, and 2.00 ppm. Resonances that overlap with starting material or decalin have been excluded from this list for clarity.



**Figure 4.8:**  $^1\text{H}$  NMR spectrum in  $\text{C}_6\text{D}_6$  of the products formed by heating a solid sample of **4.3** to  $300\text{ }^\circ\text{C}$  for 16 h. The isobutylene resonances are present at 4.75 and 1.59 ppm, the (3,5-bis(trifluoromethyl))benzimidazole resonances are present at 7.40 and 6.96 ppm, and the  $\text{H}(\text{Ar}^{\text{F}}\text{TA})$  resonances are present at 7.95, 7.70, 5.12, and 1.19 ppm. The peak at 2.13 ppm is from  $\text{C}_6\text{Me}_6$  (internal standard).



**Figure 4.9:**  $^1\text{H}$  NMR spectrum in  $\text{C}_6\text{D}_6$  of the products formed by heating a solid sample of **4.4** to  $300\text{ }^\circ\text{C}$  for 16 h. The isobutylene resonances are present at 4.75 and 1.59 ppm, the (4-tert-butyl)benzimidazole resonances are present at 7.07, 6.85, and 0.96 ppm, and the H(TPTA) resonances are present at 7.68, 7.20, 5.05, 1.35, and 1.17 ppm. The peak at 2.13 ppm is from  $\text{C}_6\text{Me}_6$  (internal standard).

### Pyrolysis to $\text{ThO}_2$

Compounds **4.1-4.4** (20-40 mg each) were added to quartz tubes and cycled onto the Schlenk line using a Cajun adapter. The samples were heated under a nitrogen atmosphere using a butane torch until full decomposition of the precursors was observed, then the tubes were evacuated to remove volatile organic byproducts and heated in direct flame under vacuum for an additional 60 seconds. After cooling to room temperature, the tubes were brought into the glovebox. The pyrolyzed solids were then sealed in capillaries under a nitrogen atmosphere and analyzed using powder X-ray diffraction.

### Powder X-ray Diffraction (PXRD)

PXRD patterns of the products formed via pyrolysis of **4.1-4.4** were collected on a Bruker AXS D8 Advance spectrometer with a LynxEye strip detector. All patterns were collected at the wavelength of  $\text{Cu K}\alpha$  ( $\lambda=1.5418\text{ \AA}$ ). Prior to measurement the samples were packed into a quartz or borosilicate glass capillaries under inert atmosphere, and flame sealed. Comparison with powder

patterns from the literature reveals that all patterns are consistent with the presence of ThO<sub>2</sub> which has a fluorite structure in the *Fm-3m* space group.<sup>51</sup> The broad feature present in all patterns at around 20° 2θ is attributed to the presence of amorphous material.

### Soft X-ray Spectromicroscopy (STXM-XAS)

Sample preparation methodology for the potentially oxygen and moisture-sensitive analytes was similar to that described previously.<sup>52,53</sup> Samples were prepared in an argon-filled glovebox by grinding the analyte into a fine powder with a mortar and pestle, and brushing the powder onto a Si<sub>3</sub>N<sub>4</sub> membrane (100 nm, Silson) with a fiber. This method arranged a large number of micron-scale particles in a relatively compact area that were suitable for O K-edge as well as Th N-edge measurements. A second membrane was placed over the sample, and the edges were sealed together using Hardman Double/Bubble® 5 minute epoxy.

Data acquisition methodology was similar to that discussed previously.<sup>52,53</sup> Single-energy images and spectra were acquired using the Advanced Light Source beamline 5.3.2.2. The ALS operated in tophoff mode (500 mA) and measurements were conducted at approximately 0.6 Torr. For these measurements, the X-ray beam was focused with a zone plate with 25 nm outer zones onto the sample, and the transmitted light was detected. Images at a single energy were obtained by raster-scanning the sample and collecting transmitted monochromatic light as a function of sample position. Spectra at particular regions of interest on the sample image were extracted from the “stack”, which is a collection of images recorded at multiple, closely spaced photon energies across the absorption edge. Dwell times used to acquire an image at a single photon energy were typically 2 ms per pixel. To evaluate the absorbance signal, the measured transmitted intensity (*I*) was converted to optical density (OD) using Beer–Lambert’s law:  $OD = \ln(I/I_0) = \mu\rho d$ , where *I*<sub>0</sub> is the incident photon flux intensity, *d* is the sample thickness, and  $\mu$  and  $\rho$  are the mass absorption coefficient and density of the sample material, respectively. Incident photon intensity was measured through the sample-free region of the Si<sub>3</sub>N<sub>4</sub> windows. O K-edge data were background-subtracted and normalized in *MATLAB* using the *MBACK* algorithm.<sup>54</sup>

### X-Ray Crystallography

In a dry nitrogen glovebox, samples of single crystals of **4.1**, **4.3**, and **4.4** were coated in Paratone-N oil for transport to diffraction facilities. Crystals were mounted on either a Kapton loop (for **4.3**) or on a MiTeGen 10 μm aperture Dual-Thickness MicroMount (for **4.1** and **4.4**). X-ray diffraction data for **4.1** and **4.4** were collected at the Advanced Light Source (ALS), Lawrence Berkeley National Laboratory, Berkeley, CA, beamline 12.2.1 using a silicon double crystal monochromator to provide a beam of 17 keV ( $\lambda = 0.7288 \text{ \AA}$ ). X-ray diffraction data for **4.3** was collected at CheXray, Berkeley, CA, using a Rigaku XtaLAB P200 equipped with a MicroMax-007 HF microfocus rotating anode and a Pilatus 200K hybrid pixel array detector, using Mo K<sub>α</sub> radiation ( $\lambda = 0.71073 \text{ \AA}$ ). All data collections were conducted at 100 K, with the crystals cooled by a stream of dry nitrogen. For **4.1** and **4.4**, Bruker APEX3 software was used for the data collections, Bruker SAINT V8.38A software was used to conduct the cell refinement and data reduction procedures, and absorption corrections were carried out by a multi-scan method utilizing the SADABS program.<sup>55</sup> For **4.3**, CrysAlisPro was used for the data collections and data processing, including a multi-scan absorption correction applied using the SCALE3 ABSPACK scaling algorithm within CrysAlisPro.<sup>56</sup> Initial structure solutions were found using direct methods (SHELXT),<sup>57</sup> and refinements were carried out using SHELXL-2014,<sup>58</sup> as implemented by Olex2.<sup>59</sup> Thermal parameters for all non-hydrogen atoms were refined anisotropically. Thermal

ellipsoid plots were made using Mercury.<sup>60</sup> Structure **4.1** displayed full molecule disorder and all components were modeled completely. While it does not cause any relevant crystallographic alerts, the model for structure **4.3** included a hexane molecule with unrealistic structural metrics in the asymmetric unit, likely a result of solvent disorder not being fully resolved. Attempts to solve the solid state structure of **4.2** were unsuccessful despite the screening of numerous single crystals grown from various solvents. These crystals produced strong and highly resolved spots in the diffraction pattern. However, these spots likely result from strong diffraction of the thorium metal center, while presumed full molecule disorder (perhaps similar to that seen in **4.1**) leads to weak or unobservable ligand diffraction peaks. As a result, workup of the data continually led to unsolvable or unreasonable structures. All structures have been deposited to the Cambridge Crystallographic Data Centre (CCDC), with deposition numbers listed in Table 4.1.

**Table 4.1:** Crystallographic details and refinement metrics for **4.1**, **4.3**, and **4.4**.

	<b>4.1</b>	<b>4.3</b>	<b>4.4</b>
Chemical formula	C <sub>16</sub> H <sub>32</sub> N <sub>2</sub> O <sub>2</sub> Th <sub>0.5</sub>	C <sub>58</sub> H <sub>62</sub> F <sub>24</sub> N <sub>4</sub> O <sub>4</sub> Th	C <sub>60</sub> H <sub>88</sub> N <sub>4</sub> O <sub>4</sub> Th
Formula weight	400.45	1567.15	1161.38
Color, habit	Colorless, block	Colorless, block	Colorless, plate
Crystal system	Monoclinic	Monoclinic	Monoclinic
Space group	C2/m	P2/n	C2/c
a (Å)	18.676(1)	10.7799(2)	26.527(2)
b (Å)	12.397(1)	14.0321(3)	11.0968(1)
c (Å)	8.8081(4)	22.2223(5)	21.060(2)
α (°)	90	90	90
β (°)	113.055(1)	102.024(2)	107.646(4)
γ (°)	90	90	90
V (Å <sup>3</sup> )	1876.4(2)	3287.7(1)	5907.6(7)
Z	4	2	4
Density (g/cm <sup>3</sup> )	1.418	1.583	1.306
F(000)	812	1552	2392
Radiation Type	Synchrotron (λ = 0.7288 Å)	Mo K <sub>α</sub> (λ = 0.71073 Å)	Synchrotron (λ = 0.7288 Å)
μ (mm <sup>-1</sup> )	4.274	2.382	2.739
Crystal size (mm)	0.18 x 0.10 x 0.09	0.40 x 0.18 x 0.18	0.085 x 0.058 x 0.026
Meas. Refl.	16912	48997	25021
Indep. Refl.	2994	6726	5433
Obsvd.	2994	6324	5433
[I>2σ(I)] Refl.			
R <sub>int</sub>	0.0314	0.0487	0.0730
Final [I>=2σ(I)] R indices	R <sub>1</sub> = 0.0187 wR <sub>2</sub> = 0.0477	R <sub>1</sub> = 0.0219 wR <sub>2</sub> = 0.0543	R <sub>1</sub> = 0.0646 wR <sub>2</sub> = 0.1532
Goodness-of-fit	1.042	1.045	1.489
CCDC	1991580	1991582	1991581

**Table 4.2:** Selected atomic distances (Å) and angles (°) for **4.1**, **4.3**, and **4.4**.

Atoms	4.1	4.3	4.4
Th1–O1	2.331(3)	2.384(2)	2.401(9)
Th1–O2	2.337(4)	2.396(2)	2.379(5)
Th1–O3	2.444(2)	-	-
Th1–O4	-	-	-
Th1–N1	2.54(1)	2.565(2)	2.533(8)
Th1–N2	2.58(1)	2.551(2)	2.522(7)
Th1–N3	2.557(4)	-	-
Th1–N4	-	-	-
C1–O1	1.30(2)	1.301(3)	1.31(2)
C2–O2	1.315(7)	1.305(3)	1.31(2)
C3–O3	1.307(5)	-	-
C4–O4	-	-	-
C1–N1	1.30(2)	1.293(3)	1.31(1)
C2–N2	1.28(2)	1.297(3)	1.255(9)
C3–N3	1.303(6)	-	-
C4–N4	-	-	-
O1–C1–N1	114.9(7)	117.7(2)	115.5(9)
O2–C2–N2	118.0(9)	116.6(2)	116.5(7)
O3–C3–N3	117.0(4)	-	-
O4–C4–N4	-	-	-

## References

- 1 J. K. Gibson and W. A. de Jong, *Experimental and Theoretical Approaches to Actinide Chemistry*, Wiley, 1<sup>st</sup> edn., 2018.
- 2 M. A. Boreen and J. Arnold, *Multiple Bonding in Actinide Chemistry*, in the *Encyclopedia of Inorganic and Bioinorganic Chemistry*, Wiley, 2018.
- 3 C. D. Tutson and A. E. V. Gorden, *Coord. Chem. Rev.*, 2017, **333**, 27-43.
- 4 S. T. Liddle, *Angew. Chem. Int. Ed.*, 2015, **54**, 8604–8641.
- 5 C. E. Hayes and D. B. Leznoff, *Coord. Chem. Rev.*, 2014, **266-267**, 155-170.
- 6 J. Leduc, J. I. Pacold, D. K. Shuh, C. L. Dong and S. Mathur, *Z. Anorg. Allg. Chem.*, 2017, **644**, 12–18.
- 7 C. Falaise, H. A. Neal and M. Nyman, *Inorg. Chem.*, 2017, **56**, 6591–6598.
- 8 S. N. Kalmykov and M. A. Denecke, *Actinide Nanoparticle Research*, Springer, 1<sup>st</sup> edn., 2011.
- 9 D. Hudry, C. Apostolidis, O. Walter, T. Gouder, E. Courtois, C. Kübel and D. Meyer, *Chem. Eur. J.*, 2012, **18**, 8283–8287.
- 10 C. Schöttle, S. Rudel, R. Popescu, D. Gerthsen, F. Kraus and C. Feldmann, *ACS Omega*, 2017, **2**, 9144–9149.
- 11 E. L. Bright, S. Rennie, M. Cattelan, N. A. Fox, D. T. Goddard and R. Springell, *Thin Solid*



- Films*, 2018, **661**, 71–77.
- 12 T. Gouder, L. Havela, L. Black, F. Wastin, J. Rebizant, P. Boulet, D. Bouexière, S. Heathman and M. Idiri, *J. Alloys Compd.*, 2002, **336**, 73–76.
  - 13 K. O. Kvashnina, A. Y. Romanchuk, I. Pidchenko, L. Amidani, E. Gerber, A. Trigub, A. Rossberg, S. Weiss, K. Popa, O. Walter, R. Caciuffo, A. C. Scheinost, S. M. Butorin and S. N. Kalmykov, *Angew. Chem. Int. Ed.*, 2019, **58**, 17558–17562.
  - 14 IAEA, *Thorium fuel cycle- Potential benefits and challenges*, 2005.
  - 15 A. J. Juhasz, R. A. Rarick and R. Rangarajan, *High Efficiency Nuclear Power Plants Using Liquid Fluoride Thorium Reactor Technology*, NASA, 2009.
  - 16 US Atomic Energy Commission, *The Use of Thorium in Nuclear Power Reactors*. US Government Printing Office, 1969.
  - 17 B. M. Elsheikh, *J. Radiat. Res. Appl. Sci.*, 2019, **6**, 63–70.
  - 18 N. Cooper, D. Minakata, M. Begovic and J. Crittenden, *Environ. Sci. Technol.*, 2011, **45**, 6237–6238.
  - 19 K. Maher, J. R. Bargar and G. E. Brown, *Inorg. Chem.*, 2013, **52**, 3510–3532.
  - 20 A. T. Nelson, *Bulletin of the Atomic Scientists*, 2012, **68**, 33–44.
  - 21 A. K. Burrell, T. M. McCleskey, P. Shukla, H. Wang, T. Durakiewicz, D. P. Moore, C. G. Olson, J. J. Joyce and Q. Jia, *Adv. Mater.*, 2007, **19**, 3559–3563.
  - 22 B. L. Scott, J. J. Joyce, T. D. Durakiewicz, R. L. Martin, T. M. McCleskey, E. Bauer, H. Luo and Q. Jia, *Coord. Chem. Rev.*, 2014, **266–267**, 137–154.
  - 23 M. M. Strehle, B. J. Heuser, M. S. Elbakhshwan, X. Han, D. J. Gennardo, H. K. Pappas and H. Ju, *Thin Solid Films*, 2012, **520**, 5616–5626.
  - 24 Y. A. Teterin, A. J. Popel, K. I. Maslakov, A. Y. Teterin, K. E. Ivanov, S. N. Kalmykov, R. Springell, T. B. Scott and I. Farnan, *Inorg. Chem.*, 2016, **55**, 8059–8070.
  - 25 K. Liu, R. Bin, H. Xiao, Z. Long, Z. Hong, H. Yang and S. Wu, *Appl. Surf. Sci.*, 2013, **265**, 389–392.
  - 26 N.-T. H. Kim-Ngan, A. G. Balogh, L. Havela and T. Gouder, *Nucl. Instruments Methods Phys. Res. B*. 2010, **268**, 1875–1879.
  - 27 L. M. Moreau, A. Herve, M. D. Straub, D. R. Russo, R. J. Abergel, S. Alayoglu, J. Arnold, A. Braun, G. J. P. Deblonde, Y. Liu, T. D. Lohrey, D. T. Olive, Y. Qiao, J. A. Rees, D. K. Shuh, S. J. Teat, H. Booth and S. G. Minasian, *Chem. Sci.*, 2020, **11**, 4648–4668.
  - 28 Y. Shiokawa, R. Amano, A. Nomura and M. Yagi, *J. Radioanal. Nucl. Chem.*, 1991, **152**, 373–380.
  - 29 L. Amidani, G. B. M. Vaughan, T. V. Plakhova, A. Y. Romanchuk, E. Gerber, R. Svetogorov, S. Weiss, Y. Joly, S. N. Kalmykov and K. O. Kvashnina, *Chem. Eur. J.*, 2021, **27**, 252–263.
  - 30 S. E. Koponen, P. G. Gordon and S. T. Barry, *Polyhedron*, 2016, **108**, 59–66.
  - 31 H. Pierson, *Handbook of Chemical Vapor Deposition (CVD)*, Noyes Publications, 1999.
  - 32 B. Vlaisavljevich, P. Miro, D. Koballa, T. K. Todorova, S. R. Daly, G. S. Girolami, C. J. Cramer, and L. Gagliardi, *J. Phys. Chem. C.*, 2012, **116**, 23194–23200.
  - 33 S. R. Daly, D. Y. Kim, and G. S. Girolami, *Inorg. Chem.*, 2012, **51**, 7050–7065.
  - 34 S. R. Daly, P. M. B. Piccoli, A. J. Schultz, T. K. Todorova, L. Gagliardi, and G. S. Girolami, *Angew. Chem. Int. Ed.*, 2010, **49**, 3379–3381.
  - 35 A. Devi, *Coord. Chem. Rev.*, 2013, **257**, 3332–3284.
  - 36 A. P. Milanov, T. B. Thiede, A. Devi, and R. A. Fischer, *J. Am. Chem. Soc.*, 2009, **131**, 17062–17063.

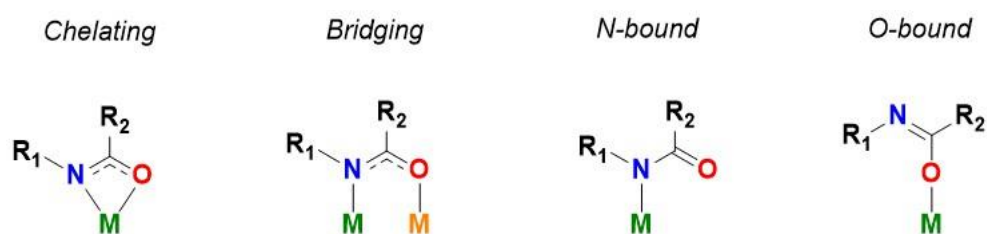
- 37 L. Appel, J. Leduc, C. L. Webster, J. W. Ziller, W. J. Evans, and S. Mathur, *Angew. Chem. Int. Ed.*, 2015, **54**, 2209–2213.
- 38 P. Marchand and C. J. Carmalt, *Coord. Chem. Rev.*, 2013, **257**, 3202–3221.
- 39 M. D. Straub, J. Leduc, M. Frank, A. Raauf, T. D. Lohrey, S. G. Minasian, S. Mathur and J. Arnold, *Angew. Chem. Int. Ed.*, 2019, **58**, 5749–5753.
- 40 A. L. Catherall, M. S. Hill, A. L. Johnson, G. Kociok-Köhn and M. F. Mahon, *J. Mater. Chem. C*, 2016, **4**, 10731–10739.
- 41 T. Perera, *Wayne State University Dissertation*, 2012.
- 42 M. D. Straub, S. Hohloch, S. G. Minasian and J. Arnold, *Dalton Trans.*, 2018, **47**, 1772–1776.
- 43 W. J. Evans, J. R. Walensky and J. W. Ziller, *Organometallics*, 2010, **29**, 945–950.
- 44 W. Henderson, A. G. Oliver and C. E. F. Rickard, *Inorganica Chim. Acta*, 2000, **307**, 144–148.
- 45 C. Li, R. K. Thomson, B. Gillon, B. O. Patrick and L. L. Schafer, *Chem. Commun.*, 2003, **98**, 2462–2463.
- 46 J. Hartwig, *Organotransition Metal Chemistry: From Bonding to Catalysis*, Vol. 2, University Science Books, 2010.
- 47 S. M. Butorin, K. O. Kvashnina, J. R. Vegelius, D. Meyer, and D. K. Shuh, *PNAS*, 2016, **113**, 8093–8097.
- 48 B.-H. Huang, T.-L. Yu, Y.-L. Huang, B.-T. Ko and C.-C. Lin, *Inorg. Chem.*, 2002, **41**, 2987–2994.
- 49 R. Zhao and W. Lu, *Org. Lett.*, 2017, **19**, 1768–1771.
- 50 T. Cantat, B. L. Scott, and J. L. Kiplinger, *Chem. Commun.*, 2010, **46**, 919.
- 51 H. J. Whitfield, D. Roman and A. R. Palmer, *J. Inorg. Nucl. Chem.*, 1966, **28**, 2817–2825.
- 52 L. M. Moreau, A. Herve, M. D. Straub, D. R. Russo, R. J. Abergel, S. Alayoglu, J. Arnold, A. Braun, G. J. P. Deblonde, Y. Liu, T. D. Lohrey, D. T. Olive, Y. Qiao, J. A. Rees, D. K. Shuh, S. J. Teat, H. Booth and S. G. Minasian, *Chem. Sci.*, 2020, **11**, 4648–4668.
- 53 A. B. Altman, J. I. Pacold, J. Wang, W. W. Lukens and S. G. Minasian, *Dalton Trans.*, 2016, **45**, 9948–9961.
- 54 T.-C. Weng, G. S. Waldo and J. E. Penner-Hahn, *J. Synchrotron Radiat.*, 2004, **12**, 506–510.
- 55 APEX3, SADABS, and SAINT. Bruker AXS. Madison, WI, USA.
- 56 CrysAlisPro 1.171.39.45f (Rigaku Oxford Diffraction, 2018).
- 57 G. M. Sheldrick, *Acta Cryst.*, 2008, **A64**, 112–122.
- 58 G. M. Sheldrick, *Acta Cryst.* 2015, **C71**, 3–8.
- 59 O. V. Dolomanov, L. J. Bourhis, R. J. Gildea, J. A. K. Howard and H. Puschmann, *J. Appl. Crystallogr.*, 2009, **42**, 339–341.
- 60 C. F. Macrae, I. J. Bruno, J. A. Chisholm, P. R. Edgington, P. McCabe, E. Pidcock, L. Rodriguez-Monge, R. Taylor, J. Van De Streek and P. A. Wood, *J. Appl. Crystallogr.*, 2008, **41**, 466–470.

## Chapter 5

# Homoleptic Uranium(III) and Uranium(IV) Amidate Complexes

## Introduction

Within the last few years, interest in improving control over the coordination chemistry of actinides has grown tremendously, leading to remarkable achievements in organometallics<sup>1-5</sup> and nanotechnology,<sup>6-9</sup> and to innovative developments in radioactive waste separation<sup>10-13</sup> and environmental remediation.<sup>13-16</sup> Uranium coordination complexes are of interest to chemists due to their wide array of accessible geometries and unusual reactivity.<sup>17-31</sup> Due to the electropositive nature and large atomic size of uranium, coordination chemists frequently employ sterically-encumbered ligands to stabilize uranium complexes in non-aqueous systems. Cyclopentadienyl (Cp) derivatives are often used to provide steric support around the uranium center, but a large amount of research has been directed towards developing actinide complexes using alternative ligand systems,<sup>18,31,32</sup> including carbenes,<sup>33,34</sup> carboxylates,<sup>20,21,35</sup> and amidinates.<sup>36-40</sup>



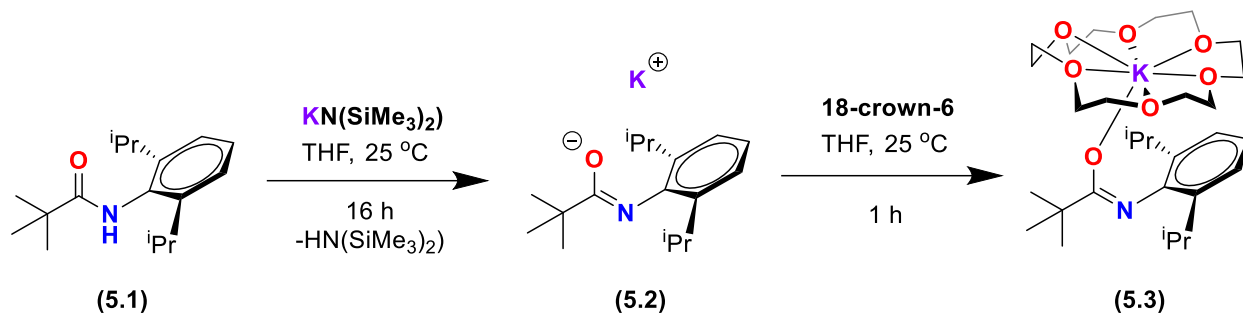
**Figure 5.1:** Binding modes of amidates to metal centers.

Interestingly, amidates, which can be seen as hybrids of carboxylates to amidinates, have been only sparsely studied as ligands in actinide chemistry.<sup>29,41</sup> In contrast, amidate complexes of group IV metals have been investigated for a variety of applications. Ti(IV) and Zr(IV) amidate complexes are well-studied as catalysts for hydroamination,<sup>42-45</sup> and recently, homoleptic zirconium amidate complexes have demonstrated high efficacy as molecular precursors for chemical vapor deposition of ZrO<sub>2</sub> thin films.<sup>46,47</sup> Due to the presence of two distinct donor sites in the amidate backbone, amidate ligands typically bond in one of four primary modes, illustrated in Figure 5.1. This variety in binding modes enables metal amidate complexes to adopt a number of different geometries and electron-donating abilities. Steric factors can affect the denticity of the binding, while electronic factors such as the hardness of the cation affect whether binding to N or O is electronically preferred.<sup>44,48</sup> Due to the high oxophilicity and the large ionic radii of U(III) and U(IV), we hypothesized that either chelating or O-bound coordination would be observed for amidate complexes of these metal centers. Here, we report the syntheses of the first homoleptic U(III) and U(IV) amidate complexes, which exhibit significant differences in their solid-state coordination geometries.

## Results and Discussion

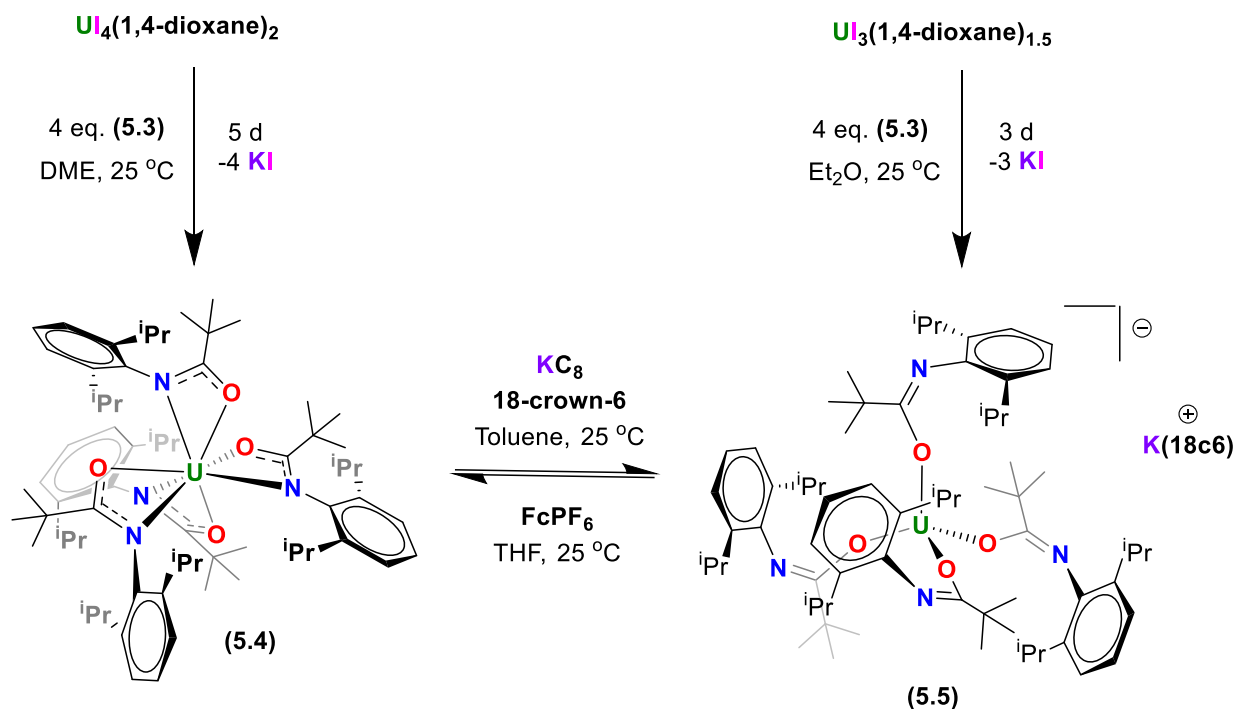
The amide proligand N-(2,6-diisopropylphenyl)pivalamide (H(TDA)) (**5.1**) was synthesized according to literature methods<sup>49</sup> and purified by sublimation. Deprotonation of **5.1** with KN(SiMe<sub>3</sub>)<sub>2</sub> afforded the corresponding potassium amidate K(TDA) (**5.2**) as a colorless powder in 86% yield. Using **5.2** as a precursor for the metalation of uranium led to the formation

of complicated mixtures of –ate complexes, resulting in poor yields of the desired uranium complexes. However, addition of 18-crown-6 to **5.2** gave the crowned potassium amidate  $K(TDA)(18c6)$  (**5.3**) in 96% yield, and this compound was substantially more effective as a starting material for metalation.



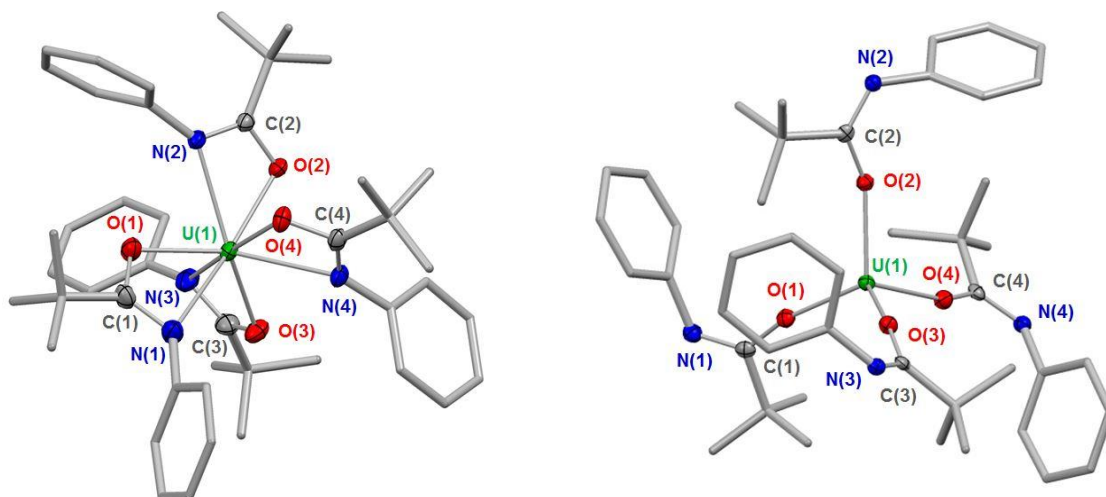
**Scheme 5.1:** Synthesis of the crowned amidate ligand  $K(TDA)(18c6)$  (**5.3**).

The homoleptic uranium amidate complex  $U(TDA)_4$  (**5.4**) was synthesized by reacting  $UI_4(1,4\text{-dioxane})_2$  with four equivalents of **5.3** (Scheme 5.2). Complex **5.4** was isolated as pale green crystals in 23% yield from a cooled solution of HMDSO. Its room temperature  $^1H$  NMR spectrum showed only a set of four paramagnetically-broadened resonances between 0 and 7 ppm, corresponding to the aromatic, *iso*-propyl methine, *tert*-butyl, and *iso*-propyl methyl protons. Using a similar salt metathesis reaction procedure, the U(III) complex **5.5** was obtained from the reaction between **5.3** and  $UI_3(1,4\text{-dioxane})_{1.5}$  in diethyl ether, and isolated in 66% yield as large red blocks. The room temperature  $^1H$  NMR spectrum of **5.5** showed a set of seven resonances, comprising six broad peaks from the uranium-bound ligands and one sharp peak at 3.5 ppm from the crown ether. The two most upfield resonances at -3.3 and 0.5 ppm were assigned to the inequivalent *iso*propyl methyl protons.



**Scheme 5.2:** Synthesis and redox interconversion of the homoleptic uranium amidate complexes **5.4** and **5.5**.

Previous studies with Hf and Zr amidate complexes have shown amidate ligands to be hemilabile at elevated temperatures, allowing for rapid interconversion between isomers.<sup>50</sup> To determine whether the solid-state coordination geometries of **5.4** and **5.5** were preserved in solution, variable-temperature NMR spectra were collected in d<sub>8</sub>-THF from -78 to +70 °C. At 70 °C, **5.4** and **5.5** both exhibited five broad and paramagnetically shifted peaks, consistent with four-coordinate geometries in which the amidate ligands were equivalent on the NMR timescale. Upon cooling below 0 °C, a complex new set of multiple resonances emerged, suggesting lower symmetries for both molecules; however, attempts to formulate <sup>1</sup>H NMR assignments were thwarted by large paramagnetic shifts and broadening of the ligand resonances arising from coupling to the uranium centers.<sup>51</sup> These observations provide only a qualitative indication that multiple structures are potentially accessible in solution for **5.4** and **5.5**.



**Figure 5.2:** X-ray crystal structures of **5.4** (left) and **5.5** (right) with 50% probability thermal ellipsoids. Hydrogen atoms and isopropyl groups are omitted for clarity.

**Table 5.1:** Selected atomic distances (Å) and angles (deg) for **5.4** and **5.5**.

Atoms	<b>5.4</b>	<b>5.5</b>
U1 – O1	2.270(2)	2.234(2)
U1 – O2	2.321(2)	2.235(2)
U1 – O3	2.316(2)	2.236(2)
U1 – O4	2.276(2)	2.253(2)
U1 – N1	2.721(3)	-
U1 – N2	2.535(2)	-
U1 – N3	2.535(2)	-
U1 – N4	2.713(2)	-
C – O avg	1.315(2)	1.330(5)
C – N avg	1.301(7)	1.279(6)
O – C – N avg	114.2(6)	125.5(7)

Since the NMR data alone were insufficient to shed light on the structures of **5.4** and **5.5**, we turned to single crystal X-ray diffraction studies to probe bonding interactions in the solid-state; these showed **5.4** to be eight-coordinate, with all four amidate ligands chelated ( $\kappa_2$ -O,N) to the U(IV) center in a distorted dodecahedral geometry with  $S_4$  symmetry (Figure 5.2). The U-N bonds in **5.4** were found to be longer than the U-O interactions by an average of  $0.33 \pm 0.11$  Å. To our surprise, the molecular structure of **5.5** showed no U-N bonding interactions; instead, the uranium in **5.5** was four-coordinate, with four ( $\kappa_1$ -O) amidates arranged in a distorted tetrahedral geometry ( $\tau_4' = 0.92$ ) around the uranium center, with  $S_4$  symmetry of the molecule. In addition, the average C–O bond distances increased from 1.315(4) to 1.330(4) Å in **5.4** vs. **5.5**, while the average C–N bond distances decreased from 1.301(7) to 1.279(6) Å in **5.4** vs. **5.5**, respectively, consistent with the resonance structures shown in Figure 5.1.

Considering the larger ionic radius of U(III) (1.03 Å vs 0.89 Å in U(III) and U(IV), respectively),<sup>52</sup> the observation of a four-coordinate geometry in the U(III) complex **5.5** and an eight-coordinate geometry in the U(IV) compound was unexpected. Several factors could be considered as influencing this behavior: i) the higher covalent character of U(IV)<sup>53</sup> could favor stronger U-N interactions in **5.4**; ii) the effect of electrostatic repulsion in U-L interactions in anionic **5.5** relative to neutral **5.4** may result in a lower coordination number; iii) the U(IV) ion in **5.4**, having a greater charge density than the U(III) ion in **5.5**, could favor a higher coordination number; iv) in situations where the energy differences are small, crystal packing effects cannot be ruled out.<sup>54</sup> Notably, **5.5** was the main product of the reaction between **5.3** and  $\text{UI}_3(1,4\text{-dioxane})_{1.5}$  regardless of the stoichiometry used; no U(III) products with increased coordination numbers were isolated.

We were next interested to determine if **5.4** and **5.5** could be interconverted by chemical reduction/oxidation reactions. Since both complexes were chemically accessible from the corresponding U(IV) and U(III) precursors, chemical reduction/oxidation reactions to interconvert between the two species were pursued. While weak reducing agents such as cobaltocene showed no reaction with **5.4**, addition of  $\text{KC}_8$  to a diethyl ether solution of **5.4** and 18-crown-6 caused the solution to darken from pale green to deep red, and we isolated **5.5** in from the reaction mixture in 32% yield after a short reaction time (2 min); prolonged reaction times led to decomposition. Furthermore, **5.5** was readily oxidized by ferrocenium hexafluorophosphate in THF to give **5.4** in 81% yield. We examined the cyclic voltammograms of **5.4** and **5.5** using  ${}^n\text{Bu}_4\text{NPF}_6$  as the electrolyte in THF or acetonitrile. No redox processes were observable within this solvent window; solvents with a larger reductive window, such as nitromethane, were not suitable for use with these complexes.

## Summary and Conclusions

We have prepared the first homoleptic U(IV) and U(III) amidate complexes **5.4** and **5.5** using the sterically-hindered N-(2,6-diisopropylphenyl)pivalamido (TDA) ligand. Complexes **5.4** and **5.5** were interconverted through reduction of **5.4** with  $\text{KC}_8$  or oxidation of **5.5** with  $\text{FcPF}_6$ . The solid-state geometry of ligands around the uranium center was seen to be highly dependent upon the oxidation state of uranium for these complexes: counterintuitively, the larger U(III) center adopted a four-coordinate tetrahedral structure, and the smaller U(IV) center adopted an eight-coordinate distorted dodecahedral structure. This unusual finding for U(IV) in comparison to U(III) further serves to highlight the delicate interplay between steric and electronic effects in these molecular systems.

## Experimental

### Materials and Methods

Unless otherwise noted, all syntheses were performed using standard Schlenk techniques under an atmosphere of nitrogen or in an MBraun glovebox under an atmosphere of nitrogen. Glassware, cannulae, and Celite were stored in an oven at 160 °C for at least 12 hours prior to use. 3 Å and 4 Å molecular sieves were activated by heating under vacuum at 300 °C for 24 hours. Hexane, pentane, toluene, benzene, diethyl ether, tetrahydrofuran, 1,2-dimethoxyethane (DME),



and acetonitrile were purified by passage through a column of activated alumina prior to use. Hexamethyldisiloxane (HMDSO) was stirred over sodium/benzophenone prior to distillation and stored over 4 Å molecular sieves. C<sub>6</sub>D<sub>6</sub> and d<sup>8</sup>-THF were purchased from Cambridge Isotope Labs and stored over 4 Å molecular sieves. C<sub>5</sub>D<sub>5</sub>N was purchased from Cambridge Isotope Labs, stirred over CaH<sub>2</sub>, transferred under vacuum, and stored over 3 Å molecular sieves. KN(SiMe<sub>3</sub>)<sub>2</sub> was recrystallized from hot toluene prior to use. H(TDA) (**5.1**) was prepared according to literature methods<sup>49</sup> and purified by sublimation at 250 °C, 10 mTorr. UI<sub>4</sub>(1,4-dioxane)<sub>2</sub> and UI<sub>3</sub>(1,4-dioxane)<sub>1.5</sub> were prepared according to literature methods.<sup>55</sup> All other chemicals were purchased from Sigma-Aldrich or Acros Organics and used as received. <sup>1</sup>H and <sup>13</sup>C NMR spectra were recorded at room temperature using Bruker AV-600, AV-500, and AVB-400 spectrometers. <sup>1</sup>H chemical shifts were referenced to C<sub>6</sub>D<sub>5</sub>H (δ = 7.16 ppm), C<sub>5</sub>D<sub>4</sub>HN (δ<sub>1</sub> = 8.74 ppm), and C<sub>4</sub>D<sub>7</sub>HO (δ<sub>2</sub> = 1.78 ppm). <sup>13</sup>C chemical shifts were referenced to C<sub>6</sub>D<sub>6</sub> (δ = 128.39 ppm) and C<sub>5</sub>D<sub>5</sub>N (δ<sub>1</sub> = 150.35 ppm). Samples for IR spectroscopy were prepared as Nujol mulls, and spectra were taken in KBr plates using a Nicolet iS10 spectrometer. Melting points were determined in sealed tubes under an atmosphere of nitrogen using a Stanford Research Systems OptiMelt instrument and are reported uncorrected.

## Synthesis of Compounds

**K(TDA) (5.2):** A THF solution (100 mL) of KN(SiMe<sub>3</sub>)<sub>2</sub> (3.84 g, 19.3 mmol) was added to a stirred THF solution (150 mL) of **5.1** (5.00 g, 19.1 mmol) maintained at -78 °C via cannula. The resulting solution was slowly warmed to room temperature and stirred for 48 h, then the solvent was removed *in vacuo* to give an off-white powder. This powder was washed with hexane (50 mL) to remove impurities, then dried *in vacuo* to give the product as a colorless powder. (4.94 g, 86% yield) <sup>1</sup>H NMR (C<sub>5</sub>D<sub>5</sub>N, 400 MHz): δ 7.17 (d, 2H, Ph-*H*), 6.99 (t, 1H, Ph-*H*), 3.77 (m, 2H, CH(CH<sub>3</sub>)<sub>2</sub>), 1.68 (s, 9H, C(CH<sub>3</sub>)<sub>3</sub>), 1.32 and 1.26 (dd, 12H, CH(CH<sub>3</sub>)<sub>2</sub>). <sup>13</sup>C NMR (C<sub>5</sub>D<sub>5</sub>N, 600 MHz): δ 176.48 (NCO), 155.37 (CCN), 141.61 (Ph), 122.91 (Ph), 120.22 (Ph), 39.80 (C(CH<sub>3</sub>)<sub>3</sub>), 30.82 (C(CH<sub>3</sub>)<sub>3</sub>), 28.80 (CH(CH<sub>3</sub>)<sub>2</sub>), 24.00 (CH(CH<sub>3</sub>)<sub>2</sub>). IR (cm<sup>-1</sup>): 1586 (w), 1542 (s), 1517 (s), 1433 (s), 1390 (m), 1349 (s), 1317 (m), 1255 (m), 1219 (m), 1176 (w), 1158 (w), 1101 (w), 1056 (w), 1041 (w), 914 (m), 883 (w), 848 (w), 808 (w), 791 (m), 751 (s).

**K(TDA)(18c6) (5.3):** A THF solution (5 mL) of 18-crown-6 (838 mg, 3.17 mmol) was added to a stirred THF solution (7 mL) of **5.2** (946 mg, 3.16 mmol) via pipette. The resulting solution was stirred for 1 h, then the solvent was removed *in vacuo*. The resulting off-white solids were triturated with hexane to give the product as a colorless powder. (1.73 g, 96% yield) <sup>1</sup>H NMR (C<sub>6</sub>D<sub>6</sub>, 600 MHz): δ 7.26 (d, 2H, Ph-*H*), 7.02 (t, 1H, Ph-*H*), 3.91 (m, 2H, CH(CH<sub>3</sub>)<sub>2</sub>), 3.05 (s, 24H, OCH<sub>2</sub>), 1.83 (s, 9H, C(CH<sub>3</sub>)<sub>3</sub>), 1.62 and 1.43 (dd, 12H, CH(CH<sub>3</sub>)<sub>2</sub>). <sup>13</sup>C NMR (C<sub>6</sub>D<sub>6</sub>, 600 MHz): δ 173.77 (NCO), 155.48 (CCN), 141.04 (Ph), 121.86 (Ph), 118.31 (Ph), 70.29 (OCH<sub>2</sub>), 39.91 (C(CH<sub>3</sub>)<sub>3</sub>), 31.07 (C(CH<sub>3</sub>)<sub>3</sub>), 29.22 (CH(CH<sub>3</sub>)<sub>2</sub>), 24.23 (CH(CH<sub>3</sub>)<sub>2</sub>). IR (cm<sup>-1</sup>): 1587 (w), 1551 (s), 1426 (m), 1392 (m), 1352 (m), 1302 (w), 1256 (w), 1225 (w), 1110 (s), 1082 (m), 960 (m), 910 (m), 839 (w), 781 (w), 741 (m).

### U(TDA)<sub>4</sub> (5.4):

**Method 1:** A THF solution (5 mL) of UI<sub>4</sub>(1,4-dioxane)<sub>2</sub> (200 mg, 0.217 mmol) was slowly added to a stirred THF solution (10 mL) of **5.3** (489 mg, 0.868 mmol) via cannula. The reaction flask

was heated to 60 °C and stirred for 3 d. Over the course of the reaction, the dark red solution turned cloudy green. The solvent was removed *in vacuo*, and HMDSO (10 mL) was added to the resulting green solids to give a pale green solution. This solution was filtered through Celite, concentrated to a volume of 3 mL, and cooled to -40 °C for 7 d, yielding pale green crystals, which were then dried *in vacuo*. (65 mg, 23% yield)

**Method 2:** A THF solution of FcPF<sub>6</sub> (6 mg, 0.018 mmol) was added dropwise to a stirred THF solution (2 mL) of **5.5** (30 mg, 0.019 mmol) via pipette. The deep red solution turned greenish-brown over the course of the reaction. The solution was stirred for 1 h, and then the solvent was removed *in vacuo*. The resulting brown-green solids were extracted into pentane and filtered through Celite, then the solvent was removed *in vacuo* to give a pale green waxy solid showing identical <sup>1</sup>H NMR shifts to the complex obtained from Method 1. (20 mg, 81% yield) <sup>1</sup>H NMR (C<sub>6</sub>D<sub>6</sub>, 600 MHz): δ 6.75 (s, 4H, Ph-*H* and 8H, Ph-*H*), 3.16 (s, 8H, CH(CH<sub>3</sub>)<sub>2</sub>), 1.66 (s, 36H, C(CH<sub>3</sub>)<sub>3</sub>), and 0.08 (s, 48H, CH(CH<sub>3</sub>)<sub>2</sub>). IR (cm<sup>-1</sup>): 1468 (m), 1536 (m), 1397 (m), 1340 (w), 1313 (m), 1255 (w), 1211 (m), 1172 (m), 1125 (w), 1098 (w), 1029 (w), 925 (w), 803 (w), 764 (m), 736 (w), 656 (w), 585 (w). Melting point: 172-177 °C EA calcd for C<sub>68</sub>H<sub>104</sub>N<sub>4</sub>O<sub>4</sub>U: C: 63.83%, H: 8.19%, N: 4.38%. Found: C: 63.59%, H: 8.00%, N: 4.56%.

#### [U(TDA)<sub>4</sub>]K(18c6) (5.5):

**Method 1:** A diethyl ether solution (7 mL) of **5.3** (300 mg, 0.532 mmol) was added dropwise to a stirred diethyl ether solution (3 mL) of UI<sub>3</sub>(diox)<sub>1.5</sub> (130 mg, 0.173 mmol) via pipette. The dark blue solution turned cloudy red over the course of the reaction. The solution was stirred for 4 d, and then the solvent was removed *in vacuo*. The solution was filtered through Celite, concentrated to a volume of 2 mL, and cooled to -40 °C for 24 h, yielding dark red crystals, which were then washed twice with benzene and dried *in vacuo*. (140 mg, 66% yield)

**Method 2:** A diethyl ether suspension (1 mL) of KC<sub>8</sub> (5 mg, 0.040 mmol) was added quickly to a stirred diethyl ether solution (2 mL) of **5.4** (33 mg, 0.026 mmol) and 18-crown-6 (8 mg, 0.032 mmol). The pale green solution turned reddish-brown over the course of the reaction. This solution was stirred for 2 min, and then the solvent was removed *in vacuo*. The resulting red solids were extracted into diethyl ether and filtered through Celite, then the solvent was removed *in vacuo* to give a dark red microcrystalline solid showing identical <sup>1</sup>H NMR shifts to the complex obtained from Method 1. (11 mg, 32% yield) <sup>1</sup>H NMR (C<sub>5</sub>D<sub>5</sub>N, 500 MHz): δ 6.61 (s, 4H, Ph-*H*), 6.44 (s, 8H, Ph-*H*), 3.46 (s, 24H, OCH<sub>2</sub>), 2.47 (s, 8H, CH(CH<sub>3</sub>)<sub>2</sub>), 1.38 (s, 36H, C(CH<sub>3</sub>)<sub>3</sub>), 0.46 (s, 24H, CH(CH<sub>3</sub>)<sub>2</sub>), and -3.32 (s, 24H, CH(CH<sub>3</sub>)<sub>2</sub>). IR (cm<sup>-1</sup>): 1647 (m), 1609 (m), 1584 (m), 1352 (w), 1294 (m), 1210 (w), 1160 (m), 1108 (m), 962 (m), 912 (m), 836 (w), 807 (w), 790 (w), 741 (m). Melting point: 201-205 °C; EA calcd for C<sub>80</sub>H<sub>128</sub>N<sub>4</sub>O<sub>10</sub>UK: C: 60.70%, H: 8.15%, N: 3.54%. Found: C: 60.41%, H: 8.23%, N: 3.20%.

#### X-Ray Crystallography

X-ray structural determination was performed at CHEXRAY, University of California, Berkeley, on a Bruker APEX II Quazar diffractometer or at the Advanced Light Source (ALS) station 11.3.1 at Lawrence Berkeley National Laboratory. The Bruker Quazar is a Kappa geometry three-circle diffractometer that couples a charge-coupled device (CCD) detector with a sealed-tube source of monochromatized Mo K<sub>α</sub> radiation. Structural data collected at ALS station 11.3.1 utilized a silicon monochromated beam of 16 keV (λ = 0.7749 Å) synchrotron radiation.

Crystals of appropriate size and quality were coated in Paratone-N oil and mounted on a Kapton loop. The loop was transferred to the diffractometer, centered in the beam, and cooled by

a nitrogen flow low-temperature apparatus that had been previously calibrated by a thermocouple placed at the same position as the crystal. All data collections were carried out at 100 K. The data were corrected for Lorentz and polarization effects; no correction for crystal decay was applied. An empirical absorption correction based on comparison of redundant and equivalent reflections was applied using SADABS. All software used for diffraction data processing and crystal-structure solution and refinement are contained in the APEX3 program suite (Bruker AXS, Madison, WI). Thermal parameters for all non-hydrogen atoms were refined anisotropically.<sup>57-61</sup> Due to a strongly disordered and unresolvable hexamethyldisiloxane (HMDSO) molecule in the structure of **4**, the SQUEEZE technique was applied for this molecular structure.<sup>62</sup> CIF files can be downloaded free of charge from <https://summary.ccdc.cam.ac.uk/structure-summary-form>.

**Table 5.2:** Crystallographic details for **5.3**, **5.4**, and **5.5**.

	<b>5.3</b>	<b>5.4*</b>	<b>5.5 · 3 Et<sub>2</sub>O</b>
Chemical formula	C <sub>29</sub> H <sub>50</sub> NO <sub>7</sub> K	C <sub>68</sub> H <sub>104</sub> N <sub>4</sub> O <sub>4</sub> U <sub>1</sub>	C <sub>80</sub> H <sub>128</sub> N <sub>4</sub> O <sub>10</sub> U <sub>1</sub> K <sub>1</sub> 3 C <sub>4</sub> H <sub>10</sub> O
<i>M<sub>r</sub></i>	563.80	1279.58	1805.34
Crystal system	Monoclinic	Triclinic	Triclinic
Space group	P 2 <sub>1</sub> / <i>n</i>	P-1	P-1
<i>a</i> (Å)	9.692(5)	13.4219(5)	13.479(4)
<i>b</i> (Å)	21.888(13)	13.6222(6)	18.049(6)
<i>c</i> (Å)	14.814(9)	21.0557(9)	20.964(7)
$\alpha$ (°)	90	88.668(2)	87.530(7)
$\beta$ (°)	101.007(4)	77.566(2)	79.614(10)
$\gamma$ (°)	90	87.760(2)	74.365(6)
<i>V</i> (Å <sup>3</sup> )	3085(3)	3756.1(3)	4831(3)
<i>Z</i>	4	2	2
Density (g/cm <sup>3</sup> )	1.214	1.131	1.241
F(000)	1224	1328	1906
Radiation Type	Synchrotron	Mo K $\alpha$	Mo K $\alpha$
$\mu$ (mm <sup>-1</sup> )	0.268	2.202	1.781
Abs. corr. type	Multi-scan	Multi-scan	Multi-scan
Abs. corr. <i>T</i> <sub>min</sub>	0.623	0.639	0.653
Abs. corr. <i>T</i> <sub>max</sub>	0.746	0.745	0.745
Crystal size (mm)	0.19 x 0.17 x 0.12	0.15 x 0.15 x 0.13	0.15 x 0.12 x 0.11
Meas. Refl.	32500	98499	100876
Indep. Refl.	7183	13844	19634
Obsvd. [ <i>I</i> > 2 $\sigma$ ( <i>I</i> )] refl.	6509	12424	16754
<i>R</i> <sub>int</sub>	0.0254	0.0403	0.0586
<i>R</i> [ <i>F</i> <sup>2</sup> > 2 $\sigma$ ( <i>F</i> <sup>2</sup> )], <i>wR</i> ( <i>F</i> <sup>2</sup> )	0.0300, 0.0814	0.0302, 0.0736	0.0394, 0.0840
<i>S</i>	1.049	1.088	1.079
$\Delta\rho_{\max}$ , $\Delta\rho_{\min}$ (e Å <sup>-3</sup> )	0.342, -0.288	2.863, -0.999	2.723, -0.522
CCDC	1559383	1559385	1559386

\*Due to a strongly disordered and unresolvable hexamethyldisiloxane (HMDSO) molecule in the lattice, the SQUEEZE technique was applied for this molecular structure.

## References

- 1 M. Falcone, L. Chatelain, R. Scopelliti, I. Živković and M. Mazzanti, *Nature*, 2017, **547**, 332–335.
- 2 J. J. Kiernicki, M. G. Ferrier, J. S. Lezama Pacheco, H. S. La Pierre, B. W. Stein, M. Zeller, S. A. Kozimor and S. C. Bart, *J. Am. Chem. Soc.*, 2016, **138**, 13941–13951.
- 3 J. A. Hlina, J. R. Pankhurst, N. Kaltsoyannis and P. L. Arnold, *J. Am. Chem. Soc.*, 2016, **138**, 3333–3345.
- 4 D. P. Halter, F. W. Heinemann, J. Bachmann and K. Meyer, *Nature*, 2016, **530**, 317–321.
- 5 M. R. MacDonald, M. E. Fieser, J. E. Bates, J. W. Ziller, F. Furche and W. J. Evans, *J. Am. Chem. Soc.*, 2013, **135**, 13310–13313.
- 6 D. Hudry, C. Apostolidis, O. Walter, T. Gouder, E. Courtois, C. Kübel and D. Meyer, *Chem. Eur. J.*, 2012, **18**, 8283–8287.
- 7 P. Miró, B. Vlasisavljevich, A. Gil, P. C. Burns, M. Nyman and C. Bo, *Chem. Eur. J.*, 2016, **22**, 8571–8578.
- 8 Q. Wang, G.-D. Li, S. Xu, J.-X. Li and J.-S. Chen, *J. Mater. Chem.*, 2008, **18**, 1146.
- 9 D. Hudry, J.-C. Griveau, C. Apostolidis, O. Walter, E. Colineau, G. Rasmussen, D. Wang, V. S. K. Chakravadhala, E. Courtois, C. Kübel and D. Meyer, *Nano Res.*, 2014, **7**, 119–131.
- 10 S. Demir, N. K. Brune, J. F. Van Humbeck, J. A. Mason, T. V. Plakhova, S. Wang, G. Tian, S. G. Minasian, T. Tyliczszak, T. Yaita, T. Kobayashi, S. N. Kalmykov, H. Shiwaku, D. K. Shuh and J. R. Long, *ACS Cent. Sci.*, 2016, **2**, 253–265.
- 11 G. Kim, W. C. Burnett and E. P. Horwitz, *Anal. Chem.*, 2000, **72**, 4882–4887.
- 12 E. M. Wylie, K. M. Peruski, J. L. Weidman, W. A. Phillip and P. C. Burns, *ACS Appl. Mater. Interfaces*, 2014, **6**, 473–479.
- 13 M. Kaur, H. Zhang, L. Martin, T. Todd and Y. Qiang, *Environ. Sci. Technol.*, 2013, **47**, 11942–11959.
- 14 A. J. Francis and C. J. Dodge, *Environ. Sci. Technol.*, 1998, **32**, 3993–3998.
- 15 T. Murakami, T. Sato, T. Ohnuki and H. Isobe, *Chem. Geol.*, 2005, **221**, 117–126.
- 16 K. Maher, J. R. Bargar and G. E. Brown, *Inorg. Chem.*, 2013, **52**, 3510–3532.
- 17 C. R. Graves and J. L. Kiplinger, *Chem. Commun.*, 2009, **0**, 3831.
- 18 S. T. Liddle, *Angew. Chem. Int. Ed.*, 2015, **54**, 8604–8641.
- 19 C. Camp, N. Settineri, J. Lefevre, A. R. Jupp, J. M. Goicoechea, L. Maron and J. Arnold, *Chem. Sci.*, 2015, **6**, 6379–6379.
- 20 W. J. Evans, J. R. Walensky, J. W. Ziller and A. L. Rheingold, *Organometallics*, 2009, **28**, 3350–3357.
- 21 M. A. Boreen, B. F. Parker, T. D. Lohrey and J. Arnold, *J. Am. Chem. Soc.*, 2016, **138**, 15865–15868.
- 22 R. K. Thomson, T. Cantat, B. L. Scott, D. E. Morris, E. R. Batista and J. L. Kiplinger, *Nat. Chem.*, 2010, **2**, 723–729.
- 23 L. Chatelain, S. White, R. Scopelliti and M. Mazzanti, *Angew. Chem. Int. Ed.*, 2016, **55**, 14325–14329.
- 24 W. J. Evans, J. R. Walensky and J. W. Ziller, *Organometallics*, 2010, **29**, 945–950.
- 25 A. R. Fox and C. C. Cummins, *J. Am. Chem. Soc.*, 2009, **131**, 5716–5717.
- 26 D. M. King, F. Tuna, E. J. L. McInnes, J. McMaster, W. Lewis, A. J. Blake, and S. T. Liddle,

- Science*, 2012, **337**, 717–720.
- 27 S. Fortier, J. R. Walensky, G. Wu and T. W. Hayton, *J. Am. Chem. Soc.*, 2011, **133**, 11732–11743.
- 28 E. M. Matson, W. P. Forrest, P. E. Fanwick and S. C. Bart, *J. Am. Chem. Soc.*, 2011, **133**, 4948–4954.
- 29 C. L. Webster, J. W. Ziller and W. J. Evans, *Organometallics*, 2014, **33**, 433–436.
- 30 M. B. Jones and A. J. Gaunt, *Chem. Rev.*, 2013, **113**, 1137–1198.
- 31 C. C. Gatto, E. Schulz Lang, A. Kupfer, A. Hagenbach, D. Wille and U. Abram, *Z. Anorg. Allg. Chem.*, 2004, **630**, 735–741.
- 32 J. Huemmer, F. W. Heinemann and K. Meyer, *Inorg. Chem.*, 2017, **56**, 3201–3206.
- 33 M. E. Garner, S. Hohloch, L. Maron and J. Arnold, *Organometallics*, 2016, **35**, 2915–2922.
- 34 M. E. Garner, S. Hohloch, L. Maron and J. Arnold, *Angew. Chem.*, 2016, **128**, 13993–13996.
- 35 T. Loiseau, I. Mihalcea, N. Henry and C. Volkringer, *Coord. Chem. Rev.*, 2014, **266**, 69–109.
- 36 N. S. Settineri, M. E. Garner and J. Arnold, *J. Am. Chem. Soc.*, 2017, **139**, 6261–6269.
- 37 C. Villiers, P. Thuéry and M. Ephritikhine, *Eur. J. Inorg. Chem.*, 2004, **2004**, 4624–4632.
- 38 I. S. R. Karmel, N. Fridman and M. S. Eisen, *Organometallics*, 2015, **34**, 636–643.
- 39 I. S. R. Karmel, T. Elkin, N. Fridman, M. S. Eisen, E. Genizi, Z. Goldschmidt, M. S. Eisen, D.-S. Liu, A. J. Blake, S. T. Liddle, D. E. Morris and J. L. Kiplinger, *Dalton Trans.*, 2014, **43**, 11376.
- 40 W. J. Evans, J. R. Walensky and J. W. Ziller, *Inorg. Chem.*, 2010, **49**, 1743–1749.
- 41 W. Henderson, A. G. Oliver and C. E. F. Rickard, *Inorg. Chim. Acta*, 2000, **307**, 144–148.
- 42 C. Li, R. K. Thomson, B. Gillon, B. O. Patrick and L. L. Schafer, *Chem. Commun.*, 2003, **98**, 2462.
- 43 A. V. Lee and L. L. Schafer, *Eur. J. Inorg. Chem.*, 2007, **2007**, 2245–2255.
- 44 S. A. Ryken and L. L. Schafer, *Acc. Chem. Res.*, 2015, **48**, 2576–2586.
- 45 G. R. Giesbrecht, A. Shafir and J. Arnold, *Inorg. Chem.*, 2001, **40**, 6069–6072.
- 46 A. L. Catherall, M. S. Hill, A. L. Johnson, G. Kociok-Köhn and M. F. Mahon, *J. Mater. Chem. C*, 2016, **4**, 10731–10739.
- 47 M. C. Karunaratne, J. W. Baumann, M. J. Heeg, P. D. Martin and C. H. Winter, *J. Organomet. Chem.*, 2017, **847**, 204–212.
- 48 M. W. Drover, J. A. Love and L. L. Schafer, *Chem. Soc. Rev.*, 2017, **46**, 2913–2940.
- 49 P. Eisenberger, R. O. Ayinla, J. M. P. Lauzon and L. L. Schafer, *Angew. Chem. Int. Ed.*, 2009, **48**, 8361–8365.
- 50 R. K. Thomson, *University of British Columbia dissertation*, 2008.
- 51 F. Gendron and J. Autschbach, *J. Chem. Theory Comput.*, 2016, **12**, 5309–5321.
- 52 R. D. Shannon, *Acta Crystallogr. Sect. A*, 1976, **32**, 751–767.
- 53 C. W. Eigenbrot and K. N. Raymond, *Inorg. Chem.*, 1981, **20**, 1553–1556.
- 54 G. R. Giesbrecht, G. D. Whitener and J. Arnold, *Organometallics*, 2000, **19**, 2809–2812.
- 55 P. Eisenberger, R. O. Ayinla, J. M. P. Lauzon and L. L. Schafer, *Angew. Chem. Int. Ed.*, 2009, **48**, 8361–8365.
- 56 M. J. Monreal, R. K. Thomson, T. Cantat, N. E. Travia, B. L. Scott and J. L. Kiplinger, *Organometallics*, 2011, **30**, 2031–2038.
- 57 SMART: Area Detector Software Package; Bruker Analytical X-ray Systems Inc., Madison, WI, 2003.

- 58 SADABS: Bruker-Nonius Area Detector Scaling and Absorption, V2.05; Bruker Analytical X-ray Systems Inc., Madison, WI, 2003.
- 59 G. M. Sheldrick, *Acta Crystallogr. Sect. A.*, 2007, **64**, 112–122.
- 60 C. L. Barnes, *J. Appl. Crystallogr.*, 1997, **30**, 568–568.
- 61 P. Van Der Sluis and A. L. Spek, *Acta Crystallogr. Sect. A*, 1990, **46**, 194–201.
- 62 A. L. Spek, *Acta Cryst.*, 2015, C71, 9-18.

## Chapter 6

# Amidinate Supporting Ligands Influence Molecularity in Formation of Uranium Nitrides

## Introduction

Uranium nitride molecules and materials have been the subject of intense study in recent years due to the diverse reactivity profile of actinide-ligand multiple bonds<sup>1-7</sup> and the utility of these compounds as model systems for next-generation nuclear fuels.<sup>7-10</sup> Molecular uranium nitride complexes have been shown to facilitate a wide range of chemical transformations, such as C–H activation,<sup>11-14</sup> C–N bond formation,<sup>15-17</sup> and activation of small molecules such as N<sub>2</sub>, H<sub>2</sub>, CO, and CO<sub>2</sub>.<sup>18-21</sup> Haber first discovered that bulk uranium nitrides could be used as effective catalysts for the conversion of N<sub>2</sub> to NH<sub>3</sub> in 1909,<sup>22</sup> and molecular models containing uranium nitride linkages have more recently been shown to undergo nitrogen fixation and conversion to NH<sub>3</sub>.<sup>23</sup> In addition to their versatile reactivity, uranium nitride complexes and clusters have also gathered interest as single-molecule magnets, and the degree of magnetic communication between metal centers has been found to vary substantially based on the ligand environment in these species.<sup>24-28</sup>

Research in uranium nitride chemistry is often motivated by the goal of synthesizing dimensionally-confined analogues that can be used to model the properties of bulk uranium mononitride (UN) fuels.<sup>29-31</sup> UN possesses a higher energy density and greater thermal conductivity than UO<sub>2</sub>, conferring higher power output per unit mass and enhanced safety margins against thermal meltdown.<sup>9,32</sup> However, the chemical reactivity and the electronic and magnetic structure of uranium nitrides are still poorly-studied in comparison to transition metal analogues, motivating the need for well-behaved models that can be used to investigate these fundamental properties.<sup>33,34</sup> Molecular uranium nitrides and related uranium-nitrogen complexes can be developed as versatile models for the physical and chemical properties of UN fuel materials, enabling us to study the electronic/magnetic structure and reactivity of uranium-nitrogen bonds in well-defined homogeneous systems.

Several ligand systems have been demonstrated to provide support for uranium nitride complexes, including azides,<sup>31,35</sup> siloxides,<sup>20,21,27</sup> cyclopentadienyls,<sup>2</sup> amides,<sup>14,36</sup> and triamidoamines.<sup>3,24,25</sup> Despite these advances, synthetic outcomes appear to be highly dependent upon small changes in the supporting ligand environment.<sup>7</sup> Our aim in this present work was to develop new nitride precursors with easily tunable supporting ligands to determine whether we could influence the pathways to – and composition of – any resulting nitride complexes. We chose amidinate ligands for this purpose because of their well-established steric and electronic tunability and because of their precedent as supporting ligands in actinide chemistry for a variety of chemical transformations.<sup>37-46</sup> In addition, amidinate ligands bind to metals only through nitrogen atoms, the latter property being potentially useful in longer term efforts aimed at using these complexes as single-source precursors to uranium nitride materials.<sup>47-51</sup>

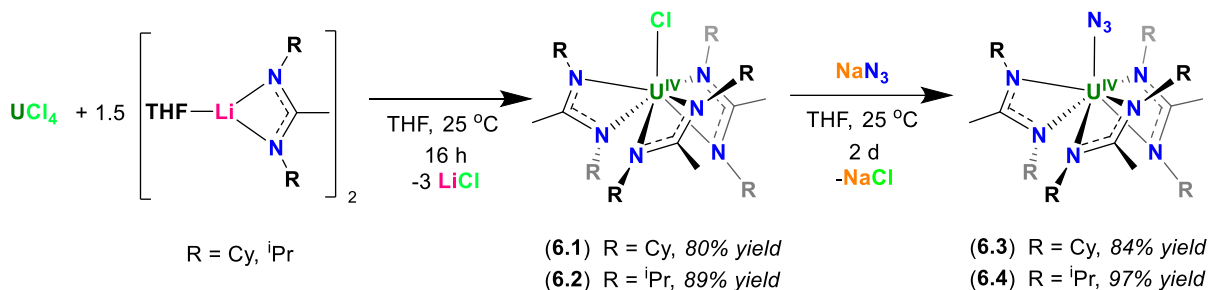
## Results and Discussion

### Synthesis of U(IV) Azide Precursors

The uranium tris(amidinate) complexes UCl(BCMA)<sub>3</sub> (**6.1**) (BCMA = N,N-bis(cyclohexyl)methylamidinate)<sup>52</sup> and UCl(BIMA)<sub>3</sub> (**6.2**) (BIMA = N,N-bis(*iso*-propyl)methylamidinate) were synthesized in good (80–89%) yields via reaction of UCl<sub>4</sub> with 1.5 equivalents of [Li(BCMA)(THF)]<sub>2</sub> and [Li(BIMA)(THF)]<sub>2</sub>, respectively. Salt metathesis of **6.1**

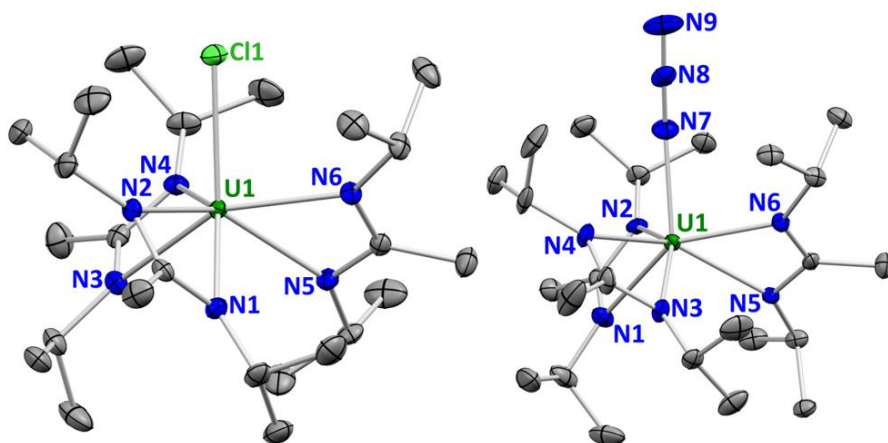


and **6.2** with  $\text{NaN}_3$  generated the azide complexes  $\text{U}(\text{N}_3)(\text{BCMA})_3$  (**6.3**) and  $\text{U}(\text{N}_3)(\text{BIMA})_3$  (**6.4**) in 84% and 97% yield, respectively (Scheme 6.1).



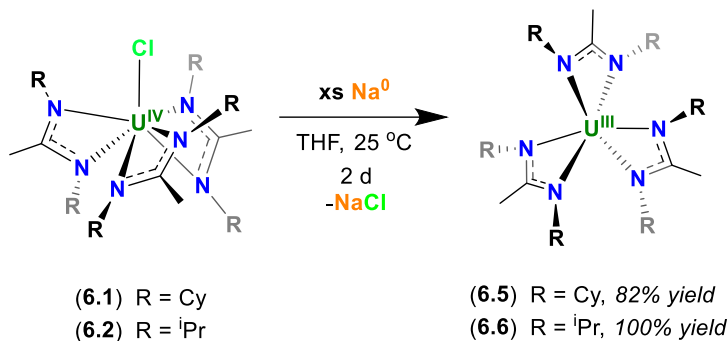
**Scheme 6.1:** Synthesis of  $\text{UCl}(\text{BCMA})_3$  (**6.1**),  $\text{UCl}(\text{BIMA})_3$  (**6.2**),  $\text{U}(\text{N}_3)(\text{BCMA})_3$  (**6.3**), and  $\text{U}(\text{N}_3)(\text{BIMA})_3$  (**6.4**).

The solid-state structures of the tris(amidinate) chloride complex **6.2** and the azide complexes **6.3** and **6.4** displayed pseudo- $C_3$  symmetry with a chloride or azide moiety bound to uranium along the pseudo- $C_3$  axis and  $\kappa^2$ -N,N coordination of all amidinates to the uranium center (Figure 6.1). The crystal structure of **6.4** contains two molecules in the asymmetric unit; these are  $\Delta$  and  $\Lambda$  isomers with similar metrical parameters. The U–Cl distance of 2.673(6) Å in **6.2** is similar to the reported U–Cl distance of 2.678(1) Å in complex **6.1**.<sup>52</sup> Comparison of the U– $\text{N}_{\text{amidinate}}$  distances in **6.3** and **6.4** (2.366(6)–2.502(2) Å), as well as the U– $\text{N}_{\text{azide}}$  distances (2.340(6) in **6.3** and 2.335(3) in **6.4**, see Table 6.4 for full analysis) shows no significant difference in U–N bond lengths for these two ligand systems.



**Figure 6.1:** X-ray crystal structure of **6.2** (left) and **6.4** (right) shown with 50% probability ellipsoids. Hydrogen atoms are omitted for clarity.

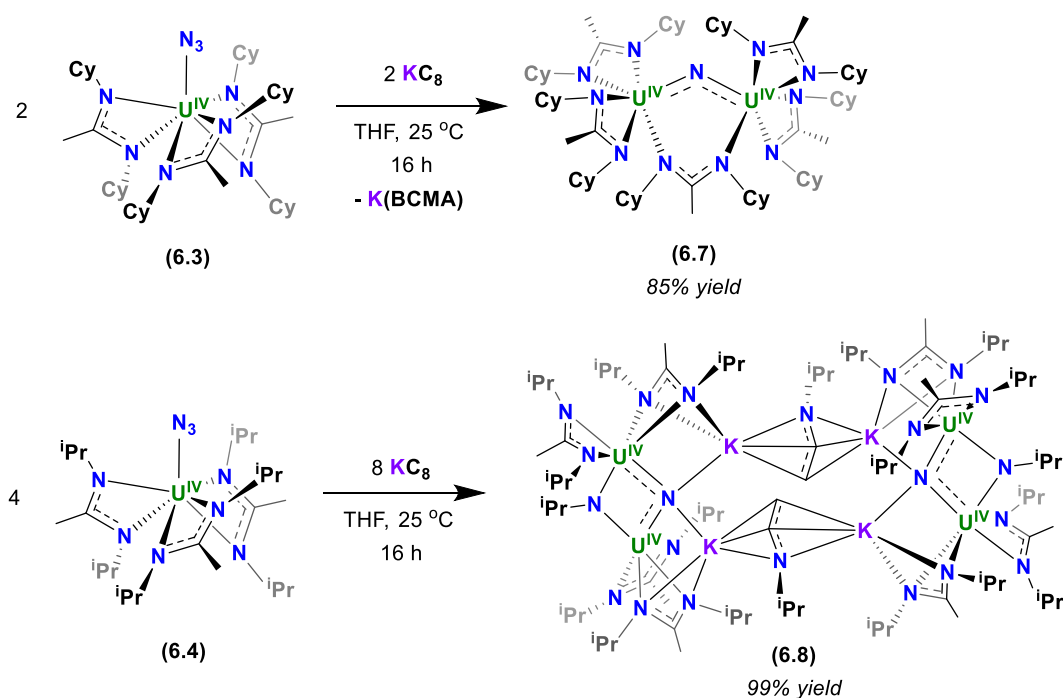
Reduction of the U(IV) chloride complexes **6.1** and **6.2** with metallic sodium in THF gave the dark blue homoleptic U(III) tris(amidinate) complexes U(BCMA)<sub>3</sub> (**6.5**)<sup>52</sup> and U(BIMA)<sub>3</sub> (**6.6**), respectively, in excellent (95-100%) yields (Scheme 6.2).



*Scheme 6.2: Synthesis of U(BCMA)<sub>3</sub> (6.5) and U(BIMA)<sub>3</sub> (6.6).*

### Synthesis of Uranium Nitrides

We next sought to determine if reduction of the azide moieties on **6.3** and **6.4** could facilitate the formation of molecular uranium nitride species by loss of N<sub>2</sub>. Photolysis of **6.3** and **6.4** with ultraviolet light yielded an intractable mixture of products, and heating these compounds to decomposition yielded insoluble and amorphous solid products. Consequently, we turned to chemical and electrochemical redox reactions. To investigate the redox behavior of **6.3** and **6.4**, we performed cyclic voltammetry in THF using [(<sup>n</sup>Bu)<sub>4</sub>N][PF<sub>6</sub>] as the supporting electrolyte. Complex **6.3** was found to undergo a reversible oxidation at  $E_{1/2} = -0.49$  V vs Fc/Fc<sup>+</sup> ( $\Delta E = 0.17$  V) and an irreversible reduction at  $E_{pc} = -3.42$  V, while complex **6.4** underwent a reversible oxidation at  $E_{1/2} = -0.29$  V vs Fc/Fc<sup>+</sup> ( $\Delta E = 0.15$  V) and an irreversible reduction at  $E_{pc} = -3.21$  V (Figures 6.8 and 6.9).



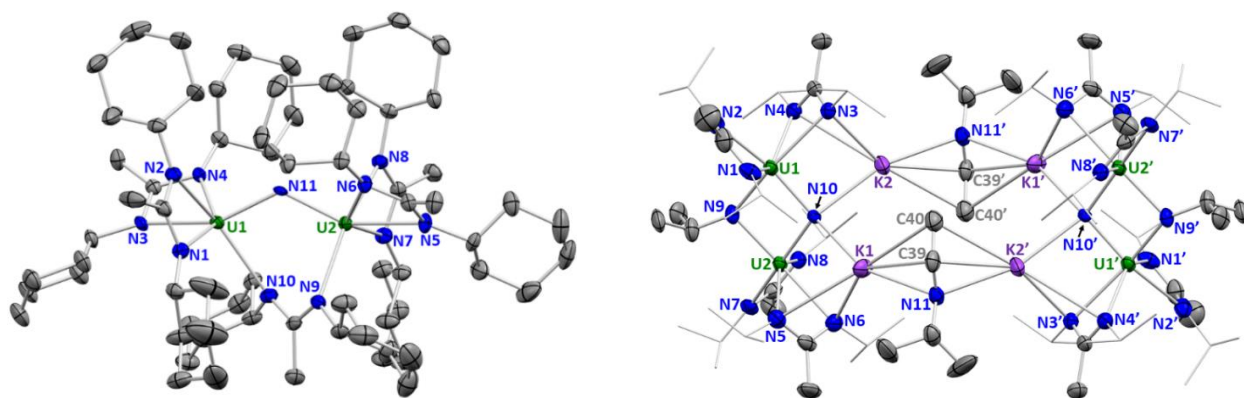
**Scheme 6.3:** Synthesis of the bridging U(IV)–U(IV) nitride  $[U(\text{BCMA})_2]_2(\mu\text{-N})(\mu\text{-}\kappa^1:\kappa^1\text{-BCMA})$  (**6.7**) and the tetra-U(IV) cluster  $[(U(\text{BIMA})_2)_2(\mu\text{-N})(\mu\text{-N}^i\text{Pr})-(\text{K}_2(\mu\text{-}\eta^3:\eta^3\text{-CH}_2\text{CHN}^i\text{Pr}))_2]$  (**6.8**) by reaction of the U(IV) azides **6.3** and **6.4**, respectively, with  $\text{KC}_8$ .

Consistent with these findings, chemical reduction of **6.3** with one equivalent of  $\text{KC}_8$  in THF did not result in a simple electron transfer, instead yielding a new red product (**6.7**). X-ray crystallography revealed **6.7** to be an unusual dinuclear uranium complex, with the two metals bridged by a nitride moiety and an amidinate. An interesting oxidative route and details of the X-ray structure of **6.7** will be discussed below (Scheme 6.4). When two equivalents of  $\text{KC}_8$  were added to a THF solution of **6.3**, the tris(amidinate) U(III) species **6.5** was isolated as the major product (70% yield, Scheme 6.3), and **6.7** was also isolated in 11% yield by fractional crystallization from hexane. In contrast, reduction of the <sup>i</sup>Pr analog **6.4** with one equivalent of  $\text{KC}_8$  in THF gave an intractable mixture of products. However, when two equivalents of  $\text{KC}_8$  were added to **6.4** in THF, the solution quickly changed color from green to blue, then again to red within 15 minutes. X-ray diffraction studies of the resulting product revealed an octametallic cluster (**6.8**) containing four uranums, four potassiums, and two bridging nitrides (99% yield, Scheme 6.3). Of particular interest in the structure of **6.8** was the presence of imido ( $(\text{N}^i\text{Pr})^{2-}$ ) and vinylamido ( $(\text{CH}_2\text{CHN}^i\text{Pr})^-$ ) fragments, no doubt formed by reductive cleavage of the amidinate ligands, which results in a unique structure in which all four uranium atoms are N-bound to ligands having formal mono-, di-, and tri-anionic character. Related fragmentation of amidinate ligands, though rare, has been documented in zirconium systems.<sup>53</sup>

Complex **6.8** crystallizes on an inversion center in the space group  $\text{P}\bar{1}$  with an asymmetric unit containing two uranium and two potassium atoms connected through bridging vinylamido moieties (Figure 6.2). Each uranium atom has two amidinate ligands coordinated in a  $\kappa^2\text{-N,N}$  geometry with  $\text{U-N}_{\text{amidinate}}$  distances of 2.452(7)–2.618(7) Å, although one of these ligands on each uranium displays inequivalent bridging  $\kappa^2\text{-N,N}$  contacts to a potassium atom, with  $\text{K-}$

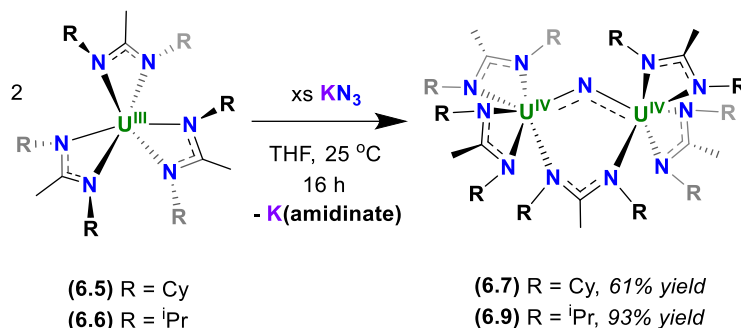
$N_{\text{amidinate}}$  distances ranging from 2.839(8) to 3.342(5) Å. The imido fragment bridging the uranium centers displays U1–N9 and U2–N9 distances of 2.187(7) and 2.233(5) Å, respectively, and a U1–N9–U2 angle of 100.1(2)°. The nitride moiety bridges the uranium centers as well, with slightly shorter U1–N10 and U2–N10 distances of 2.132(5) and 2.101(6) Å, respectively, and a U1–N10–U2 angle of 106.4(2)°. These U– $N_{\text{nitride}}$  bonds are slightly (0.01 to 0.08 Å) longer than the reported values for U– $N_{\text{nitride}}$  bonds in the bridging nitride clusters  $[(C_5Me_4R)_2U(\mu-N)U(\mu-N_3)(C_5Me_4R)_2]_4$ <sup>31</sup> and  $[K(DME)_4][\{K(DME)(Et_8\text{-calix}[4]\text{tetrapyrrole}U\}_2(\mu-NK)_2)]$ .<sup>54</sup> The nitride ligands in **6.8** are also in contact with two potassium atoms, with K–N10 distances of 2.779(6) and 2.789(6) Å. In addition to interactions with amidinate and nitride ligands, each potassium is also bound to the bridging vinylamido fragments in a  $\mu\text{-}\eta^3:\eta^3$  coordination mode.

Following isolation of these distinctly different uranium nitride compounds via  $KC_8$  reduction of **6.3** and **6.4**, we sought to investigate whether a dinuclear uranium nitride analogous to **6.7** could be isolated, as this would provide access to a second uranium nitride complex stabilized by the BIMA ligand system and also demonstrate control over product nuclearity.



**Figure 6.2:** X-ray crystal structures of  $[U(BCMA)_2]_2(\mu-N)(\mu\text{-}\kappa^1:\kappa^1\text{-BCMA})$  (**6.7**) (left) and  $[(U(BIMA)_2)_2(\mu-N)(\mu\text{-}N^iPr)(K_2(\mu\text{-}\eta^3:\eta^3\text{-CH}_2\text{CHN}^iPr)_2]$  (**6.8**) (right) shown with 50% probability ellipsoids. Hydrogen atoms are omitted and amidinate isopropyl groups in **6.8** are shown in wireframe for clarity.

Direct oxidation of **6.6** with  $\text{KN}_3$  proved effective, giving the dinuclear uranium nitride  $[\text{U}(\text{BIMA})_2]_2(\mu\text{-N})(\mu\text{-}\kappa^1:\kappa^1\text{-BIMA})$  (**6.9**) in 93% yield. Similarly, oxidation of **6.5** with  $\text{KN}_3$  resulted in the formation of **6.7**, giving the desired product in 61% yield (Scheme 6.4). In these reactions, two equivalents of the U(III) amidinates **6.5** or **6.6** react with one equivalent of  $\text{KN}_3$ , forming the dinuclear U(IV)–U(IV) nitrides **6.7** and **6.9** by reduction of the azide to a nitride and  $\text{N}_2$ , with concomitant precipitation of  $\text{K}(\text{BCMA})$  or  $\text{K}(\text{BIMA})$ .



**Scheme 6.4:** Synthesis of the bridging U(IV)–U(IV) nitrides  $[\text{U}(\text{BCMA})_2]_2(\mu\text{-N})(\mu\text{-}\kappa^1:\kappa^1\text{-BCMA})$  (**6.7**) and  $[\text{U}(\text{BIMA})_2]_2(\mu\text{-N})(\mu\text{-}\kappa^1:\kappa^1\text{-BIMA})$  (**6.9**) by oxidation of the homoleptic U(III) amidinates **6.5** and **6.6** with  $\text{KN}_3$ .

The solid-state structures of **6.7** (Figure 6.2) and **6.9** (not shown) are very similar, with two uranium centers bridged by a nitride and a  $\mu\text{-}\kappa^1:\kappa^1$  bound amidinate ligand (see Table 6.5 for full comparison). Compounds **6.7** and **6.9** contain U–N<sub>nitride</sub> bond lengths ranging from 2.023(3) to 2.057(3) Å and U1–N11–U2 angles of 127.0(2)<sup>o</sup> and 133.6(2)<sup>o</sup>, respectively; these metrics are within the typical range reported for U(IV)–U(IV) bridging nitrides.<sup>1,7</sup> The bridging amidinate ligands in both **6.7** and **6.9** adopt a  $\mu\text{-}\kappa^1:\kappa^1$  coordination mode, with each nitrogen atom bound to distinct uranium centers and U1–N10 and U2–N9 distances ranging from 2.485(3) to 2.563(2) Å. In the  $\kappa^2\text{-N,N}$  bound amidinates, U–N<sub>amidinate</sub> bond distances range from 2.422(4) to 2.577(4) Å.

Although we were able to synthesize both the BCMA- and BIMA-supported dinuclear complexes **6.7** and **6.9** via direct oxidation of **6.5** and **6.6** with  $\text{KN}_3$ , the different outcomes from reduction of the azide complexes **6.3** (R = Cy) versus **6.4** (R = <sup>i</sup>Pr) is pronounced and was surprising at first given the similarity of the amidinate ligands used. We note, however, that the cyclohexyl substituents on the BCMA ligand in **6.3** result in an overall much larger steric profile than the *iso*-propyl substituents on the BIMA ligand, thereby hindering formation of an analogous tetra-uranium cluster. The tetra-uranium cluster **6.8** could also be accessed in 68% yield by reduction of **6.9** (R = <sup>i</sup>Pr) with two equivalents of  $\text{KC}_8$ , but no new uranium products were formed when **6.7** (R = Cy) was used instead. These findings further confirm the notion that small differences in ligand sterics may lead to rather different product outcomes in uranium chemistry.<sup>55</sup>

### Acid Hydrolysis and <sup>15</sup>N Labeling

Since the structural parameters of bridging uranium nitrido and oxo complexes determined by X-ray diffraction are often quite similar,<sup>1</sup> we sought to confirm the identity of the nitride moieties through chemical means. In particular, we recognized that simple acid hydrolysis of **6.7**–**6.9** would be expected to form ammonium salts from bridging nitride but not from bridging oxo moieties.<sup>24,56</sup> Excess HCl (4.0 M in 1,4-dioxane) was added to Et<sub>2</sub>O solutions of **6.7**–**6.9**, giving

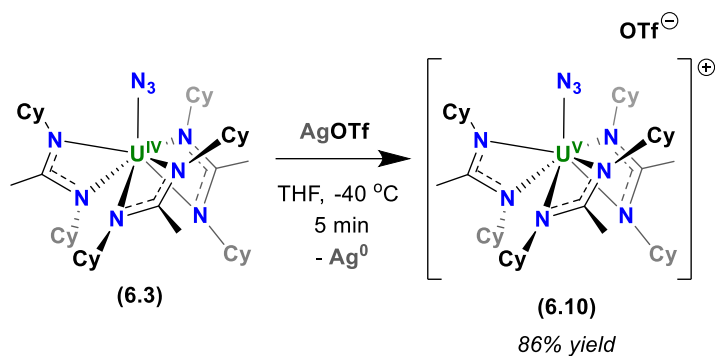
nearly colorless mixtures of decomposition products from each compound. After removal of the solvent, the soluble products were extracted into  $d_6$ -DMSO. The characteristic 1:1:1 triplet of  $\text{NH}_4\text{Cl}$  was evident in the  $^1\text{H}$  NMR spectra for all three nitrides, confirming ammonium formation via acid hydrolysis of **6.7-6.9** (see SI for further details).

To provide additional evidence that the nitride moieties in these complexes were formed via reduction of azide, we prepared the labeled nitride complexes **6.7- $^{15}\text{N}$**  and **6.9- $^{15}\text{N}$**  by stirring **6.5** and **6.6** in THF with  $^{15}\text{N}$ -labeled  $\text{NaN}_3$  labeled solely at one terminal position. Similarly, we prepared **6.8- $^{15}\text{N}$**  via reduction of **6.4- $^{15}\text{N}$**  (formed by salt metathesis of **6.2** with  $^{15}\text{N}$ -labeled  $\text{NaN}_3$ ) with  $\text{KC}_8$ . If the nitride moieties in **6.7- $^{15}\text{N}$** , **6.8- $^{15}\text{N}$** , and **6.9- $^{15}\text{N}$**  were indeed formed by reduction of the azide substituents, these complexes would be expected to contain approximately 50%  $^{15}\text{N}$  for each nitride atom, corresponding to a roughly equal chance that the  $^{15}\text{N}$ -labeled atom in each equivalent of  $\text{NaN}_3$  would be incorporated as a nitride or lost as  $\text{N}_2$ . Accordingly, one U–N stretch would be expected in the IR spectra of **6.7**, **6.8**, and **6.9**, and two U–N stretches would be expected in the IR spectra of **6.7- $^{15}\text{N}$** , **6.8- $^{15}\text{N}$** , and **6.9- $^{15}\text{N}$** , with the U– $^{15}\text{N}$  stretches at slightly lower energies than the U– $^{14}\text{N}$  stretches.

To avoid overlap with Nujol in the pertinent regions, the labeled and unlabeled versions of each complex were dissolved in pentane and drop-cast onto KBr plates. The U– $^{14}\text{N}$  stretches in **6.7**, **6.8**, and **6.9** were observed at 740, 730, and 729  $\text{cm}^{-1}$ , respectively, and additional U– $^{15}\text{N}$  stretches in **6.7- $^{15}\text{N}$** , **6.8- $^{15}\text{N}$** , and **6.9- $^{15}\text{N}$**  were also observed at 724, 704, and 711  $\text{cm}^{-1}$ , respectively (Figures S31-S36). In addition to yielding rare quantitative data regarding the energy of U–N stretching frequencies in bridging uranium nitrides, these results also provide further evidence for the formation of the nitride moieties in **6.7-6.9** through an azide reduction mechanism. Following these IR studies, **6.7- $^{15}\text{N}$** , **6.8- $^{15}\text{N}$** , and **6.9- $^{15}\text{N}$**  were hydrolyzed with HCl as described above, and a multiplet corresponding to a statistical mixture of  $^{15}\text{NH}_4\text{Cl}$  and  $^{14}\text{NH}_4\text{Cl}$  was observed in the  $^1\text{H}$  NMR spectra of these complexes (see SI for further details).

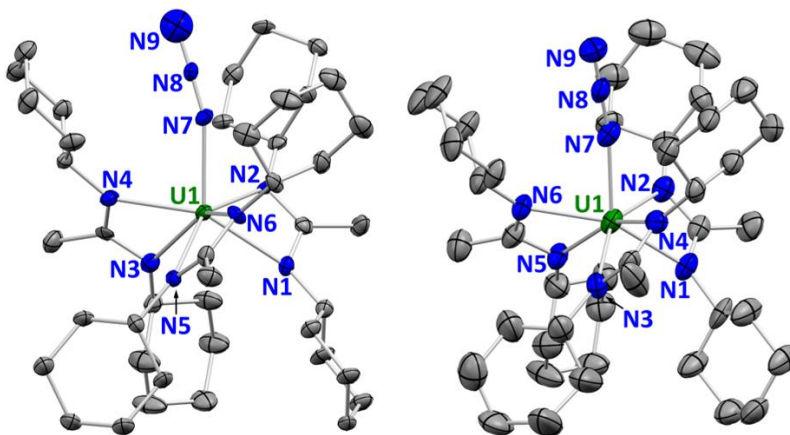
## Magnetism

Following the synthesis of the uranium nitride complexes **6.7-6.9**, we sought to develop a series of related U(III), U(IV), and U(V) complexes that could be used as a benchmark for the magnetic behavior in these amidinate systems, therefore allowing us to accurately assign the oxidation state of the uranium atoms in **6.7-6.9** and enabling us to distinguish structure-based effects from oxidation state-dependent magnetic behavior. Upon addition of a THF solution of silver(I) triflate to the U(IV) azide complex **6.3**, the solution immediately changed from green to black. The cationic U(V) complex  $[\text{U}(\text{N}_3)(\text{BCMA})_3](\text{OTf})$  (**6.10**) was isolated as a black crystalline solid in 86% yield (Scheme 6.5). Complex **6.10** was found to be thermally unstable, undergoing complete decomposition to an intractable mixture of unidentified products within one hour at room temperature as observed by  $^1\text{H}$  NMR; nonetheless, storage of solid samples at  $-40$   $^\circ\text{C}$  was sufficient to prevent any noticeable degradation over a period of months. Similarly to **6.3** and **6.4**, photolysis of **6.10** in THF resulted in an intractable mixture of products.



**Scheme 6.5:** Synthesis of  $[U(N_3)(BCMA)_3](OTf)$  (**6.10**).

Single crystal X-ray crystallographic data for **6.3** and **6.10** revealed that both possess distorted  $C_3$  symmetry, each with all three of their amidinate ligands displaying  $\kappa^2$ -N,N chelation to the uranium center and an azide moiety protruding outward along the pseudo- $C_3$  axis (Figure 6.3). Although the connectivity in these two complexes is identical, the U–N bond lengths in **6.10** are all roughly  $\sim 0.1$  Å shorter than in **6.3** (Table 6.1), likely due to the increased charge and decreased ionic radius of U(V) versus U(IV).<sup>57</sup>

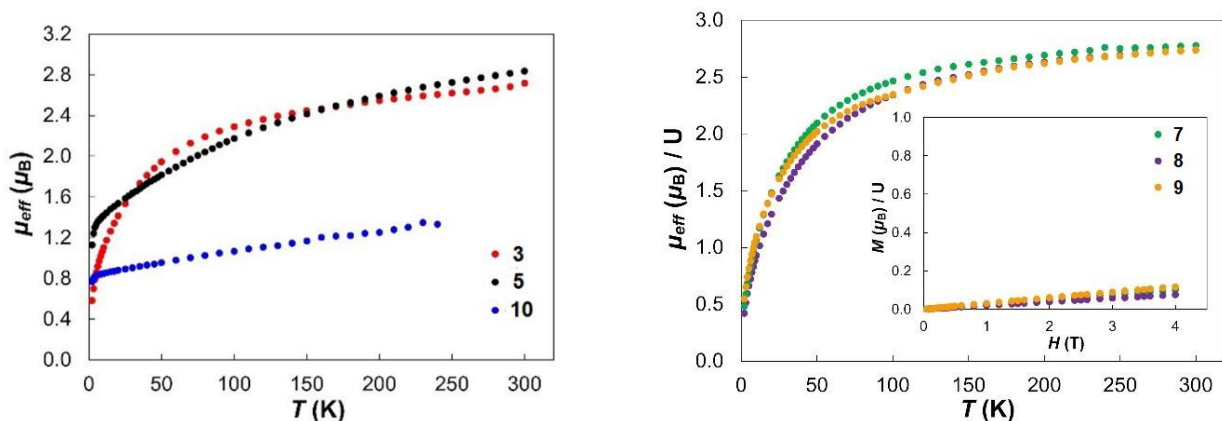


**Figure 6.3:** X-ray crystal structures of the neutral U(IV) azide **6.3** (left) and its cationic U(V) analogue **6.10** (right) shown with 50% probability thermal ellipsoids. Hydrogen atoms and an outer-sphere triflate counteranion in **6.10** are omitted for clarity. Complex **6.10** crystallizes with two formula units in the asymmetric unit; both formula units exhibit similar bond metrics. Only one formula unit is depicted here.

**Table 6.1:** Selected atomic distances (Å) for **6.3** and **6.10**.

Atoms	6.3	6.10
U1–N1	2.478(5)	2.365(8)
U1–N2	2.392(4)	2.290(7)
U1–N3	2.441(6)	2.328(8)
U1–N4	2.366(6)	2.318(9)
U1–N5	2.502(2)	2.351(9)
U1–N6	2.373(5)	2.302(7)
U1–N7	2.340(6)	2.269(8)
N7–N8	1.154(8)	1.22(2)
N8–N9	1.17(1)	1.13(2)

Magnetic susceptibility data for the U(III), U(IV), and U(V) BCMA complexes **6.5**, **6.3**, and **6.10** are shown as plots of  $\mu_{\text{eff}}$  as a function of temperature in Figure 4 (*left*). While room-temperature magnetic moments are known to be insufficient to distinguish U(IV) and U(III) in most cases,<sup>60</sup> it is worth noting that the  $\mu_{\text{eff}}$  value of **6.5** ( $2.84 \mu_{\text{B}}$ ) is lower than most reported values for U(III) species, and only slightly larger than **6.3**, which is consistent with U(IV).<sup>58–60</sup> The data for **6.10** was collected only up to 240 K due to the compound’s thermal sensitivity; the  $\mu_{\text{eff}}$  value at 240 K ( $1.33 \mu_{\text{B}}$ ) is comparable to reported values for other U(V) complexes.<sup>58–60</sup> The low-temperature data are more informative, as the moment of a  $5f^2$  U(IV) complex should decrease sharply toward a diamagnetic ground state at low temperature.<sup>4,60</sup>



**Figure 6.4:** Variable-temperature molar magnetic data ( $\mu_{\text{eff}}$ ) for **6.3** (red), **6.5** (black), and **6.10** (blue), (*left*). Variable-temperature molar magnetic data ( $\mu_{\text{eff}}$ ) for **6.7** (green), **6.8** (purple), and **6.9** (orange) (per uranium ion) and variable field data collected at 5 K (*inset*) (*right*).



Upon cooling, the  $\mu_{\text{eff}}$  values decreased steadily to  $1.13 \mu_{\text{B}}$  and  $0.76 \mu_{\text{B}}$  at 2 K for **6.5** and **6.10**, respectively, but more drastically to  $0.58 \mu_{\text{B}}$  for **6.3**. This behavior is consistent with a decrease in moments upon cooling resulting from the depopulation of crystal field levels of the uranium ions. No saturation of the magnetization in the field dependent measurement was observed at 5 K for **6.3**, also characteristic of a U(IV) species (Figure 6.10).<sup>61–63</sup> In addition, no significant difference in moments was observed between the BCMA and BIMA complexes, showing that the specific supporting ligand system minimally affects the resulting magnetic properties of these structurally similar molecules (Figure 6.12). As a result, the magnetic data indicate the oxidation states of **6.3**, **6.5**, and **6.10** as U(IV), U(III), and U(V), respectively.

Magnetic susceptibility curves for the uranium nitride complexes are shown in Figure 6.4 (*right*). No significant difference in magnetic moments (per uranium) was observed between the three nitrides **6.7–6.9** in the temperature range of 2–300 K. The room-temperature moments ( $2.74 \mu_{\text{B}}$ ) for all three complexes were consistent with the values of the monomeric U(IV) tris(amidinate) azide complexes **6.3** and **6.4**. No saturation of the magnetization in the field dependent measurement was observed at 5 K.

## Summary and Conclusions

With the discovery of these three new uranium nitrides resulting from amidinate-supported uranium precursors, we have built on the burgeoning body of recent work in this area in several significant aspects. Two different synthetic strategies were employed to access these nitride complexes: i) chemical reduction of a U(IV) azide with  $\text{KC}_8$ ; and ii) reaction of a U(III) starting material with an alkali metal azide. These two methods led to the same di-uranium nitride product when the BCMA ligand was used as a supporting ligand, but they yielded distinct di- and tetra-nuclear uranium complexes from the less bulky BIMA-supported precursors. In addition,  $^{15}\text{N}$  labeling, IR spectroscopy, and acid hydrolysis experiments confirmed the presence of the bridging nitride moieties in all three complexes. Magnetic susceptibility measurements showed oxidation state-dependent magnetic behavior for a series of related U(III), U(IV), and U(V) amidinates and confirmed a U(IV) oxidation state for the uranium atoms in all three nitrides.

## Experimental

### Materials and Methods

Unless otherwise noted, all syntheses were performed using standard Schlenk techniques under an atmosphere of nitrogen or in an MBraun glovebox under an atmosphere of nitrogen. Glassware, cannulae, and Celite were stored in an oven at  $160 \text{ }^\circ\text{C}$  for at least 12 hours prior to use.  $3 \text{ \AA}$  and  $4 \text{ \AA}$  molecular sieves were activated by heating under vacuum at  $300 \text{ }^\circ\text{C}$  for 24 hours.  $^1\text{H}$  and  $^{13}\text{C}$  NMR spectra were recorded at room temperature using Bruker AV-600, AV-500, AVB-400, AVQ-400, and AV-300 spectrometers.  $^1\text{H}$  chemical shifts were referenced to  $\text{C}_6\text{D}_5\text{H}$  ( $\delta = 7.16$  ppm),  $\text{C}_4\text{D}_7\text{HO}$  ( $\delta_2 = 1.78$  ppm), or  $\text{C}_2\text{D}_5\text{HSO}$  ( $\delta = 2.50$  ppm).  $^{13}\text{C}$  chemical shifts were referenced to  $\text{C}_6\text{D}_6$  ( $\delta = 128.39$  ppm). Unless otherwise specified, samples for IR spectroscopy were prepared as Nujol mulls, and spectra were taken in KBr plates using a Nicolet iS10 spectrometer. Melting points were determined in sealed tubes under an atmosphere of nitrogen using a Stanford Research Systems OptiMelt instrument and are reported uncorrected. Hexane, pentane, toluene, benzene,

diethyl ether (Et<sub>2</sub>O), tetrahydrofuran (THF), and acetonitrile were purified by passage through a column of activated alumina prior to use. C<sub>6</sub>D<sub>6</sub> and d<sub>8</sub>-THF were purchased from Cambridge Isotope Labs and stored over 4 Å molecular sieves. UCl<sub>4</sub>,<sup>64</sup> [Li(BCMA)(THF)]<sub>2</sub> (BCMA = N,N-bis(cyclohexyl)methyl amidinate),<sup>65</sup> [Li(BIMA)(THF)]<sub>2</sub> (BIMA = N,N-bis(*iso*-propyl)methyl amidinate),<sup>66</sup> UCl(BCMA)<sub>3</sub> (**6.1**),<sup>65</sup> and U(BCMA)<sub>3</sub> (**6.5**)<sup>65</sup> were prepared according to literature methods. Unless otherwise specified, all other chemicals were purchased from commercial sources and used as received.

## Synthesis of Compounds

**UCl(BIMA)<sub>3</sub> (6.2):** A THF solution (8 mL) of [Li(BIMA)(THF)]<sub>2</sub> (550 mg, 1.25 mmol) was added via cannula to a stirred THF suspension (2 mL) of UCl<sub>4</sub> (300 mg, 0.790 mmol). The resulting solution was stirred for 16 h, then the solvent was removed *in vacuo*. The product was triturated with hexane (10 mL), then extracted into toluene (15 mL). The resulting cloudy green suspension was left to settle for 12 h, then filtered via cannula. This solution was then concentrated to a final volume of 8 mL and cooled to -40 °C, yielding green crystals. (507 mg, 89% yield)

<sup>1</sup>H NMR (C<sub>6</sub>D<sub>6</sub>, 400 MHz): δ 21.67 (broad, 6H, CH(CH<sub>3</sub>)<sub>2</sub>), 2.58 (s, 9H, NCCH<sub>3</sub>), 0.18 (s, 36H, CH(CH<sub>3</sub>)<sub>2</sub>).

IR (cm<sup>-1</sup>): 2598 (w), 1654 (m), 1359 (s), 1336 (s), 1311 (s), 1197 (s), 1175 (s), 1137 (m), 1123 (s), 1053 (m), 1012 (m), 806 (s), 618 (m), 572 (m), 543 (m).

EA calcd for C<sub>24</sub>H<sub>51</sub>ClN<sub>6</sub>U: C: 41.35%, H: 7.37%, N: 12.05%. Found: C: 41.27%, H: 7.49%, N: 11.96%.

Melting point: decomposes above *ca.* 123 °C.

**U(N<sub>3</sub>)(BCMA)<sub>3</sub> (6.3):** THF (100 mL) was added *via* cannula to a flask containing **6.1** (2.03 g, 2.17 mmol) and NaN<sub>3</sub> (160 mg, 2.46 mmol). The resulting solution was stirred for 3 d, then the solvent was removed *in vacuo*. The product was triturated with hexane (25 mL), then extracted into toluene (25 mL). The resulting cloudy green suspension was then filtered, concentrated to a final volume of 15 mL, and cooled to -40 °C for 7 d, yielding green crystals. (1.72 g, 84% yield)

<sup>1</sup>H NMR (C<sub>6</sub>D<sub>6</sub>, 500 MHz): δ 19.97 (broad, 6H, NCHCH<sub>2</sub>), 1.47 (m, *Cy-H*), 1.37 (m, *Cy-H*), 1.11 (s, *Cy-H*), 0.47 (q, *Cy-H*), -0.86 (s, 9H, NCCH<sub>3</sub>).

IR (cm<sup>-1</sup>): 2081 (s), 1654 (w), 1363 (m), 1529 (w), 1191 (w), 1174 (w), 1075 (w), 997 (w), 887 (w), 824 (w), 799 (w).

EA calcd for C<sub>42</sub>H<sub>75</sub>N<sub>9</sub>U: C: 53.39%, H: 8.01%, N: 13.35%. Found: C: 53.78%, H: 7.80%, N: 13.15%.

Melting point: 271-273 °C; boiling point: 292 °C.

**U(N<sub>3</sub>)(BIMA)<sub>3</sub> (6.4):** THF (4 mL) was added to a vial containing **6.2** (91 mg, 0.131 mmol) and NaN<sub>3</sub> (17 mg, 0.261 mmol). The green solution was stirred for 8 d, then the solvent was removed *in vacuo* and the resulting green solids were triturated with hexane (2 mL). The product was extracted into hexane (8 mL), filtered, concentrated to a volume of 5 mL, and cooled to -40 °C, yielding green crystals. (89 mg, 97% yield)

**U(N<sub>3</sub>\*) (BIMA)<sub>3</sub> (6.4-<sup>15</sup>N):** The same general procedure as above was used, with NaN<sub>3</sub> (<sup>15</sup>N labeled at terminal position) used in place of unlabeled NaN<sub>3</sub>. (83 mg, 82% yield)

<sup>1</sup>H NMR (C<sub>6</sub>D<sub>6</sub>, 500 MHz): δ 19.82 (broad, 6H, CH(CH<sub>3</sub>)<sub>2</sub>), 0.44 (s, 9H, NCCH<sub>3</sub>), 0.41 (s, 36H, CH(CH<sub>3</sub>)<sub>2</sub>).

IR (cm<sup>-1</sup>): 2083 (s), 1333 (s), 1313 (m), 1199 (s), 1137 (w), 1123 (m), 1048 (w), 1014 (m), 805 (m), 617 (m), 603 (w), 572 (w), 542 (w).

EA calcd for C<sub>24</sub>H<sub>51</sub>N<sub>9</sub>U: C: 40.96%, H: 7.30%, N: 17.91%. Found: C: 40.57%, H: 7.07%, N: 17.82%.

Melting point: decomposes above *ca.* 272 °C.

**U(BIMA)<sub>3</sub> (6):** Na (20 mg, 0.870 mmol) was added to a THF solution (5 mL) of **6.2** (259 mg, 0.371 mmol). The green solution was stirred for 2 d, slowly turning blue over the course of the reaction. The solvent was removed *in vacuo* and the resulting dark blue solids were triturated with hexane (2 mL). The product was extracted into hexane (3 mL), filtered, concentrated to a volume of 1 mL, and cooled to -40 °C, yielding dark blue crystals (142 mg). The solvent was then removed *in vacuo* from the mother liquor to give dark blue solids, which were also found to be analytically pure by <sup>1</sup>H NMR spectroscopy. (246 mg, 100% yield) Attempts to grow X-ray quality crystals of **6.6** from hexane, pentane, HMDSO, triethylsilane, and tetramethylsilane were hindered by poor diffraction of the crystals in all cases.

<sup>1</sup>H NMR (C<sub>6</sub>D<sub>6</sub>, 500 MHz): δ 25.61 (s, 6H, CH(CH<sub>3</sub>)<sub>2</sub>), 12.17 (s, 9H, NCCH<sub>3</sub>), -5.28 (s, 36H, CH(CH<sub>3</sub>)<sub>2</sub>).

IR (cm<sup>-1</sup>): 1482 (s), 1358 (m), 1332 (m), 1312 (m), 1194 (m), 1171 (m), 1133 (w), 1121 (w), 1046 (w), 1015 (w), 890 (w), 819 (w), 797 (w), 617 (w), 568 (w), 542 (w), 509 (w).

EA calcd for C<sub>24</sub>H<sub>51</sub>N<sub>6</sub>U: C: 43.56%, H: 7.77%, N: 12.70%. Found: C: 43.39%, H: 7.56%, N: 12.55%.

Melting point: decomposes above *ca.* 110 °C.

#### [U(BCMA)<sub>2</sub>]<sub>2</sub>(μ-N)(μ-κ<sup>1</sup>:κ<sup>1</sup>-BCMA) (6.7):

**Method 1:** A THF suspension (0.5 mL) of KC<sub>8</sub> (14 mg, 0.106 mmol) was added to a THF solution (1.5 mL) of **6.3** (100 mg, 0.106 mmol). The green solution turned reddish-brown upon addition of KC<sub>8</sub>. The solution was stirred for 16 h, then the solvent was removed *in vacuo*. The product was extracted into pentane (3 mL) and filtered, then the solvent was removed *in vacuo* and the product was re-extracted into pentane (3 mL) and filtered again. The solvent was removed *in vacuo* a final time to give the product as a red solid (72 mg, 85% yield).

**Method 2:** A THF suspension (2 mL) of KC<sub>8</sub> (13 mg, 0.100 mmol) was added to a THF solution (3 mL) of **6.3** (47 mg, 0.050 mmol). The green solution immediately turned dark blue upon addition of KC<sub>8</sub>. The solution was stirred for 20 mins, then filtered, and the solvent was removed *in vacuo*. The product was extracted into hexane (3 mL), filtered, concentrated to 2 mL, and cooled to -40 °C for 24 h, yielding dark blue crystals of **6.5**. These crystals were harvested and the mother liquor was concentrated to a volume of 1 mL, then cooled again, yielding more crystals of **6.5**. The mother liquor, now red, was concentrated to a volume of 0.5 mL, then cooled once more, yielding **6.7** as red crystals (5 mg, 11% yield).

‡ The product distribution of **6.5** and **6.7** formed in this reaction was not significantly affected by cooling the reaction vessel to -40 °C, using toluene in place of THF, using sodium metal in place of KC<sub>8</sub>, or changing the concentration of the reaction mixture — we consistently isolated **6.5** in *ca.* 70% yield and **6.7** in *ca.* 10% yield.

**Method 3:** A THF suspension (2 mL) of KN<sub>3</sub> (91 mg, 1.12 mmol) was added to a THF solution (3 mL) of **6.5** (201 mg, 0.223 mmol). The dark blue solution turned red over the course of the reaction. The solution was stirred for 2 d, then the solvent was removed *in vacuo*, and the resulting red solids were triturated twice with hexane (2 mL). The product was extracted into pentane (4

mL), then the solvent was removed *in vacuo* to give the product as an analytically pure red solid (108 mg, 61% yield). Crystals suitable for x-ray diffraction were grown from pentane.

‡ The stoichiometry of this reaction only requires ½ equivalent of KN<sub>3</sub> to proceed; however, we observed higher yields of **6.7** when an excess of KN<sub>3</sub> was used.

**[U(BCMA)<sub>2</sub>]<sub>2</sub>(μ-N\*)(μ-κ<sup>1</sup>:κ<sup>1</sup>-BCMA) (6.7-<sup>15</sup>N):** The same general procedure as Method 3 was used, with NaN<sub>3</sub> (<sup>15</sup>N labeled at terminal position) used in place of KN<sub>3</sub>. (19 mg, 43% yield)

<sup>1</sup>H NMR (C<sub>6</sub>D<sub>6</sub>, 400 MHz): δ 127.39 (s), 116.19 (s), 114.20 (s), 87.37 (s), 78.43 (s), 46.33 (s), 41.22 (s), 40.09 (s), 39.56 (s), 36.56 (s), 34.19 (s), 28.02 (s), 26.88 (s), 12.70 (s), 12.35 (s), 5.66 (s), 3.74 (s), 3.58 (s), 3.01 (s), 1.90 to 1.11 (m), 0.49 (s), 0.30 (s), -0.08 (s), -1.25 (s), -1.41 (s), -2.71 (s), -3.05 (s), -3.89 (s), -4.31 (s), -4.65 (s), -6.64 (d), -7.53 (d), -7.71 (s), -9.11 (s), -10.00 (s), -10.69 (s), -11.22 (s), -11.61 (s), -13.85 (d), -14.63 (s), -16.37 (s), -17.17 (s), -17.64 (s), -18.44 (s), -18.89 (s), -19.53 (s), -21.48 (s), -22.88 (s), -24.60 (s), -27.88 (s), -34.11 (s), -37.03 (s), -37.56 (s), -38.82 (s), -59.00 (s), -64.87 (s), -71.62 (s), -92.23 (s), -111.71 (s).

<sup>15</sup>N NMR (C<sub>6</sub>D<sub>6</sub>, 600 MHz): No signal observed.

IR (cm<sup>-1</sup>): 1485 (m), 1364 (m), 1344 (w), 1309 (w), 1301 (w), 1259 (w), 1240 (w), 1191 (w), 1173 (w), 1138 (w), 1077 (w), 996 (w), 949 (w), 886 (w), 843 (w), 823 (w), 798 (w), 740 (w, U-<sup>14</sup>N), 724 (w, U-<sup>15</sup>N, **6.7-<sup>15</sup>N** only), 661 (w), 606 (w), 534 (w).

EA calcd for C<sub>70</sub>H<sub>125</sub>N<sub>11</sub>U<sub>2</sub>: C: 52.65%, H: 7.89%, N: 9.65%. Found: C: 52.94%, H: 7.68%, N: 9.43%.

Melting point: decomposes above *ca.* 142 °C.

**[(U(BIMA)<sub>2</sub>)<sub>2</sub>(μ-N)(μ-N<sup>i</sup>Pr)(K<sub>2</sub>(μ-η<sup>3</sup>:η<sup>3</sup>-CH<sub>2</sub>CHN<sup>i</sup>Pr)]<sub>2</sub> (6.8):**

**Method 1:** A THF suspension (1 mL) of KC<sub>8</sub> (28 mg, 0.207 mmol) was added to a THF solution (1 mL) of **6.4** (49 mg, 0.070 mmol). The green solution turned dark blue, then red over the course of the reaction. The solution was stirred for 6 h, then the solvent was removed *in vacuo* and the resulting red solids were triturated with pentane (2 mL). The product was extracted into pentane (3 mL), then the solvent was removed *in vacuo* to give analytically pure product as a red solid (41 mg, 99% yield). Crystals suitable for x-ray diffraction were grown from pentane.

**Method 2:** A THF suspension (0.3 mL) of KC<sub>8</sub> (4.1 mg, 0.030 mmol) was added to a THF solution (0.5 mL) of **6.9** (18 mg, 0.015 mmol). The solution was stirred for 16 h and filtered, then the solvent was removed *in vacuo* and the resulting red solids were triturated with pentane (1 mL). The product was extracted into pentane (1 mL), then the solvent was removed *in vacuo* to give the product as a red solid (13 mg, 68% yield).

**[(U(BIMA)<sub>2</sub>)<sub>2</sub>(μ-N\*)(μ-N<sup>i</sup>Pr)(K<sub>2</sub>(μ-η<sup>3</sup>:η<sup>3</sup>-CH<sub>2</sub>CHN<sup>i</sup>Pr)]<sub>2</sub> (6.8-<sup>15</sup>N):** The same general procedure as Method 1 was used, with **6.4-<sup>15</sup>N** used in place of **6.4**. (42 mg, 99% yield)

<sup>1</sup>H NMR (C<sub>6</sub>D<sub>6</sub>, 600 MHz): δ 145.87 (s), 125.72 (s), 96.14 (s), 89.86 (broad), 83.22 (s), 75.79 (s), 72.59 (s), 67.44 (broad), 64.73 (s), 61.05 (s), 44.63 (broad), 39.15 (s), 35.07 (s), 19.35 (s), 18.21 (s), 17.49 (s), 14.56 (broad), 8.27 (s), 6.20 to -1.05 (m), -2.24 (s), -3.82 (s), -6.04 (s), -8.91 (s), -10.27 (s), -10.37 (s), -18.92 (broad), -20.18 (s), -27.56 (s), -30.42 (s), -36.27 (s), -45.44 (s), -48.12 (s), -52.28 (broad), -68.89 (broad), -84.51 (s), -88.46 (s), -90.32 (s), -96.47 (s), -140.70 (s).

<sup>15</sup>N NMR (C<sub>6</sub>D<sub>6</sub>, 600 MHz): No signal observed.

IR (cm<sup>-1</sup>): 1551 (w), 1489 (m), 1335 (w), 1313 (w), 1195 (w), 1173 (w), 1120 (w), 1048 (w), 1014 (w), 802 (w), 730 (w, U-<sup>14</sup>N), 704 (w, U-<sup>15</sup>N, **6.8-<sup>15</sup>N** only), 623 (w), 584 (w), 573 (w), 540 (w), 506 (w).

EA calcd for C<sub>80</sub>H<sub>170</sub>N<sub>22</sub>K<sub>4</sub>U<sub>4</sub>: C: 37.67%, H: 6.72%, N: 12.16%. Found: C: 37.84%, H: 6.92%, N: 11.97%.

Melting point: decomposes above *ca.* 122 °C.

**[U(BIMA)<sub>2</sub>]<sub>2</sub>(μ-N)(μ-κ<sup>1</sup>:κ<sup>1</sup>-BIMA) (6.9):** A THF suspension (1 mL) of KN<sub>3</sub> (16 mg, 0.197 mmol) was added to a THF solution (1 mL) of **6.6** (30 mg, 0.045 mmol). The dark blue solution turned red over the course of the reaction. The solution was stirred for 18 h, then the solvent was removed *in vacuo* and the resulting red solids were triturated with pentane (2 mL). The product was extracted into pentane (2 mL), then the solvent was removed *in vacuo* to give the product as an analytically pure red solid (25 mg, 93% yield). Crystals suitable for x-ray diffraction were grown from pentane.

‡ The stoichiometry of this reaction only requires ½ equivalent of KN<sub>3</sub> to proceed; however, we observed higher yields of **6.9** when an excess of KN<sub>3</sub> was used.

‡ Reduction of **6.4** with one equivalent of KC<sub>8</sub> in THF led to the formation of a mixture of intractable products with very high solubility in pentane. **6.9** was present in this mixture, but we were unable to isolate this complex from the other unidentified products.

**[U(BIMA)<sub>2</sub>]<sub>2</sub>(μ-N\*)(μ-κ<sup>1</sup>:κ<sup>1</sup>-BIMA) (6.9-<sup>15</sup>N):** The same general procedure as above was used, with NaN<sub>3</sub> (<sup>15</sup>N labeled at terminal position) used in place of KN<sub>3</sub>. (45 mg, 90% yield)

<sup>1</sup>H NMR (C<sub>6</sub>D<sub>6</sub>, 400 MHz): δ 87.52 (broad), 12.85 (s), 8.32 (s), 0.44 (s), -38.50 (broad), -62.74 (s), -73.47 (s), -82.11 (broad).

<sup>15</sup>N NMR (C<sub>6</sub>D<sub>6</sub>, 600 MHz): No signal observed.

IR (cm<sup>-1</sup>): 1488 (m), 1417 (m), 1361 (w), 1337 (w), 1312 (w), 1261 (w), 1194 (m), 1174 (w), 1124 (w), 1048 (w), 1013 (w), 889 (w), 818 (w), 800 (w), 776 (w), 729 (m, U-<sup>14</sup>N), 711 (m, U-<sup>15</sup>N, **6.9-<sup>15</sup>N** only), 619 (w), 575 (w), 542 (w).

EA calcd for C<sub>40</sub>H<sub>85</sub>N<sub>11</sub>U<sub>2</sub>: C: 40.16%, H: 7.16%, N: 12.88%. Found: C: 40.08%, H: 6.95%, N: 12.59%.

Melting point: decomposes above *ca.* 155 °C.

**[U(N<sub>3</sub>)(BCMA)<sub>3</sub>](OTf) (6.10):** A THF solution (2 mL) of AgOTf (37 mg, 0.144 mmol) was added to a THF solution (3 mL) of **6.3** (151 mg, 0.160 mmol) at -40 °C. The solution of **6.3** immediately turned black upon addition of AgOTf. The resulting solution was stirred for 5 minutes, then the solvent was removed *in vacuo*. The product was then washed with Et<sub>2</sub>O (2 mL), extracted into THF (3 mL), and filtered through Celite. The resulting black solution was then concentrated to a final volume of 1 mL and cooled to -40 °C for 24 h, yielding black crystals, which were then dried *in vacuo*. (135 mg, 86% yield)

‡ Photolysis of a THF solution of **6.10** resulted in an intractable mixture of products.

No resonances were observed in the EPR spectrum of this compound in the solid state or as a d<sub>8</sub>-THF solution.

<sup>1</sup>H NMR (d<sub>8</sub>-THF, 500 MHz): δ 21.26 (broad, 6H, NCHCH<sub>2</sub>), 2.60 (s, Cy-H), 1.81 (d, Cy-H), 1.60 (s, Cy-H), 1.42 (s, Cy-H), 0.74 (broad, 9H, NCCCH<sub>3</sub>), 0.29 (s, Cy-H).

IR (cm<sup>-1</sup>): 2076 (w), 1651 (w), 1606 (m), 1377 (m), 1339 (m), 1197 (s), 1018 (m), 891 (w), 825 (w), 802 (w), 765 (w).

EA could not be obtained for this compound due to its extreme thermal instability.

Melting point: decomposes at room temperature.

**Hydrolysis of nitrides: 6.7, 6.7-<sup>15</sup>N, 6.8, 6.8-<sup>15</sup>N, 6.9, and 6.9-<sup>15</sup>N** (*ca.* 25 mg each) were dissolved in Et<sub>2</sub>O (2 mL) with stirring, then a 4.0 M solution of HCl in 1,4-dioxane (*ca.* 50 μL) was added to each flask via syringe. Upon addition of HCl, the red solutions lightened to off-white

suspensions. The solutions were stirred until no further color change was observed to ensure complete decomposition, then the volatiles were removed. An aliquot of  $d_6$ -DMSO (1.00 mL) containing  $C_6Me_6$  or  $Ph(OCH_3)_3$  as an internal standard was added to each flask, then the solutions were filtered in air into an NMR tube and a  $^1H$  NMR spectrum was collected.

Calculated yield of  $NH_4Cl$  from NMR for **6.7**: 0.43 mg, 61%.

Calculated yield of (50%- $^{15}N$  labeled)  $NH_4Cl$  from NMR for **6.7- $^{15}N$** : 0.73 mg, 65%.

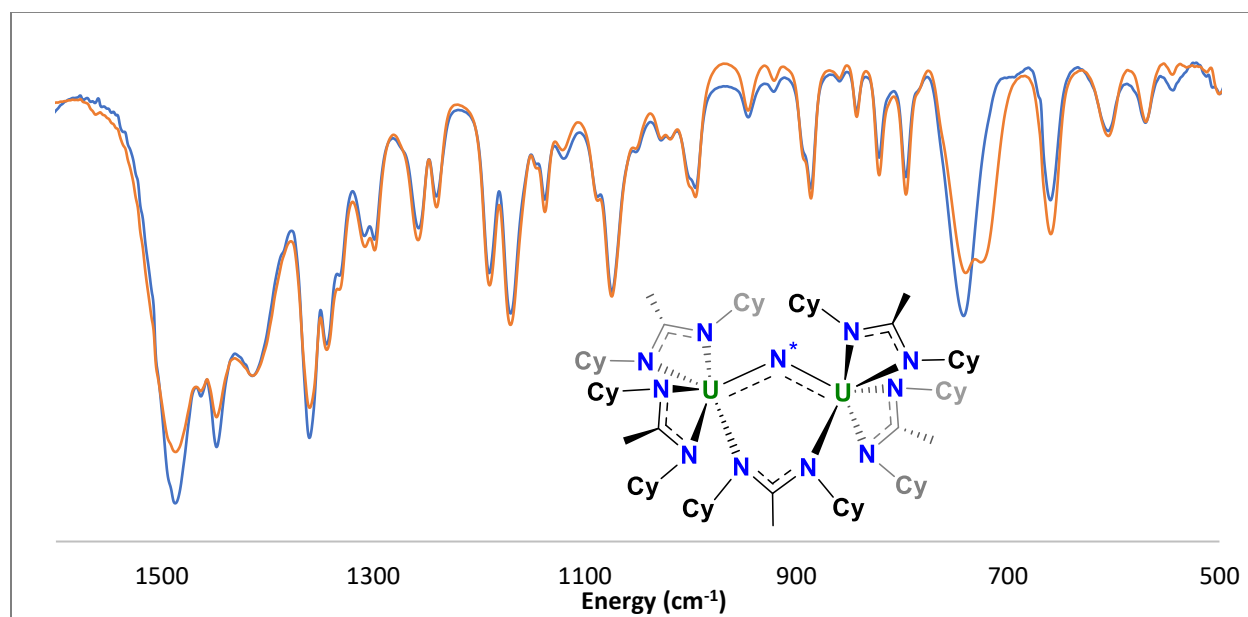
Calculated yield of  $NH_4Cl$  from NMR for **6.8**: 0.59 mg, 79%.

Calculated yield of (50%- $^{15}N$  labeled)  $NH_4Cl$  from NMR for **6.8- $^{15}N$** : 0.92 mg, 94%.

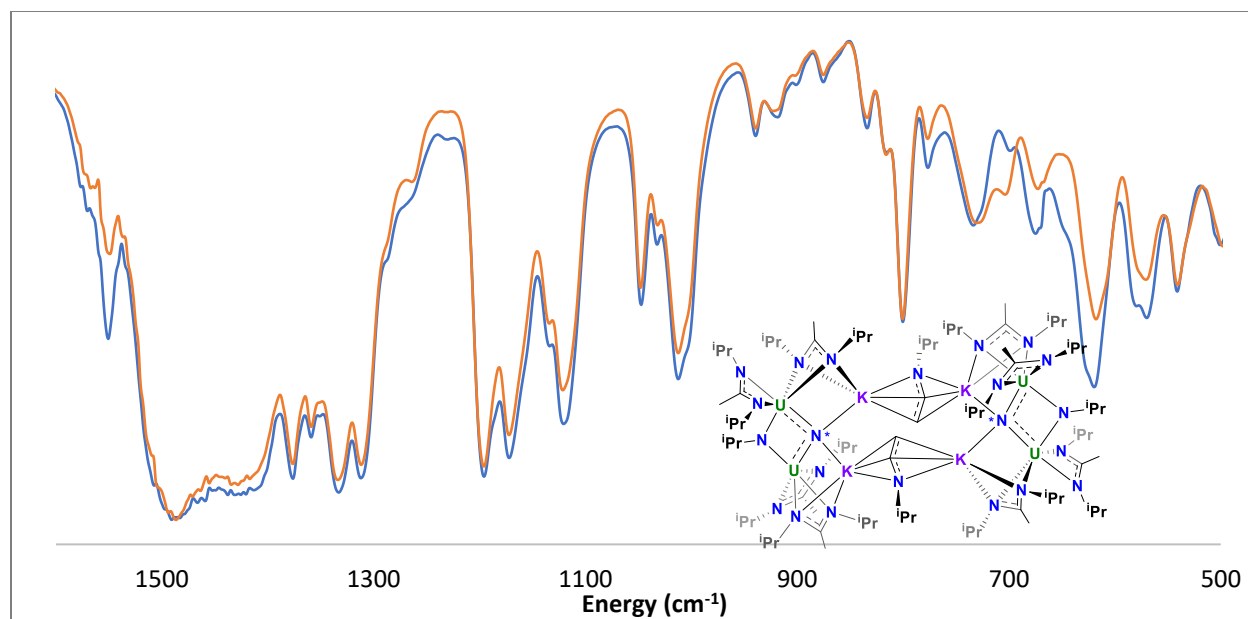
Calculated yield of  $NH_4Cl$  from NMR for **6.9**: 0.28 mg, 25%. A large quantity of material remained stuck to the walls of the flask during the workup of this reaction, leading to a lower-than-expected yield.

Calculated yield of (50%- $^{15}N$  labeled)  $NH_4Cl$  from NMR for **6.9- $^{15}N$** : 0.95 mg, 75%.

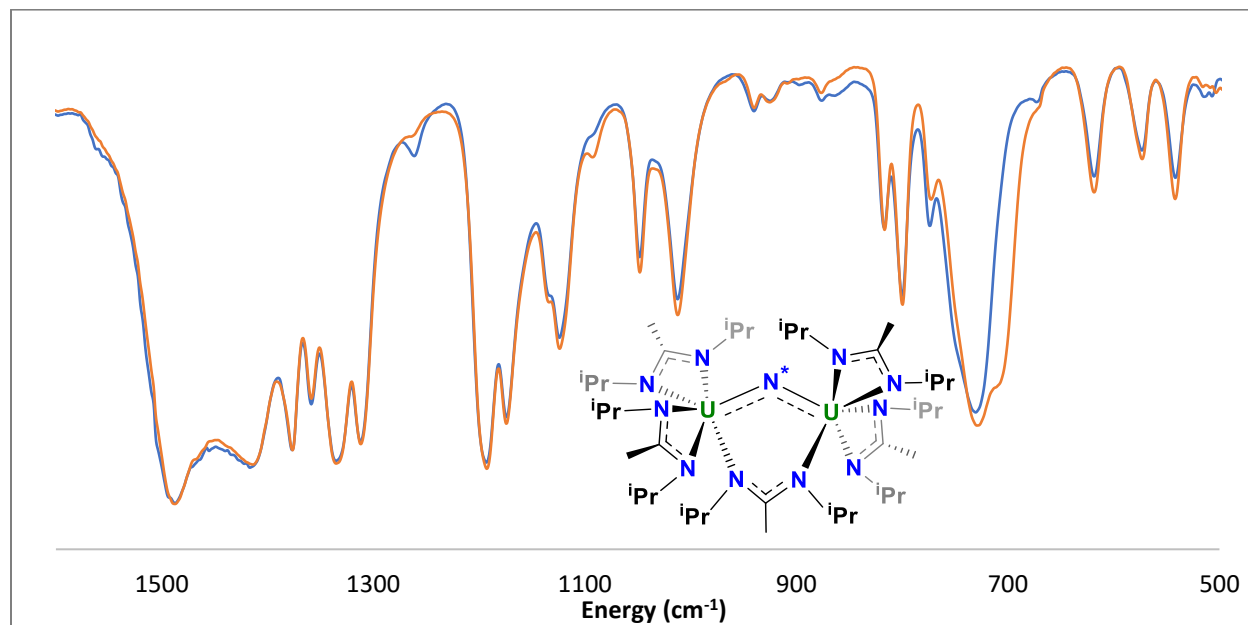
### Infrared Spectroscopy



**Figure 6.5:** Normalized IR spectrum of  $[U(BCMA)_2]_2(\mu-N)(\mu-\kappa^1:\kappa^1-BCMA)$  (**6.7**) (blue) and (50%  $^{15}N$ )-labeled  $[U(BCMA)_2]_2(\mu-N)(\mu-\kappa^1:\kappa^1-BCMA)$  (**6.7- $^{15}N$** ) (orange) prepared by drop-casting a pentane solution of each compound onto KBr plates, then sealing the edges of the plates with silicone grease. The U-N stretches of **6.7- $^{15}N$**  are visible at  $740\text{ cm}^{-1}$  ( $U-^{14}N$ ) and  $724\text{ cm}^{-1}$  ( $U-^{15}N$ ).



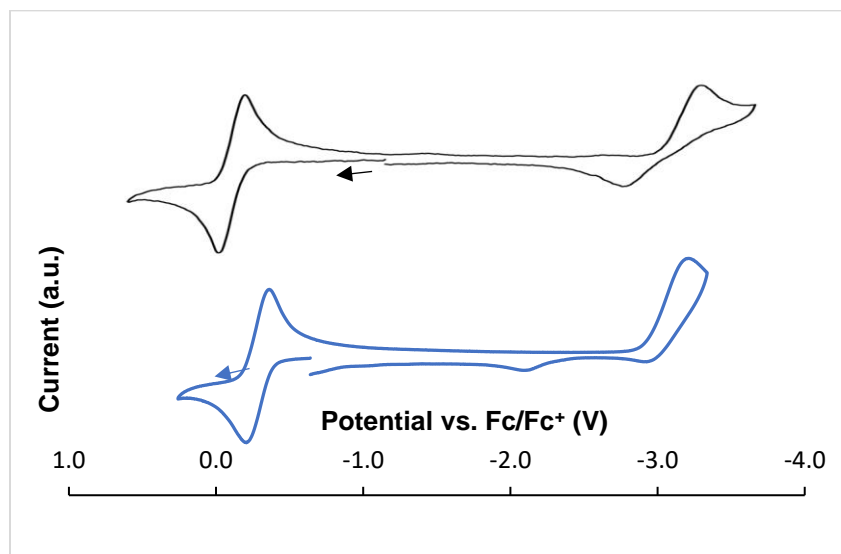
**Figure 6.6:** Normalized IR spectrum of unlabeled  $[(U(BIMA)_2)_2(\mu-N)(\mu-N^iPr)(K_2(\mu-\eta^3:\eta^3-CH_2CHN^iPr)_2)]_2$  (**6.8**) (blue) and the (50%  $^{15}N$ )-labeled analogue  $[(U(BIMA)_2)_2(\mu-N^*)(\mu-N^iPr)(K_2(\mu-\eta^3:\eta^3-CH_2CHN^iPr)_2)]_2$  (**6.8- $^{15}N$** ) (orange) prepared by drop-casting a pentane solution of each compound onto KBr plates, then sealing the edges of the plates with silicone grease. The U-N stretches of **6.8- $^{15}N$**  are visible at  $730\text{ cm}^{-1}$  ( $U-^{14}N$ ) and  $704\text{ cm}^{-1}$  ( $U-^{15}N$ ).



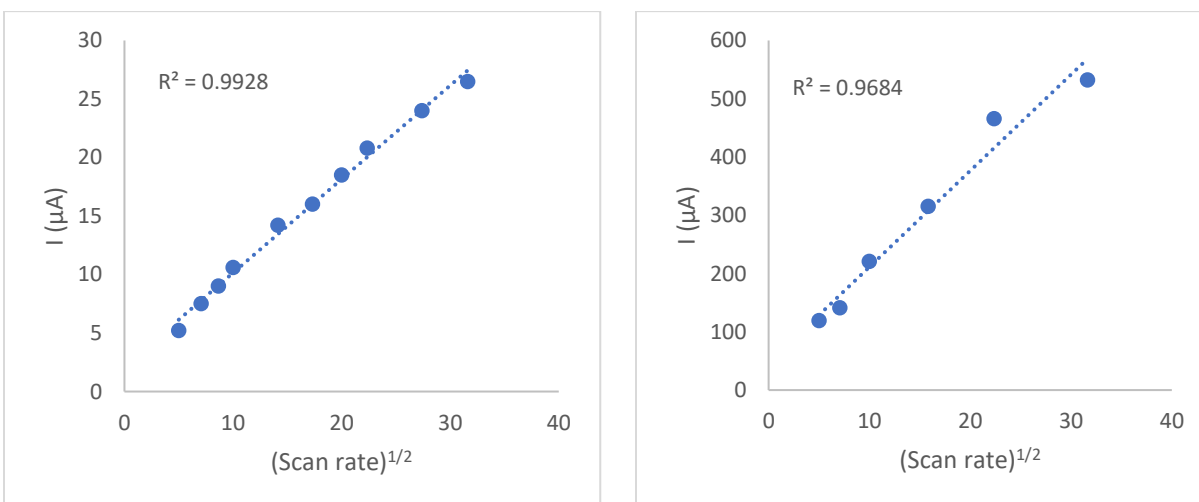
**Figure 6.7:** Normalized IR spectrum of  $[U(BIMA)_2]_2(\mu-N)(\mu-\kappa^1:\kappa^1-BIMA)$  (**6.9**) and (50%  $^{15}N$ )-labeled  $[U(BIMA)_2]_2(\mu-N)(\mu-\kappa^1:\kappa^1-BIMA)$  (**6.9- $^{15}N$** ) prepared by drop-casting a pentane solution of each compound onto KBr plates, then sealing the edges of the plates with silicone grease. The U-N stretches of **6.9- $^{15}N$**  are visible at  $729\text{ cm}^{-1}$  ( $U-^{14}N$ ) and  $711\text{ cm}^{-1}$  ( $U-^{15}N$ ).

## Electrochemistry

Cyclic voltammetry (CV) experiments were performed with a Gamry Reference 600 potentiostat using platinum working and counter electrodes and a silver pseudo-reference electrode. The measurements were conducted in a dry N<sub>2</sub> atmosphere glovebox with 2–3 mM analyte in 0.2 M solutions of [<sup>n</sup>Bu<sub>4</sub>N][PF<sub>6</sub>] in THF at room temperature. Potentials were referenced versus the ferrocene (Fc)/ferrocenium (Fc<sup>+</sup>) redox couple by adding Fc (sublimed) as an internal standard for calibration at the end of each set of measurements.



**Figure 6.8:** Cyclic voltammograms of **6.3** (black) and **6.4** (blue) carried out in THF with 0.2 M [<sup>n</sup>Bu<sub>4</sub>N][PF<sub>6</sub>] electrolyte (scan rate = 100 mV/s).



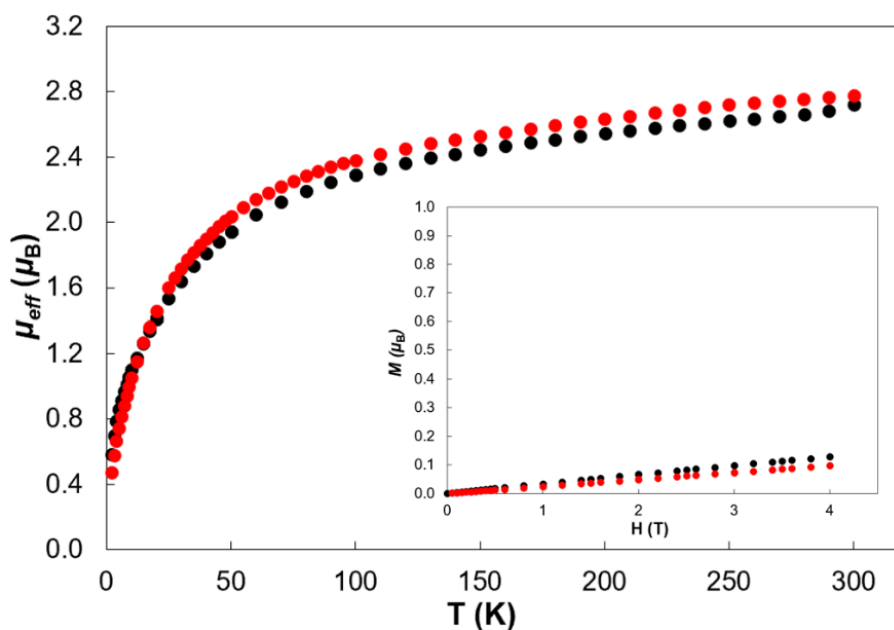
**Figure 6.9:** Plots of the square root of scan rate (mV/s) versus the measured current (μA) for the oxidation waves of U(N<sub>3</sub>)(BCMA)<sub>3</sub> (**6.3**) (left) and U(N<sub>3</sub>)(BIMA)<sub>3</sub> (**6.4**) (right).



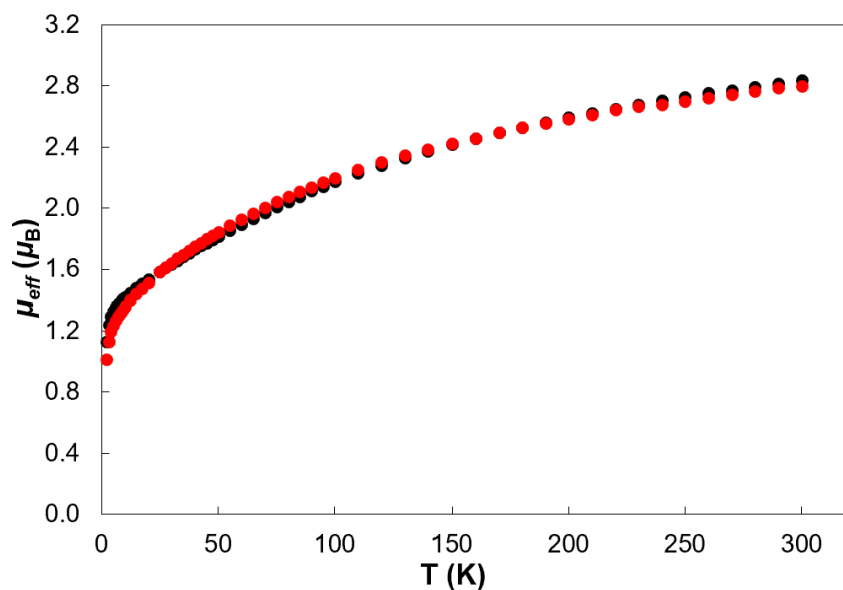
## Magnetism

Magnetic susceptibility measurements were made for all samples in a 7 T Quantum Design Magnetic Properties Measurement System that utilizes a superconducting quantum interference device (SQUID). Samples were contained in quartz tubes for measurement as described previously.<sup>67</sup> Data were collected at two different fields (0.5 and 4 T) and over a temperature range from 2–300 K unless otherwise stated. A two-field correction was applied in order to remove contributions from trace ferromagnetic impurities as described previously.<sup>68</sup> Diamagnetic corrections were made using Pascal's constants.<sup>69</sup>

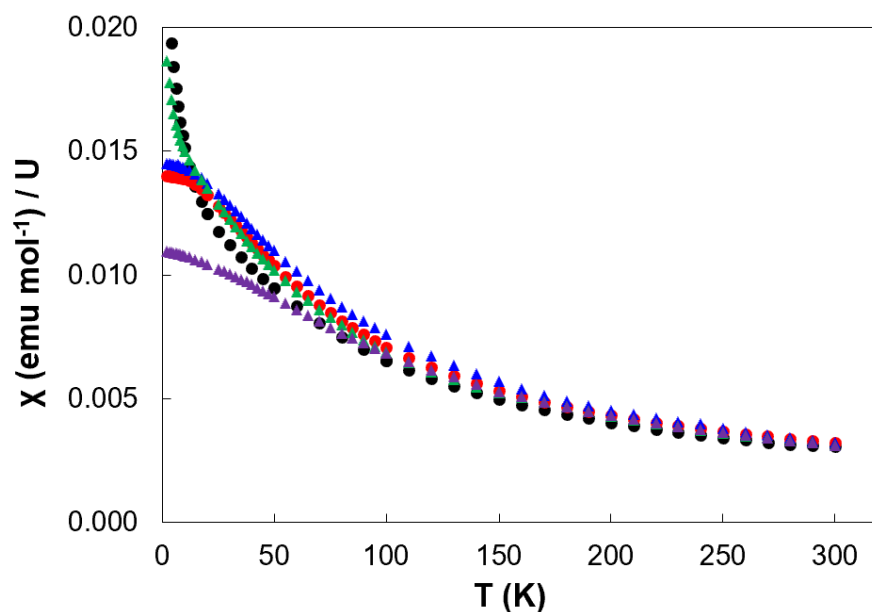
$\chi$  versus  $T$  plots revealed temperature-independent paramagnetism (TIP) for **6.4**, **6.7**, and **6.8**, derived from thermal population of low-lying crystal-field excited states of  $U^{4+}$  cations,<sup>70</sup> in the low-temperature regime  $< 15$  K (Figure 6.12). The absence of observable TIP for **6.3** and **6.9** presumably resulted from paramagnetic impurities that contributed a Curie tail to the data, yet the inability to fit the data to Curie-Weiss behavior suggests that low temperature TIP is still present. The levels of TIP in each of these samples was not extracted due to the complication of decoupling the TIP contributions from the Curie tail, as has been noted previously.<sup>70</sup>



**Figure 6.10:** Variable-temperature molar magnetic data ( $\mu_{eff}$ ) for **6.3** (black) and **6.4** (red) and variable field data collected at 5 K (inset).



**Figure 6.11:** Variable-temperature molar magnetic data ( $\mu_{\text{eff}}$ ) for **6.6** (red) and **6.10** (black).



**Figure 6.12:**  $\chi$  versus  $T$  plots for **6.3** (black), **6.4** (red), **6.7** (blue), **6.8** (purple), and **6.9** (green).

### X-Ray Crystallography

In a dry nitrogen glovebox, samples of single crystals of **6.2-6.4**, **6.6-6.8**, and **6.10** were coated in Paratone-N oil for transport to diffraction facilities. Crystals were mounted on either a Kapton loop (for **6.2-6.4**, **6.6**, **6.7**, and **6.10**) or on a MiTeGen 10  $\mu\text{m}$  aperture Dual-Thickness MicroMount (for **6.8** and **6.9**). X-ray diffraction data for **6.2-6.4**, **6.6**, **6.7**, and **6.10** were collected at CheXray, Berkeley, CA, using either a Bruker APEX II QUAZAR instrument (for **6.2**, **6.3**, and

**6.10**) or a Rigaku XtaLAB P200 instrument equipped with a MicroMax-007 HF microfocus rotating anode and a Pilatus 200K hybrid pixel array detector (for **6.4** and **6.7**), both using monochromated Mo K $\alpha$  radiation ( $\lambda = 0.71073 \text{ \AA}$ ). X-ray diffraction data for **6.8** and **6.9** were collected at the Advanced Light Source (ALS), Lawrence Berkeley National Lab, Berkeley, CA, station 12.2.1 using a silicon monochromated beam of 17 keV ( $\lambda = 0.7288 \text{ \AA}$ ) synchrotron radiation. All data collections were conducted at 100 K, with the crystals cooled by a stream of dry nitrogen. For **6.4** and **6.7**, CrysAlisPro was used for the data collections and data processing, including a multi-scan absorption correction applied using the SCALE3 ABSPACK scaling algorithm within CrysAlisPro.<sup>71</sup> For **6.2**, **6.3**, **6.6**, **6.8** and **6.10**, Bruker APEX 2 or APEX3 software was used for the data collections, Bruker SAINT V8.37A or V8.38A software was used to conduct the cell refinement and data reduction procedures,<sup>72</sup> and absorption corrections were carried out by a multi-scan method utilizing the SADABS program.<sup>73</sup> Initial structure solutions were found using direct methods (SHELXT),<sup>74</sup> and refinements were carried out using SHELXL-2014.<sup>74-76</sup> Thermal parameters for all non-hydrogen atoms were refined anisotropically. Thermal ellipsoid plots were made using Mercury.<sup>78</sup> Structure **6.9** displayed disorder in several amidinate-isopropyl groups, which was modeled completely with the aid of multiple restraints to give chemically reasonable solutions. Additionally, the pentane solvent in **6.9** was located near/on an inversion center and required modeling the molecule at half occupancy due to the presence of its crystallographically generated partner solvent molecule. Structure **6.10** displayed minor disorder, in which one of the trifluoromethanesulfonate counteranions was disordered over two positions, that was modeled completely and refined to give relative occupancies of 0.515/0.485. All structures have been deposited to the Cambridge Crystallographic Data Centre (CCDC), with deposition numbers 2050796-2050802.

**Table 6.2:** Crystallographic details and refinement metrics for compounds **6.2**, **6.3**, **6.4**, and **6.7**.

	<b>6.2</b>	<b>6.3</b>	<b>6.4</b>	<b>6.7</b>
Chemical formula	C <sub>24</sub> H <sub>51</sub> ClN <sub>6</sub> U	C <sub>42</sub> H <sub>75</sub> N <sub>9</sub> U	C <sub>24</sub> H <sub>51</sub> N <sub>9</sub> U	C <sub>75</sub> H <sub>120</sub> N <sub>11</sub> U <sub>2</sub>
Formula weight	697.18	944.04	703.76	1596.86
Color, habit	Green, block	Green, plate	Green, block	Red, block
Crystal system	Monoclinic	Monoclinic	Monoclinic	Triclinic
Space group	C2/c	P 2 <sub>1</sub> /c	P2/n	P-1
a (Å)	34.0398(15)	12.56(1)	17.5266(3)	12.6421(3)
b (Å)	10.6851(4)	18.01(2)	10.2593(2)	14.0766(3)
c (Å)	17.0368(7)	20.22(2)	33.9514(7)	23.7976(4)
α (°)	90	90	90	104.002(2)
β (°)	104.930(3)	102.60(2)	97.847(2)	92.888(2)
γ (°)	90	90	90	113.724(2)
V (Å <sup>3</sup> )	5487.4(4)	4464(6)	6047.7(2)	3709.5(2)
Z	8	4	8	2
Density (g/cm <sup>3</sup> )	1.547	1.405	1.546	1.430
F(000)	2768	1928	2800	1612
Radiation Type	Mo K <sub>α</sub>	Mo K <sub>α</sub>	Mo K <sub>α</sub>	Mo K <sub>α</sub>
μ (mm <sup>-1</sup> )	5.532	3.674	5.395	4.405
Crystal size (mm)	0.14 x 0.10 x 0.08	0.15 x 0.14 x 0.06	0.17 x 0.11 x 0.08	0.14 x 0.10 x 0.05
Meas. Refl.	52237	29003	167378	108938
Indep. Refl.	5501	8081	20570	15157
Obsvd. Refl. (I>2σ(I))	5219	5508	13344	12361
R <sub>int</sub>	0.0410	0.0665	0.1237	0.0582
R <sub>1</sub> / wR <sub>2</sub> (I>2σ(I))	0.0145 / 0.0340	0.0435 / 0.0841	0.0463 / 0.0850	0.0268 / 0.0526
R <sub>1</sub> / wR <sub>2</sub> (all data)	0.0160 / 0.0345	0.0819 / 0.0968	0.0886 / 0.0957	0.0396 / 0.0556
Goodness-of-fit	1.080	1.024	1.025	1.034
CCDC	2050796	2050797	2050802	2050799

---

**Table 6.3:** Crystallographic details and refinement metrics for compounds **6.8**, **6.9**, and **6.10**.

	<b>6.8</b>	<b>6.9</b>	<b>6.10</b>
Chemical formula	C <sub>45</sub> H <sub>97</sub> K <sub>2</sub> N <sub>11</sub> U <sub>2</sub>	C <sub>42.5</sub> H <sub>91</sub> N <sub>11</sub> U <sub>2</sub>	C <sub>43</sub> H <sub>75</sub> F <sub>3</sub> N <sub>9</sub> O <sub>3</sub> SU
Formula weight	1346.59	1232.32	1093.21
Color, habit	Red, block	Orange, block	Black, block
Crystal system	Triclinic	Triclinic	Monoclinic
Space group	P-1	P-1	P 2 <sub>1</sub> /n
a (Å)	12.2782(6)	10.4722(5)	11.7763(9)
b (Å)	13.6704(6)	13.2375(6)	41.347(3)
c (Å)	19.0097(9)	18.8592(8)	21.907(2)
α (°)	106.259(2)	100.002(2)	90
β (°)	99.170(2)	92.343(1)	103.326(4)
γ (°)	92.533(2)	99.554(2)	90
V (Å <sup>3</sup> )	3010.7(2)	2532.4(2)	10380(1)
Z	2	2	8
Density (g/cm <sup>3</sup> )	1.485	1.616	1.399
F(000)	1332	1214	4440
Radiation Type	Synchrotron	Synchrotron	Mo K <sub>α</sub>
μ (mm <sup>-1</sup> )	2.645	2.962	3.222
Crystal size (mm)	0.050 x 0.030 x 0.025	0.22 x 0.22 x 0.20	0.08 x 0.07 x 0.06
Meas. Refl.	13999	33038	75806
Indep. Refl.	13999	10343	18997
Obsvd. Refl. (I>2σ(I))	12337	9673	12494
R <sub>int</sub>	0.0673	0.0579	0.0687
R <sub>1</sub> / wR <sub>2</sub> (I>2σ(I))	0.0379 / 0.0874	0.0372 / 0.0991	0.0613 / 0.1576
R <sub>1</sub> / wR <sub>2</sub> (all data)	0.0482 / 0.0922	0.0390 / 0.1013	0.1054 / 0.1774
Goodness-of-fit	1.032	1.085	1.032
CCDC	2050801	2050800	2050798

**Table 6.4:** Comparative bond distances (Å) for the U(IV) azides **6.3** and **6.4**. Compound **6.4** contains two molecules within the asymmetric unit, thus the two values reported for each measurement.

Atoms	U(N <sub>3</sub> )(BCMA) <sub>3</sub> ( <b>6.3</b> )	U(N <sub>3</sub> )(BIMA) <sub>3</sub> ( <b>6.4</b> )	
<b>U1–N1</b>	2.478(5)	2.448(3)	2.448(3)
<b>U1–N2</b>	2.392(4)	2.382(3)	2.385(3)
<b>U1–N3</b>	2.441(6)	2.459(3)	2.455(3)
<b>U1–N4</b>	2.366(6)	2.403(3)	2.376(3)
<b>U1–N5</b>	2.502(2)	2.464(3)	2.462(3)
<b>U1–N6</b>	2.373(5)	2.371(3)	2.398(3)
<b>U1–N7</b>	2.340(6)	2.335(3)	2.335(3)
<b>N7–N8</b>	1.154(8)	1.186(4)	1.180(4)
<b>N8–N9</b>	1.17(1)	1.146(4)	1.154(4)

**Table 6.5:** Comparative bond distances (Å) and angles (degrees) for the bridging uranium nitrides 6.7 and 6.9.

Atoms	[U(BCMA) <sub>2</sub> ] <sub>2</sub> (μ-N)(μ-κ <sup>1</sup> :κ <sup>1</sup> -BCMA) (6.7)	[U(BIMA) <sub>2</sub> ] <sub>2</sub> (μ-N)(μ-κ <sup>1</sup> :κ <sup>1</sup> -BIMA) (6.9)
U1–N1	2.517(3)	2.541(3)
U1–N2	2.429(2)	2.443(3)
U1–N3	2.510(3)	2.552(4)
U1–N4	2.473(3)	2.448(4)
U2–N5	2.523(3)	2.577(4)
U2–N6	2.452(3)	2.422(4)
U2–N7	2.496(2)	2.515(3)
U2–N8	2.433(3)	2.445(3)
U1–N10	2.563(2)	2.512(4)
U2–N9	2.519(3)	2.485(3)
U1–N11	2.023(3)	2.048(3)
U2–N11	2.057(3)	2.047(3)
U1–N11–U2	127.0(2)°	133.6(2)°

## References

- 1 M. A. Boreen and J. Arnold, in *Encyclopedia of Inorganic and Bioinorganic Chemistry*, John Wiley & Sons, Ltd, 2018, pp. 1–18.
- 2 M. A. Boreen, G. Rao, D. G. Villarreal, F. A. Watt, R. D. Britt, S. Hohloch and J. Arnold, *Chem. Commun.*, 2020, **56**, 4535–4538.
- 3 D. M. King, P. A. Cleaves, A. J. Wooles, B. M. Gardner, N. F. Chilton, F. Tuna, W. Lewis, E. J. L. McInnes and S. T. Liddle, *Nat. Commun.*, 2016, **7**, 1–14.
- 4 S. Cotton, *Lanthanide and Actinide Chemistry*, John Wiley & Sons, 2006.
- 5 T. W. Hayton, *Chem. Commun.*, 2013, **49**, 2956–2973.
- 6 N. H. Anderson, S. O. Odoh, Y. Yao, U. J. Williams, B. A. Schaefer, J. J. Kiernicki, A. J. Lewis, M. D. Goshert, P. E. Fanwick, E. J. Schelter, J. R. Walensky, L. Gagliardi and S. C. Bart, *Nat. Chem.*, 2014, **6**, 919–926.
- 7 D. M. King and S. T. Liddle, *Coord. Chem. Rev.*, 2014, **266–267**, 2–15.
- 8 G. A. R. Rao, S. K. Mukerjee, V. N. Vaidya, V. Venugopal and D. D. Sood, *J. Nucl. Mater.*, 1991, **185**, 231–241.
- 9 B. Ebbinghaus, J.-S. Choi, T. Meier, B. Ebbinghaus, J.-S. Choi and T. Meier, in *ANS International 2003 Winter Meeting*, 2003.
- 10 P. Malkki, *The Manufacturing of Uranium Nitride for Possible Use in Light Water Reactors*, Royal Institute of Technology, 2015.
- 11 R. K. Thomson, T. Cantat, B. L. Scott, D. E. Morris, E. R. Batista and J. L. Kiplinger, *Nat. Chem.*, 2010, **2**, 723–729.
- 12 P. L. Arnold, M. W. McMullon, J. Rieb and F. E. Kühn, *Angew. Chem. Int. Ed.*, 2015, **54**, 82–100.
- 13 K. C. Mullane, H. Ryu, T. Cheisson, L. N. Grant, J. Y. Park, B. C. Manor, P. J. Carroll, M. H. Baik, D. J. Mindiola and E. J. Schelter, *J. Am. Chem. Soc.*, 2018, **140**, 11335–11340.
- 14 M. Yadav, A. Metta-Magaña and S. Fortier, *Chem. Sci.*, 2020, **11**, 2381–2387.
- 15 P. A. Cleaves, D. M. King, C. E. Kefalidis, L. Maron, F. Tuna, E. J. L. McInnes, J. McMaster, W. Lewis, A. J. Blake and S. T. Liddle, *Angew. Chem. Int. Ed.*, 2014, **53**, 10412–

- 10415.
- 16 L. Barluzzi, L. Chatelain, F. Fadaei-Tirani, I. Zivkovic and M. Mazzanti, *Chem. Sci.*, 2019, **10**, 3543–3555.
- 17 M. Falcone, C. E. Kefalidis, R. Scopelliti, L. Maron and M. Mazzanti, *Angew. Chem. Int. Ed.*, 2016, **55**, 12290–12294.
- 18 C. T. Palumbo, R. Scopelliti, I. Zivkovic and M. Mazzanti, *J. Am. Chem. Soc.*, 2020, **142**, 3149–3157.
- 19 L. Barluzzi, M. Falcone and M. Mazzanti, *Chem. Commun.*, 2019, **55**, 13031–13047.
- 20 M. Falcone, L. N. Poon, F. Fadaei Tirani and M. Mazzanti, *Angew. Chem. Int. Ed.*, 2018, **57**, 3697–3700.
- 21 M. Falcone, L. Chatelain and M. Mazzanti, *Angew. Chem. Int. Ed.*, 2016, **55**, 4074–4078.
- 22 F. Haber, *Verfahren Zur Herstellung von Ammoniak Durch Katalytische Vereinigung von Stickstoff Und Wasserstoff, Zweckmäßig Unter Hohem Druch*. DE 229126, 1909.
- 23 M. Falcone, L. Chatelain, R. Scopelliti, I. Živković and M. Mazzanti, *Nature*, 2017, **547**, 332–335.
- 24 D. M. King, F. Tuna, E. J. L. McInnes, J. McMaster, W. Lewis, A. J. Blake and S. T. Liddle, *Science*, 2012, **337**, 717–720.
- 25 J. Du, D. M. King, L. Chatelain, E. Lu, F. Tuna, E. J. L. McInnes, A. J. Wooles, L. Maron and S. T. Liddle, *Chem. Sci.*, 2019, **10**, 3738–3745.
- 26 S. Fortier, G. Wu and T. W. Hayton, *J. Am. Chem. Soc.*, 2010, **132**, 6888–6889.
- 27 C. T. Palumbo, L. Barluzzi, R. Scopelliti, I. Zivkovic, A. Fabrizio, C. Corminboeuf and M. Mazzanti, *Chem. Sci.*, 2019, **10**, 8840–8849.
- 28 N. Tsoureas, A. F. R. Kilpatrick, C. J. Inman and F. G. N. Cloke, *Chem. Sci.*, 2016, **7**, 4624–4632.
- 29 K. Liu, X. Wang, J. Liu, Y. Hu, H. Zhong, Q. Pan, L. Luo, S. Chen, Y. Zhang and Z. Long, *Prog. Surf. Sci.*, 2018, **93**, 47–84.
- 30 E. L. Bright, S. Rennie, M. Cattelan, N. A. Fox, D. T. Goddard and R. Springell, *Thin Solid Films*, 2018, **661**, 71–77.
- 31 W. J. Evans, S. A. Kozimor and J. W. Ziller, *Science*, 2005, **309**, 1835–1838.
- 32 R. B. Matthews, K. M. Chidester, C. W. Hoth, R. E. Mason and R. L. Petty, *J. Nucl. Mater.*, 1988, **151**, 345.
- 33 S. J. Zinkle and G. S. Was, *Acta Mater.*, 2013, **61**, 735–758.
- 34 A. Fischer, M. Antonietti and A. Thomas, *Adv. Mater.*, 2007, **19**, 264–267.
- 35 G. Nocton, J. Pécaut and M. Mazzanti, *Angew. Chem. Int. Ed.*, 2008, **47**, 3040–3042.
- 36 A. R. Fox and C. C. Cummins, *J. Am. Chem. Soc.*, 2009, **131**, 5716–5717.
- 37 N. S. Settineri, M. E. Garner and J. Arnold, *J. Am. Chem. Soc.*, 2017, **139**, 6261–6269.
- 38 C. Camp, N. Settineri, J. Lefevre, A. R. Jupp, J. M. Goicoechea, L. Maron and J. Arnold, *Chem. Sci. Chem. Sci.*, 2015, **6**, 6379–6384.
- 39 J. R. Walensky, R. L. Martin, J. W. Ziller and W. J. Evans, *Inorg. Chem.*, 2010, **49**, 10007–10012.
- 40 S. Fichter, S. Kaufmann, P. Kaden, T. S. Brunner, T. Stumpf, P. W. Roesky and J. März, *Chem. Eur. J.*, 2020, **26**, 8867–8870.
- 41 R. Kloditz, S. Fichter, S. Kaufmann, T. S. Brunner, P. Kaden, M. Patzschke, T. Stumpf, P. W. Roesky, M. Schmidt and J. März, *Inorg. Chem.*, 2020, **59**, 15670–15680.
- 42 I. S. R. Karmel, N. Fridman and M. S. Eisen, *Organometallics*, 2015, **34**, 636–643.
- 43 I. S. R. Karmel, T. Elkin, N. Fridman and M. S. Eisen, *Dalton Trans.*, 2014, **43**, 11376–11387.
- 44 W. J. Evans, J. R. Walensky and J. W. Ziller, *Organometallics*, 2010, **29**, 101–107.
- 45 W. J. Evans, J. R. Walensky and J. W. Ziller, *Inorg. Chem.*, 2010, **49**, 1743–1749.
- 46 W. J. Evans, J. R. Walensky, J. W. Ziller and A. L. Rheingold, *Organometallics*, 2009, **28**, 3350–3357.
- 47 M. D. Straub, J. Leduc, M. Frank, A. Raauf, T. D. Lohrey, S. G. Minasian, S. Mathur and J. Arnold, *Angew. Chem. Int. Ed.*, 2019, **58**, 5749–5753.

- 48 F. T. Edelmann, *Chem. Soc. Rev.*, 2012, **41**, 7649–7964.
- 49 M. Krasnopolski, C. G. Hrib, R. W. Seidel, M. Winter, H. W. Becker, D. Rogalla, R. A. Fischer, F. T. Edelmann and A. Devi, *Inorg. Chem.*, 2013, **52**, 286–296.
- 50 A. Devi, *Coord. Chem. Rev.*, 2013, **257**, 3332–3384.
- 51 T. B. Thiede, M. Krasnopolski, A. P. Milanov, T. De Los Arcos, A. Ney, H.-W. Becker, D. Rogalla, J. Winter, A. Devi and R. A. Fischer, *Chem. Mater.*, 2011, **23**, 1430–1440.
- 52 C. Villiers, P. Thuéry and M. Ephritikhine, *Eur. J. Inorg. Chem.*, 2004, **2004**, 4624–4632.
- 53 J. R. Hagadorn and J. Arnold, *Organometallics*, 1994, **13**, 4670–4672.
- 54 I. Korobkov, S. Gambarotta and G. P. A. Yap, *Angew. Chem. Int. Ed.*, 2002, **41**, 3433–3436.
- 55 M. A. Boreen and J. Arnold, *Dalton Trans.*, 2020, **49**, 15124–15138.
- 56 J. S. Anderson, J. Rittle and J. C. Peters, *Nature*, 2013, **501**, 84–87.
- 57 R. D. Shannon, *Acta Cryst.*, 1976, **A32**, 751–767.
- 58 N. H. Anderson, S. O. Odoh, U. J. Williams, A. J. Lewis, G. L. Wagner, J. L. Pacheco, S. A. Kozimor, L. Gagliardi, E. J. Schelter and S. C. Bart, *J. Am. Chem. Soc.*, 2015, **137**, 4690–4700.
- 59 I. Castro-Rodriguez, K. Olsen, P. Gantzel and K. Meyer, *J. Am. Chem. Soc.*, 2003, **125**, 4565–4571.
- 60 D. R. Kindra and W. J. Evans, *Chem. Rev.*, 2014, **114**, 8865–8882.
- 61 U. J. Williams, B. D. Mahoney, P. T. Degregorio, P. J. Carroll, E. Nakamaru-Ogiso, J. M. Kikkawa and E. J. Schelter, *Chem. Commun.*, 2012, **48**, 5593–5595.
- 62 A. J. Lewis, U. J. Williams, P. J. Carroll and E. J. Schelter, *Inorg. Chem.*, 2013, **52**, 7326–7328.
- 63 N. A. Vanagas, J. N. Wacker, C. L. Rom, E. N. Glass, I. Colliard, Y. Qiao, A. Bertke, E. Van Keuren, E. J. Schelter, M. Nyman and K. E. Knope, 2018, **57**, 7259–7269.
- 64 D. M. King, F. Tuna, E. J. L. McInnes, J. McMaster, W. Lewis, A. J. Blake and S. T. Liddle, *Science*, 2012, **337**, 717–720.
- 65 C. Villiers, P. Thuéry and M. Ephritikhine, *Eur. J. Inorg. Chem.*, 2004, **2004**, 4624–4632.
- 66 N. S. Settineri, M. E. Garner and J. Arnold, *J. Am. Chem. Soc.*, 2017, **139**, 6261–6269.
- 67 L. L. Pesterfield, *J. Chem. Educ.*, 2006, **83**, 1295.
- 68 R. L. Halbach, G. Nocton, C. H. Booth, L. Maron and R. A. Andersen, *Inorg. Chem.*, 2018, **57**, 7290–7298.
- 69 G. A. Bain and J. F. Berry, *J. Chem. Educ.*, 2008, **85**, 1–5.
- 70 E. J. Schelter, P. Yang, B. L. Scott, J. D. Thompson, R. L. Martin, P. J. Hay, D. E. Morris and J. L. Kiplinger, *Inorg. Chem.*, 2007, **46**, 7477–7488.
- 71 Rigaku Oxford Diffraction, (2015), CrysAlisPro Software system, version 1.171.39.7a, Rigaku Corporation, Oxford, UK.
- 72 APEX3, SADABS, and SAINT. Bruker AXS. Madison, WI, USA.
- 73 CrysAlisPro 1.171.39.45f (Rigaku Oxford Diffraction, 2018).
- 74 G. M. Sheldrick, *Acta Cryst.*, 2008, **A64**, 112–122.
- 75 G. M. Sheldrick, *Acta Cryst.* 2015, **C71**, 3–8.
- 76 O. V. Dolomanov, L. J. Bourhis, R. J. Gildea, J. A. K. Howard and H. Puschmann, *J. Appl. Crystallogr.*, 2009, **42**, 339–341.
- 77 C. F. Macrae, I. J. Bruno, J. A. Chisholm, P. R. Edgington, P. McCabe, E. Pidcock, L. Rodriguez-Monge, R. Taylor, J. Van De Streek and P. A. Wood, *J. Appl. Crystallogr.*, 2008, **41**, 466–470.



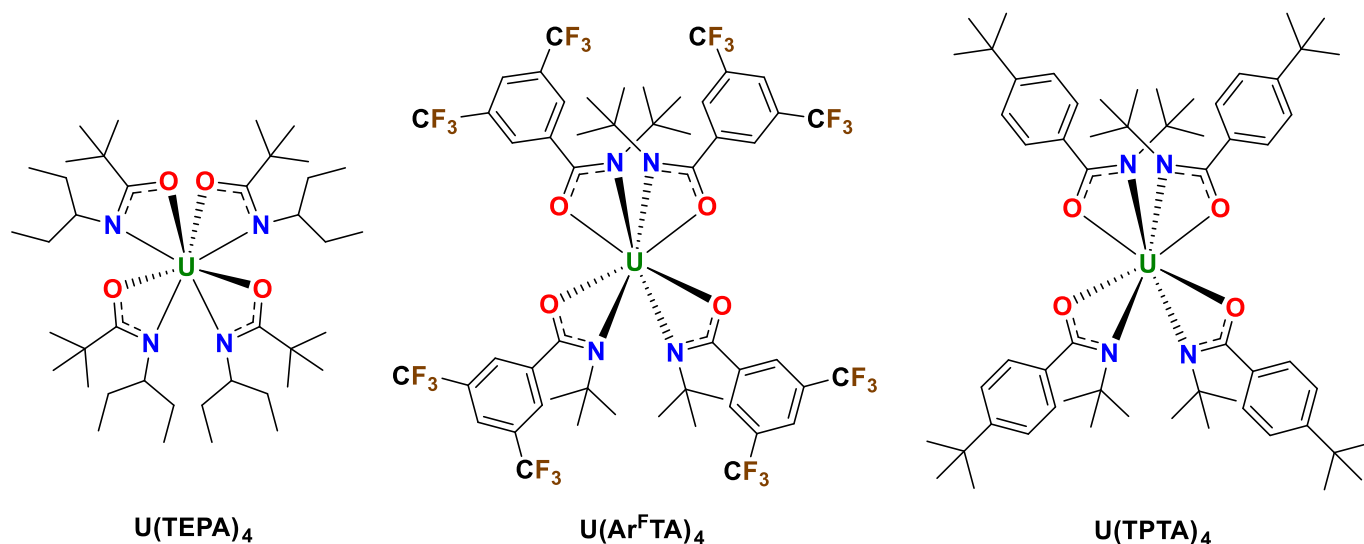
# Appendix

## Introduction

The purpose of this appendix is to present a list of previously unpublished compounds that are not suitable for a complete chapter on their own but may be useful for future projects. Each compound or group of compounds is presented here with a brief summary of their potential applications and relevant experimental data.

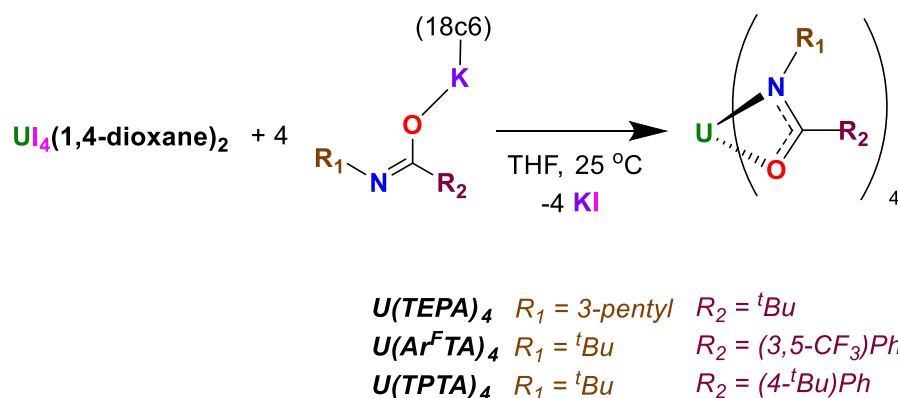
## Uranium Amidates as Precursors for $\text{UO}_2$ Materials

The following U(IV) amidate complexes were developed as molecular precursors for  $\text{UO}_2$  nanomaterials. These three precursors all undergo thermal decomposition via alkene elimination from the N-substituent (see Chapters 3 and 4 for mechanism), but they have not yet been tested in chemical vapor deposition (CVD) processes.



**Figure A1:** U(IV) amidates developed as precursors for  $\text{UO}_2$  materials.

These precursors were synthesized via salt metathesis reactions from  $\text{U}(\text{I}_4(1,4\text{-dioxane})_2)$  and four equivalents of the corresponding potassium amidates in THF. The decomposition mechanism for all three complexes was confirmed using  $^1\text{H}$  NMR spectroscopy; amide, nitrile, and alkene were all observed after thermolysis of these precursors (see Chapters 3 and 4 for procedure). Crystals of  $\text{U}(\text{TPTA})_4$  suitable for X-ray diffraction were grown from pentane. This molecule is 8-coordinate, with pseudo- $S_4$  geometry. Single crystals of  $\text{U}(\text{TEPA})_4$  could be readily grown from pentane, hexane, toluene, and  $\text{Et}_2\text{O}$ , but attempts to solve the crystal structure were hindered by full-molecule disorder, similarly to  $\text{Th}(\text{TEPA})_4$  (**4.2**). Crystals of  $\text{U}(\text{Ar}^{\text{F}}\text{TA})_4$  grown from pentane or hexane did not diffract well, hindering efforts to collect a crystal structure of this complex.

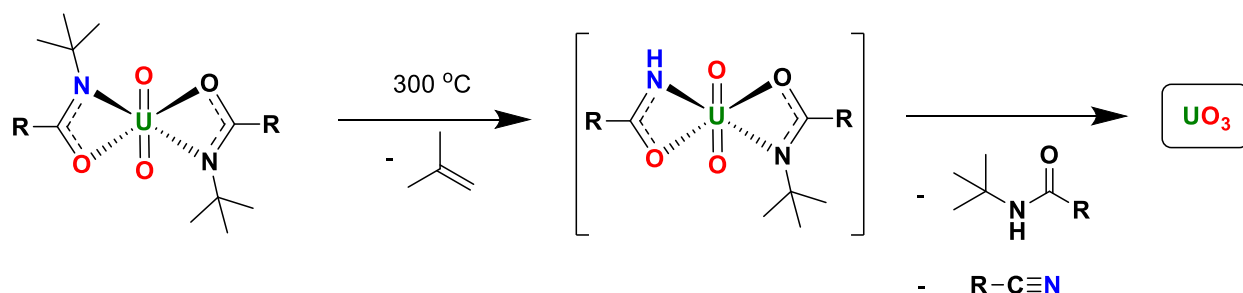


**Scheme A1:** Synthesis of  $U(\text{TEPA})_4$ ,  $U(\text{Ar}^{\text{F}}\text{TA})_4$ , and  $U(\text{TPTA})_4$ . Using the 18-crown-6 adduct of the potassium amidate salt substantially improved the yield of  $U(\text{TPTA})_4$ , but not  $U(\text{TEPA})_4$  or  $U(\text{Ar}^{\text{F}}\text{TA})_4$ .

$U(\text{TEPA})_4$  and  $U(\text{Ar}^{\text{F}}\text{TA})_4$  both display sufficient volatility for CVD; however, these complexes were synthesized after the initial batch of U(IV) amidate precursors was sent to the University of Cologne for CVD of  $\text{UO}_2$  thin films (Chapter 3)<sup>1</sup> and these new precursors have not yet been tested in actual CVD processes. Due to their volatility,  $U(\text{Ar}^{\text{F}}\text{TA})_4$  and  $U(\text{TEPA})_4$  could also be used as single-source precursors for the growth of  $\text{UO}_2$  thin films or  $\text{UO}_2$  NPs inside a framework template.  $U(\text{TPTA})_4$  is nonvolatile and decomposes *ca.* 166 °C, disfavoring its use as a CVD precursor. All three complexes are soluble in hydrocarbon solvents and could potentially be used as precursors for colloidal nanoparticle (NP) synthesis in the presence of an aprotic solvent and surfactant.

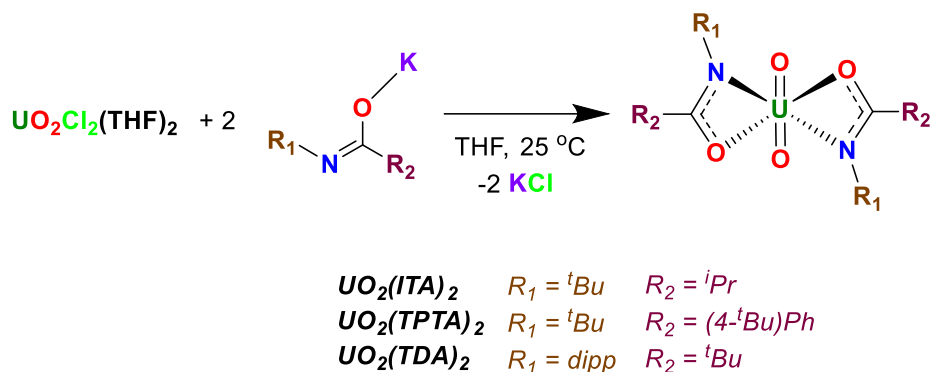
## Uranyl Amidates as Precursors for $\text{UO}_3$ Materials

After elucidating the decomposition mechanism of the U(IV) and Th(IV) amidate precursors, I wondered if related complexes could be used to access  $\text{UO}_3$  materials. Uranyl bis(amidate) complexes seemed to be a reasonable way to approach  $\text{UO}_3$  via a similar alkene elimination mechanism.



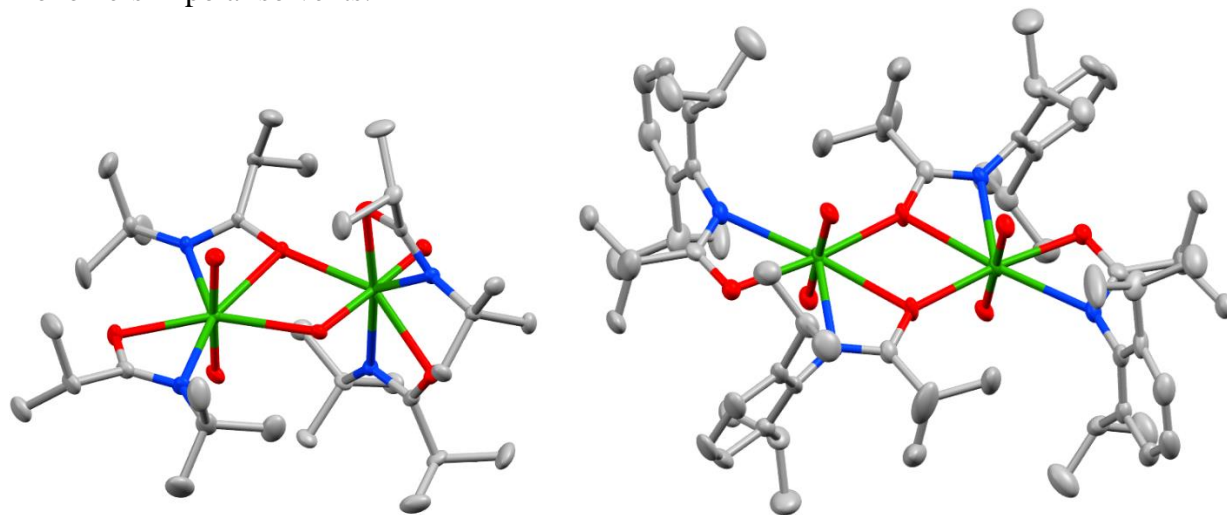
**Scheme A2:** Proposed decomposition mechanism of uranyl bis(amidates) with *N*-alkyl substituents.

Two uranyl amidates with N-alkyl substituents were synthesized, as well as one with an N-aryl substituent, via salt metathesis reactions from  $\text{UO}_2\text{Cl}_2(\text{THF})_2$  and two equivalents of the corresponding potassium amidates in THF.



**Figure A2:** Synthesis of  $\text{UO}_2(\text{ITA})_2$ ,  $\text{UO}_2(\text{TPTA})_2$ , and  $\text{UO}_2(\text{TDA})_2$ .

X-ray crystallography revealed  $\text{UO}_2(\text{ITA})_2$  and  $\text{UO}_2(\text{TDA})_2$  to be dimers in the solid state. Despite many attempts, I was unable to grow crystals of  $\text{UO}_2(\text{TPTA})_2$  suitable for X-ray crystallography; however, the NMR spectrum of this complex in  $\text{C}_6\text{D}_6$  is consistent with a dimeric species. Molecular formulas below are represented as the dimers to reflect this. Interestingly, all three of these complexes show two sets of resonances in  $\text{C}_6\text{D}_6$ , suggesting they exist as dimers in nonpolar solvents, and one set of resonances in  $\text{CD}_3\text{CN}$ , suggesting conversion of these species to monomers in polar solvents.



**Figure A3:** X-ray crystal structures of  $[\text{UO}_2(\text{ITA})_2]_2$  (left) and  $[\text{UO}_2(\text{TDA})_2]_2$  (right) with 50% probability ellipsoids. Hydrogen atoms are omitted for clarity.

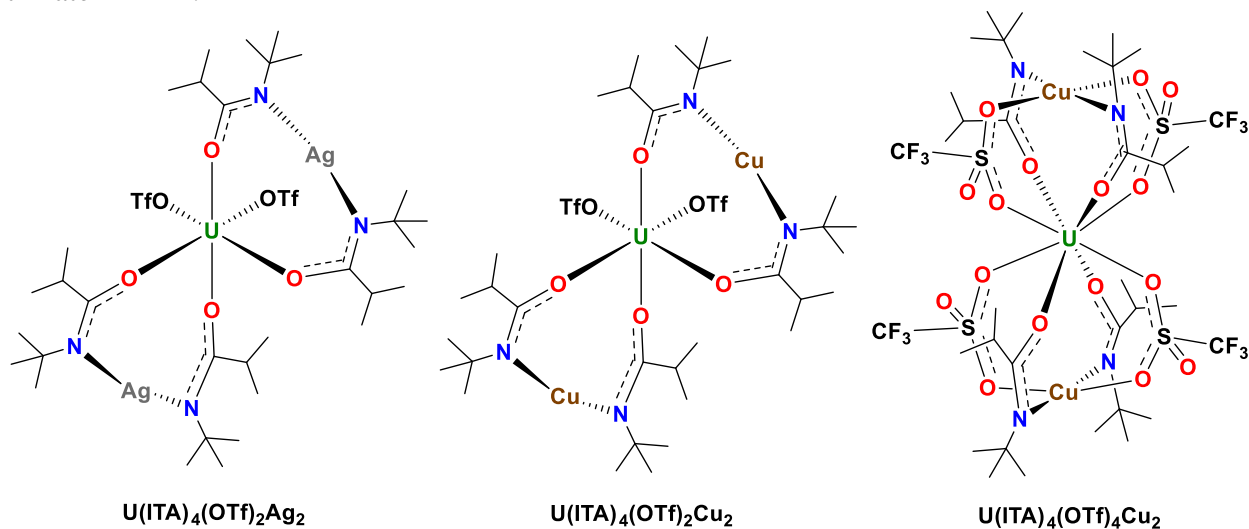
Although both  $[\text{UO}_2(\text{ITA})_2]_2$  and  $[\text{UO}_2(\text{TDA})_2]_2$  are both dimeric in the solid state, the geometries of these two dimers differ significantly from one another.  $[\text{UO}_2(\text{ITA})_2]_2$  contains two  $\text{UO}_2(\text{ITA})_2$  subunits, each with two amidate ligands bound  $\kappa^2\text{-O,N}$  to the metal centers. The trans-dioxo uranyl motifs in each subunit are perpendicular to each other, and the metal centers are bridged through one amidate oxygen and one uranyl oxygen, giving a structure with  $C_1$  point group

symmetry. In contrast, each uranium atom in  $[\text{UO}_2(\text{TDA})_2]_2$  contains two amidate ligands bound  $\kappa^2\text{-O,N}$  to the uranium atoms, with the NCO backbones of all four amidate ligands lying in the same plane as the uranium centers and the uranyl motifs perpendicular to this plane. The metal centers in  $[\text{UO}_2(\text{TDA})_2]_2$  are bridged through two amidate oxygens, giving a structure with  $C_{2h}$  point group symmetry.

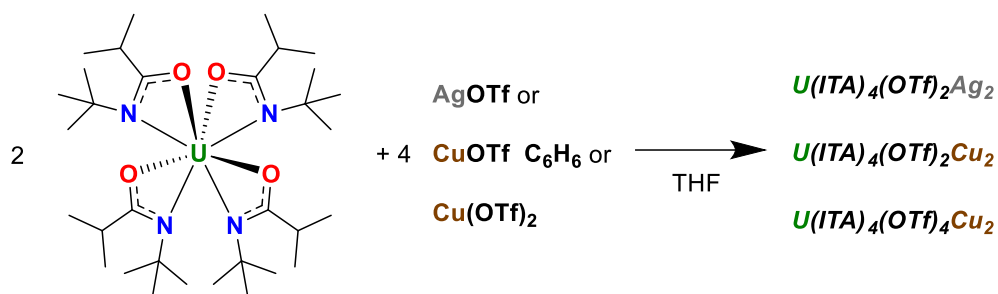
NMR decomposition experiments (see Chapters 3 and 4) confirmed the presence of amide, nitrile, and isobutylene in the thermolysis products of  $[\text{UO}_2(\text{TPTA})_2]_2$  and  $[\text{UO}_2(\text{ITA})_2]_2$ .  $[\text{UO}_2(\text{TDA})_2]_2$  is unable to access the alkene elimination mechanism shown above and decomposes through an unknown mechanism. PXRD has not been performed on the decomposition products of these precursors, but  $\text{UO}_3$  generated by thermolysis of  $[\text{UO}_2(\text{TPTA})_2]_2$  and  $[\text{UO}_2(\text{ITA})_2]_2$  could presumably be stabilized using a substrate with suitable lattice parameters for epitaxy. Many different phases of  $\text{UO}_3$  are known with a wide range of lattice parameters.<sup>2</sup> If these precursors were used for CVD of  $\text{UO}_3$  thin films, it would be important to choose a substrate that has a good lattice match with at least one polymorph of  $\text{UO}_3$  and a poor lattice match with other uranium oxides; the use of Si substrates, which epitaxially stabilize  $\text{UO}_2$ , would be best avoided for this reason.

## Heterometallic Precursors for Uranium-Group 11 Materials

The following heterometallic amidate complexes were developed as molecular precursors for new uranium-transition metal mixed oxide materials. These mixed-metal complexes were prepared by stirring the homoleptic U(IV) amidate complex  $\text{U}(\text{ITA})_4$  with Ag(I), Cu(I), and Cu(II) triflate in THF.



**Figure A4:** *U(IV)-Ag(I), U(IV)-Cu(I), and U(IV)-Cu(II) amidates developed as precursors for mixed-metal oxide materials.*

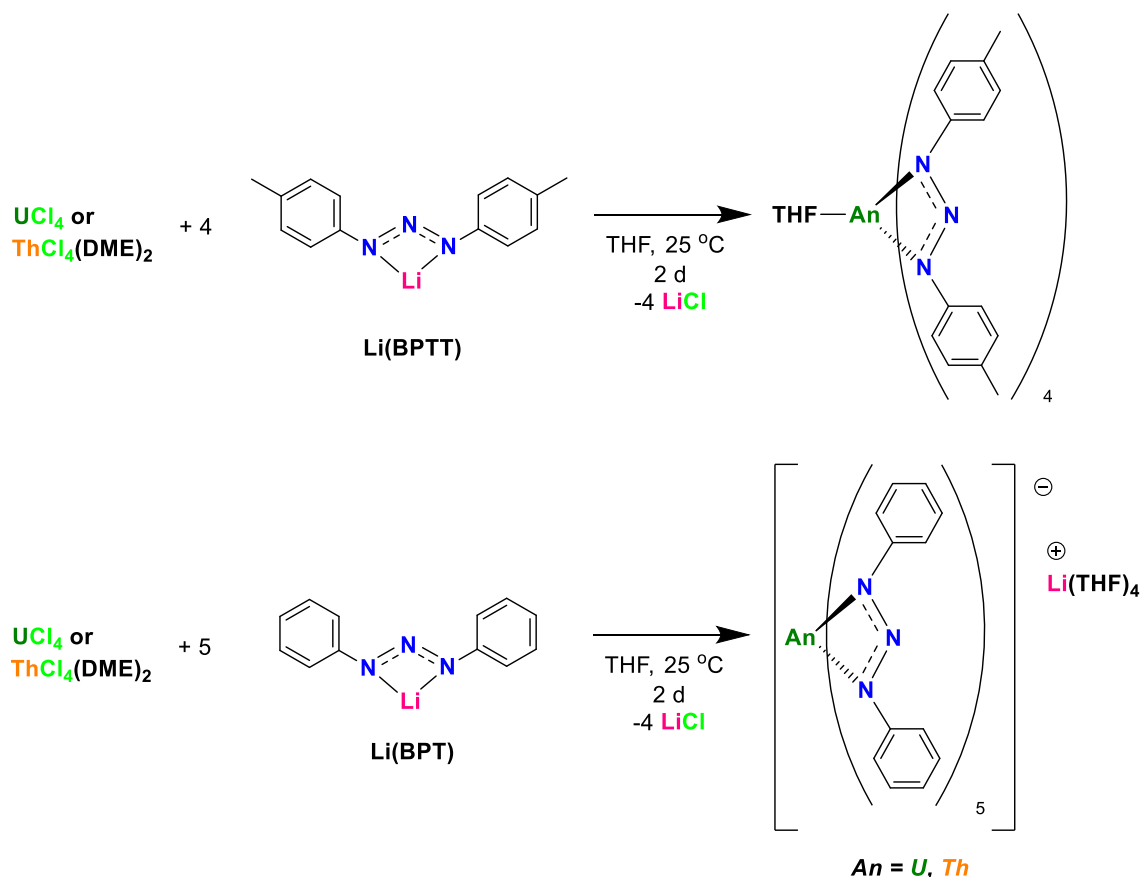


**Scheme A3:** Synthesis of uranium-group 11 heterometallic amidates.

These three complexes are thermally stable at room temperature, but nonvolatile. Thermolysis could potentially yield new mixed-metal compounds; one possibility would be the formation of the unreported spinel-type material  $\text{UCu}_2\text{O}_4$  from  $\text{U(ITA)}_4(\text{OTf})_4\text{Cu}_2$ . Another possibility would be the use of these complexes as single-source precursors for mixed-metal nanoparticles, which could potentially be useful as models for the buildup of fission products inside nuclear fuels under high-burnup conditions.

## Actinide Triazenide Complexes

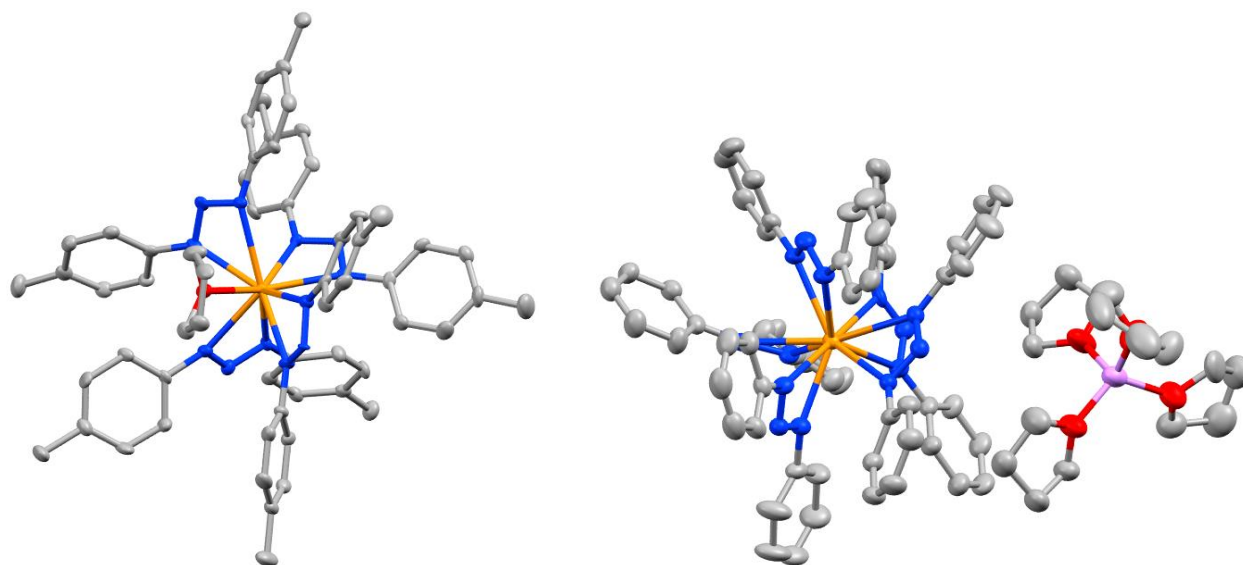
When looking into the design of new precursors, I became aware of triazenides ( $\text{RNNNR}'$ ) and believed this class of nitrogen-rich ligands might provide an excellent route to actinide nitride materials. Although triazenides remain poorly studied in comparison to related ligands such as amidinates, there has been some recent interest in developing transition metal triazenide complexes as precursors for nitride, oxide, and metallic materials.<sup>3-5</sup> Only one homoleptic actinide triazenide complex,  $\text{U}[\text{CH}_2(\text{C}_6\text{H}_5)\text{NNN}(\text{Mes})-\kappa^2-1,2-\text{N},\text{N}][\text{CH}_2(\text{C}_6\text{H}_5)\text{-NNN}(\text{Mes})-\kappa^2-1,3-\text{N},\text{N}]_3$ , has been reported; this was achieved by insertion of four equivalents of mesityl azide ( $\text{MesN}_3$ ) into tetrabenzyluranium(IV) at reduced temperature.<sup>6</sup> Given the thermal instability of this uranium alkyl starting material, I sought to develop other synthetic routes to access uranium and thorium triazenides.



**Scheme A4:** Synthesis of the actinide triazenides  $\text{U(BPTT)}_4(\text{THF})$ ,  $\text{Th(BPTT)}_4(\text{THF})$ ,  $[\text{U(BPT)}_5]\text{Li(THF)}_4$ , and  $[\text{Th(BPT)}_5]\text{Li(THF)}_4$ .

The bis(aryl)triazene proligands H(BPT) (= bis(phenyl)triazene) and H(BPTT) (= bis(para-tolyl)triazene) were synthesized by diazonium coupling using aniline and p-toluidine, respectively. Deprotonation of these triazenes with  $\text{LiN}(\text{SiMe}_3)_2$  in toluene yielded the lithium triazenides Li(BPT) and Li(BPTT). The addition of four equivalents of Li(BPTT) to  $\text{UCl}_4(1,4\text{-dioxane})_2$  or  $\text{ThCl}_4(\text{DME})_2$  in THF led to the formation of  $\text{U(BPTT)}_4(\text{THF})$  and  $\text{Th(BPTT)}_4(\text{THF})$ , respectively. The THF ligand in  $\text{U(BPTT)}_4(\text{THF})$  could not be removed by dynamic vacuum, but could be replaced by pyridine, thereby removing all oxygen from this precursor molecule in order to minimize oxygen contamination in the thermolysis products. Solvent-free  $\text{U(BPTT)}_4$  could also be isolated by using toluene in place of THF, thus avoiding the issue entirely; however, this method led to the formation of multiple products during the attempted synthesis of solvent-free  $\text{Th(BPTT)}_4$ .

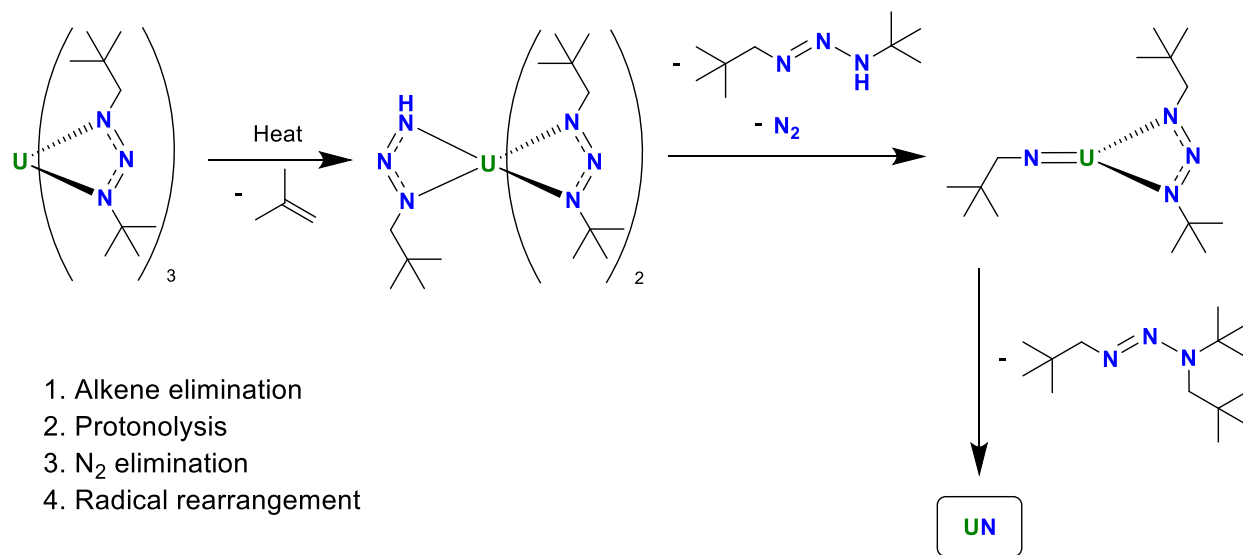
When Li(BPT) was used in place of Li(BPTT) in THF, the formation of -ate complexes was instead observed for both uranium and thorium. Although attempts to grow x-ray quality crystals of the uranium BPT complex were unsuccessful, single crystal x-ray diffraction of the thorium complex revealed this species to be the 10-coordinate  $[\text{Th(BPT)}_5]\text{Li(THF)}_4$ . Based on the  $^1\text{H}$  NMR spectra of these two complexes, and the presence of a positive lithium flame test for each, it is likely that the uranium complex adopts the same structure.



**Figure A5:** Crystal structures of  $\text{Th}(\text{BPTT})_4(\text{THF})$  (left) and  $[\text{Th}(\text{BPT})_5]\text{Li}(\text{THF})$  (right) with 50% probability ellipsoids. Hydrogen atoms are omitted for clarity.

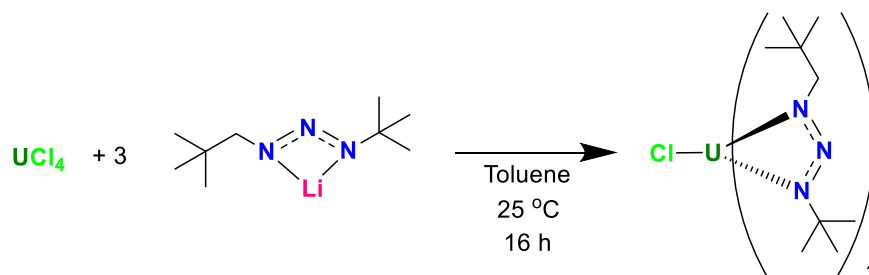
Following these results, I became interested in developing uranium bis(alkyl)triazenide complexes capable of undergoing a similar alkene elimination mechanism to the amidate complexes, allowing access to transient uranium imido species, which could then decompose to uranium nitride through a radical pathway (Scheme A5). My goal was to synthesize uranium triazenide complexes in different oxidation states, thus allowing access to multiple uranium nitride materials, e.g. UN and  $\text{U}_2\text{N}_3$ . Strongly electron-donating symmetric triazenides, such as  ${}^t\text{BuNNNH}{}^t\text{Bu}$ , were avoided due to ligand instability.<sup>7</sup> However, as the presence of a single tert-butyl substituent could be hypothesized to eliminate isobutylene relatively easily, a less electron-rich triazene could be synthesized by using one tert-butyl substituent and one substituent that is less electron donating, e.g. a primary alkyl. Using an asymmetric ligand of this type, mechanistic control could presumably be achieved by blocking alkene elimination on one substituent but not the other; the NTT (= 1-neopentyl-3-tert-butyltriazenido) ligand seemed a reasonable answer to this challenge.





**Scheme A5:** Proposed decomposition mechanism of  $U(NTT)_3$  to  $UN$ .

$Li(NTT)$  was synthesized via addition of neopentyl lithium to a toluene solution of  $tBuN_3$ . Attempts to directly synthesize the homoleptic complex  $U(NTT)_3$  via salt metathesis between  $UCl_3(1,4\text{-dioxane})_{1.5}$  and  $Li(NTT)$  were unsuccessful, as were attempts to synthesize this complex by hydrolysis of  $Li(NTT)$  with  $HCl$  in 1,4-dioxane followed by protonolysis with  $U(N(SiMe_3)_2)_3$ . Attempts to synthesize  $U(NTT)_4$  from  $UCl_4$ ,  $UCl_4(1,4\text{-dioxane})_2$ , and  $U(OTf)_4$  were similarly unsuccessful. However, the uranium tris(triazenide) chloride complex  $UCl(NTT)_3$  could readily be synthesized by adding 3 equivalents of  $Li(NTT)$  to a toluene solution of  $UCl_4$ . Unfortunately, all attempts to reduce  $UCl(NTT)_3$  to  $U(NTT)_3$  resulted in an intractable mixture of highly soluble products that could not be separated by crystallization or sublimation. Single crystals of  $UCl(NTT)_3$  could be grown from pentane, but attempts to solve the crystal structure of this molecule were hindered by full-molecule disorder.



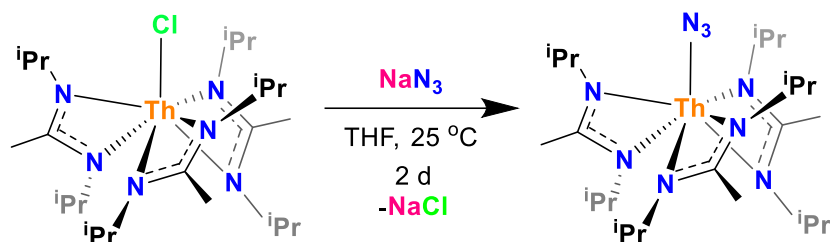
**Scheme A6:** Synthesis of the uranium tris(triazenide) chloride  $UCl(NTT)_3$ .

Looking to the future of this project,  $U(BPTT)_4$  may find application as a precursor to uranium nitride materials, although the decomposition mechanism is not yet known. However, it is possible that homoleptic uranium triazenides with greater volatility and an alkene elimination mechanism could be synthesized by using a different bis(alkyl)triazenide ligand, for example bis(*iso*-propyl)triazenide. If homoleptic uranium bis(alkyl)triazenide complexes can be isolated,

these high-nitrogen species could potentially be applied as volatile single-source molecular precursors for uranium nitride nanomaterials.

## Precursor for Thorium Nitride Materials

In addition to developing precursors for uranium nitride nanomaterials (Chapter 6), I was also interested in using the same ligand systems for thorium nitride precursors. I didn't end up spending very much time pursuing this project, but I was able to isolate and characterize the thorium nitride precursor  $\text{Th}(\text{N}_3)(\text{BIMA})_3$  (BIMA = N,N-bis(isopropyl)methyl amidinate) via salt metathesis of the previously-reported precursor  $\text{ThCl}(\text{BIMA})_3$ <sup>8</sup> with  $\text{NaN}_3$ .



*Scheme A7: Synthesis of the thorium tris(amidinate) azide  $\text{ThCl}(\text{BIMA})_3$ .*

Although I have not spent much time investigating the reactivity of this precursor, the thorium center is only bound to nitrogen atoms; no oxygen or halogens are present to contaminate the materials formed via thermolysis. Reduction of the azide site may also be able to access molecular thorium nitride species, analogous to the reduction of  $\text{U}(\text{N}_3)(\text{BIMA})_3$  (see Chapter 6). Similar ligands to BIMA, such as other amidinates, could also be used to generate a library of similar complexes in order to compare their reactivity.

## Experimental

### Materials and Methods

Unless otherwise noted, all syntheses were performed using standard Schlenk techniques under an atmosphere of nitrogen or in an MBraun glovebox under an atmosphere of nitrogen. Glassware, cannulae, and Celite were stored in an oven at 160 °C for at least 12 hours prior to use. 3 Å and 4 Å molecular sieves were activated by heating under vacuum at 300 °C for 24 hours. Hexane, pentane, toluene, benzene, diethyl ether, tetrahydrofuran (THF), 1,2-dimethoxyethane (DME), and acetonitrile were purified by passage through a column of activated alumina and degassed by sparging with nitrogen. Hexamethyldisiloxane (HMDSO) was stirred over sodium/benzophenone prior to distillation and stored over 4 Å molecular sieves.  $\text{C}_6\text{D}_6$ ,  $d_8$ -toluene, and  $d_8$ -THF were purchased from Cambridge Isotope Labs and stored over 4 Å molecular sieves.  $\text{C}_5\text{D}_5\text{N}$  was purchased from Cambridge Isotope Labs and stored over 3 Å molecular sieves.  $\text{CDCl}_3$  was purchased from Cambridge Isotope Labs and used as received.

$[\text{Li}(\text{BIMA})(\text{THF})_2]$ ,<sup>8</sup>  $\text{ThCl}(\text{BIMA})_3$ ,<sup>8</sup>  $\text{U}_4(1,4\text{-dioxane})_2$ ,<sup>9</sup>  $\text{U}_3(1,4\text{-dioxane})_{1.5}$ ,<sup>9</sup>  $\text{UCl}_4$ ,<sup>10</sup>  $\text{U}[\text{N}(\text{SiMe}_3)_2]_2[\kappa^2\text{-(C,N)-CH}_2\text{Si}(\text{Me})_2\text{N}(\text{SiMe}_3)]$ ,<sup>11</sup>  $\text{U}[\text{N}(\text{SiMe}_3)_2]_3$ ,<sup>12</sup>  $[\text{UO}_2\text{Cl}_2(\text{THF})_2]_2$ ,<sup>13</sup>  $\text{UO}_2(\text{N}(\text{SiMe}_3)_2)_2(\text{THF})_2$ ,<sup>14</sup> and  $\text{ThCl}_4(\text{DME})_2$ <sup>15</sup> were prepared according to literature methods.

All other chemicals were purchased from Sigma-Aldrich or Acros Organics and used as received.  $^1\text{H}$  and  $^{13}\text{C}$  NMR spectra were recorded at room temperature using Bruker AV-600, AV-500, AVB-400, AVQ-400, and AV-300 spectrometers.  $^1\text{H}$  chemical shifts were referenced to  $\text{C}_6\text{D}_5\text{H}$  ( $\delta = 7.16$  ppm),  $\text{C}_5\text{D}_4\text{HN}$  ( $\delta_1 = 8.74$  ppm),  $\text{C}_4\text{D}_7\text{HO}$  ( $\delta_2 = 1.78$  ppm),  $\text{C}_6\text{D}_4\text{HCD}_3$  ( $\delta_1 = 7.09$  ppm), and  $\text{CHCl}_3$  ( $\delta = 7.26$  ppm).  $^{13}\text{C}$  chemical shifts were referenced to  $\text{C}_6\text{D}_6$  ( $\delta = 128.39$  ppm) and  $\text{C}_5\text{D}_5\text{N}$  ( $\delta_1 = 150.35$  ppm).  $^{19}\text{F}$  chemical shifts were referenced to an external standard of  $\text{C}_6\text{H}_5\text{F}$  ( $\delta = -113.11$  ppm). Samples for IR spectroscopy were prepared as Nujol mulls, and spectra were taken in KBr plates using a Nicolet iS10 spectrometer. Melting points were determined in sealed tubes under an atmosphere of nitrogen using a Stanford Research Systems OptiMelt instrument and are reported uncorrected.

## Synthesis of Complexes

**H(ITA), H(TPTA), H(TDA), H(TEPA), and H(Ar<sup>F</sup>TA):** The same general procedure was used for these amides, without the exclusion of air. Acyl chloride (1 eq.), triethylamine (1.1 eq.), and  $\text{CH}_2\text{Cl}_2$  were added to a 3-neck flask equipped with a reflux condenser and a stir bar. The solution was cooled to  $0^\circ\text{C}$ , then a solution of primary amine (1 eq.) in  $\text{CH}_2\text{Cl}_2$  was slowly added through a dropping funnel. The solution was stirred for 30 mins, then heated to reflux for 5 h. After cooling to room temperature, the solution was transferred to a separatory funnel, then washed once with brine and twice with water to remove  $\text{NHEt}_3\text{Cl}$ . The organic layer was dried with  $\text{MgSO}_4$ , then the solvent was removed *in vacuo* and the product purified by vacuum sublimation.

**K(TEPA):** A THF solution (50 mL) of  $\text{KN}(\text{SiMe}_3)_2$  (4.90 g, 24.6 mmol) was added via cannula to a stirred THF solution (60 mL) of H(TEPA) (4.11 g, 23.9 mmol) maintained at  $-78^\circ\text{C}$ . The resulting solution was slowly warmed to room temperature and stirred for 16 h, then the solvent was removed *in vacuo* to give an off-white powder. This powder was washed with hexane (30 mL) to remove impurities, then dried *in vacuo* to give the product as a colorless powder. (4.91 g, 98% yield)

$^1\text{H}$  NMR ( $\text{C}_5\text{D}_5\text{N}$ , 400 MHz):  $\delta$  4.15 (m, 1H,  $\text{CH}(\text{CH}_2\text{CH}_3)_2$ ), 1.81 (m, 4H,  $\text{CH}(\text{CH}_2\text{CH}_3)_2$ ), 1.64 (s, 9H,  $\text{C}(\text{CH}_3)_3$ ), 1.18 (t, 6H,  $\text{CH}(\text{CH}_2\text{CH}_3)_2$ ).

$^{13}\text{C}$  NMR ( $\text{C}_5\text{D}_5\text{N}$ , 151 MHz):  $\delta$  177.31 (NCO), 56.88 ( $\text{C}(\text{CH}_3)_3$ ), 39.89 ( $\text{CHCH}_2\text{CH}_3$ ), 31.42 ( $\text{C}(\text{CH}_3)_3$ ), 31.13 ( $\text{CHCH}_2\text{CH}_3$ ), 12.49 ( $\text{CHCH}_2\text{CH}_3$ ).

IR ( $\text{cm}^{-1}$ ): 1534 (s), 1486 (m), 1387 (m), 1341 (m), 1327 (m), 1313 (m), 1213 (m), 1154 (w), 1122 (w), 1029 (w), 910 (w), 860 (w), 776 (w), 577 (w), 554 (w), 529 (w).

**K(Ar<sup>F</sup>TA):** A THF solution (30 mL) of  $\text{KN}(\text{SiMe}_3)_2$  (0.86 g, 4.37 mmol) was added via cannula to a stirred THF solution (50 mL) of H(Ar<sup>F</sup>TA) (1.31 g, 4.17 mmol) maintained at  $-78^\circ\text{C}$ . The resulting solution was slowly warmed to room temperature and stirred for 16 h, then the solvent was removed *in vacuo* to give an off-white powder. This powder was washed with hexane (50 mL) to remove impurities, then dried *in vacuo* to give the product as a colorless powder. (1.28 g, 87% yield)

$^1\text{H}$  NMR ( $\text{C}_5\text{D}_5\text{N}$ , 600 MHz):  $\delta$  9.33 (s, 2H, Ph-H), 7.85 (s, 1H, Ph-H), 1.88 (s, 9H,  $\text{C}(\text{CH}_3)_3$ ).

$^{13}\text{C}$  NMR ( $\text{C}_5\text{D}_5\text{N}$ , 151 MHz):  $\delta$  162.78 (NCO), 150.84 (Ph), 129.76 (q, Ph- $\text{CF}_3$ ), 129.38 (Ph), 126.22 (q, Ph- $\text{CF}_3$ ), 120.21 (Ph), 52.52 ( $\text{C}(\text{CH}_3)_3$ ), 32.02 ( $\text{C}(\text{CH}_3)_3$ ).

$^{19}\text{F}$  NMR ( $\text{C}_5\text{D}_5\text{N}$ , 565 MHz):  $\delta$  -63.60 ( $\text{CF}_3$ ).

IR (cm<sup>-1</sup>): 1622 (w), 1560 (m), 1353 (w), 1308 (m), 1282 (s), 1247 (w), 1170 (m), 1122 (m), 936 (w), 905 (w), 889 (w), 844 (w), 795 (w), 774 (w), 710 (w), 695 (w), 682 (m).

**K(TPTA):** A THF solution (100 mL) of KN(SiMe<sub>3</sub>)<sub>2</sub> (7.52 g, 37.7 mmol) was added via cannula to a stirred THF solution (150 mL) of H(TPTA) (8.00 g, 34.3 mmol) maintained at -78 °C. The resulting solution was slowly warmed to room temperature and stirred for 16 h, then the solvent was removed *in vacuo* to give an off-white powder. This powder was washed twice with Et<sub>2</sub>O (30 mL) to remove impurities, then dried *in vacuo* to give the product as a colorless powder. (8.62 g, 93% yield)

<sup>1</sup>H NMR (C<sub>5</sub>D<sub>5</sub>N, 400 MHz): δ 8.66 (d, 2H, Ph-*H*), 7.36 (d, 2H, Ph-*H*), 1.88 (s, 9H, C(CH<sub>3</sub>)<sub>3</sub>), 1.25 (s, 9H, C(CH<sub>3</sub>)<sub>3</sub>).

<sup>13</sup>C NMR (C<sub>5</sub>D<sub>5</sub>N, 151 MHz): δ 150.35 (NCO), 129.51 (*Ph*), 124.44 (*Ph*), 52.03 (NC(CH<sub>3</sub>)<sub>3</sub>), 34.48 (PhC(CH<sub>3</sub>)<sub>3</sub>), 32.73 (NC(CH<sub>3</sub>)<sub>3</sub>), 29.61 (PhC(CH<sub>3</sub>)<sub>3</sub>). Two additional resonances corresponding to the phenyl carbons are obscured by the pyridine resonances.

IR (cm<sup>-1</sup>): 1577 (m), 1544 (m), 1336 (m), 1267 (w), 1230 (w), 1211 (w), 1139 (w), 1105 (w), 1013 (w), 881 (w), 855 (w), 725 (w), 712 (w).

**K(TPTA)(18c6):** THF (4 mL) was added to a vial containing K(TPTA) (101 mg, 0.373 mmol) and 18-crown-6 (99 mg, 0.373 mmol) at room temperature. The solution was stirred for 1 h, concentrated to a volume of 1 mL, and cooled to -40 °C for 16 h. The resulting colorless crystals were washed with hexanes and dried *in vacuo*. (173 mg, 87% yield)

<sup>1</sup>H NMR (C<sub>6</sub>D<sub>6</sub>, 600 MHz): δ 8.79 (d, 2H, Ph-*H*), 7.43 (d, 2H, Ph-*H*), 3.13 (s, 24H, OCH<sub>2</sub>), 2.06 (s, 9H, C(CH<sub>3</sub>)<sub>3</sub>), 1.38 (s, 9H, C(CH<sub>3</sub>)<sub>3</sub>).

<sup>13</sup>C NMR (C<sub>6</sub>D<sub>6</sub>, 151 MHz): δ 165.67 (NCO), 129.46 (*Ph*), 123.54 (*Ph*), 70.42 (OCH<sub>2</sub>), 52.38 (NC(CH<sub>3</sub>)<sub>3</sub>), 34.84 (PhC(CH<sub>3</sub>)<sub>3</sub>), 32.47 (NC(CH<sub>3</sub>)<sub>3</sub>), 32.34 (PhC(CH<sub>3</sub>)<sub>3</sub>).

IR (cm<sup>-1</sup>): 1580 (m), 1541 (m), 1499 (w), 1352 (m), 1327 (m), 1285 (w), 1249 (w), 1327 (w), 1210 (w), 1113 (s), 962 (m), 875 (w), 837 (w), 776 (w), 711 (w).

**K(TDA):** A THF solution (100 mL) of KN(SiMe<sub>3</sub>)<sub>2</sub> (3.84 g, 19.3 mmol) was added via cannula to a stirred THF solution (150 mL) of H(TDA) (5.00 g, 19.1 mmol) maintained at -78 °C. The resulting solution was slowly warmed to room temperature and stirred for 2 d, then the solvent was removed *in vacuo* to give an off-white powder. This powder was washed with hexane (50 mL) to remove impurities, then dried *in vacuo* to give the product as a colorless powder. (4.94 g, 86% yield)

<sup>1</sup>H NMR (C<sub>5</sub>D<sub>5</sub>N, 400 MHz): δ 7.17 (d, 2H, Ph-*H*), 6.99 (t, 1H, Ph-*H*), 3.77 (m, 2H, CH(CH<sub>3</sub>)<sub>2</sub>), 1.68 (s, 9H, C(CH<sub>3</sub>)<sub>3</sub>), 1.32 and 1.26 (dd, 12H, CH(CH<sub>3</sub>)<sub>2</sub>).

<sup>13</sup>C NMR (C<sub>5</sub>D<sub>5</sub>N, 151 MHz): δ 176.48 (NCO), 155.37 (CCN), 141.61 (Ph), 122.91 (Ph), 120.22 (Ph), 39.80 (C(CH<sub>3</sub>)<sub>3</sub>), 30.82 (C(CH<sub>3</sub>)<sub>3</sub>), 28.80 (CH(CH<sub>3</sub>)<sub>2</sub>), 24.00 (CH(CH<sub>3</sub>)<sub>2</sub>).

IR (cm<sup>-1</sup>): 1586 (w), 1542 (s), 1517 (s), 1433 (s), 1390 (m), 1349 (s), 1317 (m), 1255 (m), 1219 (m), 1176 (w), 1158 (w), 1101 (w), 1056 (w), 1041 (w), 914 (m), 883 (w), 848 (w), 808 (w), 791 (m), 751 (s).

**Li(BPTT):** A toluene solution (20 mL) of LiN(SiMe<sub>3</sub>)<sub>2</sub> (2.28 g, 13.62 mmol) was added via cannula to a stirred toluene solution (50 mL) of H(BPTT) (2.92 g, 12.97 mmol) maintained at -78 °C. Upon addition of the LiN(SiMe<sub>3</sub>)<sub>2</sub>, the yellow solution became a thick yellow suspension, which was slowly warmed to room temperature and stirred for 3 h. The suspension was filtered

over a glass Schlenk frit, then dried *in vacuo* to give a bright yellow powder. This powder was washed with hexane (30 mL) to remove impurities. (2.70 g, 90% yield)

Li(BPTT) can be converted to the more soluble Li(BPTT)(THF) by stirring in THF then removing the solvent.

$^1\text{H NMR}$  ( $\text{C}_6\text{D}_6$ , 400 MHz):  $\delta$  7.70 (s, 4H, Ph-H), 7.20 (s, 4H, Ph-H), 2.26 (s, 6H,  $\text{CH}_3$ ).

$^{13}\text{C NMR}$  ( $\text{C}_6\text{D}_6$ , 151 MHz):  $\delta$  153.53 (Ph), 130.26 (Ph), 129.90 (Ph), 119.08 (Ph), 21.35 ( $\text{CH}_3$ ).

IR ( $\text{cm}^{-1}$ ): 1600 (w), 1504 (s), 1357 (m), 1309 (s), 1299 (m), 1272 (s), 1226 (m), 1194 (m), 1165 (w), 1109 (w), 825 (m), 656 (w), 621 (w), 522 (m).

**Li(BPT)(THF):** A THF solution (20 mL) of  $\text{LiN}(\text{SiMe}_3)_2$  (2.65 g, 15.9 mmol) was added via cannula to a stirred THF solution (20 mL) of H(BPT) (2.98 g, 15.1 mmol) maintained at  $-78\text{ }^\circ\text{C}$ . Upon addition of the  $\text{LiN}(\text{SiMe}_3)_2$ , the orange-red solution turned maroon. The solution was slowly warmed to room temperature and stirred for 3 h, then the solvent was removed *in vacuo* to give a maroon solid and triturated with hexane (10 mL). The solution was extracted into toluene (10 mL), filtered, then cooled to  $-40\text{ }^\circ\text{C}$  for 24 h, yielding the product as maroon crystals. (2.60 g, 63% yield)

$^1\text{H NMR}$  ( $\text{C}_6\text{D}_6$ , 400 MHz):  $\delta$  7.92 (d, 2H, Ph-H), 7.38 (t, 2H, Ph-H), 7.03 (t, 1H, Ph-H), 3.09 (m, 4H,  $\text{CH}_2\text{CH}_2\text{O}$ ), 0.84 (m, 4H,  $\text{CH}_2\text{CH}_2\text{O}$ ).

$^{13}\text{C NMR}$  ( $\text{C}_6\text{D}_6$ , 151 MHz):  $\delta$  153.34 (Ph-N), 129.65 (Ph), 123.10 (Ph), 118.88 (Ph), 68.44 ( $\text{CH}_2\text{CH}_2\text{O}$ ), 24.93 ( $\text{CH}_2\text{CH}_2\text{O}$ ).

IR ( $\text{cm}^{-1}$ ): 3061 (w), 3031 (w), 1944 (w), 1877 (w), 1800 (w), 1737 (w), 1668 (w), 1589 (s), 1481 (s), 1366 (s), 1349 (s), 1368 (s), 1299 (s), 1279 (s), 1223 (s), 1196 (s), 1161 (m), 1073 (m), 1036 (m), 993 (m), 900 (m), 773 (m), 762 (s), 693 (s), 655 (m), 612 (w), 524 (m).

**Li(NTT):** A toluene solution (10 mL) of  $^t\text{BuN}_3$  (649 mg, 6.55 mmol) was added via cannula to a stirred toluene solution (50 mL) of  $\text{LiCH}_2^t\text{Bu}$  (501 mg, 6.42 mmol) maintained at  $0\text{ }^\circ\text{C}$ . The colorless solution was slowly warmed to room temperature and stirred for 4 h, then the solution was dried *in vacuo* and triturated twice with hexane (10 mL) to give the product as a colorless solid. (978 mg, 87% yield)

$^1\text{H NMR}$  ( $\text{C}_6\text{D}_6$ , 400 MHz):  $\delta$  3.39 (s, 2H,  $\text{CH}_2\text{C}(\text{CH}_3)_3$ ), 1.35 (s, 9H,  $\text{NC}(\text{CH}_3)_3$ ), 0.97 (s, 9H,  $\text{CH}_2\text{C}(\text{CH}_3)_3$ ).

$^{13}\text{C NMR}$  ( $\text{C}_6\text{D}_6$ , 126 MHz):  $\delta$  66.83 ( $\text{NC}(\text{CH}_3)_3$ ), 57.69 ( $\text{CH}_2\text{C}(\text{CH}_3)_3$ ), 33.80 ( $\text{CH}_2\text{C}(\text{CH}_3)_3$ ), 30.86 ( $\text{NC}(\text{CH}_3)_3$ ), 28.56 ( $\text{CH}_2\text{C}(\text{CH}_3)_3$ ).

IR ( $\text{cm}^{-1}$ ): 1389 (s), 1365 (m), 1358 (m), 1314 (m), 1267 (m), 1229 (m), 1211 (m), 1159 (s), 1097 (m), 1019 (w), 937 (w), 911 (w), 886 (w), 745 (w), 645 (w), 579 (m), 503 (w).

**U(TEPA)<sub>4</sub>:** A THF solution (4 mL) of  $\text{UI}_4(1,4\text{-dioxane})_2$  (201 mg, 0.218 mmol) was added dropwise to a stirred THF solution (4 mL) of K(TEPA) (182 mg, 0.870 mmol). The color of the solution changed from red to green upon addition. The solution was stirred for 3 d and then the solvent was removed *in vacuo*. The product was extracted into pentane (5 mL), and the resulting green solution was filtered to remove insoluble KI, concentrated to a volume of 1 mL, and cooled to  $-40\text{ }^\circ\text{C}$  for 2 d, yielding green crystals. These crystals were then washed with acetonitrile to remove impurities. (105 mg, 53% yield)

$^1\text{H NMR}$  ( $\text{C}_6\text{D}_6$ , 500 MHz):  $\delta$  10.12 (s, 4H,  $\text{CH}(\text{CH}_2\text{CH}_3)_2$ ), 4.52 (s, 36H,  $\text{C}(\text{CH}_3)_3$ ), -1.24 and -3.22 (broad, 24H,  $\text{CH}(\text{CH}_2\text{CH}_3)_2$ ), -9.79 and -11.61 (broad, 16H,  $\text{CH}(\text{CH}_2\text{CH}_3)_2$ ).

IR (cm<sup>-1</sup>): 1525 (s), 1487 (w), 1402 (s), 1378 (s), 1364 (m), 1336 (s), 1311 (m), 1267 (m), 1205 (m), 1162 (w), 1140 (m), 1120 (w), 1050 (m), 1027 (w), 1016 (m), 922 (w), 872 (m), 851 (m), 807 (m), 802 (m), 773 (w), 744 (w), 607 (m), 587 (m).

Melting point: decomposes *ca.* 325 °C.

**U(Ar<sup>F</sup>TA)<sub>4</sub>:** A THF solution (2 mL) of UI<sub>4</sub>(1,4-dioxane)<sub>2</sub> (63 mg, 0.068 mmol) was added dropwise to a stirred THF solution (2 mL) of K(Ar<sup>F</sup>TA) (96 mg, 0.273 mmol). The color of the solution changed from red to green upon addition. The solution was stirred for 3 d and then the solvent was removed *in vacuo*. The product was extracted into hexane (5 mL), and the resulting green solution was filtered to remove insoluble KI, concentrated to a volume of 2 mL, and cooled to -40 °C for 2 d, yielding green crystals. (55 mg, 54% yield)

<sup>1</sup>H NMR (C<sub>6</sub>D<sub>6</sub>, 400 MHz): δ 9.37 (s, 4H, Ph-H), 8.56 (s, 8H, Ph-H), -4.41 (s, 36H, C(CH<sub>3</sub>)<sub>3</sub>).

<sup>19</sup>F NMR (C<sub>6</sub>D<sub>6</sub>, 377 MHz): δ -62.30 (s, CF<sub>3</sub>).

IR (cm<sup>-1</sup>): 1626 (w), 1610 (w), 1552 (w), 1355 (w), 1323 (w), 1278 (m), 1251 (w), 1212 (w), 1175 (w), 1132 (m), 1108 (m), 964 (w), 934 (w), 903 (w), 844 (w), 792 (w), 693 (w), 681 (w).

Melting point: 154-155 °C.

#### **U(TPTA)<sub>4</sub>:**

**Method 1:** A THF solution (2 mL) of UI<sub>4</sub>(1,4-dioxane)<sub>2</sub> (43 mg, 0.047 mmol) was added dropwise to a stirred THF solution (2 mL) of K(TPTA)(18c6) (100 mg, 0.187 mmol). The color of the solution changed from red to green over the course of the reaction. The solution was stirred for 16 h and then the solvent was removed *in vacuo*. The product was extracted into pentane (3 mL), and the resulting green solution was filtered to remove insoluble KI, concentrated to a volume of 1 mL, and cooled to -40 °C for 24 h, yielding green crystals. These crystals were then washed with acetonitrile to remove impurities. (49 mg, 91% yield)

**Method 2:** A THF solution (5 mL) of K(TPTA) (198 mg, 0.729 mmol) was added dropwise to a stirred THF solution (3 mL) of UI<sub>4</sub>(1,4-dioxane)<sub>2</sub> (168 mg, 0.182 mmol). The color of the solution changed from red to green upon addition of K(TPTA). The solution was stirred for 2 d and then the solvent was removed *in vacuo*. Pentane (5 mL) was added to the resulting green oil to give a green solution, which was then filtered to remove insoluble KI, concentrated to a volume of 2 mL, and cooled to -40 °C for 24 h, yielding green crystals. These crystals were washed with acetonitrile, then recrystallized from pentane. (90 mg, 54% yield)

**Method 3:** A toluene solution (10 mL) of H(TPTA) (136 mg, 0.585 mmol) was added dropwise to a stirred toluene solution (1 mL) of U[N(SiMe<sub>3</sub>)<sub>2</sub>]<sub>2</sub>[κ<sup>2</sup>-(C,N)-CH<sub>2</sub>Si(Me)<sub>2</sub>N(SiMe<sub>3</sub>)] (100 mg, 0.139 mmol). The color of the solution changed from brown to green over the course of the reaction. The solution was stirred for 16 h and then the solvent was removed *in vacuo*. Hexane (5 mL) was added to the resulting green oil to give a green solution, which was then filtered and cooled to -40 °C for 24 h, yielding green crystals. These crystals were washed with acetonitrile, then recrystallized from pentane. (82 mg, 50% yield)

<sup>1</sup>H NMR (C<sub>6</sub>D<sub>6</sub>, 400 MHz): δ 8.26 (s, 8H, Ph-H), 7.96 (d, 8H, Ph-H), 1.66 (s, 36H, C(CH<sub>3</sub>)<sub>3</sub>), -3.34 (s, 36H, C(CH<sub>3</sub>)<sub>3</sub>).

IR (cm<sup>-1</sup>): 3341 (w), 1680 (w), 1632 (w), 1611 (w), 1546 (m), 1494 (m), 1267 (w), 1221 (w), 1149 (w), 1104 (w), 1025 (w), 983 (m), 919 (w), 845 (m), 811 (w), 751 (w).

EA calcd for C<sub>60</sub>H<sub>88</sub>N<sub>4</sub>O<sub>4</sub>U: C: 61.68%, H: 7.60%, N: 4.80%. Found: C: 61.31%, H: 7.71%, N: 4.68%

Melting point: 166-171 °C.

**[UO<sub>2</sub>(TPTA)<sub>2</sub>]<sub>2</sub>**: A THF solution (5 mL) of [UO<sub>2</sub>Cl<sub>2</sub>(THF)<sub>2</sub>]<sub>2</sub> (300 mg, 0.309 mmol) was added dropwise to a THF solution (5 mL) of K(TPTA) (336 mg, 1.24 mmol). The pale yellow solution turned light yellow-orange over the course of the reaction. The solution was stirred for 2 d and then the solvent was removed *in vacuo*. Et<sub>2</sub>O (10 mL) was added to the resulting yellow solids to give a yellow solution, which was filtered to remove insoluble KCl, concentrated to a volume of 6 mL and cooled to -40 °C for 24 h, yielding the product as a yellow microcrystalline solid. This suspension was filtered over a glass frit, dried *in vacuo*, and the resulting yellow solids were triturated with hexane. (157 mg, 35% yield)

<sup>1</sup>H NMR (C<sub>6</sub>D<sub>6</sub>, 500 MHz): δ 7.82 (d, 4H, Ph-*H*), 7.19 (d, 4H, Ph-*H*), 7.61 (d, 4H, Ph-*H*), 7.25 (d, 4H, Ph-*H*), 1.95 (s, 9H, C(CH<sub>3</sub>)<sub>3</sub>), 1.40 (s, 9H, C(CH<sub>3</sub>)<sub>3</sub>), 1.16 (s, 9H, C(CH<sub>3</sub>)<sub>3</sub>), 1.10 (s, 9H, C(CH<sub>3</sub>)<sub>3</sub>).

<sup>13</sup>C NMR (C<sub>6</sub>D<sub>6</sub>, 151 MHz): δ 177.84 (NCO), 176.34 (NCO), 152.30 (PhCO), 151.54 (PhCO), 138.59 (Ph), 137.66 (Ph), 127.24 (PhCC), 124.87 (PhCC), 57.01 (NC(CH<sub>3</sub>)<sub>3</sub>), 55.47 (NC(CH<sub>3</sub>)<sub>3</sub>), 34.32 (PhC(CH<sub>3</sub>)<sub>3</sub>), 34.27 (PhC(CH<sub>3</sub>)<sub>3</sub>), 32.98 (NC(CH<sub>3</sub>)<sub>3</sub>), 32.61 (NC(CH<sub>3</sub>)<sub>3</sub>), 31.59 (PhC(CH<sub>3</sub>)<sub>3</sub>), 30.95 (PhC(CH<sub>3</sub>)<sub>3</sub>).

IR (cm<sup>-1</sup>): 1611 (w), 1577 (w), 1503 (w), 1323 (w), 1220 (w), 1141 (w), 1104 (w), 977 (w), 932 (m), 921 (w), 888 (w), 878 (w), 847 (w), 768 (w), 750 (w), 575 (w).

Melting point: 227-228 °C; some sublimation is also observed.

**[UO<sub>2</sub>(ITA)<sub>2</sub>]<sub>2</sub>**: A THF solution (6 mL) of [UO<sub>2</sub>Cl<sub>2</sub>(THF)<sub>2</sub>]<sub>2</sub> (100 mg, 0.103 mmol) was added dropwise to a THF solution (4 mL) of K(ITA) (75 mg, 0.412 mmol). The solution was stirred for 2 d and then the solvent was removed *in vacuo* to give a yellow oil, which was triturated with hexane (2 mL). Hexane (5 mL) was added to the resulting yellow solids to give a yellow solution, which was filtered to remove insoluble KCl, concentrated to a volume of 0.5 mL and cooled to -40 °C for 24 h, yielding yellow crystals. (110 mg, 96% yield) Half of this product was then recrystallized in Et<sub>2</sub>O (0.3 mL) over a period of 18 months to give orange crystals suitable for x-ray crystallography.

<sup>1</sup>H NMR (C<sub>6</sub>D<sub>6</sub>, 400 MHz): δ 3.41 (s, 2H, CH(CH<sub>3</sub>)<sub>2</sub>), 3.13 (s, 2H, CH(CH<sub>3</sub>)<sub>2</sub>), 2.01 (s, 18H, C(CH<sub>3</sub>)<sub>3</sub>), 1.78 (s, 12H, CH(CH<sub>3</sub>)<sub>2</sub>), 1.43 (q, 12H, CH(CH<sub>3</sub>)<sub>2</sub>), 1.35 (s, 18H, C(CH<sub>3</sub>)<sub>3</sub>).

<sup>13</sup>C NMR (C<sub>6</sub>D<sub>6</sub>, 151 MHz): δ 182.76 (NCO), 55.86 (C(CH<sub>3</sub>)<sub>3</sub>), 54.74 (C(CH<sub>3</sub>)<sub>3</sub>), 37.21 (CH(CH<sub>3</sub>)<sub>2</sub>), 36.67 (CH(CH<sub>3</sub>)<sub>2</sub>), 32.87 (C(CH<sub>3</sub>)<sub>3</sub>), 32.45 (C(CH<sub>3</sub>)<sub>3</sub>), 20.45 (CH(CH<sub>3</sub>)<sub>2</sub>), 20.36 (CH(CH<sub>3</sub>)<sub>2</sub>), 20.19 (CH(CH<sub>3</sub>)<sub>2</sub>), 19.99 (CH(CH<sub>3</sub>)<sub>2</sub>).

IR (cm<sup>-1</sup>): 1577 (w), 1547 (m), 1396 (w), 1365 (w), 1351 (m), 1324 (w), 1300 (w), 1208 (m), 1072 (m), 1010 (m), 923 (m), 896 (w), 876 (m), 819 (w), 747 (w), 648 (w), 587 (w).

Melting point: 147-152 °C.

**[UO<sub>2</sub>(TDA)<sub>2</sub>]<sub>2</sub>**: A THF solution (7 mL) of K(TDA) (142 mg, 0.544 mmol) was added dropwise to a THF solution (2 mL) of UO<sub>2</sub>(N(SiMe<sub>3</sub>)<sub>2</sub>)<sub>2</sub>(THF)<sub>2</sub> (200 mg, 0.272 mmol). The orange solution lightened slightly in color to yellow-orange over the course of the reaction. The solution was stirred for 2 d and then the solvent was removed *in vacuo*. Et<sub>2</sub>O (10 mL) was added to the resulting orange solids to give a yellow-orange solution, which was filtered, concentrated to a volume of 2 mL, and cooled to -40 °C for 24 h, yielding a yellow-orange microcrystalline solid. This solid was filtered over a glass frit, dried *in vacuo*, and then triturated with hexane. Crystals suitable for x-ray diffraction were grown by Et<sub>2</sub>O/hexane layering. (52 mg, 18% yield)

$^1\text{H}$  NMR ( $\text{C}_6\text{D}_6$ , 600 MHz):  $\delta$  7.37 (d, 4H, Ph-*H*), 7.31 (t, 2H, Ph-*H*), 7.22 (d, 4H, Ph-*H*), 7.09 (t, 2H, Ph-*H*), 3.69 and 3.64 (dm, 8H,  $\text{CH}(\text{CH}_3)_2$ ), 1.54 (s, 18H,  $\text{C}(\text{CH}_3)_3$ ), 1.35 (d, 12H,  $\text{CH}(\text{CH}_3)_2$ ), 1.31 and 1.28 (dd, 24H,  $\text{CH}(\text{CH}_3)_2$ ), 1.30 (s, 18H,  $\text{C}(\text{CH}_3)_3$ ), 1.13 (d, 12H,  $\text{CH}(\text{CH}_3)_2$ ).

$^{13}\text{C}$  NMR ( $\text{C}_6\text{D}_6$ , 151 MHz):  $\delta$  186.57 (NCO), 183.15 (NCO), 144.46 (CCN), 142.42 (Ph), 142.16 (CCN), 142.00 (Ph), 126.42 (Ph), 126.36 (Ph), 123.71 (Ph), 123.45 (Ph), 45.16 ( $\text{C}(\text{CH}_3)_3$ ), 44.40 ( $\text{C}(\text{CH}_3)_3$ ), 29.10 ( $\text{C}(\text{CH}_3)_3$ ), 29.00 ( $\text{C}(\text{CH}_3)_3$ ), 28.61 ( $\text{CH}(\text{CH}_3)_2$ ), 28.02 ( $\text{CH}(\text{CH}_3)_2$ ), 25.50 ( $\text{CH}(\text{CH}_3)_2$ ), 25.08 ( $\text{CH}(\text{CH}_3)_2$ ), 24.05 ( $\text{CH}(\text{CH}_3)_2$ ), 23.83 ( $\text{CH}(\text{CH}_3)_2$ ).

IR ( $\text{cm}^{-1}$ ): 1649 (w), 1598 (w), 1528 (w), 1403 (w), 1304 (w), 1211 (w), 1174 (w), 1102 (w), 934 (m), 803 (w), 765 (w).

Melting point: decomposes *ca.* 288 °C.

**U(ITA)<sub>4</sub>(OTf)<sub>2</sub>Ag<sub>2</sub>:** A THF solution (3 mL) of silver(I) triflate (64 mg, 0.248 mmol) cooled to -40 °C was added to a THF solution (3 mL) of U(ITA)<sub>4</sub> (100 mg, 0.124 mmol) maintained at -40 °C. The green solution turned aqua upon addition of silver(I) triflate. The resulting solution was stirred for 15 min, then the solvent was removed *in vacuo*. The product was then washed with hexane (2 mL), extracted into Et<sub>2</sub>O (10 mL), and filtered through Celite. The resulting aqua solution was then concentrated to a final volume of 8 mL and cooled to -40 °C for 24 h, yielding aqua crystals. (145 mg, 88% yield)

$^1\text{H}$  NMR ( $\text{C}_6\text{D}_6$ , 400 MHz):  $\delta$  31.56 (m, 2H,  $\text{CH}(\text{CH}_3)_2$ ), 20.15 (d, 6H,  $\text{CH}(\text{CH}_3)_2$ ), 12.95 (s, 18H,  $\text{C}(\text{CH}_3)_3$ ), 8.57 (d, 6H,  $\text{CH}(\text{CH}_3)_2$ ), 1.14 (d, 6H,  $\text{CH}(\text{CH}_3)_2$ ), -4.45 (s, 18H,  $\text{C}(\text{CH}_3)_3$ ), -7.28 (d, 6H,  $\text{CH}(\text{CH}_3)_2$ ), -9.00 (m, 2H,  $\text{CH}(\text{CH}_3)_2$ ).

$^{19}\text{F}$  NMR ( $\text{C}_6\text{D}_6$ , 377 MHz):  $\delta$  -90.99 ( $\text{CF}_3$ ).

IR ( $\text{cm}^{-1}$ ): 1583 (w), 1540 (w), 1343 (w), 1297 (w), 1195 (w), 1071 (w), 1009 (w), 994 (w), 894 (w), 821 (w), 663 (w), 637 (w), 536 (w).

EA calcd for  $\text{C}_{34}\text{H}_{64}\text{N}_4\text{O}_{10}\text{Ag}_2\text{F}_6\text{S}_2\text{U}$ : C: 30.92%, H: 4.88%, N: 4.24%. Found: C: 31.56%, H: 5.11%, N: 4.32%.

Melting point: decomposes *ca.* 93 °C.

**U(ITA)<sub>4</sub>(OTf)<sub>2</sub>Cu<sub>2</sub>:** A THF solution (4 mL) of copper(I) triflate benzene complex (17 mg, 0.034 mmol) was added to a THF solution (4 mL) of U(ITA)<sub>4</sub> (50 mg, 0.062 mmol) dropwise. The green solution turned brown upon addition of copper(I) triflate. The resulting solution was stirred for 1 h, then the solvent was removed *in vacuo*. The product was then washed with hexane (2 mL), extracted into Et<sub>2</sub>O (10 mL), and filtered through Celite. The resulting green solution was then concentrated to 2 mL and cooled to -40 °C for 24 h, yielding gray crystals. (23 mg, 55% yield)

$^1\text{H}$  NMR ( $\text{C}_6\text{D}_6$ , 400 MHz):  $\delta$  36.74 (s, 2H,  $\text{CH}(\text{CH}_3)_2$ ), 22.55 (d, 6H,  $\text{CH}(\text{CH}_3)_2$ ), 15.17 (d, 6H,  $\text{CH}(\text{CH}_3)_2$ ), 14.74 (s, 18H,  $\text{C}(\text{CH}_3)_3$ ), -4.46 (s, 18H,  $\text{C}(\text{CH}_3)_3$ ), -5.72 (d, 6H,  $\text{CH}(\text{CH}_3)_2$ ), -9.69 (d, 6H,  $\text{CH}(\text{CH}_3)_2$ ), -12.69 (s, 2H,  $\text{CH}(\text{CH}_3)_2$ ).

$^{19}\text{F}$  NMR ( $\text{C}_6\text{D}_6$ , 377 MHz):  $\delta$  -93.53 ( $\text{CF}_3$ ).

IR ( $\text{cm}^{-1}$ ): 1569 (m), 1342 (m), 1320 (m), 1305 (m), 1235 (m), 1190 (s), 1075 (m), 991 (m), 902 (w), 824 (w), 764 (w), 733 (w), 673 (m), 633 (m), 574 (w), 523 (w), 508 (w).

Melting point: Decomposes *ca.* 78 °C.

**U(ITA)<sub>4</sub>(OTf)<sub>4</sub>Cu<sub>2</sub>:** An Et<sub>2</sub>O solution (2 mL) of copper(II) triflate (55 mg, 0.152 mmol) was added to an Et<sub>2</sub>O solution (3 mL) of U(ITA)<sub>4</sub> (61 mg, 0.076 mmol) dropwise. The green solution turned olive green upon addition of copper(II) triflate. The resulting solution was stirred for 16 h, then the insoluble teal product was collected over a glass filter frit. (38 mg, 33% yield)



NMR: Insoluble in all tested solvents.

IR (cm<sup>-1</sup>): 1574 (m), 1392 (w), 1338 (s), 1329 (m), 1306 (s), 1226 (m), 1203 (s), 1183 (m), 1159 (w), 1115 (w), 1077 (m), 1012 (s), 905 (w), 824 (w), 760 (w), 743 (w), 673 (w), 635 (m), 573 (w), 513 (w).

Melting point: Decomposes *ca.* 182 °C.

**U(BPTT)<sub>4</sub>**: Toluene (100 mL) was added to a flask containing UI<sub>4</sub>(1,4-dioxane)<sub>2</sub> (1.08 g, 1.17 mmol) and Li(BPTT) (1.08 g, 4.67 mmol). The yellow suspension was stirred for 3 d, turning dark red over the course of the reaction, then the solvent was removed in vacuo to give a maroon solid. The product was extracted into toluene (15 mL), filtered to remove insoluble LiCl, concentrated to a volume of 5 mL, and cooled to -40 °C to give dark maroon crystals. (1.10 g, 82.7% yield)

<sup>1</sup>H NMR (C<sub>6</sub>D<sub>6</sub>, 500 MHz): δ 7.47 (d, 16H, Ph-*H*), 6.51 (d, 16H, Ph-*H*), 2.67 (s, 24H, Ph-*CH*<sub>3</sub>).

IR (cm<sup>-1</sup>): 1606 (w), 1505 (s), 1326 (w), 1295 (m), 1263 (s), 1191 (m), 1164 (w), 1110 (w), 1040 (w), 1016 (w), 965 (w), 844 (w), 820 (m), 747 (w), 653 (w), 616 (w), 511 (w).

EA calcd for C<sub>56</sub>H<sub>56</sub>N<sub>12</sub>U: C: 59.25%, H: 4.97%, N: 14.81%. Found: C: 59.19%, H: 5.05%, N: 14.66%.

Melting point: Decomposes *ca.* 175 °C.

**Th(BPTT)<sub>4</sub>(THF)**: A THF solution (1 mL) of ThCl<sub>4</sub>(DME)<sub>2</sub> (53 mg, 0.096 mmol) was added dropwise to a THF solution (2 mL) of Li(BPTT)(THF) (115 mg, 0.369 mmol). The yellow solution turned orange over the course of the reaction. The solution was stirred for 20 h, then the solvent was removed *in vacuo* to give orange solids, which were triturated with hexane. The product was then extracted into toluene (2 mL), filtered, and concentrated to 0.5 mL. Orange crystals of the final product were collected by layering hexane (1.5 mL) on top of the toluene solution and cooling to -40 °C overnight (87 mg, 78% yield).

<sup>1</sup>H NMR (C<sub>6</sub>D<sub>6</sub>, 500 MHz): δ 7.46 (d, 16H, Ph-*H*), 6.89 (d, 16H, Ph-*H*), 3.76 (s, 4H, OCH<sub>2</sub>CH<sub>2</sub>), 2.02 (s, 24H, Ph-*CH*<sub>3</sub>), 1.02 (s, 4H, OCH<sub>2</sub>CH<sub>2</sub>).

<sup>13</sup>C NMR (C<sub>6</sub>D<sub>6</sub>, 151 MHz): δ 148.43 (Ph), 134.44 (Ph), 129.94 (Ph), 120.41 (Ph), 25.41 (OCH<sub>2</sub>CH<sub>2</sub>), 21.21 (Ph-*CH*<sub>3</sub>).

IR (cm<sup>-1</sup>): 1607 (w), 1522 (w), 1505 (m), 1331 (w), 1298 (m), 1267 (m), 1109 (w), 1015 (w), 818 (m), 753 (w), 652 (w), 618 (w), 516 (w).

EA calcd for C<sub>60</sub>H<sub>64</sub>N<sub>12</sub>OTh: C: 59.99%, H: 5.37%, N: 13.99%. Found: C: 60.14%, H: 5.59%, N: 13.90%.

Melting point: decomposes *ca.* 79 °C.

**[U(BPT)<sub>5</sub>]Li(THF)<sub>4</sub>**: A THF solution (3 mL) of UCl<sub>4</sub> (74 mg, 0.196 mmol) was added to a THF solution (3 mL) of Li(BPT)(THF) (215 mg, 0.782 mmol) dropwise. The maroon solution darkened over the course of the reaction. The solution was stirred for 3 d, then the solvent was removed *in vacuo* and the product was triturated with hexane (3 mL). The resulting oily maroon solid was extracted into Et<sub>2</sub>O (5 mL), filtered, concentrated to 3 mL, and cooled to -40 °C, yielding small maroon crystals. (117 mg, 59% yield)

<sup>1</sup>H NMR (C<sub>6</sub>D<sub>6</sub>, 500 MHz): δ 7.97 (t, 16H, Ph-*H*), 7.45 (d, 16H, Ph-*H*), 6.38 (t, 8H, Ph-*H*), -2.68 (broad, 16H, OCH<sub>2</sub>CH<sub>2</sub>), -6.65 (broad, 16H, OCH<sub>2</sub>CH<sub>2</sub>).

IR (cm<sup>-1</sup>): 1592 (m), 1482 (m), 1343 (w), 1326 (w), 1299 (m), 1255 (s), 1229 (m), 1163 (m), 1151 (w), 1072 (w), 1039 (m), 1023 (w), 997 (w), 959 (w), 895 (w), 832 (w), 757 (s), 690 (s), 650 (m), 613 (w), 517 (m).

Melting point: decomposes *ca.* 75 °C.

**[Th(BPT)<sub>5</sub>]Li(THF)<sub>4</sub>**: A THF solution (2 mL) of ThCl<sub>4</sub>(DME)<sub>2</sub> (109 mg, 0.197 mmol) was added dropwise to a THF solution (3 mL) of Li(BPT)(THF) (217 mg, 0.787 mmol). The maroon solution turned green over the course of the reaction. The solution was stirred for 3 d, then the solvent was removed *in vacuo* and the product was triturated with hexane (3 mL). The resulting oily green solid was extracted into Et<sub>2</sub>O (4 mL), filtered twice, and cooled to -40 °C, yielding green crystals. (114 mg, 57% yield)

<sup>1</sup>H NMR (C<sub>6</sub>D<sub>6</sub>, 600 MHz): δ 7.41 (t, 16H, Ph-*H*), 7.02 (d, 16H, Ph-*H*), 6.85 (t, 8H, Ph-*H*), 3.59 (broad, 16H, OCH<sub>2</sub>CH<sub>2</sub>), 1.22 (broad, 16H, OCH<sub>2</sub>CH<sub>2</sub>).

<sup>13</sup>C NMR (C<sub>6</sub>D<sub>6</sub>, 151 MHz): δ 150.40 (Ph), 129.26 (Ph), 125.41 (Ph), 120.60 (Ph), 25.88 (OCH<sub>2</sub>CH<sub>2</sub>).

7.41 (t, 16H, Ph-*H*), 7.02 (d, 16H, Ph-*H*), 6.85 (t, 8H, Ph-*H*), 3.59 (broad, 16H, OCH<sub>2</sub>CH<sub>2</sub>), 1.22 (broad, 16H, OCH<sub>2</sub>CH<sub>2</sub>).

IR (cm<sup>-1</sup>): 1593 (m), 1483 (m), 1341 (w), 1327 (m), 1299 (m), 1259 (s), 1231 (m), 1165 (m), 1152 (w), 1073 (w), 1040 (m), 1024 (w), 998 (w), 958 (w), 894 (w), 831 (w), 757 (s), 691 (s), 652 (m), 614 (w), 518 (m).

Melting point: decomposes *ca.* 65 °C.

**UCl(NTT)<sub>3</sub>**: An Et<sub>2</sub>O solution (5 mL) of Li(NTT) (143 mg, 0.807 mmol) was added to an Et<sub>2</sub>O solution (3 mL) of UCl<sub>4</sub> (102 mg, 0.269 mmol) maintained at -40 °C. The green UCl<sub>4</sub> solution turned orange-brown upon addition of Li(NTT). The solution was stirred for 5 d, then the solvent was removed *in vacuo* and the resulting brown solids were triturated with hexane (2 mL). The product was extracted into pentane (2 mL), filtered, concentrated to a final volume of 1 mL, and cooled to -40 °C, yielding brown crystals. (112 mg, 53% yield)

<sup>1</sup>H NMR (C<sub>6</sub>D<sub>6</sub>, 500 MHz): δ 20.76 (s, 6H, CH<sub>2</sub>C(CH<sub>3</sub>)<sub>3</sub>), 1.23 (s, 27H, CH<sub>2</sub>C(CH<sub>3</sub>)<sub>3</sub>), -0.63 (s, 27H, C(CH<sub>3</sub>)<sub>3</sub>).

IR (cm<sup>-1</sup>): 1364 (m), 1288 (w), 1253 (m), 1242 (m), 1214 (m), 1183 (w), 1122 (w), 1048 (w), 1023 (w), 915 (w), 895 (w), 624 (w), 582 (w).

Melting point: Decomposes *ca.* 50 °C.

**Th(N<sub>3</sub>)(BIMA)<sub>3</sub>**: THF (50 mL) was added via cannula to a flask containing ThCl(BIMA)<sub>3</sub> (507 mg, 0.734 mmol) and NaN<sub>3</sub> (52 mg, 0.800 mmol). The resulting solution was stirred for 2 d, then the solvent was removed *in vacuo*. The product was triturated with hexane (30 mL), then extracted into Et<sub>2</sub>O (20 mL). The resulting colorless solution was filtered, concentrated to a final volume of 10 mL and cooled to -40 °C for 2 d, yielding colorless crystals. (369 mg, 72% yield)

<sup>1</sup>H NMR (C<sub>6</sub>D<sub>6</sub>, 400 MHz): δ 3.55 (m, 6H, CH(CH<sub>3</sub>)<sub>2</sub>), 1.56 (s, 9H, NCCH<sub>3</sub>), 1.25 (d, 36H, CH(CH<sub>3</sub>)<sub>2</sub>).

<sup>13</sup>C NMR (C<sub>6</sub>D<sub>6</sub>, 151 MHz): 173.41 (NCN), 48.43 (CH(CH<sub>3</sub>)<sub>2</sub>), 25.01 (CH(CH<sub>3</sub>)<sub>2</sub>), 12.24(NCCH<sub>3</sub>).

IR (cm<sup>-1</sup>): 2087 (s), 1438 (s), 1413 (s), 1336 (s), 1312 (m), 1260 (w), 1201 (s), 1137 (w), 1123 (m), 1051 (w), 1014 (m), 914 (w), 806 (m), 617 (m), 607 (w), 573 (w), 543 (w).

Melting point: decomposes *ca.* 264 °C.

## X-Ray Crystallography

In a dry nitrogen glovebox, single crystals were coated in Paratone-N oil for transport to diffraction facilities. Crystals were mounted on either a Kapton loop or on a MiTeGen 10  $\mu\text{m}$  aperture Dual-Thickness MicroMount. X-ray diffraction data were collected at the Advanced Light Source (ALS), Lawrence Berkeley National Laboratory, Berkeley, CA, beamline 12.2.1 using a silicon double crystal monochromator to provide a beam of 17 keV ( $\lambda = 0.7288 \text{ \AA}$ ), or at CheXray, Berkeley, CA, using a Rigaku XtaLAB P200 equipped with a MicroMax-007 HF microfocus rotating anode and a Pilatus 200K hybrid pixel array detector, using Mo  $K_{\alpha}$  radiation ( $\lambda = 0.71073 \text{ \AA}$ ). All data collections were conducted at 100 K, with the crystals cooled by a stream of dry nitrogen. For data collected at the ALS, Bruker APEX3 software was used for the data collections, Bruker SAINT V8.38A software was used to conduct the cell refinement and data reduction procedures, and absorption corrections were carried out by a multi-scan method utilizing the SADABS program.<sup>16</sup> For data collected at CheXray, CrysAlisPro was used for the data collections and data processing, including a multi-scan absorption correction applied using the SCALE3 ABSPACK scaling algorithm within CrysAlisPro.<sup>17</sup> Initial structure solutions were found using direct methods (SHELXT),<sup>18</sup> and refinements were carried out using SHELXL-2014,<sup>19</sup> as implemented by Olex2.<sup>20</sup> Thermal parameters for all non-hydrogen atoms were refined anisotropically. Thermal ellipsoid plots were made using Mercury.<sup>21</sup>

**Table A1:** Crystallographic details and refinement metrics for compounds  $U(TPTA)_4$ ,  $[UO_2(ITA)_2]_2$ , and  $[UO_2(TDA)_2]_2$ .

	<b><math>U(TPTA)_4</math></b>	<b><math>[UO_2(ITA)_2]_2</math></b>	<b><math>[UO_2(TDA)_2]_2</math></b>
Chemical formula	$C_{60}H_{88}N_4O_4U$	$C_{32}H_{64}N_4O_8U_2$	$C_{68}H_{104}N_4O_8U_2$
Formula weight	1167.37	1108.93	1581.61
Color, habit	Green, block	Orange, block	Orange, block
Crystal system	Triclinic	Monoclinic	Monoclinic
Space group	P-1	$P2_1/c$	$P2_1/n$
a (Å)	11.0664(3)	11.708(1)	16.0280(8)
b (Å)	14.3663(4)	12.263(1)	13.8607(7)
c (Å)	21.1094(7)	30.240(2)	16.9996(6)
$\alpha$ (°)	73.916(2)	90	90
$\beta$ (°)	89.913(2)	100.266(2)	112.506(2)
$\gamma$ (°)	67.476(2)	90	90
V (Å <sup>3</sup> )	2957.9(2)	4272.2(4)	3489.0(3)
Z	2	4	2
Density (g/cm <sup>3</sup> )	1.311	1.724	1.505
F(000)	1200	2128	1576
Radiation Type	Mo K $\alpha$	Synchrotron	Mo K $\alpha$
$\mu$ (mm <sup>-1</sup> )	2.789	3.510	4.688
Crystal size (mm)	0.20 x 0.18 x 0.14	0.20 x 0.20 x 0.20	0.14 x 0.12 x 0.10
Meas. Refl.	37823	55993	71066
Indep. Refl.	10428	9789	7173
Obsvd. Refl. ( $I > 2\sigma(I)$ )	9466	9457	5940
R <sub>int</sub>	0.0535	0.0731	0.0606
R <sub>1</sub> / wR <sub>2</sub> ( $I > 2\sigma(I)$ )	0.0493, 0.0922	0.0377, 0.0933	0.0328, 0.0759
R <sub>1</sub> / wR <sub>2</sub> (all data)	0.0574, 0.0944	0.0388, 0.0943	0.0427, 0.0794
Goodness-of-fit	1.163	1.177	1.072

**Table A2:** Crystallographic details and refinement metrics for compounds  $U(BPTT)_4$ ,  $Th(BPTT)_4(THF)$ ,  $[Th(BPT)_5]Li(THF)_4$ , and  $Th(N_3)(BIMA)_3$ .

	<b>U(BPTT)<sub>4</sub></b>	<b>Th(BPTT)<sub>4</sub>(THF)</b>	<b>[Th(BPT)<sub>5</sub>] Li(THF)<sub>4</sub></b>	<b>Th(N<sub>3</sub>)(BIMA)<sub>3</sub></b>
Chemical formula	C <sub>56</sub> H <sub>56</sub> N <sub>12</sub> U	C <sub>60</sub> H <sub>64</sub> N <sub>12</sub> OTh	C <sub>60</sub> H <sub>50</sub> N <sub>15</sub> Th, C <sub>16</sub> H <sub>32</sub> LiO <sub>4</sub>	C <sub>24</sub> H <sub>51</sub> N <sub>9</sub> Th
Formula weight	1135.15	1201.27	1508.54	697.77
Color, habit	Red, rod	Orange, block	Yellow, tablet	Colorless, block
Crystal system	Monoclinic	Triclinic	Monoclinic	Monoclinic
Space group	P2 <sub>1</sub> /n	P-1	P2 <sub>1</sub> /n	P2/n
a (Å)	14.942(1)	12.317(7)	14.766(1)	17.643(1)
b (Å)	15.241(1)	14.213(8)	19.601(2)	10.297(1)
c (Å)	23.458(1)	16.985(16)	24.723(2)	34.139(2)
α (°)	90	98.13(3)	90	90
β (°)	107.828(2)	108.19(3)	102.259(4)	97.736(2)
γ (°)	90	100.60(2)	90	90
V (Å <sup>3</sup> )	5085.7(4)	2713(3)	6992.1(1)	6145.4(5)
Z	4	2	4	8
Density (g/cm <sup>3</sup> )	1.483	1.471	1.433	1.508
F(000)	2272	1212	3072	2784
Radiation Type	Synchrotron	Mo K <sub>α</sub>	Synchrotron	Synchrotron
μ (mm <sup>-1</sup> )	1.519	2.801	2.338	5.202
Crystal size (mm)	0.210 x 0.045 x 0.030	0.05 x 0.05 x 0.04	0.100 x 0.085 x 0.025	0.06 x 0.06 x 0.05
Meas. Refl.	72846	33670	89215	80194
Indep. Refl.	10464	9926	12799	11605
Obsvd. Refl. (I>2σ(I))	8957	7930	9928	10090
R <sub>int</sub>	0.0595	0.0856	0.0734	0.0876
R <sub>1</sub> / wR <sub>2</sub> (I>2σ(I))	0.0261, 0.0577	0.0512, 0.0927	0.0485, 0.1030	0.0336, 0.0829
R <sub>1</sub> / wR <sub>2</sub> (all data)	0.0343, 0.0617	0.0706, 0.0988	0.0692, 0.1112	0.0382, 0.0865
Goodness-of-fit	1.026	1.000	1.120	1.033

## References

- 1 M. D. Straub, J. Leduc, M. Frank, A. Raauf, T. D. Lohrey, S. G. Minasian, S. Mathur and J. Arnold, *Angew. Chem. Int. Ed.*, 2019, **58**, 5749–5753.
- 2 L. Sweet, C. J. Henager, S. Hu, T. Johnson, D. Meier, S. Peper and J. Schwantes, *Investigation of Uranium Polymorphs*, 2011.
- 3 K. Soussi, S. Mishra, E. Jeanneau, A. Mantoux and S. Daniele, *Polyhedron*, 2018, **152**, 84–89.

- 4 K. Soussi, S. Mishra, E. Jeanneau, J. M. M. Millet and S. Daniele, *Dalton Trans.*, 2017, **46**, 13055–13064.
- 5 K. Soussi, Claude Bernard University Lyon Dissertation, 2017.
- 6 S. J. Kraft, P. E. Fanwick and S. C. Bart, *Organometallics*, 2013, **32**, 3279–3285.
- 7 T. P. Ahern, H. Fong and K. Vaughan, *Can. J. Chem.*, 1977, **55**, 1701–1709.
- 8 N. S. Settineri, M. E. Garner and J. Arnold, *J. Am. Chem. Soc.*, 2017, **139**, 6261–6269.
- 9 M. J. Monreal, R. K. Thomson, T. Cantat, N. E. Travia, B. L. Scott and J. L. Kiplinger, *Organometallics*, 2011, **30**, 2031–2038.
- 10 D. M. King, F. Tuna, E. J. L. McInnes, J. McMaster, W. Lewis, A. Blake and S. T. Liddle, *Science*, 2012, **337**, 717–720.
- 11 S. J. Simpson, H. W. Turner and R. A. Andersen, *Inorg. Chem.*, 1981, **20**, 2991–2995.
- 12 R. A. Andersen, *Inorg. Chem.*, 1979, **18**, 1507–1509.
- 13 M. P. Wilkerson, C. J. Burns, R. T. Paine and B. L. Scott, *Inorg. Chem.*, 1999, **38**, 4156–4158.
- 14 R. A. Andersen, *Inorg. Chem.*, 1979, **18**, 209.
- 15 T. Cantat, B. L. Scott, and J. L. Kiplinger, *Chem. Commun.*, 2010, **46**, 919.
- 16 APEX3, SADABS, and SAINT. Bruker AXS. Madison, WI, USA.
- 17 CrysAlisPro 1.171.39.45f (Rigaku Oxford Diffraction, 2018).
- 18 G. M. Sheldrick, *Acta Cryst.*, 2008, **A64**, 112–122.
- 19 G. M. Sheldrick, *Acta Cryst.* 2015, **C71**, 3–8.
- 20 O. V. Dolomanov, L. J. Bourhis, R. J. Gildea, J. A. K. Howard and H. Puschmann, *J. Appl. Crystallogr.*, 2009, **42**, 339–341.
- 21 C. F. Macrae, I. J. Bruno, J. A. Chisholm, P. R. Edgington, P. McCabe, E. Pidcock, L. Rodriguez-Monge, R. Taylor, J. Van De Streek and P. A. Wood, *J. Appl. Crystallogr.*, 2008, **41**, 466–470.